ULTRAVIOLET DAMAGE TO FUSED SILICA

by

Richard Elliot Schenker

Memorandum No. UCB/ERL M97/20

3 March 1997

ULTRAVIOLET DAMAGE TO FUSED SILICA

by

Richard Elliot Schenker

Memorandum No. UCB/ERL M97/20

3 March 1997

Abstract

Ultraviolet Damage to Fused Silica

by

Richard Elliot Schenker

Doctor of Philosophy in Engineering

University of California, Berkeley

Professor William G. Oldham, Chair

Ultraviolet (UV)-induced damage in fused silica is investigated to identify and predict the limitations of using refractive optics in UV lithography. A 193nm ArF laser and a 213nm frequency quintupled Nd-YAG laser are used to characterize UV-induced compaction and color center formation in fused silica, the primary optical material used in UV-lithography systems.

A new technique using birefringence measurements is developed which enables the real-time monitoring of irradiation-induced compaction. The method is capable of measuring compaction in the 10 parts per billion range, orders of magnitude more sensitive than interferometric methods. Densification induced from lithographic intensity levels can be measured in less than 6 hours. Using this method, a universal relation describing UV-induced compaction is discovered in which, using the total energy absorbed from two-photon absorption as the dose parameter, density changes equal a material dependent constant times the dose parameter to a power of about 0.7. This dose dependence is consistent with past compaction studies using electron beam and gamma radiation, suggesting like densification mechanisms. A two-photon absorption damage mechanism is supported by the observation that color center formation and compaction show a super-linear dependence on pulse intensity and have damage rates which scale with the two-photon absorption coefficient of the radiation wavelength.

Several different fused silicas are evaluated for their durability to UV-irradiation. Drastically different transient and thermal properties between color center formation and compaction are observed, indicating two distinct damage forms. Despite having

equivalent two-photon absorption coefficients, substantially different damage rates are found among the fused silicas; implying that subtle differences in the material synthesis process are important to damage susceptibility.

To determine how the optical properties of a damaged element are effected, we characterize the components contributing to optical path difference (OPD) in damaged fused silica. Polarizability changes resulting from compaction are extracted in order to establish the relation between refractive index changes and density changes in fused silica. Using known physical relations, experimental data and finite element analysis, we describe the dependence of OPD on sampling wavelength and exposure geometry.

The evaluation of the effects of damage is then extended to a complicated optical system. Using the experimental compaction rates, ray-tracing and Fourier optics, a prediction of practical lifetime is made for a model lithographic system. We find that index changes greater than about 50ppB are unacceptable in some elements in the model system, whereas a factor of 10 higher compaction-induced index changes are acceptable in other elements. The estimated useful life of the model system depends strongly on the throughput, resist sensitivity, and partial coherence. Based on the degradation performance of today's best fused silica, we predict that a resist with high sensitivity (5 - 20 mJ/cm^2) will be needed to insure acceptable 193-nm lithographic system lifetime under production conditions.

Prof. W.G. Oldham
Committee Chairman

Dedicated to my family

Table of Contents

Acknowledgments

I would like to express my appreciation first to Professor William G. Oldham for serving as my research advisor. Throughout my four years here at Berkeley, his guidance has been clear and insightful. I would also like to thank Professors Andy Neureuther, Jeff Bokor and Sanjay Govindjee from which I have also learned a great deal.

My fellow students, both past and present have made my experience at Berkeley truly excellent. John Hutchinson patiently served as my mentor when I first arrived despite the pressure of the final "crunch" of finishing his dissertation which I only now fully appreciate. Charlie Fields, Bob Socha and Edita Tejnil were all in my "generation" of students and have been great people to bounce ideas off of whether at work or at Jupiter's. It was good to go to work and have so many friends there. I would also like to thank Fan Piao who will follow up on this work. I hope that I have been able to repay John's help though him.

This work would not have been nearly as rewarding were not for the support of several people out in the "real world". I thank Paul Schermerhorn of Corning for getting me started on the study of fused silica and Douglas Allan also of Corning for his help with interferometry measurements and for invaluable discussions. Mordy Rothschild's group at MIT-Lincoln Labs. was also a key resource in our research, both because of Jan Sedlacek's tutoring on running excimer laser and Mordy's expertise advice on materials research. Working with them was truly a pleasure. Even though more than two years have past since the summer I spent at Bell Labs. in Murray Hill, I am still in awe at the ability of Lou Eichner and Hem Vaidya to turn a trash heap into a working laser. There skill and good humor inspired me even on the swampiest days of the New Jersey summer. I also thank Sheila Vaidya for the chance to work in her group at Bell Labs.

The earliest experiments performed in this work were performed in the Berkeley microlab. Richard Hsu, formally of the microlab staff, "showed me the ropes" in GL4 for which I think him. One of the highlights of this work was the building of a new laser laboratory here in Cory Hall. I must thank the Berkeley microlab and especially Phil

Chapter 1

Background

1.1 Introduction

Improvements and innovations in optical lithography have been one of the main driving forces in the production of ever denser integrated circuits (ICs). In order to continue this progress, lower wavelength radiation sources will be used to allow for printing of even smaller device patterns. Currently, 248-nm lithography (KrF excimer laser source) is being used in advanced production to manufacture device features of $0.25\mu m$. The introduction of 193-nm lithography (ArF excimer laser source) in production for future device "generations" seems almost inevitable. While the ArF source offers the obvious advantage of high power at a short wavelength, the use of 193-nm radiation adds constraints to the already difficult task of designing a large field, high numerical aperture (NA), lithography system. Perhaps most restrictive is the availability of only one material at this time, fused silica, as an optical material with enough transmission, surface quality and homogeneity to be used in a diffraction-limited system. Fused silica itself adds yet another constraint in that it undergoes compaction and forms absorptive E' color centers when ultraviolet (UV) irradiated. Experiments, simulations, and analytical modeling were conducted to characterize the limitations of using refractive optics in UV lithography.

The study of the intrinsic properties and structure of fused silica is a field of research on its own. Because of the relevance to the study of radiation-induced changes to fused silica, a

summary review of the structure of fused silica and the different types are fused silica is included in this chapter. Thousands of papers are already published dealing the effects of radiation on optical materials. The chapter also summarizes some of the basic understanding of the mechanisms behind radiation-induced damage in materials. A summary of significant previous work on the two major forms of UV-induced damage in fused silica, compaction and color center formation, is included in this chapter. Because of the quantity of earlier work, this review is not comprehensive.

1.2 Types of Fused Silica

Like quartz, the basic building block of fused silica is SiO_2. Unlike quartz, fused silica is an amorphous solid, thus long range order. So despite the like chemical structure, quartz and fused silica have significantly different mechanical and optical properties and must be treated as two distinct materials.

Bruckner[1] describes the different types of silica glasses:

Type 1 - Type 1 silica glasses are produced from natural quartz by electrical fusion in an inert atmosphere or vacuum. They tend to contain high levels of metallic impurities especially Al and Na. They generally contain less than 5ppm OH groups. Examples are Infrasil[2], IR-Vitreosil[3], G. E[4]. 105, 201 and 204.

Type 2 - Type 2 silica glasses are produced by flame fusion of quartz crystal powder. Metallic impurities are lower than type 1 glasses and OH levels range from 150-400ppm. Some examples are Herasil[2], Homosil[2], Optosil[2], O. G. Vitreosil[3], T-08[2] and G. E. 104. Ultrasil[2] is a type 2 glass which also receives a special thermal treatment in an oxygen atmosphere to improve UV transparency.

Type 3 - Type 3 fused silica glasses are produced by hydrolyzation of $SiCl_4$ when spraying into an oxygen-hydrogen flame. The material is almost totally free of metallic impurities but contains about 1000ppm OH. Chlorine concentrations can be as high as 100ppm. Suprasil[2], Spectrosil[3] and Corning 7940 are type 3 silica glasses. Suprasil 1, 2 and 3 differ only in level of homogeneity with Suprasil 1 being the most homogeneous. All UV-grade fused silicas are type 3 silica. Corning 7940 uses CH_4 as the hydrogen source instead of H_2.

Type 4 - Type 4 silica glasses are manufactured from $SiCl_4$ in a water vapor-free plasma flame. They are similar to type 3 silica glass except they contain less than 1ppm OH. They are generally used for IR applications where the presence of OH results in additional absorption bands in the IR spectra. Trade names include Suprasil W[2], Spectrosil WF[3], and Corning 7943.

Type 5 - Glasses manufactured using newer proprietary synthetic processes will be grouped in Type 5. Examples include Suprasil[2] 200, 300, 311, and 312; Corning 7957 and

7980. Suprasil 311 (OH content ~ 200 ppm) is a three-dimensionally homogeneous

version of Suprasil 312 and is the most homogeneous fused silica produced by Heraeus.

The same starting material used to manufacture Suprasil 311 is chemically dehydrated to

make Suprasil 300 (less than 1 ppm OH).

1.3 Structure of Undamaged Fused Silica

In order to be able to describe the effects of radiation on fused silica, an undamaged or

ideal structure needs to be defined for silica. Raman spectroscopy[5], X-ray[6] and neutron

diffraction measurements serve as the best tools for gaining insight into the structure of

fused silica. The transform of diffraction spectra, in the absence of intrinsic scattering, can

be considered proportional to the electron distribution in the material which in turn gives

structural information. Because neutrons penetrate much deeper into a material, neutron

diffraction tends to provide more information on bulk structure than do X-ray diffraction

experiments. Raman spectroscopy generally gives information on the strength of

molecular vibrational models in the material which in turn provides structural information.

In 1932 Zachariasen[7] proposed a continuous random network (CRN) theory of the glass

structure. The basic concept to the model is that vitreous silica is composed of SiO_2

building blocks where the O - Si - O bond angles are held relatively constant (109.5°)

while the Si - O - Si bond angle is allowed to randomly vary over a wide range centered

around an angle of about 150°. The Si - O bond distance is held constant while the Si - Si

distance varies depending upon bonding angles. Since then, several continuous random

network models[8,9] have been constructed that agree with X-ray[10,11,12,13] and neutron[14]

diffraction studies of fused silica. CRN models[15] differ in the distribution of bond angles and in ring sizes. The size of a ring is defined as the number of silicon atoms contained in the shortest bonding path required to form a closed loop of alternating silicon and oxygen atoms.

While the CRN model for the structure of vitreous silica is generally accepted, other models[16,17,18] describing glass as an ensemble of "micro-crystals" have been published which agree with X-ray diffraction data. Debate over the molecular structure of vitreous silica has been on-going for over half a century. At the recent forefront of the debate is the ability of two models to describe the D_1 and D_2 bands in the Raman spectra of vitreous silica. The D_1 and D_2 bands are narrow peaks at $495cm^{-1}$ and $606cm^{-1}$ in the Raman spectra, which, unlike the broader bands in the spectrum, have magnitudes that depend strongly upon the fabrication method. The presence of the bands is not predicted by the conventional CNR model[19]. Phillips[20] assigns the bands to surface vibrational modes at cristobalite interfaces. Galeener[21] argues that the bands result from the presence of planer 3 and 4 member ring structures within the CRN structure (D_2 and D_1 bands respectively). The controversy is somewhat put to rest by the recent development of high-resolution solid state nuclear magnetic resonance spectroscopy using magic angle sample spinning (MASS NMR). The method is able to deduce changes in the average Si-O-Si bond angle[22]. Comparison of MASS NMR data to Raman spectra for samples exposed to a variety of different heat treatments and hydration steps correlated the formation of the D_2 band to a decrease in average Si-O-Si bond angle which is consistent with the formation of

5

strained three member rings. Brinker[22] writes, "our results unambiguously relate the 608 cm $^{-1}$ Raman 'defect' in a-SiO$_2$ with reduced Si-O-Si bond angles indicative of strained 3-membered rings of silicate tetrahedra." Griscom[23] also criticizes the micro-cristobalite model because the intercluster bonding that would be required is inconsistent with defect densities and absorbance spectra. Galeener devotes an entire publication[24] to point out the short-comings of the micro-cristobalite model.

1.4 Basic Damage Mechanisms

"Damage" is defined as the existence of post-irradiation local structures (either atomic or electronic) which are different from the original structure[25]. The energy to induce damage can be provided by a wide range of sources including UV light, X-rays, γ-rays, electron beams, ion beams and neutrons. Energy from those particles can be transferred either by a radiolytic ("ionization") or a knock-on process (only for electrons, ions and neutrons)[26]. Knock-on damage results from the direct transfer of momentum and energy from the incident particle or secondary particle to the lattice via a collision. Energy transfer from a radiolytic processes occurs when a radiation generated electron-hole pair recombines nonradiatively so as to transfer its energy to the lattice.

The majority of work on optical material damage is centered on what can be considered "catastrophic" damage. Such studies are concerned with very high power laser applications (Joules per square centimeter) for single pulse or very low pulse count applications (less than 1000). The damage associated with "catastrophic" damage is

severe enough to produce defects visible to the unaided eye. The basic mechanism behind single-shot damage for most dielectrics is a radiation-induced electron avalanche process[27]. In the electron avalanche process, intrinsic photon-induced electrons interact with the high applied electric field from the laser pulse. If the rate at which the electrons receive energy exceeds that which they lose from electron-phonon interactions, they gain a large amount of energy. When the energetic electrons collide with the lattice, additional electron-hole pairs are produced providing positive feedback to the ionization process. The entire process is thus highly non-linear. A threshold energy density is assigned to a material at which the electric field generally induces a plasma at the surface. For pulse widths longer than a few pico-seconds, the ionization rate depends on the electric field strength and is thus proportional to the square root of the pulse width[28]. For some materials, single-shot damage is initiated by heating of localized inclusions or defects[29] in the sample rather than by the electron avalanche process.

The types of damage presented in this thesis yield gradual and subtle changes in the optical properties of fused silica over several thousands to billions of pulses. Often, changes of properties in the parts per billion range will be considered important. The basic damage process here is a radiolytic process where radiation-induced electron-holes recombine to provide energy for structural or electronic changes in the material. Because fused silica is an insulator, the electron-hole pairs are effectively localized and are more precisely referred to as excitons[30].

1.5 Color Center Formation

1.5a Structural Form of Color Centers

A wealth of data[31-61] exist on UV-induced color center formation in fused silica. Color centers are structural defects which correspond to induced absorption bands in the optical spectrum of a material. The formation of color centers can reduce transmission through a lithography system. Absorption-induced temperature changes, furthermore, cause refractive index changes which can induce imaging aberrations in a lithographic system. The E' color center produces an absorption band centered around 210 to 215nm with a full width at half maximum (FWHM) of about 50nm so is therefore of considerable concern for UV applications. Electron spin resonance (ESR)[62] studies[26] have thoroughly characterized the structure of the E' center to be a silicon atom bonded to only three oxygens with a single unpaired electron. Three distinct E' center variants, differing in the structure of the nearest neighbors to the E' center, are identified[26] in fused silica. The E'$_\alpha$ center is predominant in dry fused silicas and the E'$_\beta$ center is predominant in high OH content fused silicas. The reactions producing the E' centers are as follows:

$$\text{E'}_\alpha\text{:} \quad \equiv\text{Si - O - Si}\equiv \Rightarrow \equiv\text{Si}^+ + =\text{Si}\bullet\text{ - O - O} + \text{e}^- \tag{1}$$

$$\text{E'}_\beta\text{:} \quad \equiv\text{Si}^+ + \text{H} \Rightarrow \equiv\text{Si}\bullet + \text{H}^+ \tag{2}$$

$$\text{E'}_\gamma\text{:} \quad \equiv\text{Si - O - Si}\equiv \Rightarrow \equiv\text{Si}^+ + \equiv\text{Si}\bullet + \text{O} + \text{e}^- \tag{3}$$
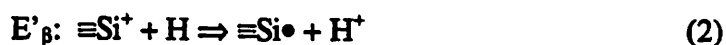
where the symbol (≡) represents bonding to three oxygens, (=) represents bonding to two oxygens, (•) represents an unpaired electron, and (≡Si•) is the E' center, a silicon atom bonded to three oxygens with a single unpaired electron.

Another important defect formed from UV-radiation is the non-bridging oxygen hole center (NBOHC) which is an oxygen bonded to only one silicon atom and having one unpaired electron[63]. "Wet" fused silicas have a natural annealing mechanism for the NBOHC where a mobile hydrogen can bond to the unpaired electron in the oxygen[64]. An absorption band centered around 260nm with a FWHM of about 40nm is often attributed to the NBOHC. Griscom[65] reviews the experimental evidence to support this theory and also describes some new data which conflict with this designation. One of the biggest contradictions with this model is the observation that 5 eV laser bleaching of the 260nm absorption band is accompanied by no change in the NBOHC ESR signal[66]. Additional studies[67] also show no correlation between the ESR signal and isochronal annealing behavior of the 260nm absorption band induced when the band is generated with 157nm irradiation in Suprasil W. Tsai[68] gives evidence that the 260nm absorption band results from the formation of unrelaxed oxygen deficiency centers (ODC's) which have the structural form (≡Si - Si≡).

Another color center of interest is the Peroxy[69] Radical which is an oxygen bonded to an oxygen and having an unpaired electron. The Peroxy Radical is generally attributed to an

absorption band with a peak around 163 - 167nm. The peak is about 15nm in full width at half maximum so has little effect on transmission at 193 or 248nm.

1.5b Dose Dependence of Color Center Formation

When incident UV-laser pulse counts are held constant, the defect concentration in fused silica is generally found to depend approximately on the pulse intensity squared[56,70,71]. This suggests a two-photon damage mechanism because the total energy absorbed via two-photon absorption also depends on the pulse intensity squared. A two-photon damage mechanism becomes somewhat intuitive when one considers that two UV-photons (5 - 6.5 eV) are required to surpass the effect bandgap of fused silica (~ 8.5 eV). The role of two-photon absorption in damage will be developed further in Chapter 4.

The dose dependence of the two most studied defects, the E' color center and the NBOHC, has been found to follow a power law that is:

$$\eta = A \, D^c \tag{4}$$

where η is the defect density (proportional to the ESR spin count), D is the dose and A and c are constants. The power c varied with the type of radiation and fused silica. Table 1 summarizes the extracted dose exponent coefficients (c) obtained from ESR measurements. A discussion of the origin of the power law is included in Chapter 8.

Table 1
Dose Exponent for Defect Formation from Previous Studies

Work	Radiation Source	Defect Density Range (spins/cm^3)	Fused Silica	Defect	Dose Exponents
Griscom[40]	X-ray (77°K)	2×10^{13} - 2×10^{15}	Suprasil 1	E'	0.88
	X-ray (77°K)	2×10^{14} - 10^{16}	Suprasil 1	OHC$	0.65*
	193nm (77°K)	10^{14} - 10^{15}	Suprasil 1	OHC$	0.35*
	X-ray (77°K)	2×10^{13} - 2×10^{15}	Suprasil W1	E'	0.7
	X-ray (77°K)	2×10^{14} - 10^{16}	Suprasil W1	OHC$	0.7
	193nm (77°K)	10^{14} - 10^{15}	Suprasil W1	OHC$	0.65*
Galeener[72]	X-ray	1 order of mag.#	Suprasil 1	E'	1
	X-ray	1 order of mag.#	Suprasil 1	NBOHC	0.6*
	X-ray	1 order of mag.#	Suprasil W1	E'	0.6*
Imai[73]	gamma	5×10^{14} - 3×10^{16}	"dry" silicas	E'	0.55*
	gamma	5×10^{14} - 10^{16}	"dry" silicas	NBOHC	0.45*
	193nm, 248nm	10^{14} - 10^{16}	"dry" silicas	E'	0.65*
Devine[74]	gamma	10^{14} - 3×10^{15}	Suprasil 1	E'	0.77
	gamma	10^{15} - 10^{16}	Suprasil 1	NBOHC	0.69
	gamma	10^{14} - 3×10^{15}	Suprasil W1	E'	0.58
Tsai[70]	193nm	10^{16} - 2×10^{17}	Suprasil 2	E'	0.45*
	193nm	10^{15} - 10^{17}	Suprasil W	E'	0.55*
Tsai[71]	193nm	5×10^{15} - 2×10^{16}	Suprasil 2	NBOHC	0.5*
	193nm	2×10^{16} - 10^{18}	Suprasil W	NBOHC	0.4*

*denotes values that were estimated from published data plots.
#because the X-ray penetration depths was not known, only total spin counts were given.
$the majority of the OHC signal is believed to be a result of NBOHC's but peroxy radicals may also contribute.

A number of the studies summarized in Table 1 used gamma-ray sources rather than UV-radiation. Imai[73] showed that 193-nm and 248-nm radiation had approximately the same efficiency in producing defects as gamma-ray irradiation when he computed the UV dose as the UV energy absorbed from two-photon absorption. This suggested that similar defect production mechanisms were involved in defect generation from both gamma-rays and UV-radiation. The UV-induced defects in low temperature tests performed by Griscom[40] appeared to result from a single photon process so a comparison of standard

UV-induced defect generation to X-ray-induced defect generation was not possible. Despite having only relative defect measurements from X-ray radiation, Galeener[72] concluded that 1.25 MeV γ-rays were at least 10 times more efficient in producing defects per unit dose (defined as total energy absorbed) than 8 keV X-rays. He compared the X-ray doses required to produce equal defect concentrations in Suprasil 1 and Suprasil W1 (at low doses Suprasil W1 has a higher E' center concentration while at higher doses Suprasil 1 has a higher concentration) to the γ-ray doses found by Devine[74] to reach the same crossover to reach this conclusion.

1.5c Transient Properties of Color Centers

The group at IBM were among the first to characterize some of the transient annealing properties of color centers[32-33]. By independently monitoring the absorbance spectra of different fused silicas during and after KrF (248nm) irradiation, they were able to show that much of the E'-color-center-induced absorption relaxed after the irradiation was stopped in some samples. This relaxation of color centers, however, was artificial in that as soon as the irradiation was continued, the absorbance returned to its previous higher level. Samples were labeled as either "slow-relaxers" or "fast-relaxers", depending upon the rate of self annealing when irradiation was suspended in a specimen. No color center formation was observed in quartz[34].

The group at IBM was the first to report a phenomenon which they termed "strong absorption transition[32-33] (SAT). SAT occurred in "slow-relaxing" samples after a few

million 500mJ/cm^2, 248nm pulses. "Fast-relaxers" also showed SAT with the major difference that SAT did not occur until much later in the irradiation (about 40 million pulses). The main features of SAT were the following:

(1)   A rapid increase in 248-nm absorption followed by an abrupt saturation at a maximum value. Before the onset of SAT, the 248nm transmission was generally unchanged or decreased slightly.

(2)   A rapid increase in 210nm absorption followed by saturation.

(3)   Almost complete "freezing-in" of the induced-absorption spectrum after SAT. Room temperature annealing was no longer observable.

NMR[75] studies have provided data to construct a reasonable model to explain both the relaxing properties and SAT properties of fused silicas. Defining T_1 as the spin-lattice relaxation time, the following observations were made:

(1) "Fast-relaxers" have a higher intrinsic $1/T_1$ than do "slow-relaxers[76]." This implies[77] a higher concentration of Silanol, SiOH.

(2) $1/T_1$ decreases with irradiation[77].

(3) $1/T_1$ correlates with the number of pulses required to reach SAT[76].

(4) $1/T_1$ decreases with higher anneal temperature used during sample manufacturing[78]. Since most "fast-relaxers" are simply unhomogenized or unannealed precursors to "slow-relaxing" fused silicas this is in agreement with observation (1).

The following model was proposed to explain the role of hydrogen in color center formation and annealing:

(1) The annealing process breaks up silanol pairs.

(2) Silanol pairs act as a source of hydrogen to passivate E' centers.

(3) Exhaustion of susceptible silanol brings about SAT.

Given the characteristics of SAT, the model above should emphasize that silanol pairs act as a source of hydrogen to passivate the defect associated with the 260nm absorption band and well as the E' center. The above referenced publications also concluded that the annealing process formed "strained bonds" which act as sites for color center formation. This conclusion was based on the observation that two annealed samples had higher color-center-induced absorption than an unannealed sample measured 24 hours after irradiation. The unannealed sample was most likely a "fast-relaxer" so this conclusion was not necessary valid. Little difference in color center densities were measured between the two annealed samples which were annealed at different temperatures.

14

1.6 Compaction

Fused silica (density 2.2 g/cm^3) compacts when exposed to X-rays[79,80], γ-rays[79,80,72,81,82,83], electron-beams[79,80,84,85,86,87,88,89], neutrons[79,80,90,91,92,93,94,95], ions[79,80], and UV-radiation[31-39,60,96]. Compaction leads directly to refractive index changes in fused silica which would produce imaging aberrations in a lithography system. Upon heavy exposure or application of high external pressure the maximum extent of the compaction is about 3% to a density of 2.26 g/cm^3. Quartz (density 2.65 g/cm^3), on the other hand, expands when irradiated with particles capable of producing knock-on damage with the density saturating also at 2.26 g/cm^3. This well established form of silica is known as the metamict state[97]. Figure 1 shows the density of both quartz and vitreous silica versus neutron irradiation as the metamict state is approached and reached at high doses. A model proposed by Revesz[98] is reviewed in Chapter 8 which describes the metamict state as an equilibrium between the tendencies to minimize bond strain and to maximize the level of π-bonding. π-bonding orbitals, unlike spherically shaped σ bonds, are "figure-eight" shaped with a null in the electron probability function half way between the centers of the two bonding atoms. In the SiO_2 network, π-bonding results[98] from the overlap of the originally empty Si 3d orbitals with the O 2p orbital containing the lone pair electron. As will be detailed in Chapter 8, this model is consistent with many of the observed property changes in fused silica induced from radiation.

Like with the E' color center and NBOHC, the dose dependence of compaction has been shown to follow a power law that is:

$$\Delta\rho/\rho = AD^c \tag{5}$$

where ρ is the density, D is the dose and A and c are constants. The power c varied with the type of radiation and fused silica. For neutron, He^+ and D^+ exposures linear growth of compaction was observed[79,80] (c=1). For the other irradiation sources, the extracted value of c varied from 0.3 to 0.8. A table in Chapter 6 will detail the past findings. A discussion of the origin of the power law is included in Chapter 8.

A comparison of X-ray diffraction patterns before and after irradiation gives insight into the structural rearrangements coinciding with compaction. Figure 2 shows typical results[94] for a neutron irradiation experiment. Transforming the spectra in Figure 2 yields electron distribution densities which suggest a reduction in average Si-Si spacing consistent with neutron irradiation. The extracted Si-O bond distance, however, is unchanged indicating that neutron-induced compaction is a result of more efficient packing of the basic SiO_2 units. The precise structural rearrangement leading to compaction is still unclear. X-ray diffraction measurements of gamma-ray, X-ray, electron-beam and UV radiated samples have not been published so it is unknown if the changes to the X-ray diffraction pattern depend upon the type of damaging radiation. Of
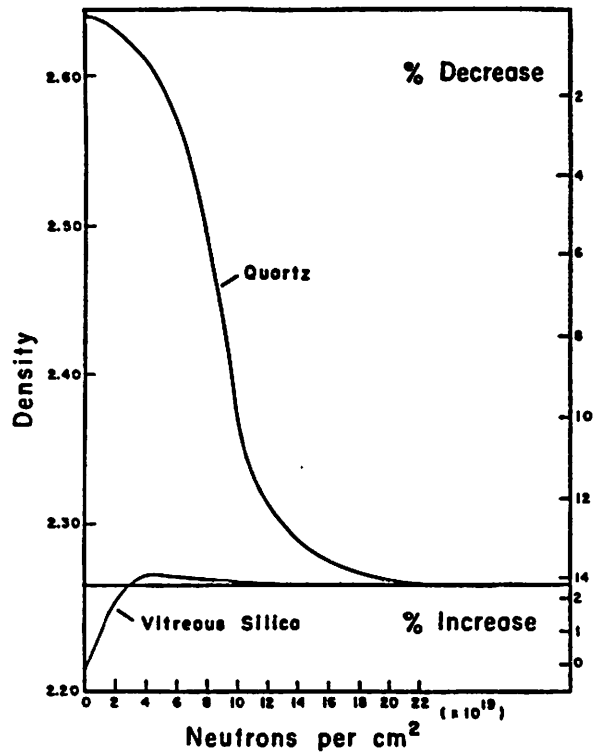
Figure 1 Copied from reference (97). Change in density with neutron irradiation of crystalline quartz and fused silica.
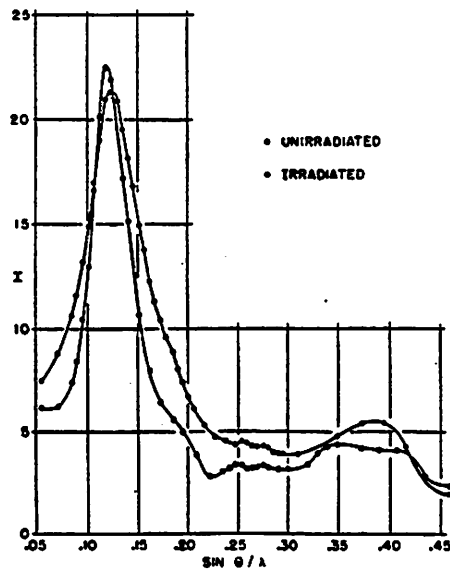
Figure 2 Copied from reference (94). X-ray diffraction intensity curves of neutron irradiated and unirradiated vitreous silica. Vertical scale arbitrary.

17

all the radiation sources mentioned, neutron radiation produces the most "knock-on" events which may result in different structural changes than from ionization-induced events alone.

Attempts have been made to correlate density changes with specific defect structures in fused silica. Higby and Friebele[99] reported a linear relationship between compaction and E' color center formation from electron exposures. Later observations of continued compaction after E' color center formation saturation dismissed the E' color center as the cause of compaction. Results presented in Chapter 3 showing significantly different transient properties of compaction and E' color center formation further rule out the E' color center as the cause of compaction.

Annealed forms of the E' color center and NBOHC could also be considered as structural forms leading to compaction. Experiments performed by Shelby[83] suggested that these molecular forms led to expansion rather than compaction. Vitreous silica which had been impregnated with molecular hydrogen was found to expand with increasing gamma irradiation. Using infrared spectroscopy, Shelby found that the expansion was directly proportional to SiOH and SiH formation. Both the expansion and the measured hydroxyl and hydride formation followed dose to about the 0.5 power. Furthermore, NMR studies[76] suggested that SiOH levels saturated (after SAT) while no saturation of compaction was observed after SAT[33,34].

Friebele and Higby[85] suggested that compaction results from radiation-induced cleavage of ring structures and the subsequent formation of smaller ring structures. The smaller ring structures would pack together more closely and hence led to densification. Bates[90] found a significant increase in the D_2 Raman peak, which is assigned to 3 silicon ring structures[21], after neutron densification. Raman spectra from gamma-irradiated samples[81] and heavily UV-irradiated samples[49], however, showed little or no increase in the D_2 Raman peak.

The best correlation between a specific defect and radiation-induced compaction are found with the NBOHC. Rajaram et al. reported[86], for example, a linear relationship between compaction-induced surface depression depths and NBOHC concentrations for some silicas from electron exposures. The possibility of the NBOHC being a defect responsible for densification is explored in Chapter 8.

1.7 This Work

Despite the vast wealth of studies performed on the effects of radiation on optical materials, still much is unknown about the effects of UV-radiation on fused silica. This is especially true when one considers the level of damage relevant to lithography applications is orders of magnitude smaller than that characterized in previous work. As well, while UV-induced color center formation has been well examined, UV-induced compaction is not characterized in any detail. The goals of this works are as follows:

(1) More accurately characterize compaction damage.

(2) Extend damage characterization to much lower doses and intensity levels.

(3) Examine the damage susceptibility of newer materials both for compaction behavior and possible correlated color center formation behavior.

(4) Develope the machinery to relate compaction data to the optical properties of single elements and the imaging performance of a lithographic tool.

References

[1] R. Bruckner, "Properties and Structure of Vitreous Silica. I," Journal of Non-Crystalline Solids, Vol. 5, pp. 123-175, 1970.

[2] Trademark of W. C. Heraeus-Schott Comp., Germany, and Amersil Quartz Division, Engelhard Industries, Inc.

[3] Trademark of Thermal Syndicate Ltd., England.

[4] Trademark of General Electric Comp., U.S.A.

[5] for a background on Raman Spectroscopy, see for example A. Yariv, Quantum Electronics, third edition, John Wiley and Sons, 1989.

[6] basic concepts on diffraction spectroscopy can be found in Kittel, Introduction to Solid State Physics, and applications to amorphous samples is described in B. E. Warren, H. Krutter, O. Morningstar, "Fourier Analysis of X-Ray Patterns of Vitreous SiO_2 and B_2O_3," Journal of the American Ceramic Society, 19, pp.202-206, 1936.

[7] W. H. Zachariasen, J. Am. Chem. Soc. 54, (1932) 3841.

[8] D. L. Evans, S. V. King, "Random Network Model of Vitreous Silica," Nature, Vol. 212, No. 5068, pp. 1353-1354, Dec. 1966.

[9] R. J. Bell, P. Dean, "The Structure of Vitreous Silica: Validity of the Random Network Theory," Phil. Magazine, Vol. 25, pp. 1381-1398, 1972.

[10] R. L. Mozzi, B. E. Warren, J. Appl. Cryst., Vol. 2, (1969) 164.

[11] J. R. G. DaSilva, D. G. Pinatti, C. E. Anderson, M. L. Rudee, Phil. Mag., Vol. 31, (1975) 713.

[12] I. Simon, "Structure of Neutron-Irradiated Quartz and Vitreous Silica," Journal of the American Ceramic Society, Vol. 40, No. 5, pp. 150-153, May 1957.

[13] B. E. Warren, "X-ray Determination of the Structure of Liquids and Glass," Journal of Applied Physics, Vol. 8, pp. 645-654, Oct. 1937.

[14] R. N. Sinclair, A. C. Wright, Journal of Non-Crystalline Solids 42 (1980) 107.

[15] A. C. Wright and J. A. E. Desa, Phys. Chem. Glasses 19 (1978) 140.

[16] J. R. Banavar and J. C. Phillips, Phys. Rev. B28 (1983) 4716.

[17] J. T. Randall, H. P. Rooksby, B. S. Cooper, "The Structure of Glasses; The Evidence of X-Ray Diffraction," Journal of the Society of Glass Technology, Vol. 14, pp. 219-229.

[18] J. C. Phillips, "Microscopic Origin of Anomalously narrow Raman Lines in Network Glasses," Journal of Non-Crystalline Solids 63 (1984) 347-355.

[19] F. L. Galeener, "Planar Rings in Vitreous Silica," Journal of Non-Crystalline Solids 49 (1982) pp. 53-62.

[20] J. C. Phillips, "Structural significance of Raman spectra of OH- and F-doped vitreous silica," Physical Review B, Vol. 33, No. 6, pp. 4443-4445, Mar. 1986.

[21] F. L. Galeener, F. A. Barrio, E. Martinez, R. J. Elliott, "Vibrational Decoupling of Rings in Amorphous Solids," Physical Review Letters, Vol. 53, No. 25, pp. 2429-2432, Dec. 1984.

[22] C. J. Brinker, R. J. Kirkpatrick, D. R. Tallant, B. C. Bunker, B. Montez, "NMR Confirmation of Strained "Defects" in Amorphous Silica," Journal of Non-Crystalline Solids 99 (1988) pp. 418-428.

[23] D. L. Griscom, "Defect Structure of Glasses, Some outstanding questions in regard to vitreous silica," Journal of Non-Crystalline Solids 73 (1985) 51-77.

[24] F. L. Galeener, A. C. Wright, "The J. C. Phillips Model for Vitreous SiO_2: A Critical Appraisal," Solid State Communications, Vol. 57, No. 8, pp. 677-682, 1986.

[25] E. J. Friebele, D. L. Griscom, in Treatise on Materials Science and Technology, Vol. 17, Glass II, eds. M. Tomozawa and R. H. Doremus (Academic Press, New York, 1979) p. 257.

[26] D. L. Griscom, "Nature of defects and defect generation in optical glasses," SPIE Vol. 541, Radiation Effects in Optical Materials (1985) pp. 38-59.

[27] E. S. Bliss "Laser-damage mechanisms in transparent dielectrics," ASTM Boulder Damage Conference, 1969. Damage in Laser Glass, ASTM Spec. Pub. 469, 1969, pp. 9-20.

[28] D. Du, X. Liu, G. Korn, , J. Squier, G. Mourou, "Laser-induced breakdown by impact ionization in SiO_2 with pulse widths from 7 ns to 150 fs," Appl. Phys Lett. 64 (23), pp. 3071-3073, 6 June 1994.

[29] M. F. Koldunov, A. A. Manenkov, I. L. Pokotilo, "The theory of inclusion initiated laser damage in optical materials: The thermal explosion mechanism," Laser-Induced Damage in Optical Materials: 1988, NBS Special Publication, vol. 775, pp. 502, 1989.

[30] T. E. Tsai, D. L. Griscom, "Experimental Evidence for Excitonic Mechanism of Defect Generation in High-Purity Silica," Physical Review Letters, Vol. 67, No. 18, pp. 2517-2520, 28 Oct. 1991.

[31]P. Schermerhorn, "Excimer laser damage testing of optical materials," SPIE Vol. 1835, pp. 70-79, 1992.

[32]D.J. Krajnovich, I.K. Pour, A.C. Tam, W.P. Leung, M.V. Kulkarni, "248 nm lens materials: performance and durability issues in an industrial environment," Proc. SPIE 1848, 544-560, 1993.

[33]D.J. Krajnovich, I.K. Pour, A.C. Tam, W.P. Leung, M.V. Kulkarni, "Sudden onset of strong absorption followed by forced recovery in KrF laser-irradiated fused silica," Optics Letters, 15, Vol. 18, (no. 6), pp. 453-5, March 1993.

[34]D.J. Krajnovich, I.K. Pour, "Long-term effects of pulsed KrF laser radiation on crystalline and amorphous SiO_2," SPIE Vol. 2114, 1994.

[35]R. Schenker, P. Schermerhorn, W.G. Oldham, "Deep-UV damage to fused silica," , Journal of Vacuum Science, pp. 3275-3279, Nov/Dec 1994.

[36]R. Schenker, L. Eichner, H. Vaidya, S. Vaidya, P. Schermerhorn, D. Fladd, W.G. Oldham, "Ultraviolet damage properties of various fused silica materials," Laser-Induced Damage in Optical Material: 1994, 26th Annual Boulder Damage Symposium Proceedings, pp. 458-468, SPIE proceedings 2428.

[37]R. Schenker, L. Eichner, H. Vaidya, S. Vaidya, W.G. Oldham, "Degradation of fused silica at 193 nm and 213 nm," Optical/Laser Microlithography VIII, pp. 118-125, SPIE proceedings 2440, 1995.

[38]Rothschild, D.J. Ehrlich, and D.C. Shaver, "Effects of excimer laser irradiation on the transmission, index of refraction, and density of ultraviolet grade fused silica," Appl. Phys. Lett. 55 (13), pp. 1276-1278, Sept. 25, 1989.

[39]J.H.C. Sedlacek and M. Rothschild, "Optical materials for use with excimer lasers," SPIE Vol. 1835, pp. 80-88, 1992.

[40]D.L. Griscom, "Growth and Decay Kinetics of Defect Centers in High-Purity Fused Silicas Irradiated at 77 K with X-Rays or 6.4-eV Laser Light," Nuclear Instruments and Methods in Physics Research B46 (1990) pp. 12-17.

[41]T. E. Tsai, D. L. Griscom, E. J. Friebele, "Si E' Centers and UV-Induced Compaction in High Purity Silica," ," Nuclear Instruments and Methods in Physics Research B46 (1990) pp. 265-268.

[42]G. C. Escher, "KrF Laser Induced Color Centers in Commercial Fused Silicas," SPIE Vol. 998 *Excimer Beam Applications* (1988) pp. 30-37.

[43]R. A. Weeks, R. H. Magruder, III, P. Wang, "Some effects of 5 eV photons on defects in SiO_2," Journal of Non-Crystalline Solids 149 (1992) pp. 122-136.

[44]R. H. Magruder, III, P. Wang, R. A. Weeks, D. L. Kinser, "KrF laser light interaction with intrinsic defects in silica," SPIE Vol. 1327 *Properties and Characteristics of Optical Glass II* (1990) pp. 50-59.

[45]E. A. Nevis, "Alteration of the transmission characteristics of fused silica optical fibers by pulsed ultraviolet radiation," SPIE Vol. 540 Southwest Conference on Optics (1985) pp. 421-424.

[46]H. Hitzler, Ch. Pfleiderer, N. Leclerc, J. Wolfrum, K. O. Greulich, H. Fabian, "KrF-laser irradiation induced defects in all silica optical fibers," Journal of Non-Crystalline Solids 149 (1992) pp. 107-114.

[47]N. Leclerc, Ch. Pfleiderer, H. Hitzler, J. Wolfrum, K. O. Greulich, S. Thomas, W. Englisch, "Luminescence and transient absorption bands in fused SiO_2 induced by KrF laser radiation at various temperatures," Journal of Non-Crystalline Solids 149 (1992) pp. 115-121.

[48]H. Hitzler, Ch. Pfleiderer, N. Leclerc, J. Wolfrum, K. O. Greulich, S. Thomas, H. Fabian, R. Takke, W. Englisch, "Transient 210-nm absorption in fused silica induced by high-power UV laser irradiations," Optics Letters, Vol. 16, No. 12, pp. 940-942, June 15, 1991.

[49]Ch. Pfleiderer, N. Leclerc, K. O. Greulich, "The UV-induced 210 nm absorption band in fused silica with different thermal history and stoichiometry," Journal of Non-Crystalline Solids 159 (1993) pp. 145-153.

[50]N. Leclerc, Ch. Pfleiderer, H. Hitzler, S. Thomas, R. Takke, W. Englisch, J. Wolfrum, K. O. Greulich, "KrF excimer laser induced absorption and fluorescence bands in fused silica related to the manufacturing process," SPIE Vol. 1327 Properties and Characteristics of Optical Glass II (1990) pp. 60-68.

[51]K. Mann, H. Gerhardt, "Damage testing of optical components for high power excimer lasers," SPIE Vol. 1503 Excimer Lasers and Applications III (1991) pp. 176-184.

[52]E. Eva, K. Mann, "Calorimetric measurement of two-photon absorption and color-center formation in ultraviolet-window materials," Appl. Phys. A 62, pp. 143-149 (1996).

[53]E. Eva, K. Mann, "Nonlinear absorption phenomena in optical materials for the UV-spectral range," preprint of paper to be published in 1996 Proceedings of Boulder Damage Symposium.

[54]A. Fujinoki, "Silica with High Resistance to Excimer Laser," SPIE Vol. 2428, pp. 170-173.

[55]H. Nishikawa, R. Nakamura, R. Tohmon, Y. Ohki, Y. Hama, Y. Sakurai, K. Nagasawa, " Paramagnetic centers induced by ArF excimer laser irradiation in high-purity silica glasses," SPIE Vol. 1327 Properties and Characteristics of Optical Glass II (1990) pp. 69-78.

[56]K. Arai, H. Imai, H. Hosono, Y. Abe, H. Imagawa, "Two-photon processes in defect formation by excimer lasers in synthetic silica glass," Appl. Phys. Lett. 53 (20), 14 Nov. 1988, pp. 1891-1893.

[57]N. Kuzuu, Y. Komatsu, M. Murahara, "ArF-excimer-laser-induced emission and absorption bands in fused silica synthesized under oxidizing conditions," Physical Review B Vol. 45, No. 5, 1 Feb. 1992, pp. 2050-2054.

[58]N. Kuzuu, Y. Komatsu, M. Murahara, "ArF-excimer-laser-induced emission and absorption bands in fused silica synthesized in reducing conditions," Physical Review B Vol. 44, No. 17, 1 Nov. 1991, pp. 9265-9270.

[59]V. P. Pashinin, N. Yu. Konstantinov, V. G. Artjushenko, V. I. Konov, A. S. Silenok, G. Muller, B. Schaldach, R. Ulrich, "Mechanism of UV Laser-Induced Absorption in Fused Silica Fibers," Fiber and Integrated Optics, Vol. 10, pp. 365-372.

[60]N. V. Morozov, "Laser induced damage in optical materials under UV excimer laser radiation," SPIE Vol. 2428, pp. 153-169.

[61]M. Rothschild, D. J. Ehrlich, D. C. Shaver, "Excimer Laser Induced Damage in Fused Silica," Microelectronic Engineering 11 (1990) pp. 167-172.

[62] Kittel, Introduction to Solid State Physics, is a good reference for background.

[63] M. Stapelbroek, D. L. Griscom, E. J. Friebele, G. H. Sigel, "Oxygen-Associated Trapped-Hole Centers in High-Purity Fused Silicas," Journal of Non-Crystalline Solids, 32, pp. 313-326, 1979.

[64] D. L. Griscom, "Thermal Bleaching of X-ray-induced defect centers in high purity fused silica by radiolytic molecular hydrogen," Journal of Non-Crystalline Solids 68, pp. 301-325, 1984.

[65] D. L. Griscom, "Optical Properties and Structure of Defects in Silica Glass," Journal of the Ceramic Society of Japan, Vol. 99, No. 10, pp. 923-942, 1991.

[66] H. Hosono, R. A. Weeks, "Bleaching of Peroxy Radical in SiO_2 Glass with 5 eV Light," Journal of Non-Crystalline Solids 117, pp. 289-292, 1990.

[67] J. H. Stathis, M. A. Kastner, "Vacuum-ultraviolet generation of luminescence and absorption centers in α-SiO_2," Phil. Mag., Vol B49, No. 4, pp. 357-362, 1984.

[68] T. E. Tsai, J. M. Jewell, J. S. Sanghera, "Dynamics of the 5 eV optical absorption in SiO_2 glass," Applied Physics Letters, Vol. 62, No. 26, pp. 3396-3398, 1993.

[69] E. J. Friebele, D. L. Griscom, M. Stapelbroek, R. A. Weeks, "Fundamental defect centers in glass: the peroxy radical in irradiated, high-purity, fused silica," Physical Review Letter, Vol. 42, No. 20, pp. 1346-1349, 14 May 1979.

[70] T. E. Tsai, D. L. Griscom, E. J. Friebele, "Mechanism of Intrinsic Si E'-Center Photogeneration in High-Purity Silica," Physical Review Letters, Vol. 61, No. 4, pp. 444-446, 25 July 1988.

[71] T. E. Tsai, D. L. Griscom, E. J. Friebele, "Defect Centers Induced by Linear and Non-linear Absorption of UV Light in High Purity Silica," SPIE Vol. 970 Properties and Characteristics of Optical Glass, pp. 165-169, 1988.

[72] F. L. Galeener, "Non-linear γ-ray activation of defect spins in vitreous silica," Journal of Non-Crystalline Solids 149, pp. 27-31, 1992.

[73] H. Imai, H. Hirashima, "Similarity of defect generation in silica glasses irradiated with γ-rays and 5.0- and 6.4-eV excimer lasers," Nuclear Instruments and Methods in Physics Research B, Vol. 91, pp. 400-404, 1994.

[74] R. A. B. Devine, J. Arndt, "Correlated defect creation and does-dependent radiation sensitivity in amorphous SiO_2," Physical Review B, Vol. 39, No. 8, pp. 5132-5138, 15 March, 1989.

[75] Kittel, Introduction to Solid State Physics, is a good reference for background.

[76] B. E. Scruggs, K. K Gleason, "The role of proton nuclear magnetic resonance spin-lattice relaxation centers in the strong absorption transition at 210 nm in fused silica," J. Appl. Phys. 76 (5) pp. 3063-3067, 1 Sept. 1994.

[77] D. H. Levy, K. K. Gleason, M. Rothschild, J. H. C. Sedlacek, R. Takke, "The role of hydrogen in excimer-laser-induced damage of fused silica," J. Appl. Phys. 73 (6), pp. 2809, 15 March 1993.

[78] D. H. Levy, K. K. Gleason, M. Rothschild, J. H. C. Sedlacek, R. Takke, "Reactions of hydrogenated defects in fused silica caused by thermal treatment and deep ultraviolet irradiation," Appl. Phys. Lett. 60 (14), pp. 1667-1669, 6 April 1992.

[79] W. Primak, R. Kampwirth, "The Radiation Compaction of Vitreous Silica," Journal of Applied Physics, Vol. 39, No. 12, pp. 5651-5657, Nov. 1968.

[80] W. Primak, R. Kampwirth, "Impurity Effect in the Ionization Dilation of Vitreous Silica," Journal of Applied Physics, Vol. 39, No. 13, pp. 6010-6017, Dec. 1968.

[81] J. A. Ruller, E. J. Friebele, "The effect of gamma-irradiation on the density of various types of silica," Journal of Non-Crystalline Solids 136, pp. 163-172, 1991.

[82] J. E. Shelby, "Effect of radiation on the physical properties of borosilicate glasses," Journal of Applied Physics, Vol. 51, No. 5, pp. 2561-2565, May 1980.

[83] J. E. Shelby, "Radiation effects in hydrogen-impregnated vitreous silica," Journal of Applied Physics, Vol. 50, No. 5, pp. 3702-3706, May 1979.

[84] P. L. Higby, E. J. Friebele, C. M. Shaw, M. Rajaram, E. K. Graham, D. L. Kinser, E. G. Wolff, "Radiation Effects on the Physical Properties of Low-Expansion-Coefficient Glasses and Ceramics," Journal American Ceramic Society, Vol. 71, No. 9, pp. 796-802, 1988.

[85] E. J. Friebele, P. L. Higby, "Radiation Effects in Amorphous SiO_2 for Windows and Mirror Substrates," in Laser Induced Damage in Optical Materials: 1987, NIST Spec. Pub. 756, pp. 89-97, 1988.

[86] M. Rajaram, T. Tsai, E. J. Friebele, "Radiation-Induced Surface Deformation in Low-Thermal-Expansion Glasses and Glass-Ceramics," Advanced Ceramic Materials, Vol. 3, No. 6, pp. 598-600, 1988.

[87] C. I. Merzbacher, E. J. Friebele, J. A. Ruller, P. Matic, "Finite element analysis of deformation in large optics due to space environment radiation," SPIE Vol. 1533 Optomechanics and Dimensional Stability, pp. 222-228, 1991.

[88] T. A. Dellin, D. A. Tichenor, E. H. Barsis, "Volume, index-of-refraction, and stress changes in electron-irradiated vitreous silica," Journal of Applied Physics, Vol. 48, No. 3, pp. 1131-1138, March 1977.

[89] C. B. Norris, E. P. EerNisse, "Ionization dilation effects in fused silica from 2 to 18-keV electron irradiation," Journal of Applied Physics, Vol. 45, No. 9, pp. 3876-3882, Sep. 1974.

[90] J. B. Bates, R. W. Hendricks, L. B. Shaffer, "Neutron irradiation effects and structure of noncrystalline SiO_2," The Journal of Chemical Physics, Vol. 61, No. 10, pp. 4163-4176, 15 Nov. 1974.

[91] W. Primak, R. Kampwirth, "Ionization Expansion of Pile-Exposed Vitreous Silica," Journal of Applied Physics, Vol. 40, No. 6, pp. 2565-2570, May 1969.

[92] W. Primak, "Fast-Neutron-Induced Changes in Quartz and Vitreous Silica," Physical Review, Vol. 110, No. 6, pp. 1240-1254, 15 June, 1958.

[93] W. Primak, "Radiation Behavior of Vitreous Silica," Nuclear Science and Engineering, 65, pp. 141-145, 1978.

[94] J. S. Lukesh, "Neutron Damage to the Structure of Vitreous Silica," Physical Review, Vol. 97, No. 2, pp. 345-346, 15 Jan. 1955.

[95] A. Hiramatsu, M. Arai, H. Shibazaki, M. Tsunekawa, T. Otomo, A. C. Hannon, S. M. Bennington, N. Kitamura, A. Onodera, "Investigation on permanently densified vitreous silica by means of neutron scattering," Physica B, 219 and 220, pp. 287-289, 1966.

[96] R. Schenker, F. Piao, W. G. Oldham, "Material Limitations to 193-nm Lithographic System Lifetimes," SPIE vol. 2726, Optical Microlithography IX, 1996

[97] E. Lell, N. J. Kreidl, J. R. Hensler, *Radiation Effects in Quartz, Silica and Glasses*, chapter 1 in Progress in Ceramic Science Volume 4, Editor J. E. Burke, Pergamon Press 1966.

[98] A. G. Revesz, "π Bonding and Delocalization Effects in SiO_2 Polymorphs," Physical Review Letters, 27 (23), pp. 1578-1581, 1971.

[99] P. L. Higby, E. J. Friebele, American Ceramic Society Bulletin, 67, (1988) 615.

Chapter 2

Birefringence Monitoring to Measure Compaction

Birefringence monitoring is capable of measuring the compaction-induced birefringence distribution at very low damage levels. The birefringence distributions resulting from less than 30 parts per billion (ppB) net UV-induced densification, for example, are easily measured with a "third-generation" birefringence monitor. In order to extract the corresponding stresses and densification from birefringence distributions, a three-region stress model is developed assuming plane strain.

2.1   Introduction

The Photoelastic effect has long been used to determine stresses in transparent specimens[1]. The basic concept behind the photoelastic effect is that directional refractive indices change when a sample is under stress. This phenomenon is described for isotropic materials by:

$$(n_2 - n_1) = \Re (\sigma_2 - \sigma_1) \tag{1}$$

where n_2 and n_1 are the refractive indices seen by light polarized in the (2) and (1) direction respectively; σ_2 and σ_1 are the stresses in the (2) and (1) directions; and $\Re$ is the stress-optic constant which is both material and wavelength dependent.

Several previous applications have utilized the photoelastic effect. By examining the birefringence produced in glass replicas of bridge or building structures, for example, civil engineers have been able to study the effects of different loading on the stresses within the structures. Glass blowers, as well, have long used the examination of a specimen between crossed polarizers to determine the success of annealing to remove residual stress from glass structures.

Compaction in fused silica leads to refractive index changes and hence optical path changes in a sample. From an optical system lifetime point of view, the optical path difference (OPD) is the most important property of interest. Interferometry is a well-established method for measuring optical path length changes in optical materials. The disadvantages of interferometry for determining OPD's from compaction is that intrinsic inhomogeneities and surface imperfection make detection of changes from irradiation more difficult. While a sample can be pre-measured for such inhomogeneities, interferometry is still limited by such irregularities. Even in perfect, homogeneous specimens, the ultimate precision of interferometry limits sensitivity to damage in the hundreds of ppB range for samples with a few centimeters of path length. Furthermore, high accuracy interferometry measurements are usually time consuming and equipment intensive.

The use of birefringence measurements to determine compaction offers the advantage of simplicity as well as improved accuracy. Samples can be measured during brief pauses in

radiation so that the dependence of compaction on pulse count can be more easily determined. Furthermore, through successive improvements of the experimental setup, relative refractive index changes of about 10ppB can be measured, at least an order of magnitude better than most interferometry tools. Stress-induced birefringence measurements are insensitive to by surface quality and bulk inhomogeneities.

2.2   Experimental Method

Figure 1 shows the standard geometry used to irradiate a fused silica sample. The center irradiated region is compacted. Resistance to this compaction by the unirradiated portion of the sample leads to stress in the sample. Compaction-induced stress causes directional refractive index variations in a sample, which leads to birefringence and polarization scattering of incoming light. Changes in polarization of an initially linearly polarized Helium-Neon (He-Ne, $\lambda = 633$ nm) beam through a fused silica sample are measured to detect compaction-induced birefringence during the irradiations. Figure 2 shows the configuration used to detect those changes. A high gain photodiode measured the 633-nm reflectance of a thin calcium fluoride plate oriented at Brewster's angle to detect small changes in polarization resulting from UV-induced stress within the fused silica sample. The He-Ne polarization is such that the plate had zero reflectance when no birefringence occurred. Spatial distributions of stress-induced birefringence are recorded by stepping the damaged fused silica sample through the He-Ne probe beam and measuring polarization shifts in and around the irradiated region.
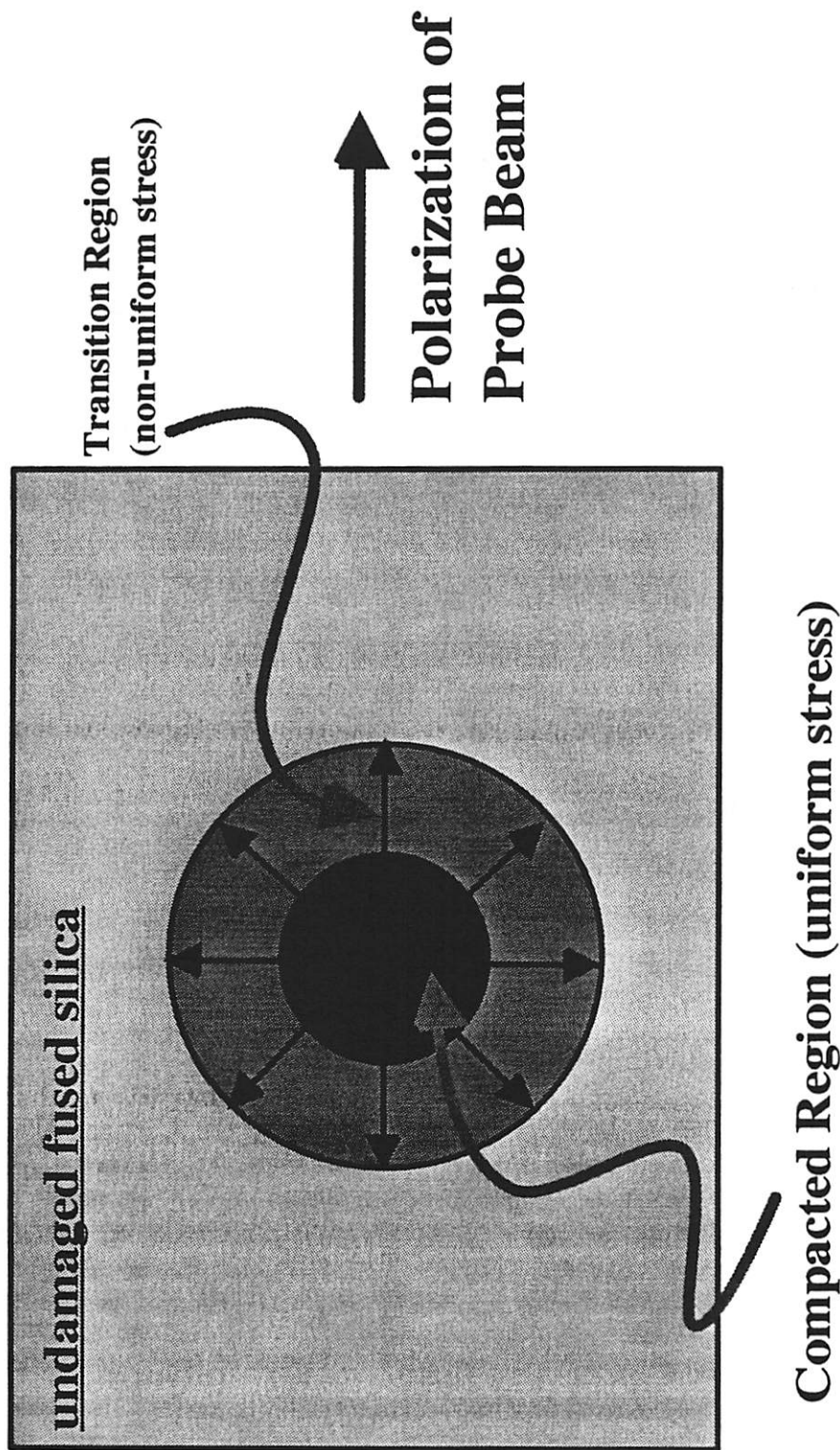
Figure 1. Fused silica irradiation geometry. The typical beam dimeter is about 3mm and the typical sample dimension is 2cm.

Detector

Filter

CaF Plate at
Brewster's Angle

De-Polarized
Probe Beam

Stressed Region

Polarized
HeNe Beam

Region of Compaction
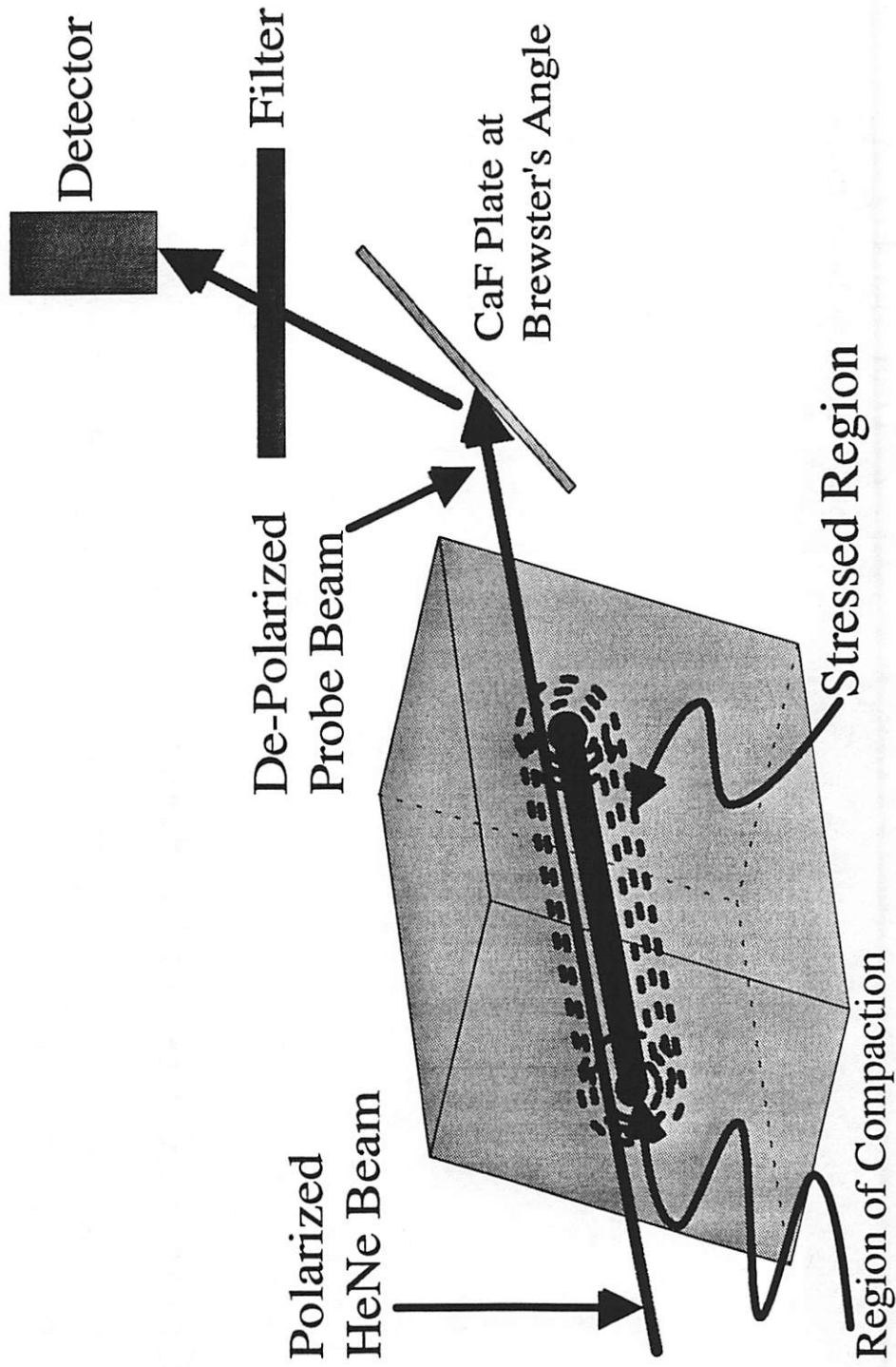
Figure 2. Configuration used to detect stress-induced polarization shifts in a polarized probe beam.

Figure 3a portrays the entire optical bench setup used for both birefringence and transmission measurements at AT&T Bell Laboratories in Murray Hill. The setup is considered the "second generation" configuration, having improved upon that used previously for 213nm damage testing[2]. In the 213nm optical configuration, the 213nm beam was used as the probe for stress-induced birefringence. The use of a He-Ne probe beam in the "second generation" setup improved both spatial accuracy by having a probe beam smaller than the damaging beam and accuracy in measuring polarization changes by having a probe with better polarization purity. The polarization of the 213nm beam degraded before reaching the sample because of inhomogeneities in optics before the sample.

The He-Ne probe beam in the setup shown in Figure 3a is inserted to the primary 193nm (ArF beam) beam path by transmission through a 193nm dielectric mirror. The mirror while being over 90 percent reflective to 193nm radiation at 45 degrees, is over 80 percent transmitting to p-polarized 633nm radiation. Having the He-Ne beam along the same path as the damaging beam allows for monitoring of radiation-induced compaction during exposure. A long focal length lens is used to reduce the probe beam diameter at the plane of the sample. Since a large spread of input angles at the plane of the Brewster plate would reduce the p-polarization extinction, short focal length lenses should not be used to reduce the He-Ne beam size. A Glan-Thompson polarizer is placed after the lens to fine tune the input polarization. Tubes and pin-holes are used to reduce background light.
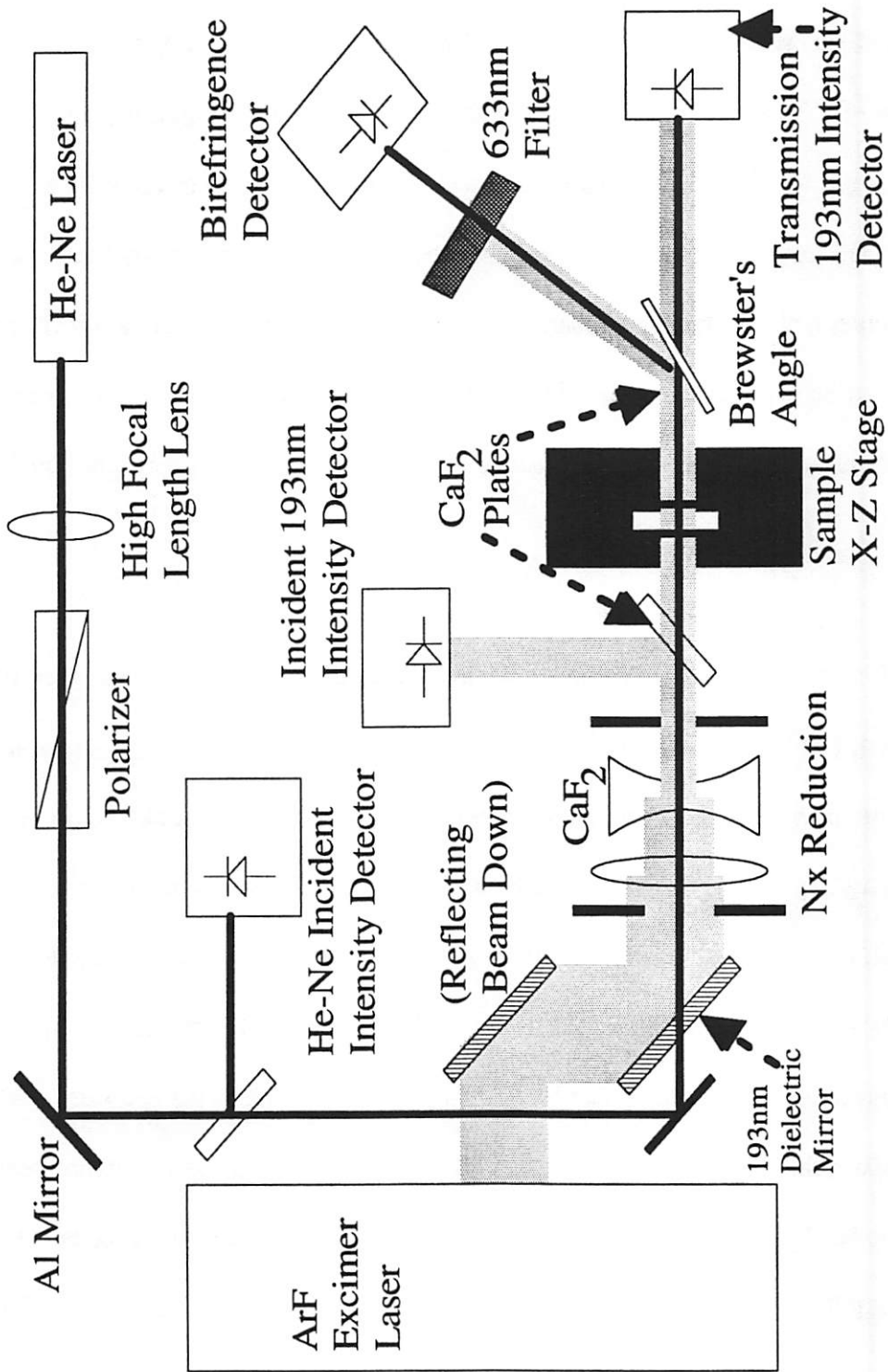
Figure 3a. "Second generation" 193nm material damage testing instrumentation. (implemented at At&T Bell Labs.)
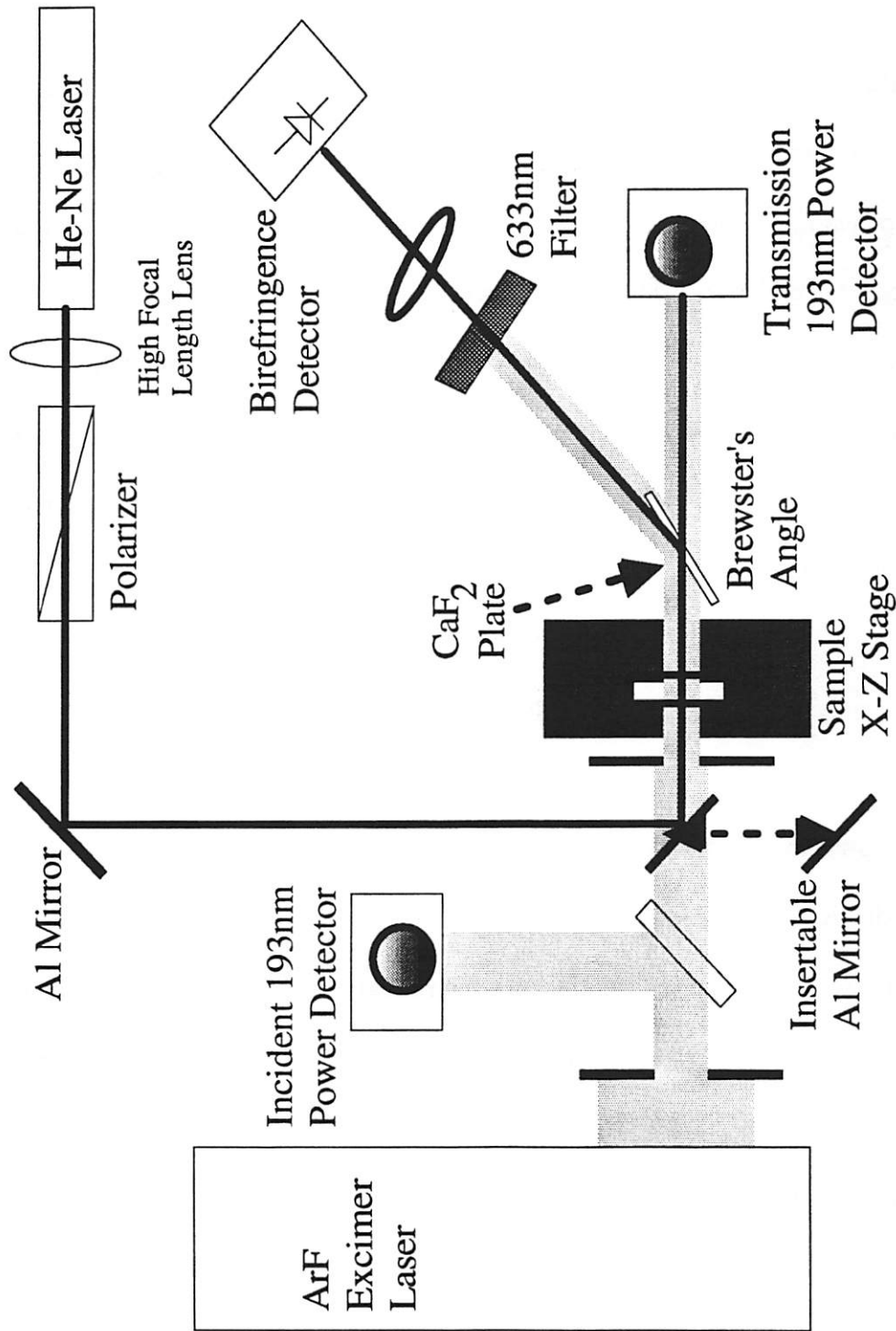
Figure 3b. "Third generation" 193nm material damage testing instrumentation. A Z-stage inserts the He-Ne probe beam down the primary optical paths to scan for birefringence during pauses in exposure.

The "third generation" configuration for measuring birefringence is illustrated in Figure 3b. The He-Ne probe beam is input into the primary beam line by reflection from a standard Aluminum mirror which is inserted into the beam line via a mechanical stage. While this does not allow for the monitoring birefringence while the 193nm laser is firing, the purity of the probe beam is greatly improved by avoiding travel through any element before reaching the sample. A lens is used after the Brewster plate to insure that the entire probe beam is within the active area of the photodiode. A second polarizer, crossed with the first, can be placed after the Brewster plate to further improve extinction of p-polarized light. Care is taken to keep the entire path of the He-Ne beam at the same height above the optical table in order to prevent any unwanted polarization shifts upon reflection off the mirrors used to guide the beam.

2.3   Analytical Compaction Model

2.3a Two-region model for long cylindrical, large radius samples

The production of stress-induced birefringence by compaction is modeled using basic material mechanics. The simplest model which could be applied is a two-region model where the inner region has been uniformly compacted and the outer region has an unchanged density for infinitesimal kinematics. A three step approach is taken to solve for the stress distributions resulting from the compaction of a cylindrical volume within a larger cylinder. The first step calculates the strains that would be present if the cylinder is permitted to compress without any resistance from the uncompacted material. The initial

conditions for such a case would be a compacted cylinder with radius r'_1 within a body with an opening with radius r_2 as shown in Figure 4 where r_2 is larger than r'_1. The length of the inner cylinder is also shorter than the outer region length. The second step stretches the compacted cylinder back to its original length in order to emulate the restriction of shortening of the compacted cylinder by the larger, uncompacted volume. The third and final step rejoins the compacted and uncompacted region where stresses and displacements are calculated using infinitesimal kinematics. The notation used in this work will be that used by Shames and Cozzarelli[3] where ε is used for strains, u for displacements, and τ and σ are used interchangeably for stresses.

For both the two and three region models, the following assumptions were made:

1) A circularly symmetric compacted region

2) Isotropic media

3) Large specimen so that end effects are small and all the strain is in the plane perpendicular to the direction of travel of the damaging beam (Plane Strain). This sets u_3 (displacement in the z direction) and all derivative with respect to the z direction equal to zero. The z direction will always be taken as the direction of travel of the damaging beam.

4) The compacted area is much smaller than the bulk so that stresses go to zero at the sample edge. This is equivalent to assuming an infinitely large sample.

5) The body forces are zero (i.e. gravitational effects are ignored).

6) Displacements are small, giving simple elastic behavior.

Let us find the strain fields for an initial condition in which the center of the sample has undergone a compaction of $(\Delta\rho/\rho)_u$. Here we define $(\Delta\rho/\rho)_u$ as the unconstrained densification, which is the compaction which would be observed if the entire sample had been uniformly compacted. As will be seen, the net compaction found in a sample compacted only in the center region is less than the unconstrained compaction because of the resistance of the undensified portions of the sample. Unconstrained compaction in a cylindrical volume within a larger volume is illustrated in Figure 4 where the densified material is allowed to separate from the undensified material in order to compress without resistance. Both the radius and length of the compressed cylinder are shortened. Using the notation illustrated in Figure 4, the linear unconstrained compaction $[(\Delta r'/r)_u]$ is defined as $(r'_1 - r_2)/r_1$, making $(\Delta\rho/\rho)_u$ equal to $-3(r'_1 - r_2)/r_1$.
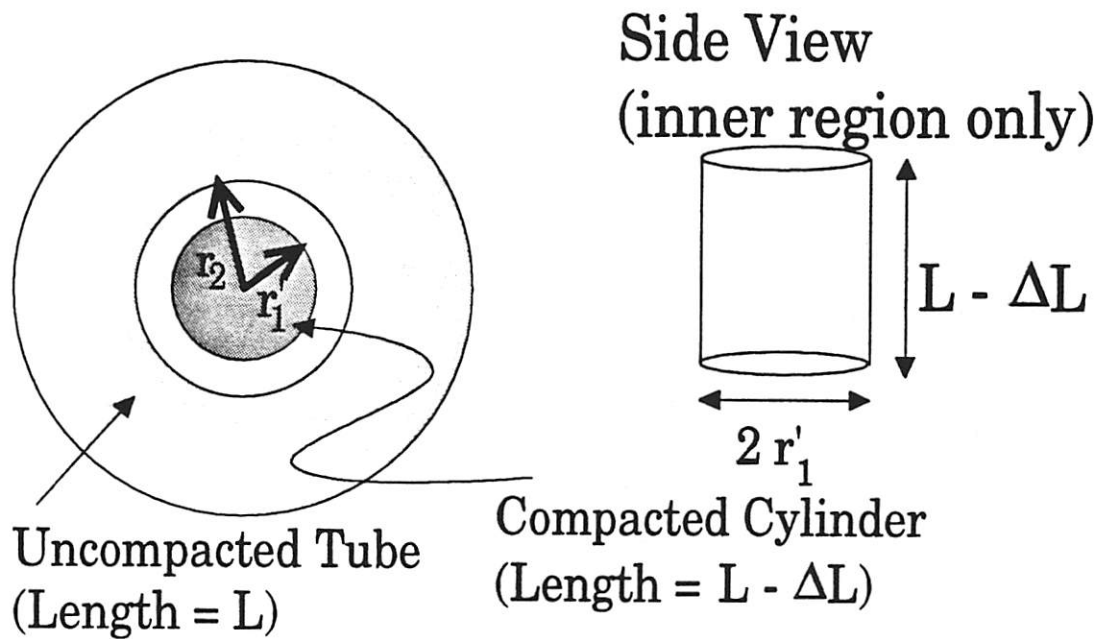
Figure 4. Step 1 in two region stress model analysis of cylindrical compacted region. The center region is densified without restriction from the undensified material such that its radius and length are shortened as given by: $\dfrac{\Delta L}{L} = \dfrac{\Delta r'}{r} = -\dfrac{1}{3}\left(\dfrac{\Delta \rho}{\rho}\right)_u$. Where $(\Delta \rho / \rho)_u$ is the relative unconstrained density change and $\Delta r'$ here equals $(r'_1 - r_2)$. A gap exists between the inner cylinder and the outer tube.

To properly apply a plane strain analysis (essentially a two-dimensional description) to volume densification, however, the initial conditions must be modified to account for sample length changes. As described above, a plane strain model is assumed which prescribes a zero final strain in the z-direction. To emulate this zero z-strain condition, a second initial condition is added where the center section is stretched out (by stress in z direction) to its pre-compaction length. The effect of this z-stress, as suggested in Figure 5, is to add an additional radial length decrease of $v \, \Delta L/L$ or equivalently $v \, (r_2 - r_1)/r_1$ by the Poisson effect where v is Poisson's ratio (0.17 for fused silica). This makes:

$$\frac{\Delta r}{r} = \frac{(r_1 - r_2)}{r_1} = -\frac{(1+v)}{3}\left(\frac{\Delta\rho}{\rho}\right)_u.$$

(2)

Uncompacted Tube
(Length = L)

Compacted Cylind
(Length = L)
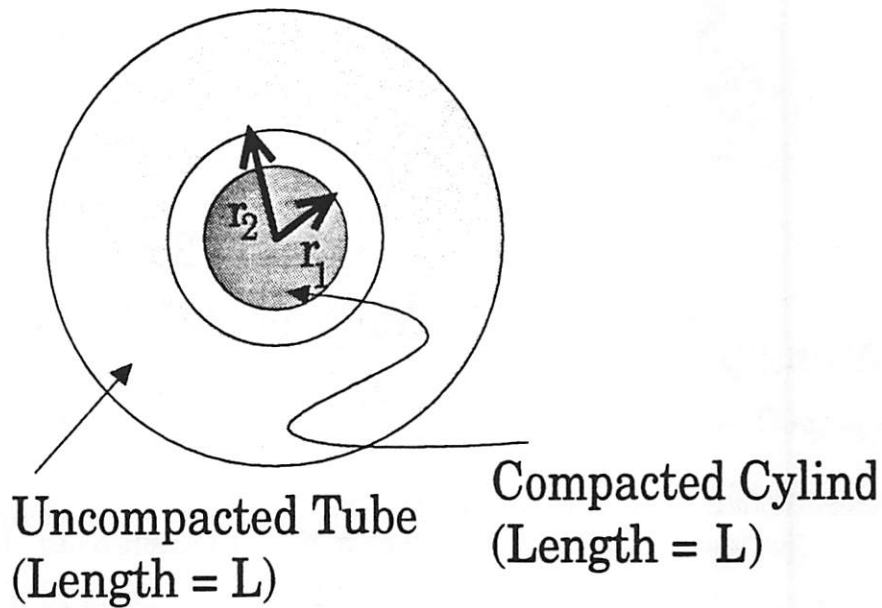
Figure 5. Step 2 in two-region stress model analysis of cylindrical compacted region. The inner compacted region is stretched such that its length equals that of the uncompacted material. In doing so the radius of the inner compacted region decreases such that:

$$\frac{(r_1 - r_2)}{r_1} = -\frac{(1+v)}{3}\left(\frac{\Delta\rho}{\rho}\right)_u.$$

Using the relation between unconstrained compaction and the initial radial displacements,

a plane strain analysis can now be applied to a sample with a cylindrical compacted center

in order to calculate stresses and displacements. Figure 6 illustrates the joining of the

compacted cylinder and uncompacted tube where the final radius, r ($r_2 > r > r_1$), can be

calculated using kinematics.
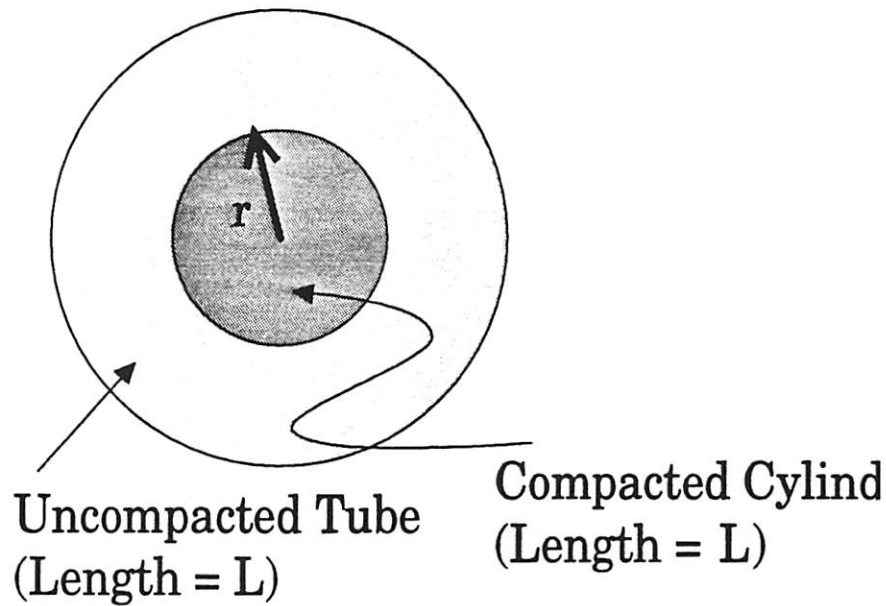
Figure 6. Step 3 in two-region stress model analysis of cylindrical compacted region. The inner compacted cylinder and outer uncompacted tube are joined such that the normal stress is continuous at the interface at radius r. The stresses and displacements are calculated within this chapter using a plane strain assumption.

Shames[3] derived the general solution for stresses for an axially symmetric plane strain case using an Airy stress function. The use of the Airy stress function insures satisfying the compatibility equations which insure that the solutions for displacements are single-valued and continuous.

In polar coordinates, one gets:

$$\tau_{rr} = K_1 [\ln(r) - 0.5] + K_2 + K_3/r^2 \tag{3}$$

$$\tau_{\theta\theta} = K_1 [\ln(r) + 0.5] + K_2 - K_3/r^2 \tag{4}$$

$$\varepsilon_{rr} = \frac{1-v^2}{E} \cdot \left(\tau_{rr} - \frac{v \cdot \tau_{\theta\theta}}{(1-v)} \right) \tag{5}$$

$$\varepsilon_{\theta\theta} = \frac{1-v^2}{E} \cdot \left(\tau_{\theta\theta} - \frac{v \cdot \tau_{rr}}{(1-v)} \right) \tag{6}$$

$$u_r = r \cdot \frac{1-v^2}{E} \cdot \left(\tau_{\theta\theta} - \frac{v \cdot \tau_{rr}}{(1-v)} \right) \tag{7}$$

where K_1, K_2, and K_3 are constants; v is Poisson's ratio and E is Young's Modulus (743 x

10^3 kg/cm^2). The constants K_1, K_2, and K_3 will be determined by the boundary conditions

and related to the total densification in the center region.

Application of boundary conditions for the two-region model is straightforward. To

satisfy the physical requirement that stresses must be finite and by examining Equations (3)

and (4) for the center region, one gets:

$$\tau_{rr} = \tau_{\theta\theta} = K_2 \tag{8}$$

In the outer region, stresses must go to zero as r approaches infinity so one gets:

$$\tau_{rr} = K_3/r^2 \tag{9}$$

$$\tau_{\theta\theta} = -K_3/r^2 \tag{10}$$

Using Equation (1), it is clear that birefringence would only be produced in the outer region with a maximum at the boundary between the inner and outer region.

In joining the two regions, the radial stress must be continuous at $r = r_1 = r_2$ (small $r_2 - r_1$ assumed) so that:

$$K_3/r_1^2 = K_2 \tag{11}$$

This reduces the description of stresses for the entire area to a single variable, K_2, the stress (radial and tangential) in the central core. Using Equation (11), we can evaluate Equation (7) to relate compaction in the system to a single variable K_2. In the center region, both the radial and tangential stresses equal K_2 (using Equation (7)) so the displacement at the edge of the center cylinder is:

$$u_r(r_1)_I = r_1 K_2 (1 + v) (1 - 2v)/E. \tag{12}$$

where the subscript (I) refers to the inner region. At the inner edge of the outer tube, the radial stress again equals K_2, but the tangential stress equals $-K_2$ (from Equations (10) and (11)), so evaluating Equation (7) there gives:

$$u_r(r_1)_\mathrm{II} = -r_1 \, K_2 \, (1 + v)/E. \qquad (13)$$

Since the initial conditions for this analysis involves two discrete objects, the inner cylinder and the outer tube, the displacements at the boundary of the joined objects is discontinuous, (i.e., material in the inner cylinder is pulled outward while material in the outer tube is pulled inward). The above gives:

$$\Delta r = (r_1 - r_2) = - u_r(r_1)_\mathrm{I} + u_r(r_1)_\mathrm{II} = -2 \, r_1 \, K_2 \, (1 - v^2)/E \qquad (14)$$

for the initial separation of the two sections. Plugging in for Δr given by Equation (2), the relation between unconstrained densification and the center stress (K_2) is:

$$\left(\frac{\Delta\rho}{\rho}\right)_u = -\frac{3}{(1+v)} \cdot \frac{\Delta r}{r_1} = \frac{6 \cdot K_2 \cdot (1-v)}{E} \qquad (15a)$$

or

$$K_2 = \frac{E}{6 \cdot (1-v)} \cdot \left(\frac{\Delta\rho}{\rho}\right)_u. \qquad (15b)$$

The outer section acts to restrict some of the radiation-induced compaction of the center region as well as to suppress strain in the z direction. The net expansion from resistance to compaction is the trace of the final strain matrix. ε_{zz} is zero in the plane strain approximation. Using Equations (5) and (6) one gets the strains from resistance to compaction to be:

$$\varepsilon_{rr} = \varepsilon_{\theta\theta} = K_2 (1 + v) (1 - 2v)/E \qquad (16)$$

and

$$(\Delta\rho/\rho)_{ex} = - (\varepsilon_{rr} + \varepsilon_{\theta\theta}) = -2 K_2 (1 + v) (1 - 2v)/E \qquad (17)$$

where $(\Delta\rho/\rho)_{ex}$ is the expansion from resistance to compaction. To calculate the net density change, we use superposition of the density changes in steps 1, 2 and 3 illustrated in Figures 4, 5 and 6. The density of the stretched cylinder (after step 2) before being joined to the outer uncompacted region is given by:

$$(\Delta\rho/\rho)_i = -[(\varepsilon_{rr})_i + (\varepsilon_{\theta\theta})_i] = -2 \Delta r / r_1 = 4 K_2 (1 - v^2)/E \qquad (18)$$

which includes the contribution from stretching the cylinder back to its original length. Adding the expansion component from joining the stretched cylinder to the bulk to this initial density, one finds the net density change to be:

$$(\Delta\rho/\rho)_{net} = (\Delta\rho/\rho)_i + (\Delta\rho/\rho)_{ex} = [4 K_2 (1 - v^2)/E] - [2 K_2 (1 + v) (1 - 2v)/E]$$

$$= 2 K_2 (1 + v)/E \qquad (19)$$

The mechanical effects predicted from the plane strain analysis of a fused silica sample densified in the center cylindrical volume are summarized in Table 1 below.

Table 1
**Mechanical Effects in Cylindrical Fused Silica Sample
from 1ppm Unconstrained Densification in Center Volume
(calculated from two-region stress model)**

Maximum Radial and Tangential Stress (K_2)	0.149 kg/cm^2
Maximum Net Radial and Tangential Strain	0.235-ppm
Net Densification	0.47-ppm

Note that the net density change is only about half the density change one would observe in a sample which had its entire volume uniformly irradiated.

2.3b Comparison of Two-region stress model to Finite Element Analysis

Finite Element Analysis (FEA) simulations were performed to confirm the validity of the analytical stress modeling. The program FEAP[4] was used for all simulations. Irradiation-induced compaction was emulated by setting the section considered compacted to have a different reference temperature than the uncompacted material. The initial compacted condition is hence reproduced by thermal contraction of the material to the equilibrium temperature. A axis-symmetric geometry is used where the center region is set to have a reference temperature and coefficient of thermal expansion equivalent to a 1ppm densification (1/3 ppm linear densification). Regions near the surface and interface between the compacted cylinder and uncompacted region are meshed more finely to improve accuracy by creating more elements in regions with larger stress gradients.

Figures 7 and 8 show the radial stress distribution calculated using FEAP for 1cm and 2.5cm long samples and using the two-region stress model for a total 1ppm unconstrained

density increase. A 3mm compaction diameter is used for both methods and a 30mm diameter sample is used in the FEAP simulations. Using Equation (15b), a value of 0.149 kg/cm^2 is used for K_2 in the two-region stress model. The stresses shown in the figures are the average stresses integrated through the length of the sample at the given radial distance from the center of the damaged region. Simple FORTRAN programs were written to read in appropriate nodal stresses and to calculate the average. As seen in Figures 7 and 8, the stress distribution predicted from the two-region stress model agrees closely with the FEA result. The agreement for the longer sample is slightly better as the plane strain assumption becomes more valid.
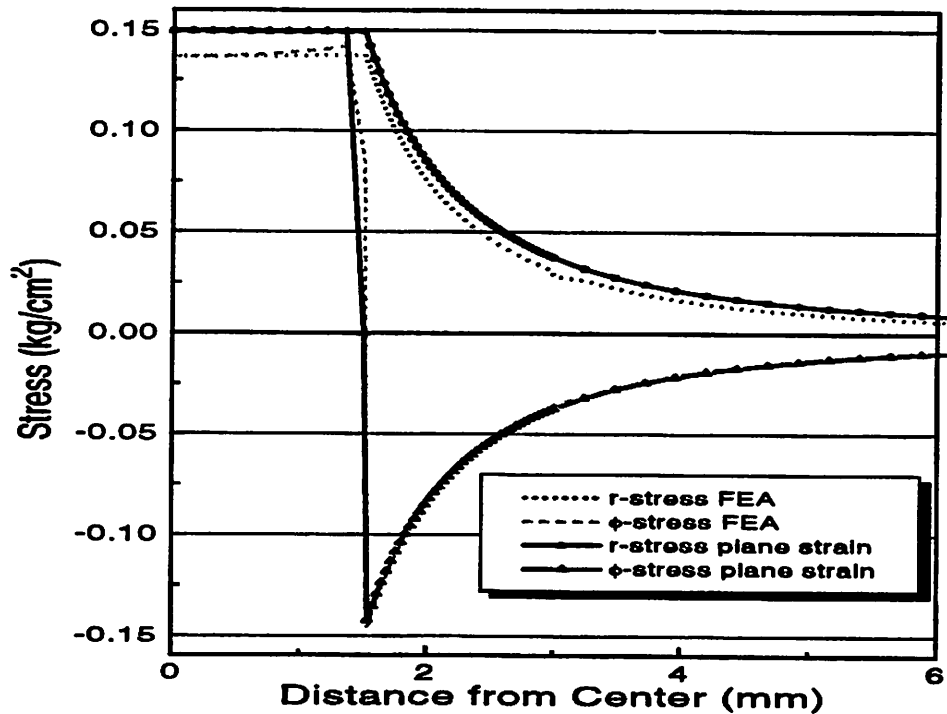
Figure 7. Stress distributions versus distance from center of damage calculated using FEAP and a two-region stress model. Calculations use a 3mm damage diameter and 1cm long sample. The FEA uses a 30mm diameter sample size.

Stress (kg/cm²)

0.15
0.10
0.05
0.00
-0.05
-0.10
-0.15

0   2   4   6
Distance from Center (mm)

.... r-stress FEA
- - - - - φ-stress FEA
———— r-stress plane strain
———— φ-stress plane strain
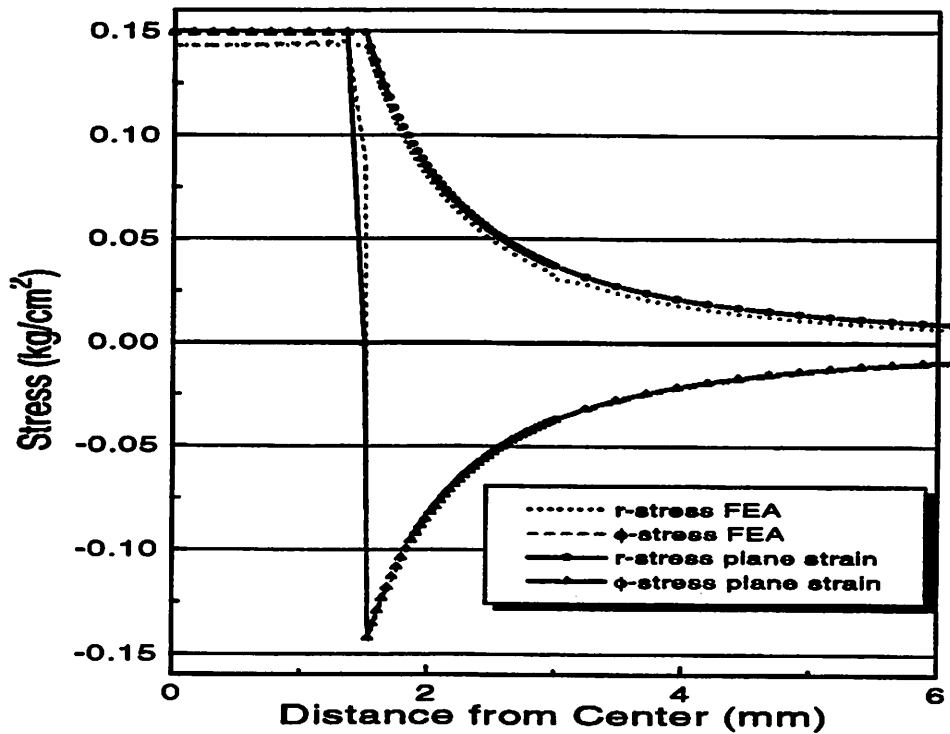
Figure 8. Stress distributions versus distance from center of damage calculated using FEAP and a two-region stress model. Calculations use a 3mm damage diameter and 2.5cm long sample. The FEA uses a 30mm diameter sample size.

The accuracy of using the two-region stress model for different sample geometries is further investigated using FEA. Table 2 shows the calculated radial and tangential stresses using FEA at two distances from the center of the compacted region as the sample length is varied from 3 to 40mm. The results shown are for simulations performed using a 30mm diameter sample with a 3mm diameter compacted region ($r_d = 1.5mm$). The two-region model is more accurate near the boundary between the compacted and uncompacted region than closer to the edge. Even for samples with lengths equal to the diameter of the damaged region, the two-region model predicts the maximum stress difference, ($\sigma_r - \sigma_\theta$), within 10% of the value calculated with FEA.

48

Table 2
Comparison of Stress Calculated with FEA and
Predicted by Two-Region Stresses Model for Different Sample Lengths
(sample diameter 30mm, damage diameter 3mm)

Length	@ (r = 1.025r_d)			@ (r = 1.5r_d)		
	σ_r	σ_θ	$(\sigma_r - \sigma_\theta)_{FEA}/$ $(\sigma_r - \sigma_\theta)_{2RM}$ *	σ_r	σ_θ	$(\sigma_r - \sigma_\theta)_{FEA}/$ $(\sigma_r - \sigma_\theta)_{2RM}$
3mm	0.121	-0.143	0.93	0.053	-0.059	0.85
6mm	0.127	-0.146	0.96	0.055	-0.064	0.90
10mm	0.131	-0.146	0.97	0.058	-0.066	0.94
25mm	0.137	-0.145	0.99	0.062	-0.067	0.97
40mm	0.138	-0.144	0.99	0.063	-0.068	0.98
Model	0.142	-0.142	1	0.066	-0.066	1

*$(\sigma_r - \sigma_\theta)_{2RM}$ is the stress difference predicted by the two-region stress model.

Table 3 shows the calculated radial and tangential stresses using FEA at two distances from the center of the compacted region as the sample diameter is varied from 6 to 60mm. The results shown are for simulations performed using a 25mm long sample with a 3mm diameter compacted region. For small diameter samples (equivalent to large samples with large damage diameters), the two-region model does not predict well either the radial or tangential stresses in the sample. The two-region model, however, does predict well the difference between the radial and tangential stresses (within 5% for these geometries) for samples with diameters as small as twice the damage region diameter because the errors in predicting σ_r and σ_θ are of similar magnitudes. Because the quantity of interest, birefringence, depends upon the difference between the radial and tangential stresses and not directly on the stresses, the two-region model is still applicable for interpreting birefringence measurements in small diameter samples.

Table 3
Comparison of Stressed Calculated with FEA and
Predicted by Two-Region Stress Model for Different Sample Diameters
(sample length 25mm, damage diameter 3mm)

Sample Diameter	@ (r = 1.025r_d)			@ (r = 1.5r_d)		
	σ_r	σ_θ	$(\sigma_r - \sigma_\theta)_{FEA}/ (\sigma_r - \sigma_\theta)_{2RM}$	σ_r	σ_θ	$(\sigma_r - \sigma_\theta)_{FEA}/ (\sigma_r - \sigma_\theta)_{2RM}$
6mm	0.106	-0.182	1.01	0.027	-0.100	0.96
10mm	0.126	-0.156	0.99	0.051	-0.078	0.97
20mm	0.135	-0.146	0.99	0.060	-0.060	0.97
30mm	0.137	-0.145	0.99	0.062	-0.067	0.97
60mm	0.138	-0.144	0.99	0.063	-0.066	0.97
Model	0.142	-0.142	1	0.066	-0.066	1

2.3c Three-region model derived for long cylindrical, large radius samples

The two-region model for radiation-induced compaction described above gives an abrupt

transition from compacted to uncompacted material. Because of the difficulty in getting a

uniform laser beam profile with a sharp cutoff in intensity, a more general model was

developed to better account for compaction distributions with a finite slope. A three

region model will be used with a uniformly compaction center region ($r < r_i$), an

uncompacted region ($r > r_o$), and a transition region ($r_i < r < r_o$). We assume the same

functions (Equations 3 and 4) are valid for some (as yet unknown) form of compaction

versus radius in region (2). We will find Equation (30) for the form of compaction in

region (2). The Airy stress function, given by Equations (3) and (4), again can be used to

describe the general equations for stress in each of the three regions separately. Applying

the boundary conditions as before, the stresses in the three regions are given as follows:

Region I: $(r < r_i)$ $\tau_{rr} = \tau_{\theta\theta} = K_2$ (20)

Region II: $(r_i < r < r_o)$ $\tau_{rr} = D_1 [\ln(r) - 1/2] + D_2 + D_3/r^2$ (21)

$\tau_{\theta\theta} = D_1 [\ln(r) + 1/2] + D_2 - D_3/r^2$ (22)

Region III: $(r > r_o)$ $\tau_{rr} = K_3/r^2$ (23)

$\tau_{\theta\theta} = - K_3/r^2$ (24)

where K_2, D_1, D_2, D_3, and K_3 are constants. The stress distribution becomes a function of

a single unknown, the stress in the center irradiated region when the boundary conditions

of continuous radial stress and displacements at the two interfaces are applied. The

stresses in the three regions are given as:

$$\tau_{rr}(r)_I = \tau_{\theta\theta}(r)_I = K_2$$ (25)

$$\tau_{rr}(r)_{II} = K_2 [\ln(r/ r_o) - 1/2 + r_i^2/(2r^2)]/[\ln(r_i/ r_o)]$$ (26)

$$\tau_{\theta\theta}(r)_{II} = K_2 [\ln(r/ r_o) + 1/2 - r_i^2/(2r^2)]/[\ln(r_i/ r_o)]$$ (27)

$$\tau_{rr}(r)_{III} = [K_2 (r_i^2 - r_o^2)]/[2 r^2 \ln(r_i/ r_o)]$$ (28)

$$\tau_{\theta\theta}(r)_{III} = [-K_2 (r_i^2 - r_o^2)]/[2 r^2 \ln(r_i/ r_o)]$$ (29)

51

Shames shows that K_1 in Equations (3) and (4) must be zero for a multiply connected domain in order to essentially ensure compatible strains. Since the three-region model presented above has a transition region with a gradually changing initial density, K_1 need not be zero in this region. In fact, the three-region solution can be represented as the summation of two-region stress solutions. The unconstrained densification in the transition region, which is proportional to the net density change in that region, is:

$$(\Delta\rho/\rho)_{\Pi}(r) = (\Delta\rho/\rho)_u(r=0) \, [\ln(r/r_o)]/[\ln(r_i/r_o)]. \tag{30}$$

This is nearly linear for typical values of r_i and r_o, i.e. $\left(r_o - r_i\right) \le r_i$.

Figure 9 shows the radial and tangential stress distributions as described by the three-region model for inner and outer radii of 1.2mm and 1.8mm respectively. For comparison, the stress-distribution found using the two-region model and a boundary at 1.5mm is also illustrated. While variations in the stress levels are found near the boundary, similar stresses are predicted away from the boundary using both models.
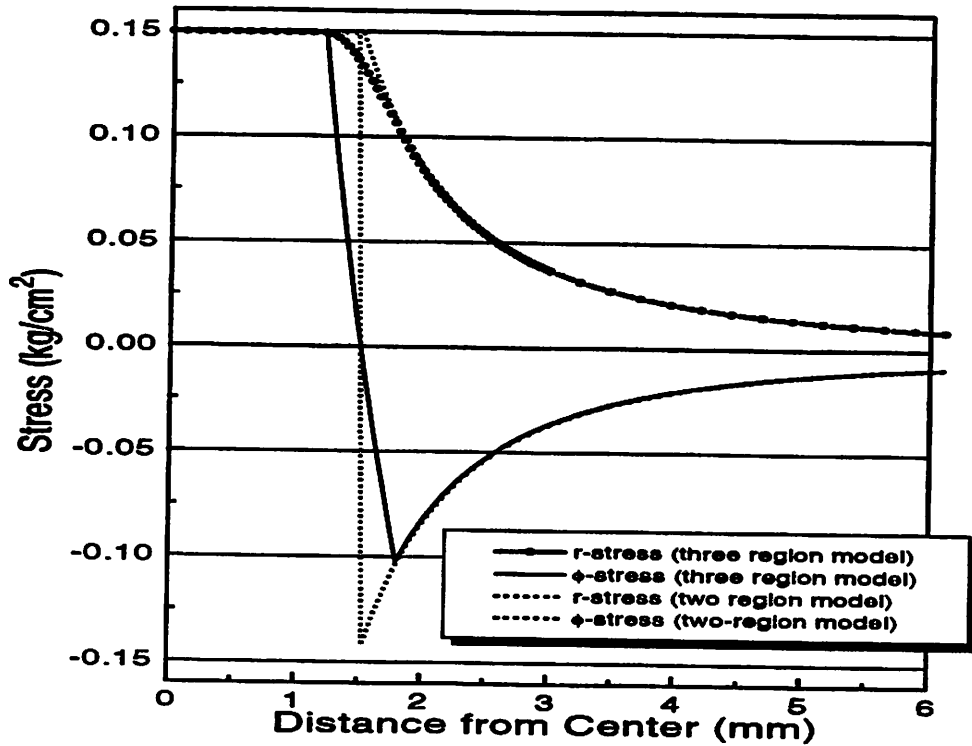
Figure 9. Stress distributions versus distance from center of damage calculated using a two and a three-region stress model. The two region model uses a boundary radius of 1.5mm while the three-region model uses inner and outer radii of 1.2mm and 1.8mm.

Remarkably, because the three-region model can be represented as a summation of two-region solutions, Equation (15) still describes the relation between the maximum radial stress (K_2) and the unconstrained densification in the center of the sample. For both the two and three region models, the maximum stress depends only upon the center unconstrained densification, not the location of the boundaries. For the three-region model, however, the maximum stress difference $(\tau_{rr} - \tau_{\theta\theta})$ is less than $2K_2$. As will be derived in the next section, the maximum birefringence signal is proportional to the maximum stress difference squared. With the three-region model, the maximum stress difference is found at r_o and is equal to:

$$\left(\tau_{rr} - \tau_{\theta\theta}\right)_{max} = \frac{K_2 \cdot \dfrac{r_i^2 - r_o^2}{r_o^2}}{\ln\left(\dfrac{r_i}{r_o}\right)} \equiv \eta \cdot K_2 \qquad (31)$$

For small $(r_o - r_i)$, η is approximately equal to $2[1 - (r_o - r_i)/r_o]$. If the outer radius is 1.1 times that of the inner radius, the maximum stress difference is equal to $1.82 \, K_2$.

2.4 Using the compaction model to analyze birefringence distributions

2.4a Calculating Stress-Induced Birefringence

The input radiation, traveling in the z direction, is assumed to be a linearly polarized wave with an electric field $A \underline{x} \sin(\omega t - kz)$, where $\underline{x}$ is a vector and A a constant. The electric field can be resolved into two equal orthogonal components[5] if the vectors are chosen to be at 45 degree angles with respect to the input polarization. The electric field can thus be expressed as $\dfrac{\sqrt{2}}{2} A \cdot [\bar{x}' + \bar{y}'] \cdot \sin(wt + kz)$ where the vectors ($\underline{x}'$ and $\underline{y}'$) are defined in Figure 10. A phase difference between the two polarizations, $\underline{x}'$ and $\underline{y}'$, of β will be assumed to have formed after the beam has transmitted through the sample. The field exiting the sample is then $\dfrac{\sqrt{2}}{2} A \cdot [\bar{x}' \sin(wt) + \bar{y}' \sin(wt + \beta)]$.
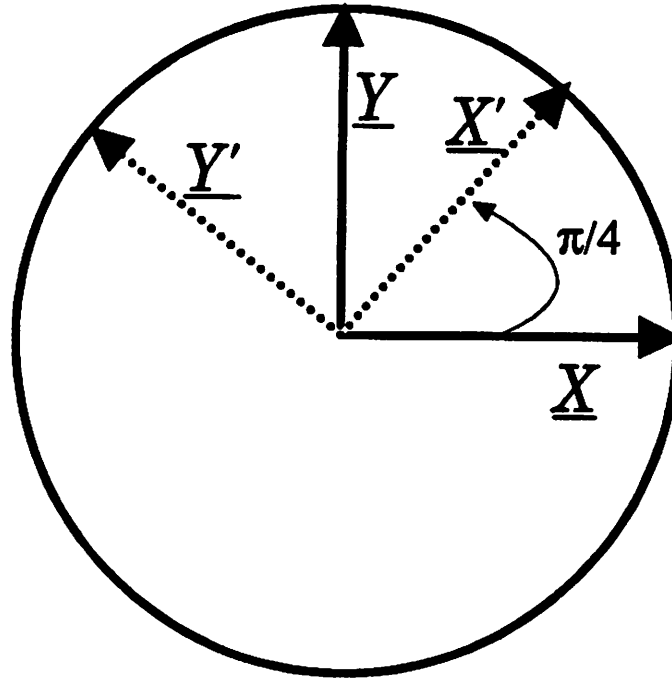
Figure 10. Vector definitions for birefringence analysis.

Transforming back to (x, y) coordinates one gets:

$$\underline{E}_{out} = \underline{x}\,\{1/2\ A\ [\sin(\omega t) + \sin(\omega t+\beta)]\} + \underline{y}\,\{1/2\ A\ [\sin(\omega t+\beta) - \sin(\omega t)]\} \qquad (32)$$

or

$$\underline{E}_{out} = 1/2\ A\{\underline{x}\ [\sin(\omega t)\ (\cos\beta+1)+\cos(\omega t)\ \sin\beta]\}+\underline{y}\ [\sin(\omega t)\ (\cos\beta - 1)+\cos(\omega t)\ \sin\beta]\} \qquad (33)$$

The magnitude of the output intensity which is s-polarized is given as:

$$I_p = \frac{1}{T}\int_T (E_y(t))^2\,dt \qquad (34)$$

55

which is equal to 1/4 A^2 [1 - cosβ]. Normalizing to unit intensity ($A^2 = 2$) and for small β

this gives the fraction s-polarized to be $β^2/4$. The phase difference β, is that originated by

the stress-optic effect which is:

$$β = Δ(kz) = 2 π L Δn/λ = 2 π L ℜ (σ_{y'} - σ_{x'})/λ \tag{35}$$

where L is the length of the sample, λ the wavelength (633nm), and ℜ the stress-optic

coefficient [-3.5 (nm/cm)/(kg/cm^2) at 633nm][6]. Thus the fraction s-polarized is equal to:

$$(\text{fraction s-polarized}) = [π L ℜ (σ_{y'} - σ_{x'})/λ]^2 \tag{36}$$

showing that the birefringence signal goes as both the stress (proportional to compaction)

and the length of the sample squared.

One can use the index ellipsoid to find the direction refractive index changes and hence

fraction polarized signal for cases when the principle stress axes are not perpendicular to

the probe beam polarization. For small differences in direction indices, $(n_2 - n_1)(φ) =$

$\sin(2φ) (n_o - n_e)$, where n_2 and n_1 are the principle refractive indices seen by the probe

beam, n_o and n_e are the indices in the principle stress directions, and φ is the angle between

the probe beam polarization and the principle radial stress direction.

The model birefringence distribution can now be described as:

56

$$(\text{fraction s-polarized}) = [\sin(2\phi)\ \pi\ L\ \Re\ (\sigma_r - \sigma_\theta)/\lambda]^2 \tag{37}$$

where σ_r and σ_θ are the radial and tangential stresses and, in this case, also the principle

stresses. The fraction (energy) of a p-polarized probe beam shifted to s-polarized for any

location in and around a compacted region can be calculated using Equation (37) and the

previously determined relations for σ_r and σ_θ. The maximum depolarization occurs when

the probe beam is orientated at 45 degrees with respect to the principle stress axes ($\phi =$

45) and at the edge of the compacted region. The maximum depolarization is given by:

$$(\text{fraction s-polarized})_{max} = \left(\frac{\eta \cdot K_2 \cdot \pi \cdot L \cdot \Re}{\lambda}\right)^2 = \left(\frac{\eta \cdot \pi \cdot L \cdot \Re \cdot E \cdot (\Delta\rho/\rho)_u}{6 \cdot \lambda \cdot (1-v)}\right)^2 \tag{38}$$

where the maximum difference between the principle stresses is $\eta\ K_2$ ($\eta = 2$ for two-

region model).

2.4b Example experimental result

Figure 11 shows a measured birefringence distribution for a sample irradiated by a 3mm

diameter 193nm beam with 12 million, 1-mJ/cm^2 pulses applied. The four peaks

correspond to locations where the probe beam polarization is at 45 degrees with respect to

the principle stress axes. The z-ordinate is directly proportional to the current produced

Figure 11. Measured birefringence for linearly polarized light (at 633nm) scanned across a 6.6mm square sample region which has been exposed to a 3mm diameter 193nm excimer laser beam (12 million pulses, $1.05mJ/cm^2$).
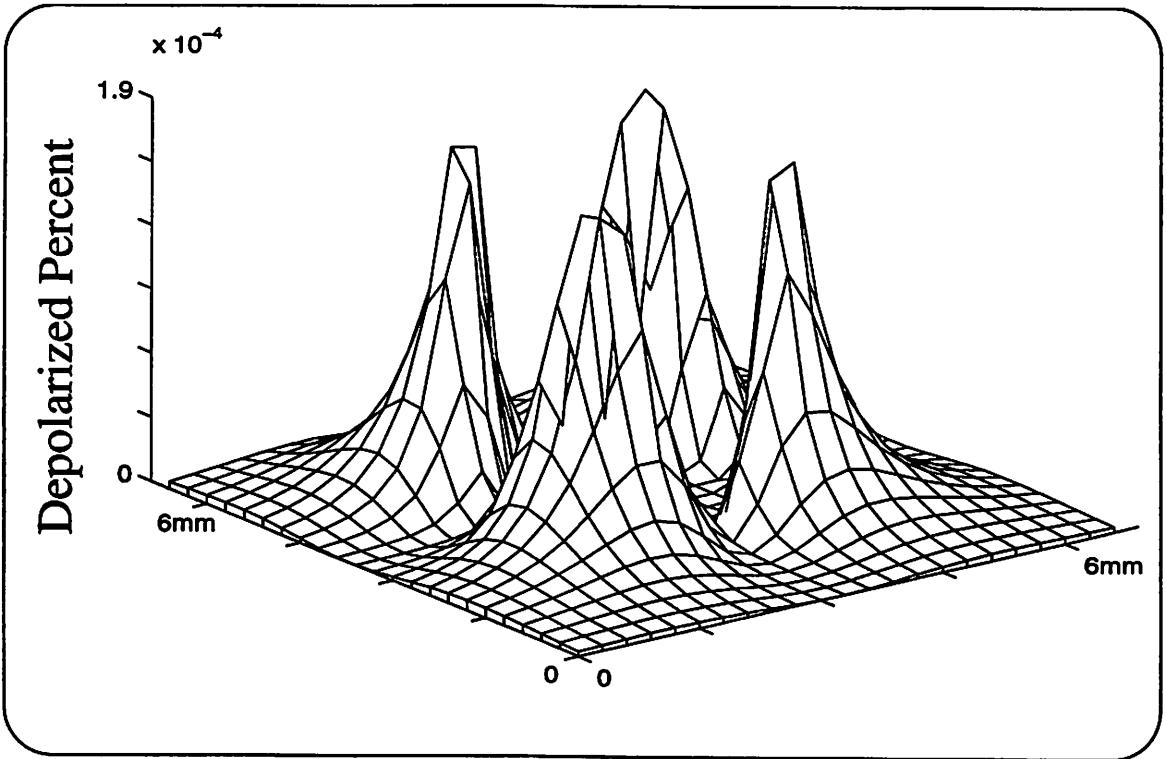
Figure 12. Simulated birefringence for the same sample assuming a net 95ppB densification (using a plane strain compaction model) in a 3mm diameter compaction zone.

by the photodiode detecting the reflectance of the Brewster plate used in the experimental setup.

Matlab was used to fit the calculated general birefringence distribution from the three-region stress model to the measured distributions by adjusting the level of stress in the center region to the optimum magnitude. The locations of the boundaries (r_i and r_o) were selected as the 90% and 10% intensity radii as measured by a CCD camera (typical values 1.4mm and 1.56mm). A simple technique was employed to partially emulate the smearing of the birefringence distribution owing to the finite size of the probe beam. The routine first calculated the birefringence distribution at discrete locations assuming a point probe beam. The birefringence at each location was then modified using the following relation:

$$F(i, j) = A \, f(i, j) + (B/4) \, [f(i+1, j) + f(i-1, j) + f(i, j+1) + f(i, j-1)] \tag{39}$$

where $f(i, j)$ is the calculated birefringence at matrix location (i, j), A and B are constants where A + B equals 1, and $F(i, j)$ is the modified birefringence taking into account the finite probe beam size. Using concepts of numerical integration, B was selected to be one fourth times the ratio of the probe beam diameter (~0.5mm) to measurement spacing.

Figure 12 shows the best fit of the three-region stress model to the data in Figure 11. The center radial stress (K_2) corresponding to the birefringence distribution in Figure 11 is 0.030 kg/cm^2. Using Equations (15a) and (19) and this value of K_2, the unconstrained and

net densifications are calculated to be 200ppB and 95ppB respectively. The accuracy of using these Equations for extracting compaction levels will be discussed in Chapter 5.

The level of compaction which produced the birefringence distribution in Figure 11 would only produce about 1/500 of a wavelength (633nm) OPD through the sample. This is very difficult to measure with interferometry using a perfect sample and virtually impossible for a sample with imperfect surface polish or bulk inhomogeneities.

2.5 Effect of intrinsic birefringence on accuracy

As one might expect, the presence of intrinsic birefringence in a sample adversely effects the measurement of stress-induced birefringence. Figure 13 shows a very highly birefringent sample which was unirradiated. Figures 14 and 15 show how the total birefringence progressed after the sample was irradiated for 610 thousand and 1.2 million 15 mJ/cm^2 pulses. In Figure 14, only two of the four characteristic peaks have been formed and valleys are actually formed where the other two peaks would normally have formed. The valleys form because the induced stresses cancel out intrinsic stresses, reducing the birefringence. The two peaks are higher than they would be in a sample without intrinsic birefringence because the compaction-induced stresses add constructively with the intrinsic stresses to get an artificially high peak. Figure 15 shows the birefringence distribution when the compaction-induced stress is just large enough to completely cancel out the intrinsic stresses and form four peaks. If an uniformly directed

60
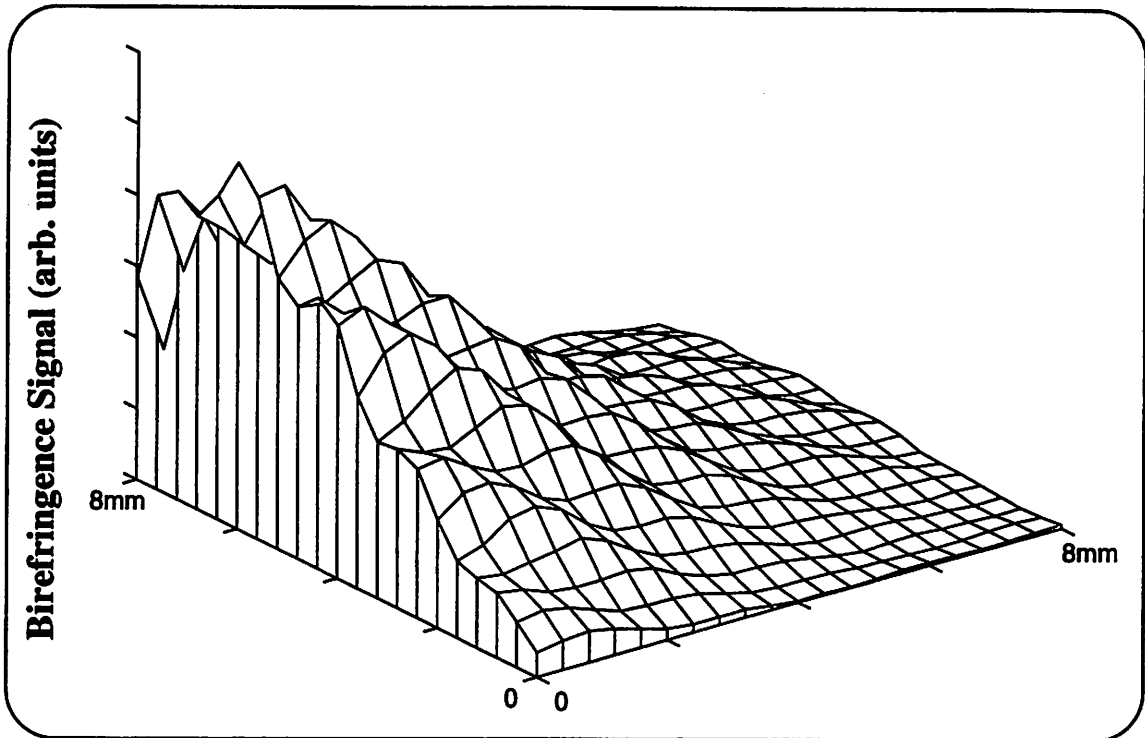
Figure 13. Measured intrinsic birefringence for linearly polarized light (at 633nm) scanned across a 8mm square unexposed sample region.
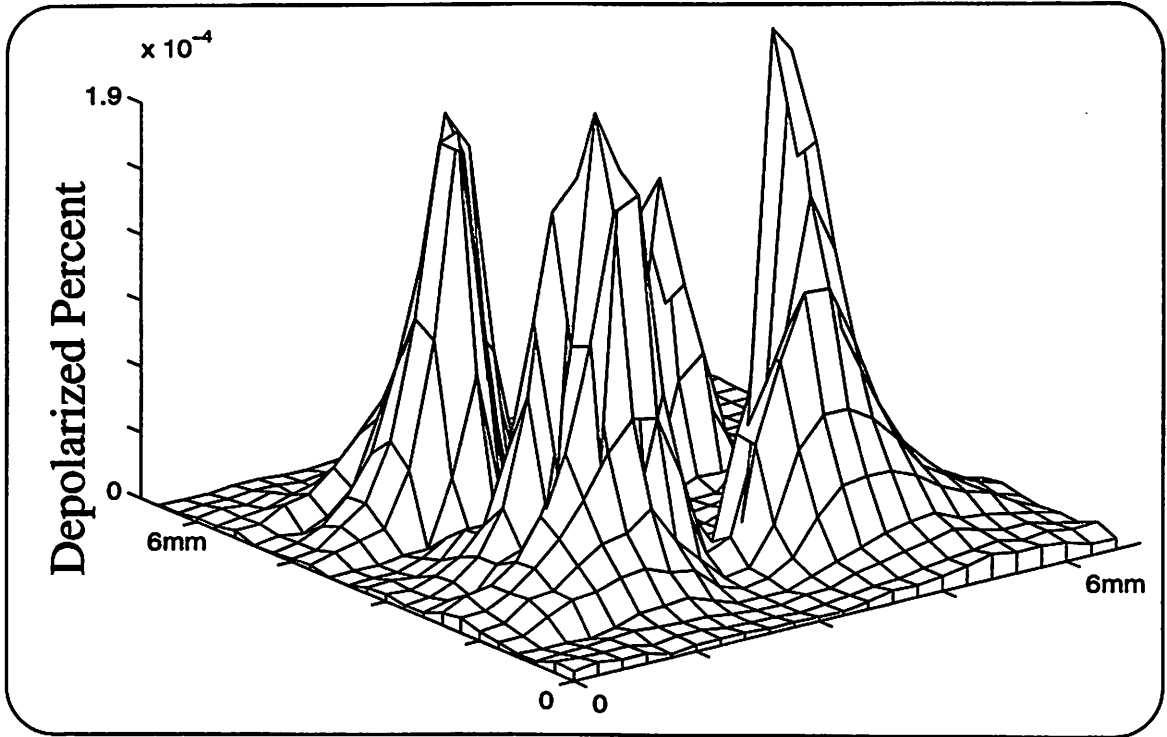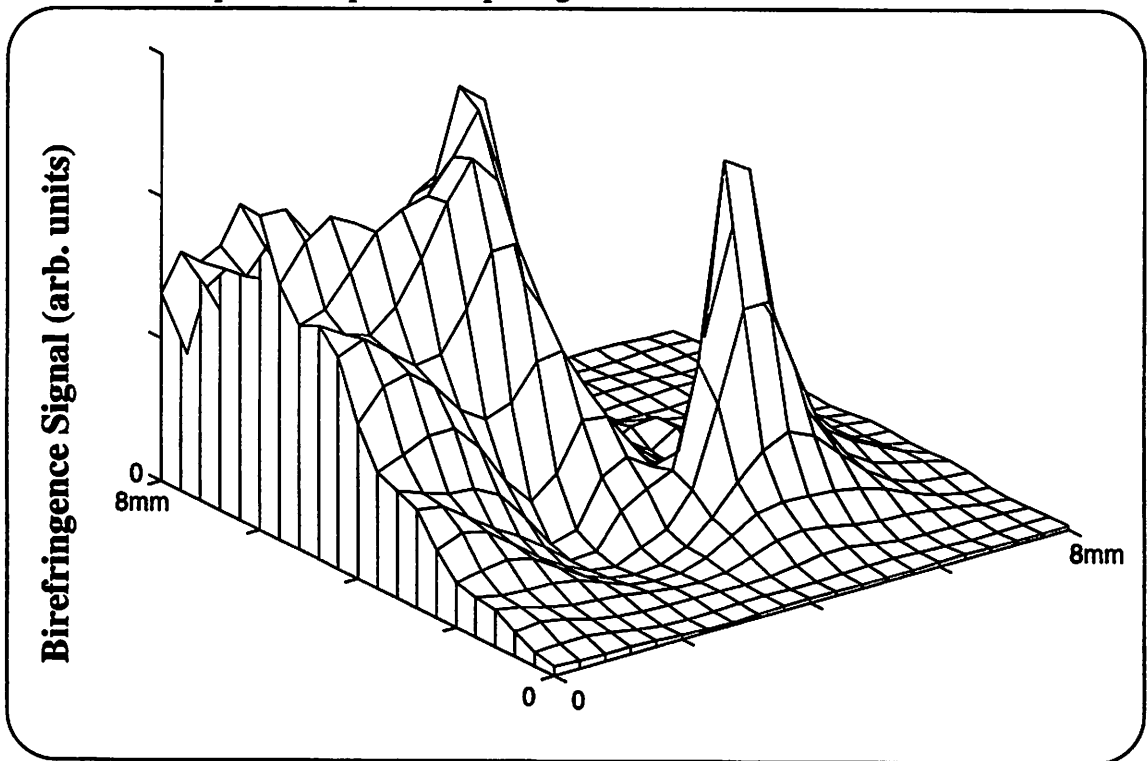

Figure 14. Measured birefringence for linearly polarized light (at 633nm) scanned across a 8mm square sample region (intrinsic birefringence shown in Figure 8) which has been exposed to a 3mm diameter 193nm excimer laser beam (610 thousand pulses, 15 mJ/cm^2).
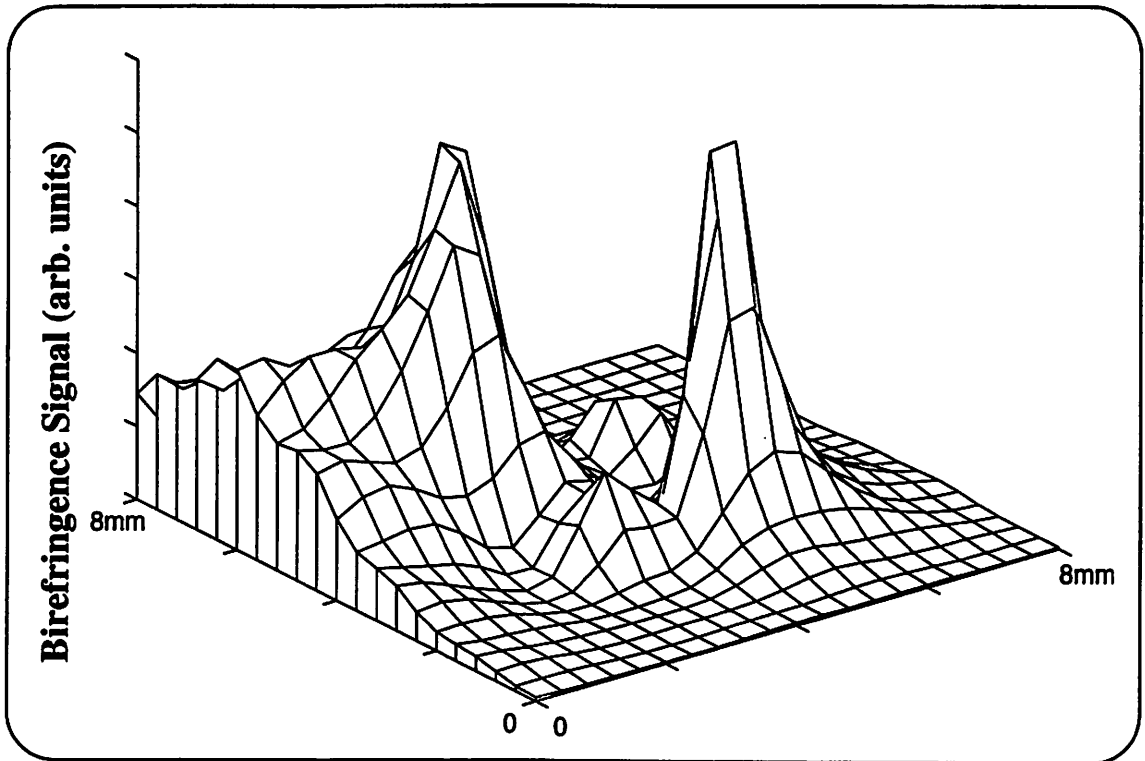
Figure 15. Measured birefringence for linearly polarized light (at 633nm) scanned across a 8mm square sample region (intrinsic birefringence shown in Figure 8) which has been exposed to a 3mm diameter 193nm excimer laser beam (1.2 million pulses, 15 mJ/cm^2).

stress is intrinsic in the sample, two of the four peaks will have increased magnitudes while the other two will be reduced. For such a case, the error from intrinsic birefringence is partially canceled out. One can see from the above figures, however, that monitoring birefringence at only one location around the compaction site could result in misleading readings if significant intrinsic birefringence is present. Fortunately, lithographic grade samples have low intrinsic birefringence.

2.6 Conclusions

Experimental measurements of stress-induced birefringence resolve the birefringence produced from samples with very low damage levels. In order to extract compaction levels from the birefringence distributions, the stress distribution from a cylindrical compacted area is modeled using both a two and three-region analytical construction for long, large-diameter samples. The analytical stress distribution agrees with finite element simulations. Basic electromagnetic theory is applied to calculate the birefringence distribution from the model stress distributions. The calculated birefringence distribution using stresses described by the three-region stress model agrees with measured birefringence distributions. By using the stress models to extract densification levels from birefringence measurements, one can measure compaction at levels an order of magnitude smaller than that resolvable with conventional interferometry.

References

---

[1] for more information, see for example A.J. Durelli, and W.F. Riley, *Introduction to Photomechanics*, 1965.

[2] for details see R. Schenker, *Issues in the Industrial Application of Deep-UV Photolithography Sources*, Master's thesis UC-Berkeley, school of Electrical Engineering and Computer Sciences, 1994.

[3] I. H. Shames and F. A. Cozzarelli, *Elastic and Inelastic Stress Analysis*, Prentice Hall Inc., 1992.

[4] developed and written by Prof. R. L. Taylor at the civil engineering department of UC-Berkeley.

[5] for more background, see for example, E. Hecht, Optics, Second Edition, Addison-Wesley Publishing Co., 1987.

[6] W. Primak, D. Post, "Photoelastic constants of vitreous silica and its elastic coefficient of refractive index," J. Appl. Phys. 30 (5), pp. 779-788, May 1959.

Chapter 3

Comparison of Compaction and Color Center Formation in Fused Silica

Five different fused silicas were evaluated for their resistance to UV-induced compaction and color center formation at 193-nm. Real-time monitoring of color-center-induced absorption showed three distinct dependencies of transmission on pulse count. The initial rates of color center formation varied by well over a factor of ten between the materials tested while compaction rates varied by at most a factor of four. Total compaction was measured using both interferometry and compaction-induced birefringence measurements. Real-time monitoring of stress-induced birefringence showed that fused silica densifies with irradiation independent of color center formation. While color center formation saturates in some samples, no indication of saturation of compaction was observed.

3.1 Introduction

In 1993 Krajnovich et. al. at IBM Almaden[1] showed that different fused silica types displayed markedly different color center formation rates and annealing properties when irradiated with high energy density (500 mJ/cm^2) 248-nm pulses. Only qualitative observations regarding compaction-induced birefringence were recorded. Because of the potentially large impact of compaction on 193-nm optical system lifetime, we performed experiments to better characterize the transient properties of both color centers and compaction under UV irradiation.

3.2 Experimental Setup

The 193-nm experiments described in this chapter were performed at AT&T Bell Laboratories in Murray Hill and used a Lambda Physic EMG 103 Excimer Laser operated at 30Hz. The laser pulse duration was approximately 20 nanoseconds. A 2.5mm aperture was used to insure a uniform and circularly symmetric beam profile. UV sensitive photodiodes measured individual pulse transmission by monitoring pulse intensity before and after the fused silica sample. The E' color center[2] has an absorption peak at about 215-nm with a half maximum at about 185-nm so induced 193-nm absorption is a measure of E' center formation. Compaction was monitored using stress-induced birefringence as described in Chapter 2.

The fused silica samples tested in these experiments were Suprasil 300, Suprasil 2, SV2G1, and Suprasil 311, manufactured by Heraeus Amersil[3], and Corning Excimer Grade 7940. Suprasil 300 and Suprasil 311 are manufactured from the same starting material with an OH content of about 200ppm. Suprasil 311 receives a proprietary homogenization step while Suprasil 300 is chemically dehydrated. Suprasil 300 is known as a "dry" fused silica (OH < 1ppm), which have been shown in the past to be more prone to UV damage than fused silicas with a higher OH content[4]. Suprasil 2 and Corning 7940 are both "wet" fused silicas (OH > 1000ppm) and were classified as "slow relaxers" by the group at IBM Almaden[1]. "Slow relaxers," have been demonstrated to have a significantly slower rate of induced absorption relaxation after UV irradiation is discontinued than with "fast relaxers," like SV2G1. Suprasil 2 and SV2G1 are manufactured from the same raw

fused silica material, but Suprasil 2 is processed to have higher homogeneity. The properties of the five fused silica types are summarized below in Table 1 as are the exposure conditions for each sample. The homogeneity "grades" are entirely arbitrary and are only listed for a relative comparison of the samples with "Grade A" being the most homogeneous. The energy densities listed in Table 1 are averages, where the individual pulse energy densities had a standard deviation of about 8 mJ/cm^2.

Table 1
Fused silica sample descriptions and irradiation experimental conditions

Material and Length	OH content	Homogeneity	Average Pulse Energy Density	Total Pulses
Suprasil 311 (5mm)	1000 ppm	Grade A	83 mJ/cm^2	1000K
SV2G1 (10mm)	1000 ppm	Grade B	79 mJ/cm^2	500K
Suprasil 300 (10mm)	200 - 300 ppm	Grade A	83 mJ/cm^2	467K
Suprasil 2 (10mm)	1000 ppm	Grade D	77 mJ/cm^2	400K
Corning Excimer Grade 7940 (25.4mm)	< 1ppm	Grade AB	79 mJ/cm^2	450K

3.3 Real-time color center monitoring

Figures 1-3 show the dose dependence of Suprasil 2, Suprasil 311 and SV2G1. Data points correspond to the average of 20 individual pulse transmission measurements.

Figure 1 shows that induced absorption in Suprasil 2, which is proportional to color center density, increases approximately linearly with pulse count. Suprasil 311, on the other hand, seems to begin with a large color center formation rate, but then the rate decreases approximately exponentially with pulse count. SV2G1, has an enormous initial absorption loss rate, followed by a small gradual recovery. The "fast relaxing" property of SV2G1
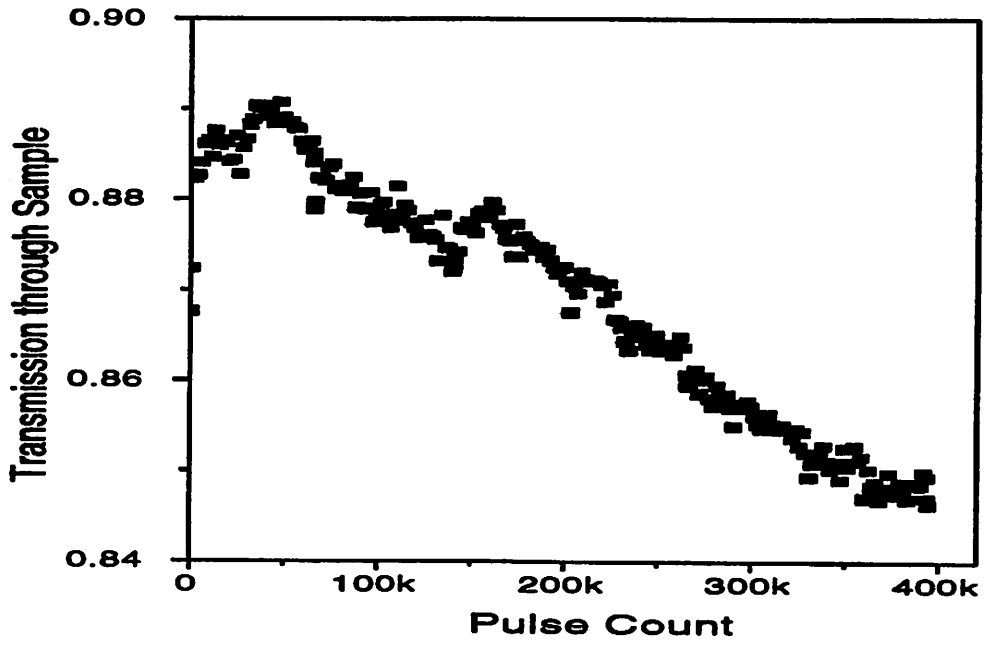
Figure 1. Transmission through 1-cm long Suprasil 2 versus 77(mJ/cm^2), 193-nm pulse count
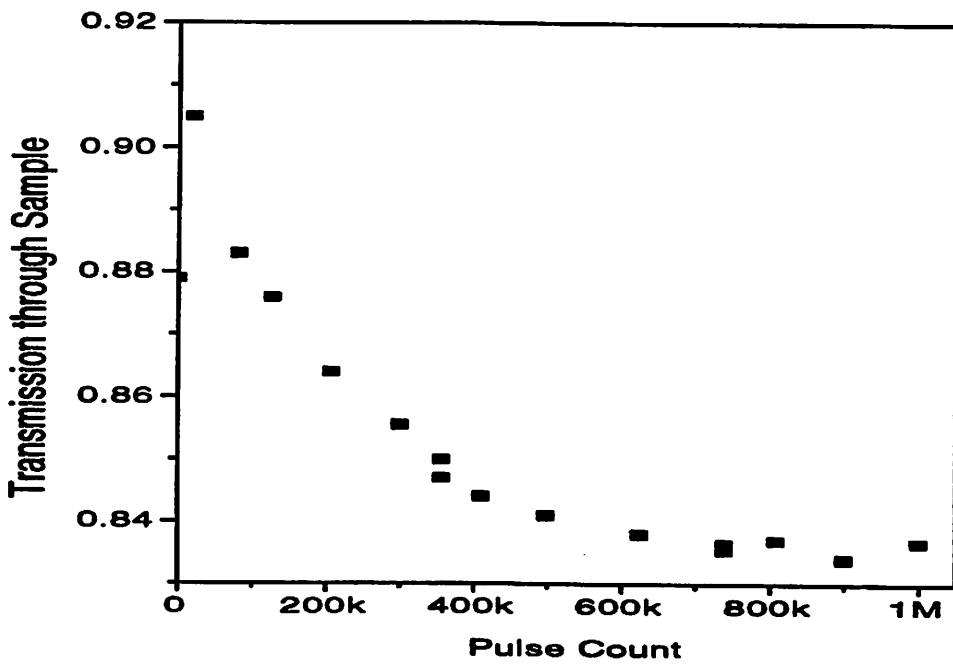
Figure 2. Transmission through 0.5-cm long Suprasil 311 versus 83(mJ/cm^2), 193-nm pulse count.

68
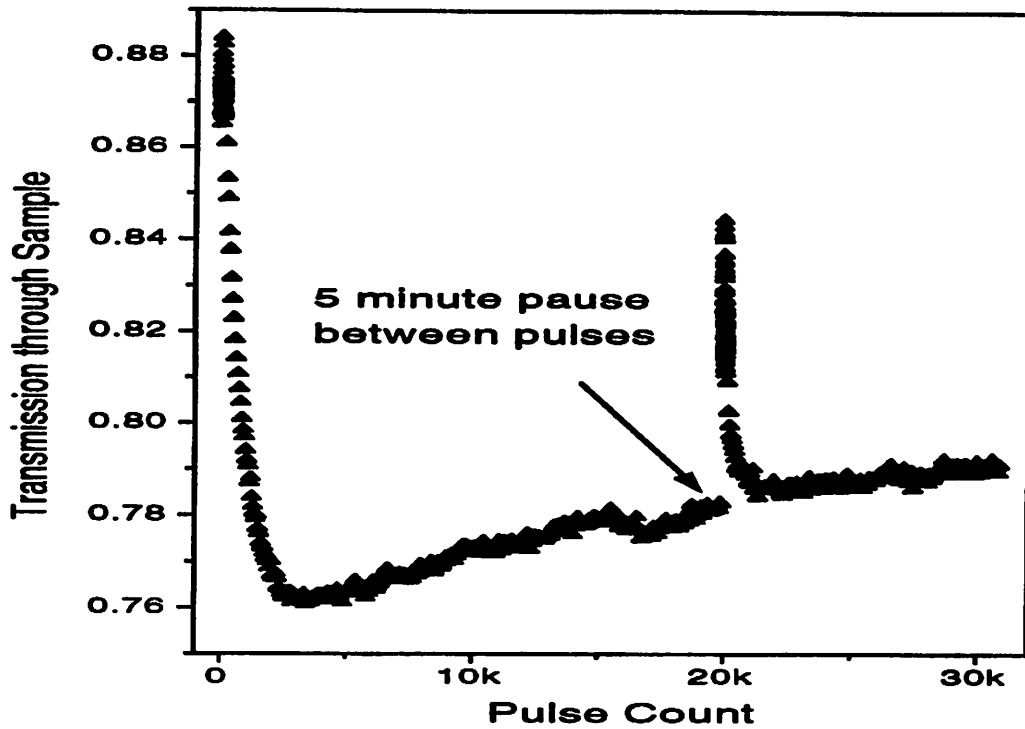
Figure 3a. Transmission through 1-cm long SV2G1 "fast relaxer" versus 80(mJ/cm^2), 193-nm pulse count. During a five minute pause in sample exposure, the transmission superficially returned near its undamaged value. When exposure was continued, the transmission returned to its previous damaged value in about two minutes.
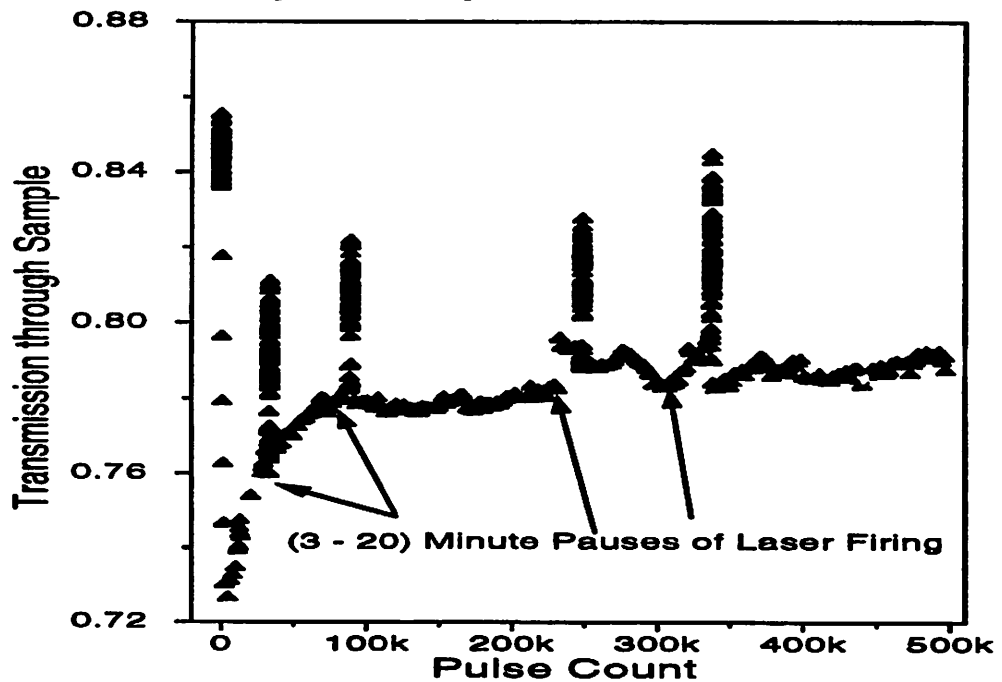
Figure 3b. Transmission through another 1-cm long SV2G1 "fast relaxer" versus 79(mJ/cm^2), 193-nm pulse count. "Fast-relaxing" behavior is again seen as is a gradual improvement in transmission after the sharp initial drop.

was observed in a five minute pause in an exposure in Figure 3a. The sample

transmission, which had recovered to nearly its undamaged value, quickly returned to its

previous damaged transmission value in less than two minutes after continuing exposure.

Individual pulse transmission is plotted in Figure 3a at the highly sloped regions. Figure

3b shows how the induced absorption in SV2G1 (a different test than that in Figure 3a)

saturates very early in the exposure and then actually improves with continuing irradiation.

The other samples tested, Corning Excimer Grade 7940 and Suprasil 300 exhibited linear

color center formation versus pulse count dependence like Suprasil 2. Suprasil 300

darkened about twice as fast as Suprasil 2 while Corning Excimer Grade 7940 was about

ten times more resistant to color center formation than was Suprasil 2.

3.4 Compaction monitoring

3.4a Transient stress-induced birefringence

The depolarization dependence of Suprasil 2, Corning Excimer Grade 7940 and SV2G1

on 193-nm pulse count is shown in Figures 4-6. The signal in the plots is the birefringence

generated at a location near the edge of the irradiation region as the samples are damaged.

The other two fused silicas show a similar functional dose dependence. Because of the

difficulty in positioning the probe beam at the same location with respect to the damaging

beam from exposure to exposure, the magnitude of the signals should not be compared.
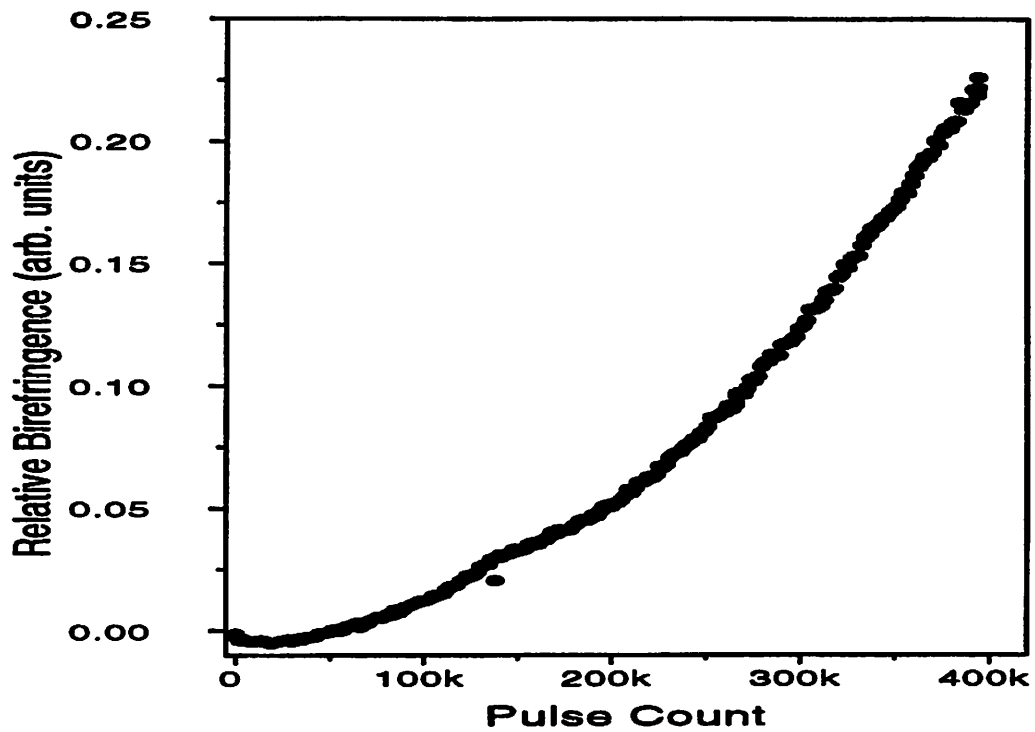
Figure 4. Pulse Count dependence of stress induced birefringence through 1-cm Suprasil 2 fused silica for 77(mJ/cm^2), 193-nm pulses. Birefringence is measured by detecting changes in a polarized He-Ne probe beam.
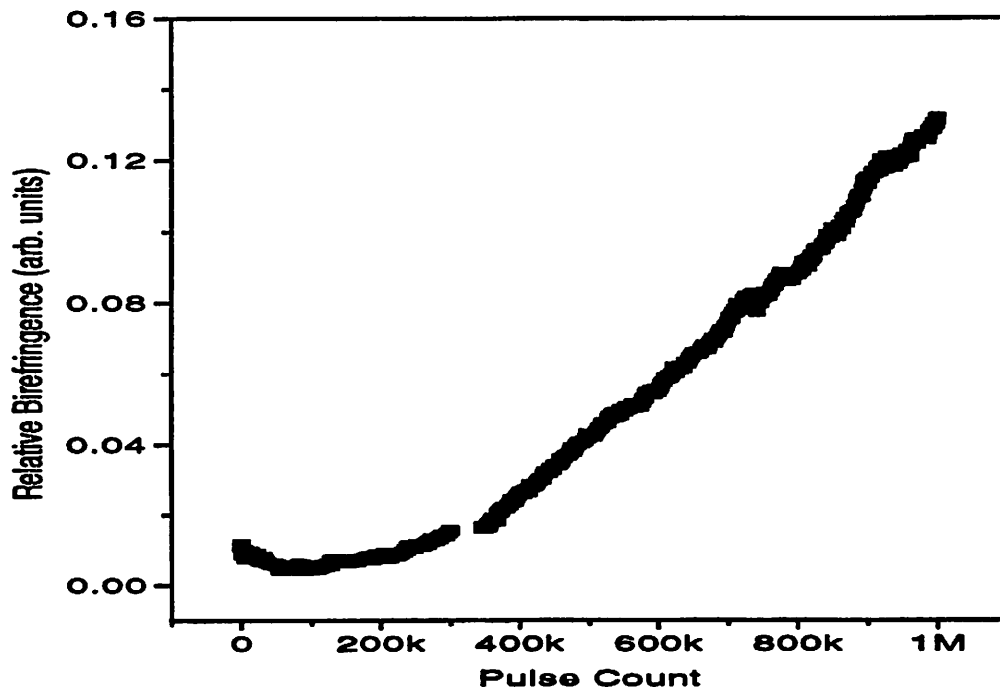
Figure 5. Pulse Count dependence of stress induced birefringence through 0.5-cm long Suprasil 311 fused silica for 83(mJ/cm^2), 193-nm pulses.

71

All fused silicas showed roughly the same pulse count dependence of the birefringence signal. Since the birefringence signal follows the compaction level squared, a quadratic dependence of birefringence signal with pulse count would indicate a linear dependence of compaction on pulse count. For all samples measured, the birefringence signal is found to be super-linear but sub-quadratic, indicating a slightly less than linear dependence of compaction on pulse count. More rigorous data characterizing the pulse count dependence of compaction will be presented in Chapter 6.
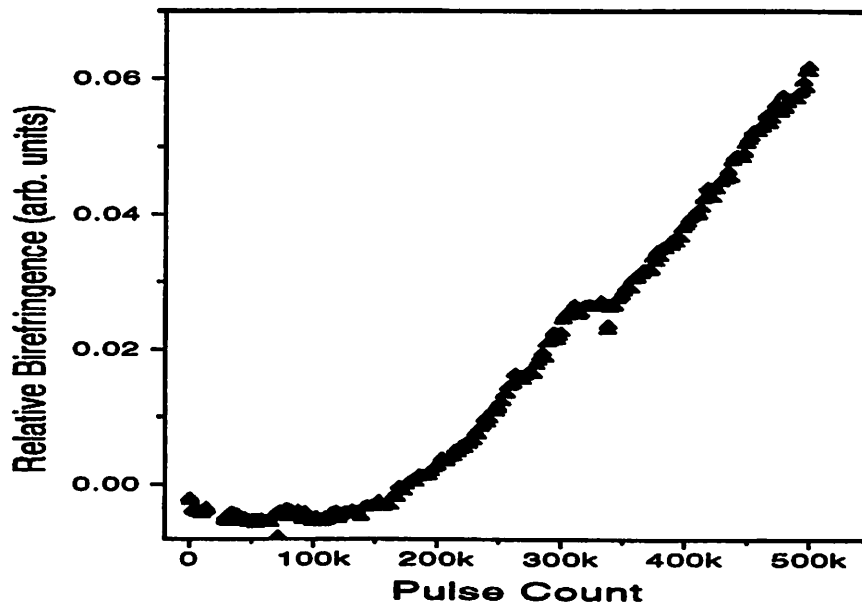
Figure 6. Pulse Count dependence of stress induced birefringence through 1-cm long SV2G1 fused silica for $79(mJ/cm^2)$, 193-nm pulses.

For some of the tests, the birefringence signal actually drops initially followed by the characteristic near-quadratic increase. This drop is believed to be caused by the initial cancellation of intrinsic birefringence followed by the building of compaction-induced birefringence. This phenomenon was noted in Chapter 2. The real-time monitoring of birefringence showed that compaction in fused silica forms independent of color center formation. In the "fast-relaxing" sample, for example, the color center density increases to

its maximum at almost the beginning of the irradiation while the compaction-induced

birefringence builds gradually with the exposure and does not exhibit any indications of

saturation. The birefringence, furthermore, never displays any transient behavior resulting

from halting or reinstating an exposure unlike color-center-induced absorption.

3.4b Interferometry measurements of compaction-induced OPD's

Transmitted and reflected phase interferometry measurements on the damaged samples

were conducted at Corning Inc. using a Zygo phase interferometer[5]. A fit of the first 36

Zernike phase terms was subtracted from the raw data to give a residual wavefront.

Induced optical path differences (OPD's) were extracted from the residual wavefront,

because the magnitude of the OPD's from intrinsic inhomogeneities were larger than many

of the radiation-induced OPD's. Most of the intrinsic inhomogeneities resulted from poor

surface finish as observed in the reflection interferometry measurements.

Table 3 below lists the extracted OPD's from the residual wavefronts. The gross optical

path length increase from compaction in the samples is equal to the net path length

increase as measured from the transmitted wavefront minus the path length decrease from

surface depressions. A bulk index change for each sample is calculated by dividing the

gross optical path length change by the sample length using Equation 1:

$$\frac{\Delta n}{n} = \frac{\left(OPD - \Delta L \cdot (n-1)\right)}{L \cdot n} \tag{1}$$

73

where n is the index of refraction at 633nm (1.46), L is the sample length, OPD is the net optical path difference as measured by transmission interferometry, and ΔL is the sum of the front and back surface depressions as measured by reflection interferometry. ΔL is negative in this notation. The UV-induced reflected wave retardations from the SV2G1 and Suprasil 2 surfaces were too small to measure due to significant intrinsic surface roughness.

Table 2
Measured irradiation-induced optical path changes (λ = 632.8-nm)
(conditions in Table 1)

Material and Length	Transmitted Wave Retardation	Front Surface Reflected Wave Retardation$	Back Surface Reflected Wave Retardation$	Calculated Bulk Index (633-nm) Change Δn/n
Suprasil 311 (5mm)	0.015λ	0.019λ	0.018λ	2.04 ppm
SV2G1 (10mm)	0.013λ	*0.0064λ	0.0055λ*	#0.68 ppm
Suprasil 300 (10mm)	0.045λ	0.022λ	0.019λ	2.36 ppm
Suprasil 2 (10mm)	0.023λ	*0.011λ	0.0097λ*	#1.20 ppm
Corning 7940 (25.4mm)	0.047λ	0.0064λ	0.004λ	0.85 ppm

*estimated from Suprasil 300 measurements.

#calculated from measured transmitted wave retardation and estimated reflected wave retardation.

$depth of surface trench is equal to 1/2 of this due to double pass.

3.4c Birefringence distributions to extract compaction

After the five fused silica sample types were irradiated at 193-nm, they were probed with a polarized He-Ne laser to measure the stress-induced birefringence around the damage site as described in Chapter 2. Figure 7 is a typical birefringence distribution. Figure 8 is the best fit to the data using the three-region stress model presented in Chapter 2. Table 3
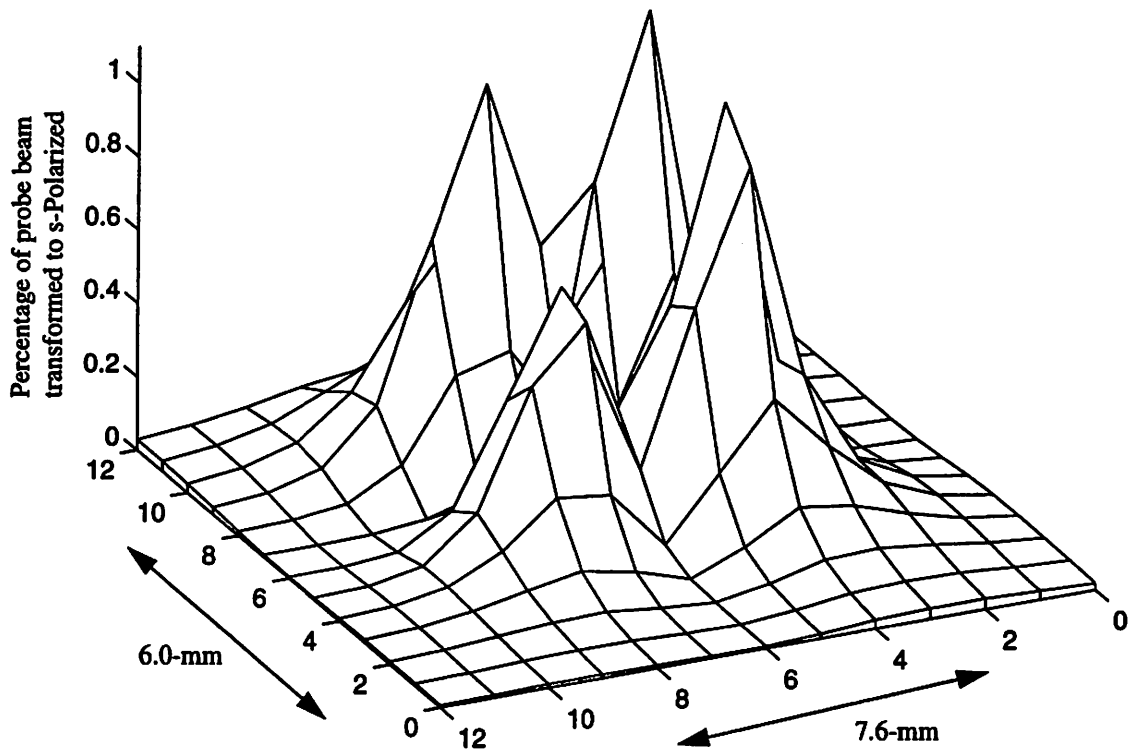
Figure 7. Spatial scan with polarized He-Ne beam of stress-induced birefringence in one inch thick Corning Excimer Grade 7940 due to 193-nm radiation after 450,000, 2.6-mm, 79 mJcm2 pulses.
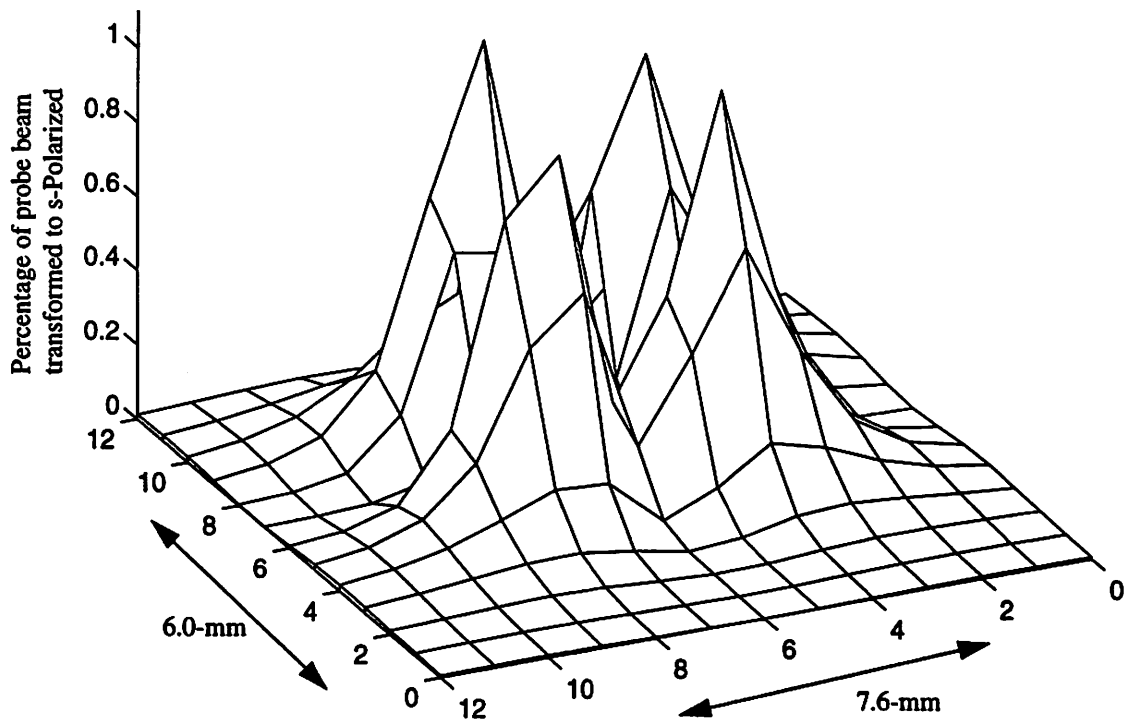
Figure 8. Calculated distribution of stress-induced birefringence from a circular region with 8.1 ppm unconstrained compaction in one inch thick fused silica.

lists the extracted unconstrained compaction levels for the five tests using the plane strain

model. The corresponding bulk refractive index changes from density increases were also

calculated using a method to be described later in Chapter 5 (method 2). Refractive index

changes for a given sample and damaging beam geometry are directly proportional to the

unconstrained density change in the sample.

Table 3
Extracted Compaction Levels from stress-induced birefringence distributions
(irradiation conditions listed in Table 1)

Material	Unconstrained Compaction $\Delta V/V$	*633-nm Refractive Index Change $\Delta n/n$
Suprasil 311	19.4 ppm	4.00 ppm
SV2G1	6.22 ppm	1.15 ppm
Suprasil 300	16.7 ppm	3.08 ppm
Suprasil 2	11.7 ppm	2.16 ppm
Corning 7940	8.12 ppm	1.35 ppm

*derived for a later comparison of interferometry measurements to density measurements.

The average ratio of $\Delta n/n$ extracted from birefringence to $\Delta n/n$ determined by

interferometry was 1.67 with a sigma of 0.25. It turns out, however, that the

interferometry results presented here gave erroneously small compaction levels most likely

because a portion of the radiation-induced OPD's are subtracted when generating the

residual wavefront. Interferometry measurements performed later on the Corning sample

after re-polishing but without subtraction of any phase terms measured $\Delta n/n$ to be 1.52

ppm. A more detailed comparison of the refractive index changes extracted from

birefringence measurements to those from interferometry will be presented in Chapter 5.

The interferometry data as well as the birefringence measurements are believed to be more

accurate for those tests. The fact that birefringence measurements here were able to

extract a change in relative refractive index proportional to that found with interferometry for a wide range of fused silicas and exposure conditions verified that the technique could be used to measure compaction.

The stress-induced birefringence distributions of several of the samples were re-measured days and, in one case, years later and found to be essentially unchanged from the distributions measured immediately following the exposure. This was a strong indication that room temperature annealing of compaction does not occur to any significant level.

3.5 Material Comparison

Table 4 summarizes the transient damage properties of the five fused silicas tested. Since only modest levels of induced absorption are allowed in lithographic systems, a transmission lifetime is defined as the number of 75 mJ/cm^2 pulses to add one percent per centimeter absorption. Real lithographic systems have pulse energies in the range of 100 times less than those used in these experiments. It will be shown in Chapter 4, that fused silicas with a linear pulse count dependence of color center formation have a roughly squared color center formation rate dependence of pulse energy density. It is unclear, however, how the fused silicas with saturating color center behavior will perform at lower intensities. Because of this, it is not truly valid to compare the transmission lifetimes of the materials with linear behavior to those with saturating color center behavior. Indeed, recent results show that at lithographic intensity levels, fused silicas with saturating color center behavior have superior performance to those which do not[6].

Table 4
Damage Characteristics Comparison of Fused Silicas

Material	Corning 7940	Sup. 2	SV2G1	Sup. 311	Sup. 300
[#]Transmission "Life"	1000K	100K	150	40K	70K
[*]Compaction "Life"	310K	130K	420K	170K	100K
Color Center Pulse Dependence	linear	linear	saturating	saturating	linear
Color Center Relaxation Rate	slow	slow	fast	zero	slow

[#]Transmission "Life" is defined as the number of 75 mJ/cm^2, 193-nm pulses to induce one percent additional absorption.

[*]Compaction "Life" is defined as the number of 75 mJ/cm^2, 193-nm pulses to induce 1 ppm change in relative index of refraction.

The compaction lifetime tabulated above is defined as the number of 75 mJ/cm^2, 193-nm pulses to induce 1 ppm change in relative index of refraction where the compaction values extracted from the stress-induced birefringence measurements have been used. An $(N * I^2)^{0.7}$ dependence of compaction has been assumed to adjust for pulse count and energy density differences between the tests where N is the number of pulses in millions and I is the energy density in mJ/cm^2. Experimental support of this functional dependence will be presented in Chapter 6.

The material with the worst induced-absorption performance, SV2G1, had the best compaction performance. The ratio of compaction lifetime to transmission lifetime varied widely from sample to sample; a further indication that compaction and color center formation are two distinct forms of damage. Suprasil 300, a low OH fused silica, had the worst compaction rate in addition to having the faster color center formation rate among the fused silicas with linear color center formation behavior. This result agrees with past

work which found that low water contest fused silicas damage faster than "wet" fused silcas[4].

3.6 Conclusions

Color center formation and compaction appear to be two separate forms of damage. The ratio of compaction rate to color center formation rate varies widely from sample to sample. Furthermore, color centers show self-annealing behavior in some samples while compaction does not anneal at room temperature even after years. The annealing of color centers is artificial because the color center density returns to its previous unannealed level shortly after UV radiation is re-applied. The diversity of responses to UV radiation from different fused silica types is somewhat surprising, because the materials have fundamentally the same atomic composition and molecular structure. Variations in fused silica manufacturing appear to result in subtle material differences which have significant effects on their resistance to UV damage. Although it is difficult to pinpoint the causes for the different material responses, these variations are encouraging, because the ability to produce a less UV damage prone material seems likely.

References

[1] D.J. Krajnovich, I.K. Pour, A.C. Tam, W.P. Leung, M.V. Kulkarni, "248 nm lens materials: performance and durability issues in an industrial environment," Proc. SPIE 1848, 544-560, 1993.

[2] M. Rothschild, D.J. Ehrlich, and D.C. Shaver, "Effects of excimer laser irradiation on the transmission, index of refraction, and density of ultraviolet grade fused silica," Appl. Phys. Lett. 55 (13), pp. 1276-1278, Sept. 25, 1989.

[3] for more information on materials see *Heraeaus Application Note*, "Considerations for UV excimer optics and other high intensity UV light source," 1994.

[4] D.L. Griscom, "Nature of defects and defect generation in optical glasses," SPIE Vol. 541, pp. 38-58, 1985.

[5] special thanks to David Fladd of Corning Inc. for performing measurements.

[6] M. Rothschild, J. H. C. Sedlacek, R. Uttaro, M. Fritze, R. Schenker, W. G. Oldham, "Laser Induced Damage in Optical Materials," presentation at the Second International Symposium on 193nm Lithography, 8/96.

Chapter 4

The Role of Two-Photon Absorption and Temperature in Damage

Several experiments using 213nm radiation have been performed with the goals of

characterizing and understanding better the mechanisms behind UV damage to fused silica.

The super-linear dependence of color center formation and compaction on pulse intensity

suggested a two-photon damage process. Comparison of damage rates at 213nm to those

at 193nm and 248nm further supported a two-photon damage mechanism as the rates

scaled with the two-photon absorption coefficient at each wavelength. The two-photon

coefficients at 213nm for all materials measured including crystalline quartz and under all

applied conditions were statistically equivalent, leading to the conclusion that the energy

dissipation mechanism, in addition to two-photon absorption, is important to UV damage

to fused silica. Color center formation rates increased by a factor of over 100 when the

sample temperature was raised to 120C while compaction rates only increase by about a

factor of 4 over the same temperature range.

4.1 Introduction

When radiation travels through a material, there is a non-zero probability that multi-

photon absorption will occur[1]. The second-order description of the intensity in a sample

as it propagates through that sample can be written as:

$$-\frac{1}{I} \bullet \frac{dI}{dz} = \alpha_1 + \alpha_2 \bullet I \qquad (1)$$

where I is the intensity, usually in Watts/cm^2, α_1 is the linear absorption coefficient in cm^{-1}, z is length increasing the direction of propagation (cm), and α_2 is the two-photon absorption coefficient in cm/Watts. If the two-photon absorption term were ignored, one would get the familiar equation for intensity versus depth in a dielectric sample: $I(z) = I_0 \cdot \exp(-\alpha z)$. Further assuming a small value of αL, the approximate total absorption in a sample of thickness (L) would be αL.

While two-photon absorption comprises only a small portion of the total absorption in samples when the intensity is at typical levels, two-photon absorption is important to UV damage in fused silica. This point becomes more intuitive when one considers that the effective energy band gap of fused silica is about 8.3eV[2]. Because the photon energies are smaller than this (193nm 6.4eV, 213nm 5.8eV, 248nm 5.0eV), two UV-photons are needed to surpass this barrier. Experimental support for a two-photon absorption initiated damage process will be presented in this chapter.

The dependence of damage rates on temperature will also be presented in this chapter. By characterizing the effective activation energies of irradiation-induced damage, it is hoped to better understand the chemical and transport phenomenon involved in damage.

4.2 Dependence of damage rates on temperature

4.2a Color Center Formation Rate as a Function of Temperature

A temperature controlled container was constructed in order to characterize the

dependence of UV-damage rates on ambient temperature. The dependence of the color-

center-induced transmission loss rate on fused silica temperature is shown in Figure 1 for

Corning Excimer Grade 7940. The data are plotted on an Arrhenius-type scale, which

best fit by an effective activation energy of 0.5eV. The room temperature data point was

extrapolated from previous experiments (Figure 5) performed on the same fused silica

sample type (Corning Excimer Grade 7940). All the elevated temperature experiments

used the same 213nm beam shape and 130(mJ/cm^2) pulses.
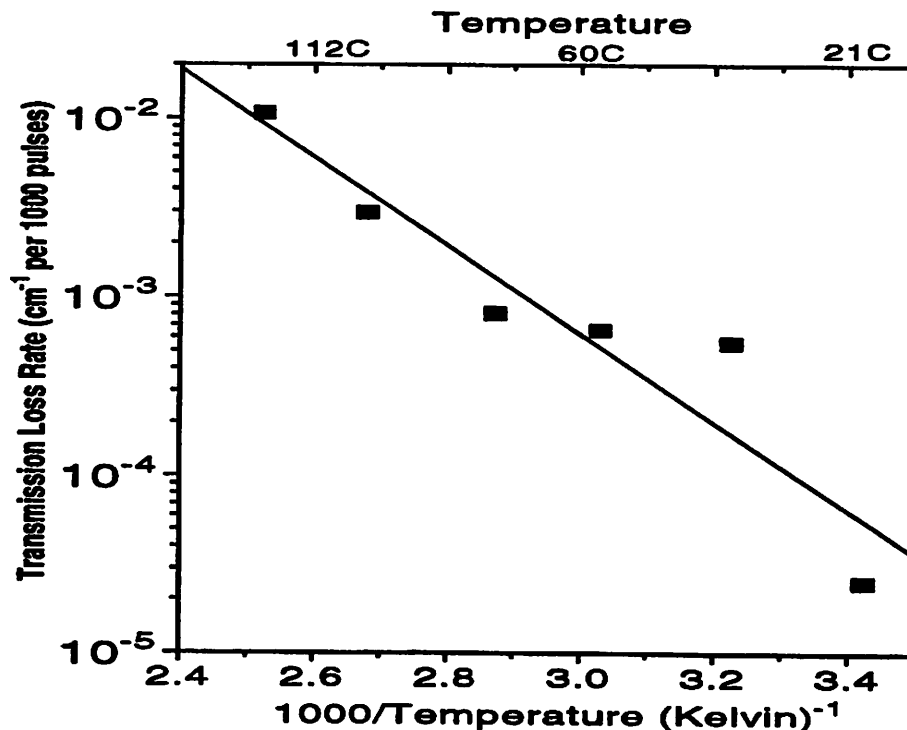
Figure 1. Temperature dependence of induced transmission loss per cm in a 1 inch long Corning 7940 fused silica sample for 130(mJ/cm^2) 213nm pulses. The curve fit suggests an effective activation energy of 0.5eV for 213nm-induced color center formation.

It is worth noting that several of the published diffusion activation energies of hydrogen species in fused silica have similar values to the effective activation energy of UV-induced color center formation. Wakabayashi[3] measures the effective diffusion activation energy for H_2O at temperatures below 400C to be about 0.42eV while that for H_2 is measured[4] to be between 0.3 and 0.45eV. Further research is necessary to determine if enhanced diffusion of hydrogen species at elevated temperatures leads to the higher UV-induced color center formation rates.

4.2b Compaction Rate as a Function of Temperature

The stress-induced birefringence distributions of the damage sites were measured with the "third generation" birefringence monitor several months later. Previous repeated measurements of birefringence distributions showed no measurable relaxation of compaction-induced stress even after several months, so the time between exposure and birefringence measurement should not have effected the results. A relatively large amount of intrinsic birefringence was present near the damage spots, reducing accuracy. The 213nm beam profile resembled a guassian shape with a full width at half maximum of only about 0.45mm. The small damage size and absence of an abrupt transition between compacted and uncompacted material complicated the extraction of the compaction level from the birefringence distribution. Because the damage spot and He-Ne probe beam (0.3 mm diameter) were about the same size, the characteristic four birefringence peaks of a typical birefringence distribution was convolved to a single peak. The compaction model developed in Chapter 2 was used with the relations that describe the dependence of index

on densification from Chapter 5 to extract bulk refractive indices corresponding to the measured birefringence distributions. The results were listed in Table 1. Values of 0.15mm and 0.30mm were used for r_1 and r_2 respectively.

OPD measurements of the damage sites were also performed both two months[18] after the exposures and then after two years[5]. Because the radiation-induced OPD's were small compared to intrinsic inhomogeneities in the sample, a high pass filter was utilized for data enhancement with the first set of measurements. The index changes, listed in Table 1, were calculated using the extracted OPD's. Because surface effects were small, the equation (Δn = OPD/L) was used to calculate the index changes where L is the sample length..

Table 1
UV-induced 633nm refractive index changes in fused silica
at different sample temperatures
(130 mJ/cm^2 213nm pulses in 1 inch long fused silica)

Temperature	Number of Pulses	$\Delta n/n$ (birefringence)	$\Delta n/n$ (high-pass) (interferometry)	$\Delta n/n$ (interferometry)
37 C	65K	135 ppB	29 ppB	229 ppB
47 C	56K	295 ppB	16 ppB	50 ppB
57 C	44K	107 ppB	16 ppB	47 ppB
75 C	39K	223 ppB	29 ppB	189 ppB
100 C	15K	143 ppB	43 ppB	80 ppB
123 C	9K	118 ppB	43 ppB	125 ppB

The interferometry results are inherently inaccurate because of the small OPD's being resolved and the small size of the damage sites. The interferometry data, nonetheless,

qualitatively follow the compaction levels extracted from birefringence distributions. The

use of a the high pass filter seemed to give erroneously low OPD data.

In Chapter 6, it will be shown that compaction follows $\Delta n/n = \kappa \, (NI^2)^{0.7}$ where N is the

number of pulses in millions, I is the pulse energy density in mJ/cm^2, and κ is a material

dependent constant. Figure 2 shows the dependence of κ on inverse temperature

calculated by both the interferometry and birefringence measurements. Using the

birefringence data, the value of κ increases by about a factor of 3.5 going from 37C to

123C and is best fit with an activation energy of 0.13eV. Activation energies of 0.27eV

(high pass filter data) and 0.18eV (1996 data) and are fit to the interferometry data.
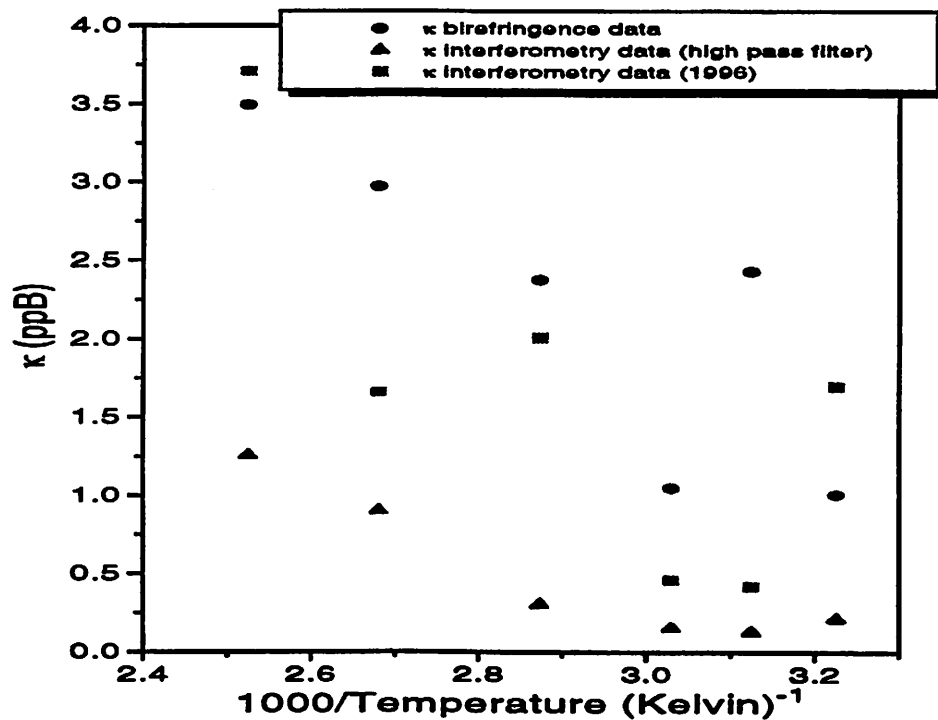
Figure 2. Temperature dependence of compaction in Corning 7940 fused silica sample for 130(mJ/cm^2) 213nm pulses. The compaction determined by stress-induced birefringence and interferometry measurements was fit by the relation $\Delta n/n = \kappa \, (N \, I^2)^{0.7}$.

The temperature dependence of damage rates found here agrees qualitatively with previous experiments performed by Rothschild[20] at 193nm on Suprasil 2[6]. In that work, the compaction rate is shown to increase by about a factor of 4 going from 40C to 100C while the color center rate increased by over 50 for the same temperature range. Because only one fused silica was examined here, it is unknown if the temperature dependence of damage rates is a material-dependent property.

4.3 Two-photon absorption coefficients

4.3a Material dependence of two-photon absorption coefficient

The 213-nm two-photon absorption coefficient (slope of absorbance versus energy density curve) was measured for several fused silica types, for fused silica at elevated temperature, and for quartz. The source was a quintupled Nd-YAG laser (213nm) with an eight nanosecond pulse length and a 10Hz repetition rate. Pulse transmission through the sample was measured using UV photodiodes while the pulse energy density was varied from 50 to over 1400(mJ/cm^2). Since the beam profile of the 213nm beam resembled a guassian shape, the energy density was defined as the energy divided by the full-width at half maximum area. A waveplate used in the non-linear optical system which quintuples the 1064nm Nd-YAG output was rotated to control pulse energy. Since the efficiency of mixing the third and second harmonic of the Nd-YAG laser is extremely dependent on the relative phases of the harmonics, a wide range of output 213nm power could be achieved without altering the beam shape, direction or location. Figure 3 shows a typical

absorption versus pulse energy density measurement used to extract the two-photon absorption coefficient.

Table 2 displays the measured two-photon absorption coefficient for several fused silicas and for one sample of quartz. Many of the fused silicas, Suprasil 2, Suprasil 300, Suprasil 311, Corning 7940, and SV2G1 are described in Chapter 3. Suprasil P20 and Suprasil P30 are "fast-relaxers" manufactured by Shin-Etsu. The quartz sample has been "swept". "Sweeping" is an electo-chemical process to remove impurities. The table shows two standard deviation limits calculated from measurements of the two-photon coefficient for a single fused silica sample at six separate locations. All two-photon absorption coefficients fall within two standard deviations around a mean of 4.3×10^{-4} (cm/MW). This holds true for the quartz specimen as well which has been shown to be essentially completely resilient to UV-induced damage[7].
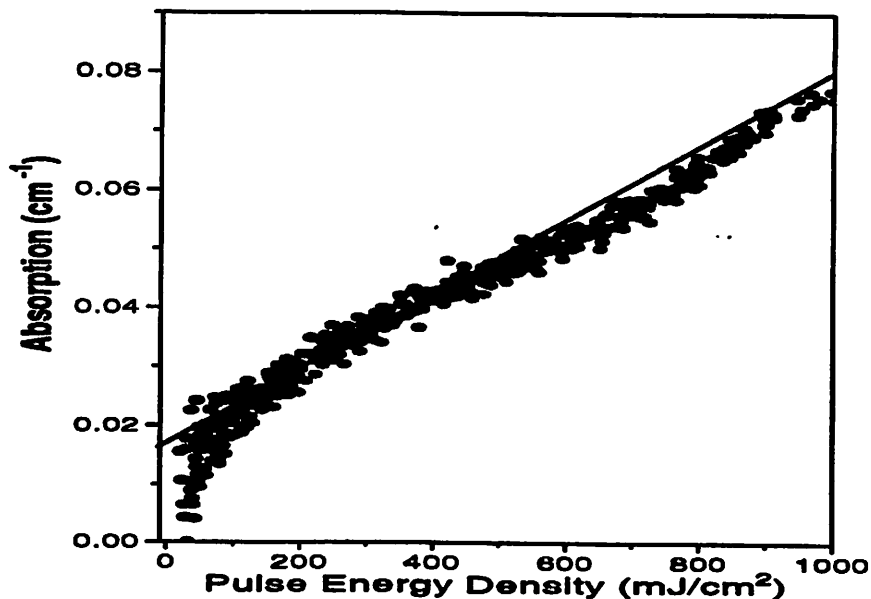
Figure 3. Absorption per cm in a 1 inch long Corning 7940 fused silica sample versus 213nm energy density. The slope of the curve fit divided by the pulse length gives the two-photon absorption coefficient which was on average (4.3×10^{-4} cm/MW).

Table 2
Measured Absorption Coefficients
of Optical Materials at 213nm

Material	α_2 (cm/MW)
Suprasil 2 (#12)	$4.6 +/- 0.9 * 10^{-4}$
Suprasil 2 (b)	$3.5 +/- 0.9 * 10^{-4}$
Corning Excimer 7940 (#18)	$3.7 +/- 0.9 * 10^{-4}$
Corning Excimer 7940 (#26)	$3.7 +/- 0.9 * 10^{-4}$
Corning Excimer 7940 (#04)	$3.9 +/- 0.9 * 10^{-4}$
Corning Excimer 7940 (#34)	$4.7 +/- 0.9 * 10^{-4}$
Corning Excimer 7940 (#34)	$4.1 +/- 0.9 * 10^{-4}$
Sawyer Cultured Quartz	$4.2 +/- 0.9 * 10^{-4}$
Suprasil 300	$4.5 +/- 0.9 * 10^{-4}$
Suprasil 311	$4.6 +/- 0.9 * 10^{-4}$
Suprasil P20	$5.2 +/- 0.9 * 10^{-4}$
Suprasil P30	$4.7 +/- 0.9 * 10^{-4}$
SV1A1 (#47)	x
SV2G1 (#48)	x
Corning Excimer 7940 (#18)	
T=21° C	$3.5 +/- 0.9 * 10^{-4}$
T=56° C	$4.7 +/- 0.9 * 10^{-4}$
T=100° C	$3.5 +/- 0.9 * 10^{-4}$
undamaged ($\alpha = 0.015 +/- 0.01$)	$4.7 * 10^{-4}$
damaged ($\alpha = 0.075 +/- 0.01$) after 55k, 560mJ/cm^2, 213-nm pulses	$5.2 * 10^{-4}$

The two-photon absorption coefficients of SV1A1 and SV2G1 could not be measured because induced absorption formed too rapidly. The two-photon absorption coefficient was not changed at elevated temperatures or after a sample was damaged by UV-radiation as seen in Table 2. Measurements of the two-photon absorption coefficient for a Corning sample gave statistically identical results when probing the sample through both a 25mm and 37mm path, indicating that the rate of two-photon absorption is not different at the surface of the sample compared to the bulk.

4.3b The wavelength dependence of the two-photon absorption coefficient

Table 3 lists the previously published ultraviolet two-photon absorption coefficients and the pulse widths used to make the measurements.

Table 3
UV Two-Photon Absorption Coefficients for Fused Silica

Work	Wavelength	Pulse Width	Two-photon absorption coefficient
Brimacombe[8]	193-nm	5 ns	$2.0 +/- 0.8 \times 10^{-3}$ cm/MW
	248-nm	9 ns	$2.1 +/- 0.8 \times 10^{-4}$ cm/MW
Taylor[9]	248-nm	0.7 ps	$4.5 +/- 2.2 \times 10^{-5}$ cm/MW
Liu[10]	266-nm	30 ps	$1.7 +/- 0.3 \times 10^{-5}$ cm/MW
Mizunami[11]	282-nm	3 ns	$5 +/- 1 \times 10^{-6}$ cm/MW
Eva[12]	248-nm	25 ns	7.8×10^{-5} cm/MW
Tomie[13]	248-nm	8 ps	$8 +/- 2 \times 10^{-5}$ cm/MW
Morozov[14]	193-nm	60 ns	1.6×10^{-3} cm/MW
	248-nm	70 ns	5×10^{-4} cm/MW

Brimacombe and Mizunami give data on fused silica optical fibers. Because of the invariance of the 213-nm two-photon absorption coefficients with fused silica material shown in the previous section, bulk and fiber fused silica are expected to have identical two-photon absorption characteristics. The two-photon absorption coefficients measured for pulses in the pico-second regime are generally smaller than the coefficients found with nano-second pulse widths, indicating that a different quantum electronic regime may be reached for very low pulse widths. Figure 4 shows the previously published two-photon absorption coefficients and the 213-nm coefficient found in this work. The measured 213nm two-photon coefficient of 4.3×10^{-4} (cm/MW) corresponds well previous results and the basic trend where the fused silica coefficient increases by about a factor of ten for each 40nm decrease in laser wavelength.
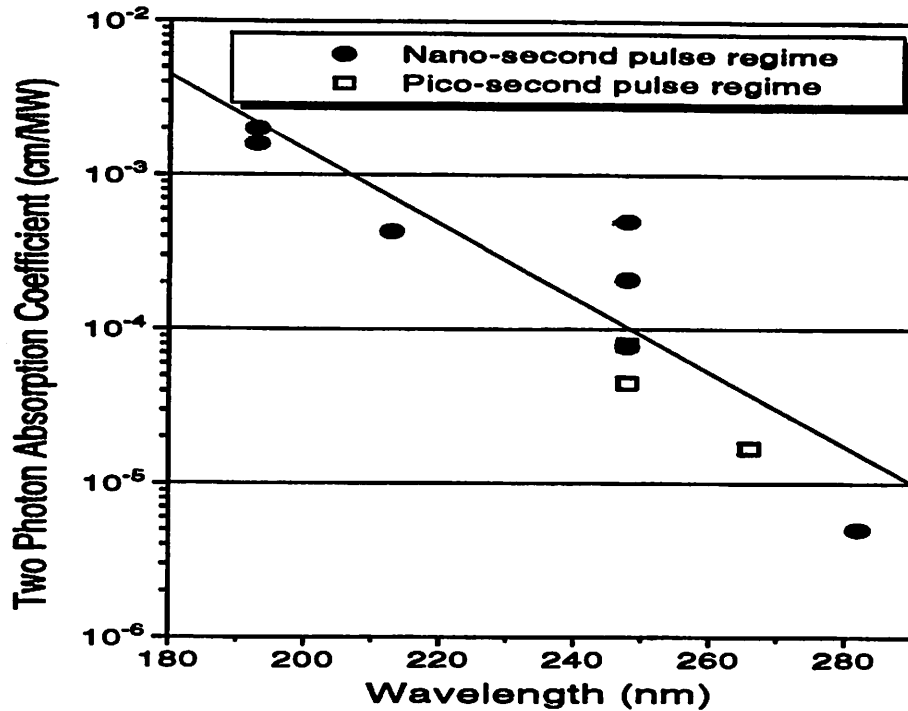
Figure 4. Previously published two-photon absorption coefficients. The line shown is a linear fit to the long pulse width data as plotted. The 213-nm two-photon absorption coefficient measured in this work is also shown.

4.4 Damage rates as a function of radiation intensity

Experiments were performed at 213nm to determine the dependence of color center formation and compaction on pulse intensity. As previously described, UV sensitive photodiodes measured individual pulse transmission by monitoring pulse intensity before and after the fused silica sample. Compaction was monitored using the "first generation" birefringence monitor where the nearly linearly polarized 213nm beam was used as both the damaging beam and birefringence probe beam. The reflectance off a calcium fluoride plate placed behind the sample and oriented near Brewster's angle was measured to monitor beam polarization. Two samples of Corning Excimer Grade 7940 were analyzed.

The density of color centers as indicated by decreased transmission through the irradiated fused silica increased nearly linearly with total dose at a fixed laser fluence. The rate of color center formation (slope of transmission loss versus pulse count) shown in Figure 5 followed a super-linear dependence on pulse energy density. Comparison with a fitted quadratic curve suggests that a two-photon process is the catalyst for UV-induced color center formation in fused silica.
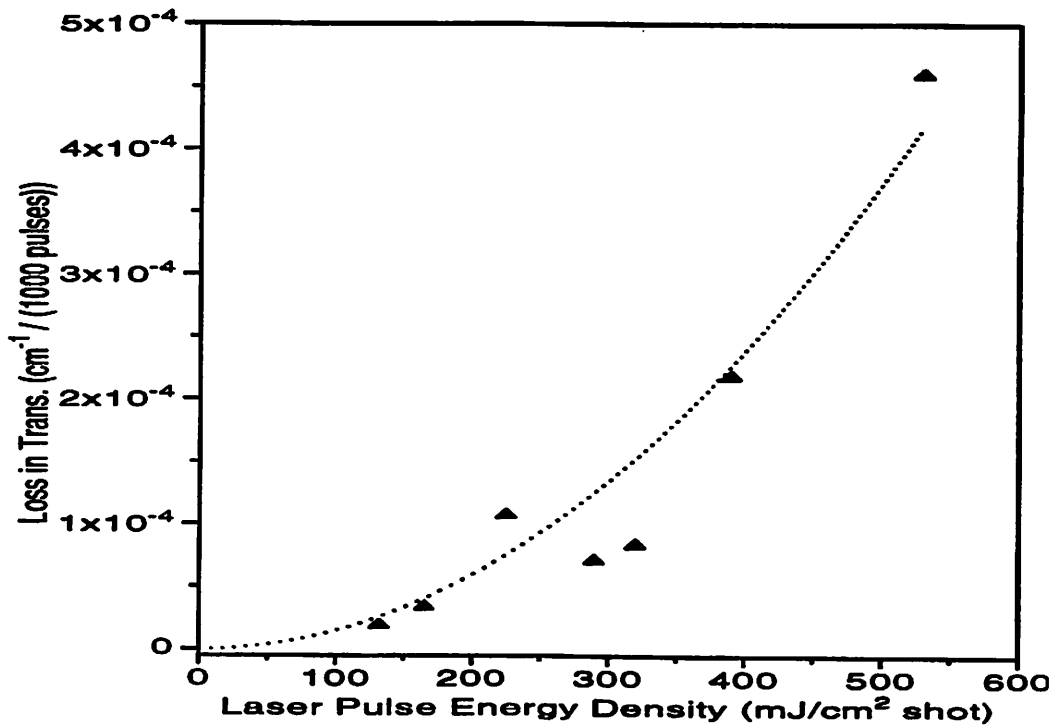
Figure 5. UV-induced transmission loss per cm in a 1 inch long Corning 7940 fused silica sample versus 213nm pulse energy density. The dotted curve is a quadratic fit of the data.

Compaction rates, as indicated by both stress-induced birefringence and interferometry, followed a super-linear dependence on pulse energy density[15]. Because of the superior quality of data taken using the "third generation" birefringence monitor with 193nm radiation, the precise dependence of compaction on energy density and pulse count will be deferred until Chapter 6.

4.5 Damage rates as a function of radiation wavelength

4.5a Compaction rate as a function of wavelength

As seen in Chapter 3, different fused silicas display a wide range of color center and compaction rates. To compare damage rates at different wavelengths, one must, therefore, use the same material at each wavelength. Because of this, tests at Corning[16] (248nm), UC-Berkeley (213nm), and Lincoln Laboratories[17] (193nm) all used identically sized Corning Excimer Grade 7940 fused silica samples cut from the same boule.

A Zygo Phase Measuring Interferometer[18] is used to measure the induced optical path length changes caused by 193nm, 213nm and 248nm irradiation on Corning Excimer grade 7940 fused silica. The optical path length change is a combined measure of increased path length due to fused silica densification and decreased path length due to the formation of surface depressions on the fused silica entrance and exit faces. The net resulting path length is longer. Figure 6 shows the net optical path length through the 2.5cm samples versus a dose parameter proportional to the integrated intensity squared within the samples, number of pulses multiplied by the pulse energy density squared divided by the pulse length. At a given two-photon absorption coefficient or wavelength, the x-axis in Figure 6 is directly proportional to the total number of two-photon interactions to have occurred in the samples. The pulse lengths are approximately 11ns, 8ns and 18ns for the 193-nm, 213-nm and 248-nm respectively.
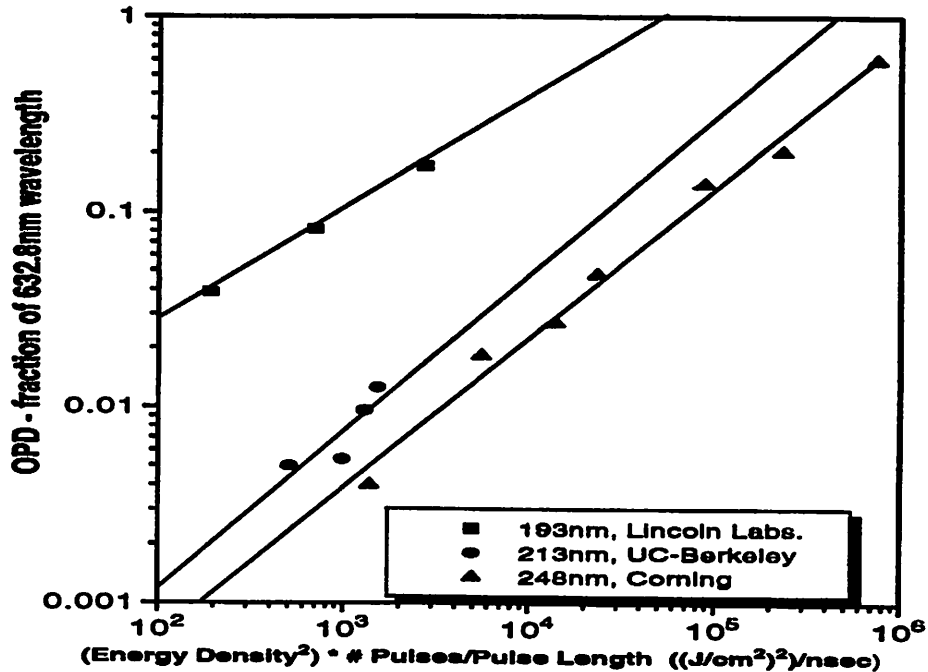
Figure 6. Comparison of UV-induced optical path length changes in 1 inch long Corning 7940 fused silica at different wavelengths. At a given wavelength, the x-axis is proportional to the number of two-photon "events".

To compare the OPD formation rates per two-photon "event" at each wavelength, we replot the data in Figure 6 to account for the different two-photon absorption coefficients at each wavelength. Figure 7 shows the OPD's at each wavelength plotted versus the total amount of energy absorbed by two-photon absorption (energy density squared times the two-photon absorption coefficient times the number of pulses divided by the pulse length) at that wavelength. Two-photon absorption coefficients of 2×10^{-3}, 4.3×10^{-4} and 5×10^{-5} (cm/MW) are used for 193-nm, 213-nm and 248-nm lasers respectively.
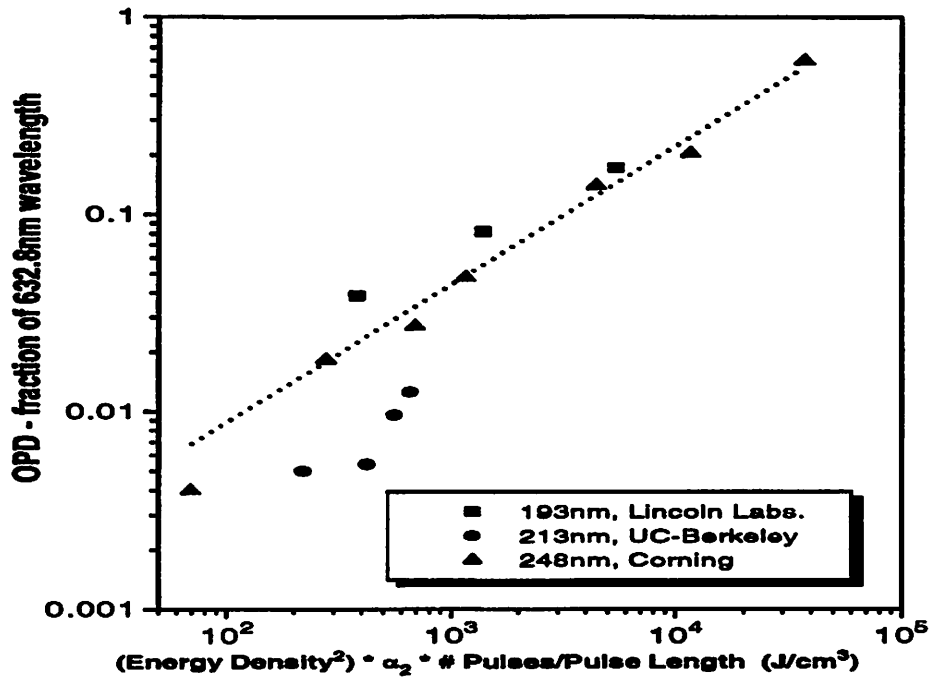
Figure 7. Comparison of UV-induced optical path length changes in 1 inch long Corning 7940 fused silica at different wavelengths versus energy absorbed by two-photon absorption at each wavelength. The line shown is $3.5 \times 10^{-4} \lambda$ (two-photon energy absorbed)$^{0.7}$.

As seen in Figure 7, the induced optical path length differences from 193-nm and 248-nm radiation per two-photon "event" are roughly equivalent. Differences in the OPD formation per two-photon "event" at each wavelength are likely a result of the uncertainties in the measurement of the energy densities, pulse lengths and two-photon absorption coefficients needed for the comparison. The 213-nm data lies substantially below the 193-nm and 248-nm data (by about 2 to 3X). As explained below, we believe this discrepancy is a result of inaccurate interferometry measurements, possibly due to the smaller 213-nm spot area.

95

Table 4 gives the 213nm exposure conditions and interferometry data. As will be shown

in Chapter 5 (Figure 4), total OPD formation for geometries used here is only a weak

function of damage spot size. So, even though the 213nm beam used was much smaller

than the beams used in the Excimer experiments, the OPD's can be used to compare

compaction rates.

Table 4
213nm Irradiation Conditions and Interferometry Data
(1 inch long Corning 7940 fused silica)

Energy Density	Total Pulse Count	(Energy Density)^2 x Pulse Count	OPD (λ = 633nm)
290 mJ/cm^2	125K	1.05 x 10^4 (J/cm^2)^2	0.0096λ
320 mJ/cm^2	120K	1.23 x 10^4 (J/cm^2)^2	0.0126 λ
390 mJ/cm^2	52K	0.79 x 10^4 (J/cm^2)^2	0.0054 λ
165 mJ/cm^2	150K	0.41 x 10^4 (J/cm^2)^2	0.005 λ

Fitting the data in Table 4 to a $\Delta n/n = \eta \ (NI^2)^{0.7}$ relation would give an average η value of

0.24ppB where N is the pulse count in millions and I is the energy density squared in

mJ/cm^2. Extrapolating the temperature data in Figure 2 to room temperature, however,

would give a value for η of 1ppB when the birefringence data are used to extract

compaction levels. Furthermore, a later transmission interferometry measurement[5] that

found a 0.017λ OPD from a spot irradiated by 200,000, 130 mJ/cm^2, 213nm pulses, also

equates to an η value of 1. These data and the agreement of later interferometry results

on larger compacted areas with index changes calculated from birefringence distributions

(presented in Chapter 5) suggest that the OPD's from 213-nm radiation found here with

interferometry were erroneously small. Using the temperature data or the later

interferometry data point, the 213-nm compaction rate per two-photon "event" agrees with the 193-nm and 248-nm rates.

4.5b Color center formation rate as a function of wavelength

Fused silica samples were exposed at 193nm and 213nm to characterize the dependence of color center formation on radiation wavelength. Because past experiments showed that the color center formation rate of different fused silica samples varied significantly even among the same fused silica type[19], the 193-nm and 213-nm irradiations were performed on identical specimens. Table 5 lists the experimental conditions under which the fused silica samples described in Chapter 2 were irradiated. The diameters of the 193-nm and 213-nm beams used were approximately 2.6 mm and 0.4 mm respectively. As described in Chapter 2; Suprasil 2, Suprasil 300, and Corning Excimer Grade 7940 fused silica all showed an approximate linear increase of color-center-induced absorption with laser pulse count. The absorption loss rates (slope of transmission versus pulse count plot) of these samples are also listed in Table 5.

Table 5
Fused silica irradiation experimental conditions and measured transmission loss rates

Material and Thickness	Laser Wavelength	Pulse Energy Density	Total Pulses	Measured Transmission Loss Rate
Suprasil 311 (5mm)	193-nm	83 mJ/cm^2	1000K	*
SV2G1 (10mm)	193-nm	79 mJ/cm^2	500K	*
Suprasil 300 (10mm)	193-nm / 213-nm	83 mJ/cm^2 / 197 mJ/cm^2	467K / 55K	1.40%/(cm•100K pulses) / 7.41%/(cm•100K pulses)
Suprasil 2 (10mm)	193-nm / 213-nm	77 mJ/cm^2 / 204 mJ/cm^2	400K / 93K	0.96%/(cm•100K pulses) / 5.38%/(cm•100K pulses)
Corning Excimer Grade 7940 (25.4mm)	193-nm / 213-nm	79 mJ/cm^2 / 132 mJ/cm^2	450K / 200K	0.096%/(cm•100K pulses) / 0.19%/(cm•100K pulses)

* transmission loss is non-linear so no single loss rate is defined.

97

Table 6 lists the extrapolated transmission loss rates (transmission at 215nm) for 20

nanosecond, 100-mJ/cm^2 pulses of both 193nm and 213nm radiation. It assumes that the

absorption loss at 193-nm corresponds to 65% of the loss occurring at the 215-nm

absorption peak based on previously published E' color center absorption spectra[20]. The

loss rates are also assumed to depend quadratically on pulse energy density following the

data shown above in Section 4.4.

Table 6
Estimated fused silica transmission loss (at 215nm) rates
per 100K, 20 nsec., 100 mJ/cm^2 pulses

Material	Suprasil 300	Suprasil 2	Corning 7940
Estimated 215-nm Trans. Loss Rate (193-nm radiation)	3.13%/cm	2.49%/cm	0.24%/cm
Estimated 215-nm Trans. Loss Rate (213-nm radiation)	0.81%/cm	0.55%/cm	0.046%/cm
193-nm radiation rate/ 213-nm radiation rate	3.9	4.5	5.2

The results listed in Table 6 indicate that the color center formation rate at 193-nm is

approximately 4.5 times larger than the rate at 213-nm. This is in agreement with a two-

photon damage mechanism because the published 193-nm two-photon absorption

coefficient[8] (2 x 10^{-3} cm/MW) and 213-nm two-photon absorption coefficient (4.3 x 10^{-4}

cm/MW) have roughly the same ratio (4.7).

4.6 Conclusions

The rate of color center formation increased significantly with sample temperature and was found to follow and effective activation energy of 0.5eV. Compaction as indicated by stress-induced birefringence had a much weaker temperature dependence. The different temperature dependencies between color center formation and compaction is yet another indication that the two are distinct forms of fused silica damage.

Two strong indications that UV-induced damage in fused silica is initiated by a two-photon process are reported. Firstly, the rates of both compaction and of color center formation depend super-linearly on pulse energy density. Secondly, the rates of both compaction and color center formation at different wavelength scale roughly with the two-photon absorption coefficient at that wavelength.

The large differences in damage rates and transient characteristics between fused silicas and quartz, however, cannot be attributed to varying levels of two-photon absorption. The two-photon absorption coefficients at 213nm for all fused silicas measured including crystalline quartz and under all applied conditions were statistically equivalent, suggesting that the energy dissipation mechanism, in addition to two-photon absorption, is important to UV damage to fused silica.

References

[1] for more information see A. Yariv, *Quantum Electronics*, third edition, John Wiley and Sons, 1989.

[2] D. L. Griscom, "Nature of Defects and Defect Generation in Optical Glasses", SPIE Vol. 541 Radiation Effects in Optical Materials, 1985.

[3] H. Wakabayashi and M. Tomozawa, "Diffusion of Water into Silica Glass at Low Temperature," Journal of the American Ceramic Society, 72 [10], pp. 1850-1855, 1989.

[4] G. Braun, J. Kirchhof, W. Heitmann, "OH Diffusion in Fused Silica at Elevated Temperatures," Journal of Optical Communications, 14 (1993) 1, pp. 25-27.

[5] measured by Douglas Allan of Corning Inc.

[6] sample type given in personal communication.

[7] D.J. Krajnovich, I.K. Pour, "Long-term effects of pulsed KrF laser radiation on crystalline and amorphous SiO_2," SPIE Vol. 2114, 1994.

[8] R. K. Brimacombe, R. S. Taylor, K. E. Leopold, "Dependence of the nonlinear transmission properties of fused silica fibers on excimer wavelength," J. Appl. Phys. 66 (9), pp. 4035-4040, Nov. 1, 1989.

[9] A. J. Taylor, R. B. Gibson, J. P. Roberts, "Two-photon absorption at 248 nm in ultraviolet window materials," Optics Letters, Vol. 13, No. 10, pp. 814-816, Oct. 1988.

[10] P. Liu, W. L. Smith, H. Lotem, J. H. Bechtel, N. Bloembergen, R. S. Adhav, "Absolute two-photon absorption coefficients at 355 and 266 nm, "Physical Review B, Vol. 17, No. 12, pp. 4620-4632, 15 June 1978.

[11] T. Mizunami, K. Takagi, "Two-photon absorption in silica optical fibers measured with a XeBr excimer laser," Optics Communications, Vol. 68, No. 3, pp. 223-227, 1 Oct. 1988.

[12] E. Eva, K. Mann, "Calorimetric measurement of two-photon absorption and color-center formation in ultraviolet-window materials," Applied Physics A 62, pp. 143-149, 1996.

[13] T. Tomie, I. Okuda, M. Yano, "Three-photon absorption in CaF_2 at 248.5 nm," Applied Physics Letters, Vol. 55, No. 4, pp. 325-327, 24 July 1989.

[14] N. V. Morozov, "Laser induced damage in optical materials under UV excimer laser radiation," Laser-Induced Damage in Optical Material: 1994, 26th Annual Boulder Damage Symposium Proceedings, SPIE Vol. 2428, pg. 153-169, 1995.

[15] for data see R. Schenker, *Issues in the Industrial Application of Deep-UV Photolithography Sources*, Master's thesis UC-Berkeley, school of Electrical Engineering and Computer Sciences, 1994.

[16] performed by Paul Schermerhorn and colleagues.

[17] performed by Mordy Rothschild and colleagues.

[18] measured by David Fladd at Corning Inc.

[19]J.H.C. Sedlacek and M. Rothschild, "Optical materials for use with excimer lasers," SPIE Vol. 1835, pp. 80-88, 1992.

[20]Rothschild, D.J. Ehrlich, and D.C. Shaver, "Effects of excimer laser irradiation on the transmission, index of refraction, and density of ultraviolet grade fused silica," Appl. Phys. Lett. 55 (13), pp. 1276-1278, Sept. 25, 1989.

Chapter 5

Optical Changes from UV-Damage in Fused Silica

The three major components to OPD formation from UV-damage in fused silica are surface depression formation; and refractive index changes from color center formation and irradiation-induced densification. Refractive index changes from color center formation, predicted from the Kramers-Kronig relations, are not found to be significant to the total index change from damage. Refractive index changes from densification are calculated using the differentiated Lorentz-Lorenz relation. Index changes from unconstrained irradiation-induced densification and from expansion resulting from resistance to compaction from undamaged areas are calculated separately using the absolute stress-optic coefficients because refractive index changes depend upon the method of densification (elastic versus inelastic). Density changes in irradiated samples are extracted from both stress-induced birefringence and surface crater depth measurements. At 633nm, an index change of 0.42 ppm is deduced for a 1ppm unconstrained irradiation-induced densification by comparing density changes to index changes extracted directly from interferometry data. This value is in agreement with index changes found from other forms of stress-free compaction including gamma and neutron-induced compaction. The dependence of OPD formation on the sampling wavelength, the size of the compacted area, and the sample geometry for a given level of damage is characterized.

5.1 Introduction

The true measure of the consequences of damage on the performance of an optical element is in its imaging performance. Optical Path Differences (OPD's) are the best "unit" for quantifying imperfections in optical elements. The optical path length is simply the refractive index of the material times the length, so having a measure of index and length changes is sufficient to calculate OPD's. The sample length change is only a function of density changes and the distribution of damage in the sample. Changes in the refractive index, on the other hand, are a complex function of the sampling wavelength, densification level, the size of the compacted area, the sample geometry and the color center density within the sample. While birefringence monitoring is an optical measure of compaction, it is a measure of differences in directional stresses (or strains) at a given location, not absolute index change. This chapter will develop the relations between refractive index and density, stress and color center density to not only allow for calculations of OPD's from transmission and birefringence measurements, but to allow for characterization of the dependence of OPD formation on sample geometry and wavelength.

5.2 Refractive index changes from color center formation

The formation of color centers corresponds to a distinct chemical change within fused silica. As might be expected, a change in refractive index results from the chemical transformation. Because of the complexity of the glassy structure, we are unable to determine the change in index from color center formation based on chemical information

103

alone. The absorbance spectra of the E' color center, however, is well characterized[1].

Using the Kramers-Kronig relation[2], we are able to estimate the change in the refractive

index spectra from the color center absorption spectra. The Kramers-Kronig relations are

based on the principle that the real and imaginary parts of the refractive index of a material

depend on each other. If either the real or the imaginary component of the refractive

index is known for all wavelengths, the other component can be calculated. If we define

$n(\omega)$ to be the real part of the refractive index and $k(\omega)$ to be the imaginary part, then the

Kramers-Kronig relations are:

$$n(\omega) = 1 + \frac{2}{\pi} \cdot P \int_0^\infty \frac{\omega' \cdot k(\omega)}{(\omega')^2 - \omega^2} \cdot d\omega' \tag{1}$$

$$k(\omega) = \frac{-2\omega}{\pi} \cdot P \int_0^\infty \frac{n(\omega') - 1}{(\omega')^2 - \omega^2} \cdot d\omega' \tag{2}$$

where P denotes the principle value of the integral which essentially calls for integration of

the integrand at all points except when the integrand goes to infinity ($\omega' = \omega$). The more

rigid definition requires selection of the imaginary integrand with phase between zero and

2π. The relation between absorbance and the imaginary component of the refractive index

is given by the following:

$$k(\omega) = \frac{\alpha(\omega) \cdot c_o}{2\omega} = \frac{\lambda \cdot \alpha(\omega)}{4\pi} \tag{3}$$

where $\alpha(\omega)$ is the absorbance and c_o is the speed of light in vacuum. We assume a

guassian shaped absorbance band given by the generic relation:

$$\Delta k(\omega') = A \cdot \exp\left[\frac{-(\omega' - \omega_o)^2}{(\Delta\omega)^2}\right] \tag{4}$$

where A is a constant, ω_0 is the center frequency and 1.67 $\Delta\omega$ is the full width at half maximum (FWHM) of the distribution. Given a 40-nm FWHM band centered at 210nm (the E' color center peak) and a peak absorption of 0.01/cm; Figure 1 shows the calculated corresponding change in refractive index. A characteristic sharp transition occurs around the absorption peak, where at 193nm the index change is negative. At 633nm, about a 2.5ppB increase in refractive index is calculated for the given absorption band.
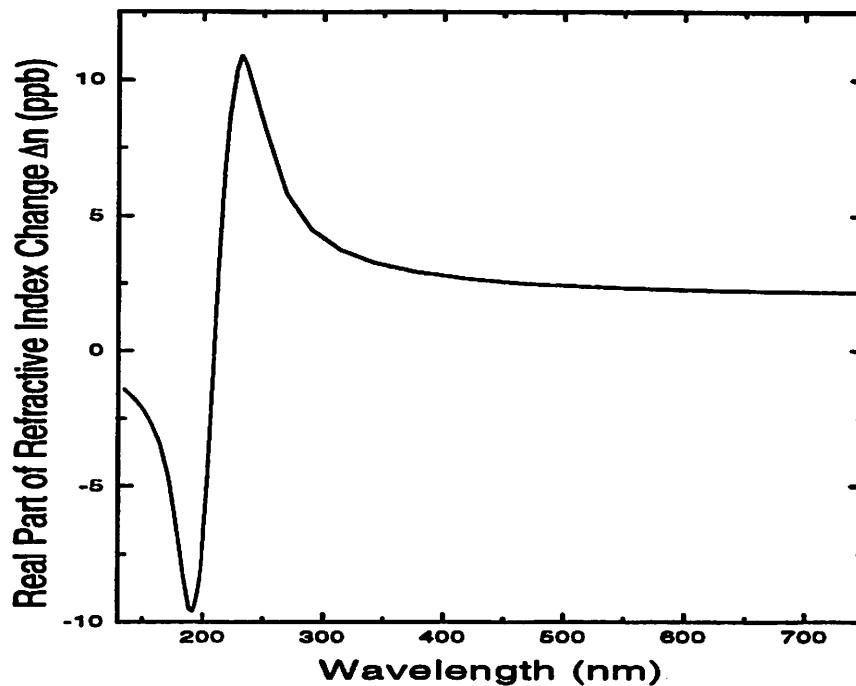
Figure 1. Refractive Index Spectra change calculated for a 40nm FWHM, 0.01/cm peak absorption band centered at 210nm using the Kramers-Kronig relations.

It should be emphasized that the use of the Kramers-Kronig relations assumes knowledge of either the real or imaginary components of the refractive index for all wavelengths. Since it is impossible to measure the entire spectrum of either, one must make the

assumption that the only changes within the absorption band are those which are measured. Other bands from UV-radiation are found for some UV-irradiated fused silicas[3], including peaks at 265nm and 167nm. Furthermore, a small change in the absorption band over a wide band could result in significant alterations of the refractive index spectra.

Keeping the above caution in mind, it appears that for most cases, refractive index changes induced from color center formation are a small portion of the overall radiation-induced refractive index change. For example, the most heavily darkened sample damaged at room temperature had less than 0.1/cm induced absorption while having a total change in refractive index of no less than 1ppm. The index spectra in Figure 1 then suggests that the color-center-induced refractive index change ($<$ 25 ppB @ 633nm) constitutes less than 3% of the total refractive index change ($>$ 1ppm) at 633nm.

5.3 Formation of surface depressions from compaction

Radiation-induced compaction within fused silica causes the formation of a surface depression on the entrance and exit surfaces of the irradiated region. The depth of these surface craters are measured using reflection interferometry[4]. Table 1 lists reflection interferometry results for samples exposed to a 3mm diameter 193nm beam. The irradiation conditions are described later in Chapter 6.

Because the surface features are a direct result of densification, the depth of the depressions can be used as another method to extract density changes. Finite Element Analysis (FEA) is used to determine the magnitude of unconstrained compaction required to generate a surface crater equal to the depth of those measured with interferometry. As in the simulations presented in Chapter 2, irradiation-induced compaction was emulated by setting the section considered compacted to have a different reference temperature than the uncompacted material. Figure 2 shows distortion output from the FEA program FEAP[5] where mesh distortions have been exaggerated 300,000 times. A radially symmetric geometry is used where the center region is set to have a reference temperature and coefficient of thermal expansion equivalent to a 1ppm linear compaction (3ppm by volume). Only the top half of the cylindrical cross section is shown in the figure. Regions near the surface and interface between the compacted cylinder and uncompacted region are again meshed more finely to improve accuracy by creating more elements in regions with larger stress gradients. The results from the FEA simulations are listed in Table 1. The unconstrained compaction level is simply the level of initial compaction required to produce a surface depth equal to the average of the front and back surface depths measured with interferometry.
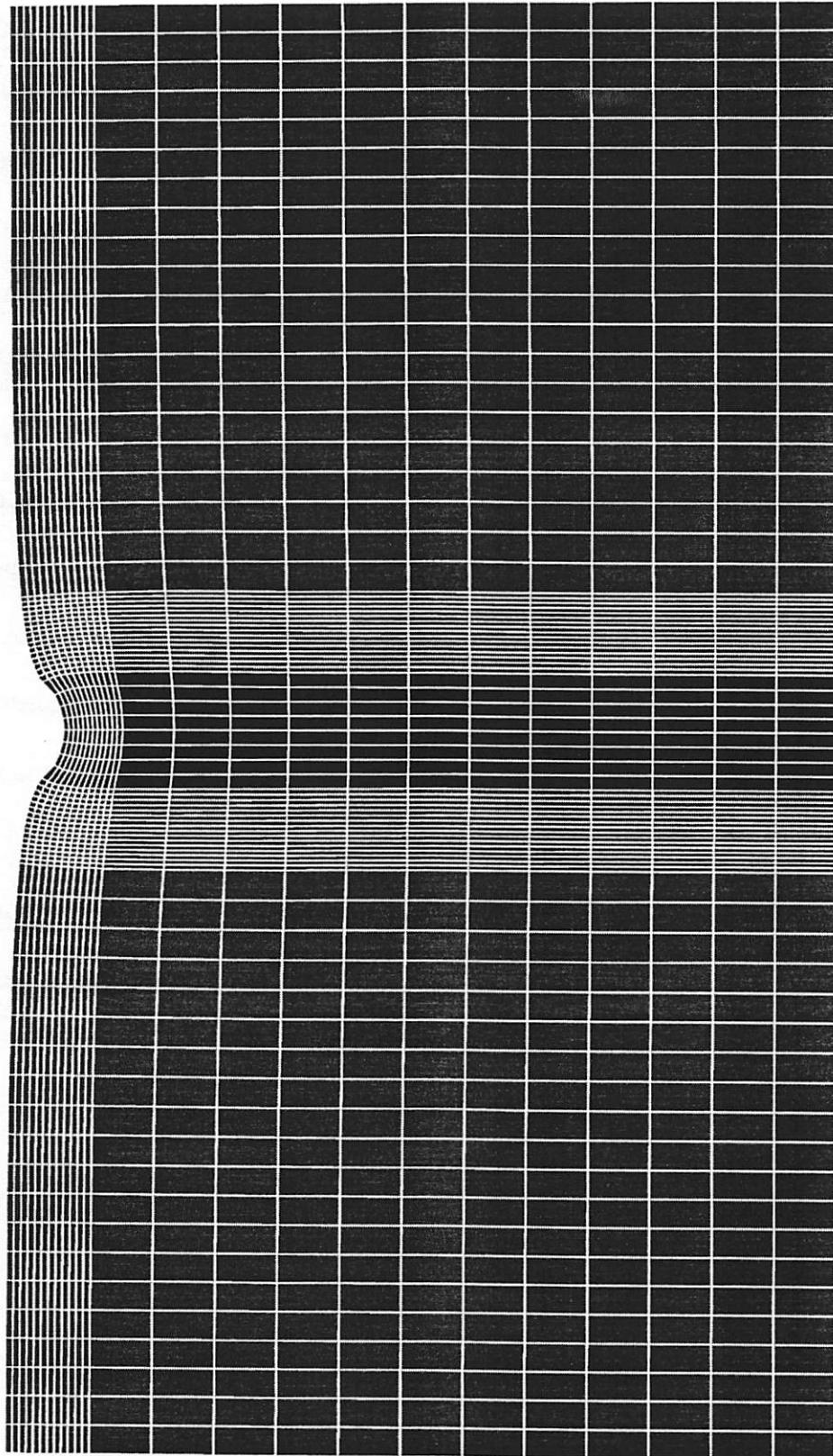
Figure 2. 300,000 magnification of distortions from a 3ppm unconstrained compaction in the center 1mm diameter region. The total sample size is 10mm in diameter and 10mm in thickness. A 1.2nm trench is calculated to form due to the compaction.

Table 1
Measured Densification-Induced Surface Depths and Corresponding Extracted Compaction (from average of front and rear surface depths)

Sample and Length	Front Surface Depth	Back Surface Depth	Extracted $(\Delta\rho/\rho)_u$
7940 spot #1 (25mm)	17.1 nm	13.9 nm	14.1 ppm
7940 spot #2 (25mm)	16.5 nm	15.2 nm	14.4 ppm
Suprasil 2 (9.5mm)	8.4 nm	5.1 nm	7.0 ppm
SV2G1 (9.5mm)	10.3 nm	8.4 nm	9.7 ppm
Suprasil 311 (25mm)	27.0 nm	17.2 nm	20.1 ppm

The front surface crater depths were consistently larger than the exit surface, indicating that the front part of the sample is more heavily compacted than the rear. The magnitude of the differences in the depths was surprising because absorption by the samples was generally less than a few percent though the entire sample length. Differences in the color of radiation-induced fluorescence at the front and rear of the Suprasil 311 sample indicated that the composition and hence radiation hardness through the length may not have been uniform in that sample. The front half fluoresced red while the back half fluoresced green. When the sample was turned around with respect to the incoming beam, the front then fluoresced green and the back red. Radiation-induced fluorescence will be discussed in more detail in Chapter 8.

The extracted compaction levels from FEA simulations of measured surface depressions are compared to compaction levels extracted from birefringence distribution measurements. Table 2 shows the extracted unconstrained compaction levels using both methods. The unconstrained compaction levels from the birefringence data were

calculated using Equation (15a) in Chapter 2, $(\Delta\rho/\rho)_u = 6\,K_2\,(1 - v)\,/E$. The K_2 values

were extracted using the three region stress model described in Chapter 2.

Table 2
Unconstrained Compaction Levels Extracted from Surface Depression Depth
Measurements and Birefringence Measurements

Sample and Length	Extracted $(\Delta\rho/\rho)_u$ from Surface Depths	Extracted $(\Delta\rho/\rho)_u$ from Birefringence Distributions
7940 spot #1 (25mm)	14.1 ppm	13.6 ppm
7940 spot #2 (25mm)	14.4 ppm	15.2 ppm
Suprasil 2 (9.5mm)	7.0 ppm	10.5 ppm
SV2G1 (9.5mm)	9.7 ppm	10.4 ppm
Suprasil 311 (25mm)	20.1 ppm	22.0 ppm

The unconstrained compaction data extracted from surface crater depth measurements

were on average 13% less than those extracted from birefringence measurements. FEA of

the two-region stress model instead of the three region model, which was used to extract

K_2 values, may have led to some of the discrepancies. The two methods agreed better for

higher damage levels where reflection interferometry measurements are less plagued by

errors from surface roughness. For the irradiation geometry used in these experiments,

the OPD decrease from surface crater formation off-sets less than 25% of the OPD

increase from bulk densification. As will be seen later, for geometries where the irradiated

region is a more substantial portion of the total sample volume, the OPD contribution

from surface effects becomes more important.

5.4 Non-Uniform Refractive Index Changes from Directional Stress Differences

In Chapter 2, the simple relation between the difference in refractive indices of orthogonal polarizations of radiation and the stress difference in those directions was given as:

$$(n_2 - n_1) = \Re (\sigma_2 - \sigma_1) \tag{5}$$

where n_2 and n_1 are the refractive indices seen by light polarized in the (2) and (1) direction respectively; σ_2 and σ_1 are the stresses in the (2) and (1) directions; and $\Re$ is the stress-optic constant which is both material and wavelength dependent.

The center of a symmetric damage region has, in general, uniform stress and hence the refractive index is independent of input polarization. The boundary between irradiated and unirradiated material has non-uniform stress as can be observed in the stress-induced birefringence distributions resulting from a circularly compaction region. Here one could observe a maximum direction index difference of $\Delta n = 2 K_2 \Re$ or $(\Delta n/n)_{max} \approx 0.5$ ppm K_2 (kg/cm^2). As before, K_2 is the radial stress in the center compaction region. As a rough rule of thumb, the index change from densification in the center follows $(\Delta n/n)_{max} \approx 1.2$ ppm K_2, only about a factor of two larger. So, if polarized radiation is used, the effects of stress-induced index changes at the edge of the irradiation region will be nearly as significant as bulk densification.

5.5 Refractive Index and Polarizability Changes from Densification

Bulk refractive index changes from density changes are traditionally calculated using the well-known differentiated Lorentz - Lorenz relation[6]:

$$\frac{\Delta n}{n} = \frac{\Delta \rho}{\rho} \bullet (1 + \Omega) \bullet \frac{(n^2 - 1) \bullet (n^2 + 2)}{6n^2}, \tag{6}$$

where n is the refractive index (1.457 at 633nm), ($\Delta \rho / \rho$) is the relative compaction and Ω is equal to [($\Delta \alpha / \alpha$) / ($\Delta \rho / \rho$)], the ratio of relative polarizability change to relative density change. A comparison of previously extracted values of Ω suggests that Ω depends on whether the densification is elastic or inelastic.

Vedam[7] finds a value of -0.38 for Ω by comparing refractive index changes to density changes in fused silica densified by reversible hydrostatic pressure (elastic). In tests where fused silica is inelastically compacted, however, a value of -0.19 +/- 0.04 for Ω is consistently found for fused silica. Table 3 summarizes the published Ω's and the corresponding compaction method for tests where fused silica was permanently densified (inelastic).

112

Table 3
Extracted Compaction-Induced Polarizability Changes
for Inelastic Densification ($\Omega = \Delta\alpha/\alpha / \Delta\rho/\rho$) at 633nm

Work	Ω	Compaction Method
Kitamura[8] (1993)	-0.15	Hot Isostatic Pressing
Shelby[9] (1980)	-0.22	^{60}Co Gamma Irradiation (1 MeV)
Arndt[10, 11]	-0.19	High Temperature Mechanical Pressure
Arndt[12]	-0.22	Shock-waves
Primak[13] (1958)	-0.16	Neutron Irradiation
Dellin[14] (1977)	-0.15*	18-keV Electron Irradiation

*see text for explanation

Dellin et al.[14] erroneously listed values for Ω of 0.39 for low electron doses and -0.25 for

high electron doses. In that work, the authors irradiated periodic strips of fused silica with

electrons to produce a phase grating. Refractive index changes were measured by

employing the grid as a transmission phase grating while compaction was measured by

using the sample as a reflection phase grating. The values of Ω were extracted by

comparing the extracted index change to the net density change. By treating the index

changes from unconstrained electron-induced densification and index changes from

resistance of the unirradiated portions of the sample to compaction as separate

contributors, however, a much different result was obtained. Dellin[14], in fact, addressed

this in an appendix where he showed for his geometry that $\dfrac{\Delta n}{n} = 0.45 \cdot \left(\dfrac{\Delta \rho}{\rho}\right)_{net}$ when a

value of -0.15 was used for Ω and the two contributors to the net density change were

treated separately. This closely fit his experimental data. Different approaches in

computing refractive index changes from densification will be detailed later in this chapter.

The Hot Isostatic Pressing method used by Kitamura permanently densified fused silica by applying atmospheric pressure at high temperatures. The final density changes produced by this method were stress-free as is the case with the irradiation-induced densifications. Arndt permanently densified a wide variety of glasses by applying uniform mechanical pressure at high temperature. The value given for neutron-induced densification was that found in the early stages of irradiation. There, Ω shifted gradually to -0.30 after longer irradiations.

Since polarizability changes from stress-inducing or elastic compaction appear to be larger than those produced by densifications yielding no stress (inelastic), the net compaction in a UV-irradiated sample needs to considered as two separate compaction types. The first type is irradiation-induced compaction and the second type is pressure-induced expansion from the resistance of the undamaged portion of the sample to the compaction in the irradiated region. Since there is no well established value of Ω for UV-induced compaction, the value will be deduced from a comparison of density levels extracted from birefringence and surface crater depth measurements to refractive index levels extracted from interferometry measurements. Refractive index changes from stresses corresponding to the pressure-induced compaction will be calculated using the absolute stress-optic coefficients as described in the next section.

5.6 Refractive Index Changes from Elastic Resistance to Compaction

When only a portion of a fused silica is densified by radiation, the unexposed portion of the sample acts to resist the distortions driven by that compaction. The forces and strains associated with this resistance to densification are equivalent to those which would develop by placing negative external pressure on a uniformly damaged sample. To determine the refractive index changes resulting from the resistance of the undamaged portion of the sample to compaction in the irradiated region, the absolute stress-optic coefficients will be used. The stress-optic coefficients give the absolute refractive index changes in directions both parallel and perpendicular to an applied stress. The phenomenon of stress producing refractive indices which depend upon the relative orientation of the input light polarization with respect to the applied stress is know as the stress-optic effect. The stress-optic effect is often referred to interchangeably with the strain-optic effect. It is often pointed out that the reshaping of atomic orbitals by strains is the true cause of birefringence and the notion of forces or stresses directly causing index changes is not precise[15]. Since stresses and strains are linearly related for elastic amorphous materials such as fused silica, no distinction is needed here.

Accurate measurements of the absolute refractive index change from stress are published by both Primak[16] and Borrelli[15]. Primak uses a static pressure interferometric technique while Borelli uses an ultrasonic technique. Primak defines C_1 as the absolute index change in the direction of the applied stress (σ) and C_2 as the absolute index change for a ray polarized perpendicular to the applied stress. The photoelastic constant is thus given by:

$\Re = (C_2 - C_1)$. At a wavelength of 546nm, Primak gives average values for $\Re$, C_2 and C_1 to be -3.56, -4.22 and -0.65 respectively where all three values were measured independently. Primak finds a value at $(\lambda = 644nm)$ of -4.19(nm/cm)/(kg/cm^2) for C_2 and -3.51(nm/cm)/(kg/cm^2) for $\Re$. C_1 is then calculated to be -0.68(nm/cm)/(kg/cm^2). At 633nm and with Corning 7940 fused silica, Borrelli gives results which can be used to calculate a value of -0.403 for C_2 and -0.101 for C_1. Because Primak tested several more samples and because his results agree better with the well established value for $\Re$, his values for C_1 and C_2 will be used. Primak's values fall within the stated uncertainty of Borelli's results. Using stress-optic coefficient values of -0.7 and -4.2(nm/cm)/(kg/cm^2) for C_1 and C_2 is equivalent to using Neumann strain-optic constants of 0.196 and 0.091 for p and q. The Neumann strain-optics are defined by: The index change for light polarized in the direction of a unit strain is equal to $(q\,n^2)$ and the index change for light polarized perpendicular to the strain is $(p\,n^2)$.

Confidence in the validity of using the absolute stress-optic coefficients is gained by comparing the index change predicted by the coefficients and that found for a sample under uniform external pressure. As alluded to earlier, Vedam[7] finds that Δn in fused silica follows approximately -0.33 $\Delta\rho/\rho$ $(\lambda = 589nm)$ in a sample under uniform static pressure. Primak's photoelastic constants predict the same result independently. This can be shown simply by considering a sample where a uniform pressure has been applied such that $\sigma_1 = \sigma_2 = \sigma_3 = 1$ kg/cm^2. The net expansion would then be $3(1 - 2v)/E$, making $\Delta\rho/\rho$ equal to 2.66ppm. The photoelastic constants would predict an index change for any

polarization equal to $C_1 + 2C_2$ or -0.906ppm using like units . Symmetry is used here where the stress in the direction of light polarization contributes an index change of C_1 while the other two stresses each contribute an index change of C_2. The total index change for any polarization is then given by: $\Delta n = -0.34 \Delta\rho/\rho$, in agreement with the value found by Vedam.

5.7 Total OPD Formation from Density Measurements

5.7a Direct Measurements of Compaction-Induced Index Changes

Interferometry measurements were performed to get a direct measure of refractive index increases from compaction. The transmitted and reflected phase interferometry measurements on the (1990-1994) grade fused silica samples were conducted at Corning Inc. using a Zygo phase interferometer[17]. Unlike with the interferometry measurements described in Chapter 3, the fit of the first 36 Zernike phase terms was not subtracted from the raw data to give a residual wavefront. Only tilt was subtracted to account for the inability to align the sample absolutely normal to the interferometry beams. Superior surface polish[18] made the need to subtract intrinsic wavefront aberrations unnecessary. Table 4 below lists measured OPD's. The gross optical path length increase from compaction in the samples is equal to the net path length increase as measured from the transmitted wavefront minus the path length decrease from surface depressions. A bulk index change for each sample was calculated by dividing the gross optical path length change by the sample length using Equation 7:

$$\frac{\Delta n}{n} = \frac{\left(OPD - \Delta L \cdot (n-1)\right)}{L \cdot n} \tag{7}$$

where n is the index of refraction at 633nm (1.457), L is the sample length, OPD is the net

optical path difference as measured by transmission interferometry, and ΔL is the sum of

the front and back surface depressions as measured by reflection interferometry. ΔL is

negative in this notation. The reflection interferometry data listed in the table are single

pass values. The UV-induced reflected wave retardations from the Suprasil 300 surfaces

are too small to measure due to significant intrinsic surface roughness.

Table 4
Measured irradiation-induced optical path changes (λ = 632.8-nm)

Material and Length	Transmitted Wave Retardation	Front Surface Reflected Wave Retardation	Back Surface Reflected Wave Retardation	Calculated Bulk Index (633-nm) Change $\Delta n/n$
Suprasil 311 (25mm)	0.163λ	0.0427λ	0.0271λ	3.39 ppm
SV2G1 (9.5mm)	0.0407λ	0.0162λ	0.0132λ	2.48 ppm
Suprasil 300 (9.5mm)	0.042λ	#0.0179λ	#0.0126λ	2.56 ppm
Suprasil 2 (9.5mm)	0.029λ	0.0133λ	0.0080λ	1.77 ppm
7940 spot #1 (25mm)	0.119λ	0.027λ	0.022λ	2.46 ppm
7940 spot #2 (25mm)	0.121λ	0.026λ	0.024λ	2.50 ppm
7940 spot #3 (25mm)	0.054λ	0.013λ	*0.011λ	1.13 ppm

*estimated from front surface and 7940 spot #1 and #2 measurements.
#estimated from SV2G1 and Suprasil 2 measurements.

5.7b FEA Calculations of Final Density and Stresses from UV-Induced Compaction

FEA simulations are used to compute the net density changes and stresses resulting from

UV-induced densification in different shaped fused silicas samples. The net density and

stresses are needed to calculate the refractive index change resulting from the damage. The simulations use identical methods and geometries to those previously described. The constrained compaction is taken as the average final density change along the center of the damage region through the sample. The average stresses along the center of the damage region are also calculated. Simple FORTRAN programs are used to read in appropriate nodal strain and stress values and to calculate the averages along the length of the sample. Table 5 summarizes the calculated average stress in the z-direction (along length of sample), constrained and unconstrained densifications normalized for a compaction producing a radial stress of K_2. This normalization is used because K_2 can be extracted from the analysis of birefringence data as described in Chapter 2. A 3mm damage diameter and 30mm sample diameter are used for the simulations.

In Chapter 2, a plane strain assumption was assumed to model the stress distribution in a compacted sample. The model predicted that the net density change in a compacted sample would be $[2\ K_2\ (1 + v)/E]$ where K_2 is the radial stress in the center of the compacted region, v is Poisson's ratio (0.17) and E is Young's Modulus (743 x 10^3 kg/cm^2). This is 0.47 of the derived unconstrained compaction level $[6\ K_2\ (1 - v)\ /E]$. The stress models presented in Chapter 2 (assuming plane strain) predict an average z-stress equal to:

$$\sigma_{zz} = \frac{(1-v)E}{(1-2v)(1+v)} \cdot \frac{\Delta L}{L} + \frac{2vE}{(1-2v)(1+v)}\varepsilon_{\pi}. \tag{8}$$

ε_{π}, the radial strain, is equal to:

$$K_2 \cdot \frac{(1+v) \cdot (1-2v)}{E} - v\frac{\Delta L}{L} \qquad (9)$$

from Equation (16) in Chapter 2 and taking into account the radial strain resulting from

stretching the initially compacted cylinder in the z-direction. Using Equation (15) in

Chapter 2 and following that $\Delta L/L$ equals one third of the unconstrained compaction,

$\Delta L/L$ equals $2 \cdot K_2 \cdot \frac{(1-v)}{E}$. Using the known elastic constants for fused silica one gets a

z-stress of 2.02 K_2.

Table 5
Comparison of Final Density and Stress in 30mm diameter sample
with 3mm Damage Diameter
(center radial stress = K_2 in (kg/cm^2))

Method	Sample Length	Unconstrained Densification	Constrained Densification	Average z-stress
Stress Model	X	6.69 K_2 (ppm)	3.15 K_2 (ppm)	2.02 K_2
FEA	2.5 cm	6.77 K_2 (ppm)	3.66 K_2 (ppm)	1.64 K_2
FEA	1 cm	6.90 K_2 (ppm)	4.28 K_2 (ppm)	1.10 K_2

Despite predicting stress distributions for samples as short as 1cm within 5% given the

unconstrained densification, the plain strain model is less accurate in predicting net

compaction and z-stresses for thin specimens. When these quantities are required for

OPD calculations, the FEA simulation results will be utilized to improve accuracy.

5.7c Calculating Refractive Index Changes from Densification

Three methods for calculating (633nm) refractive index changes are considered here.

They are listed in order of increasing complexity and accuracy. Refractive index changes

from color center formation are ignored here because of their relatively small contribution to total index changes. No more than 0.05/cm absorption is measured in any of the samples described in this section which should correspond to less than a 25ppB index increase at 633nm.

(1) Method (1) calculates Ω by using the Lorentz-Lorenz relation shown in Equation (10) and the "observed" 633-nm refractive index changes and net density levels.

$$\left(\frac{\Delta n}{n}\right)_{net} = \frac{\left(n^2 - 1\right) \cdot \left(n^2 + 2\right)}{6n^2} \cdot \left(1 + \Omega_t\right) \cdot \left(\frac{\Delta \rho}{\rho}\right)_{net}. \tag{10}$$

Since this method does not delineate between density changes from irradiation and those from resistance of the undamaged portion of the sample to compaction, the value of Ω_t, defined by Equation (10), will depend upon the distribution of damage and sample geometry.

(2) Method (2) calculates the refractive index change by using the Lorentz-Lorenz relation and dividing up the net densification into two components, unconstrained densification from irradiation and expansion from resistance by the undamaged area to compaction. A value[7] of -0.38 for Ω is used for the expansion while Ω for irradiation-induced densification will be inferred from measurements. The unconstrained compaction levels are first extracted from birefringence distribution measurements by the method

121

described in Chapter 2. From those, the net density change will be computed using results from FEA simulations. The net refractive index change is then given by:

$$\left(\frac{\Delta n}{n}\right)_{net} = \frac{(n^2-1)\cdot(n^2+2)}{6n^2}\cdot\left\{(1+\Omega_{UV})\cdot\left(\frac{\Delta\rho}{\rho}\right)_u - (1+\Omega_p)\cdot\left[\left(\frac{\Delta\rho}{\rho}\right)_u - \left(\frac{\Delta\rho}{\rho}\right)_{net}\right]\right\} \qquad (11)$$

where $(\Delta\rho/\rho)_u$ is the unconstrained compaction from UV radiation, $(\Delta\rho/\rho)_{net}$ is the net densification, Ω_{UV} is relative polarizability change per relative density change due to UV-induced compaction, and Ω_p is relative polarizability change per relative density change due to pressure-induced expansion (-0.38).

(3) Method (3) again considers refractive index changes from irradiation and from pressure as separate components. Here, however, refractive index changes resulting from expansion due to resistance by the undamaged area to compaction are calculated using the individual stress-optic coefficients measured by Primak. Refractive index changes from unconstrained irradiation-induced densification are then calculated using the Lorentz-Lorenz relation and with Ω inferred from measurements. When method (3) is used to calculate refractive index changes from densification, the following expression is used:

$$\left(\frac{\Delta n}{n}\right)_{net} = \frac{(n^2-1)\cdot(n^2+2)}{6n^2}\cdot(1+\Omega_{UV})\cdot\left(\frac{\Delta\rho}{\rho}\right)_u + \frac{(C_1+C_2)\overline{\sigma}_r + C_2\overline{\sigma}_z}{n} \qquad (12)$$

where C_1 and C_2 are Primak's stress-optic coefficients (-0.07 and -0.42); and σ_r and σ_z are the average radial and z-stresses respectively. Equation (12) utilizes the property that in the center of the damaged region the radial and tangential stresses are equal. The z-stresses are predicted using FEA simulations using like geometries of the experiments and unconstrained density changes extracted from either birefringence or surface depression depth measurements. If the average z-stress was equal to the average radial and tangential stresses, the sample would be under uniform pressure and method (3) would be equivalent to method (2) except that it would use a value of -0.36 for Ω_{uv} instead of -0.38.

The refractive index changes calculated from interferometry measurements listed in Table 4 will be used to extract polarizability changes for all three methods. Table 6 lists unconstrained compaction levels extracted from birefringence measurements and the extracted values of Ω from all three methods.

Table 6
Unconstrained Densification Levels Extracted from Birefringence
Measurements and Extracted Polarizability Changes Ω [($\Delta\alpha/\alpha$) / ($\Delta\rho/\rho$)]

Sample and Length	$(\Delta\rho/\rho)_u$	Ω_t (method 1)	Ω_{UV} (method 2)	Ω_{UV} (method 3)
Suprasil 311 (25mm)	22.0 ppm	-0.224	-0.296	-0.251
SV2G1 (9.5mm)	10.4 ppm	0.027	-0.128	-0.102
Suprasil 300 (9.5mm)	19.6 ppm	-0.438	-0.416	-0.390
Suprasil 2 (9.5mm)	10.5 ppm	-0.274	-0.314	-0.289
7940 spot #1 (25mm)	13.6 ppm	-0.089	-0.223	-0.178
7940 spot #2 (25mm)	15.2 ppm	-0.172	-0.267	-0.223
7940 spot #3 (25mm)	6.58 ppm	-0.135	-0.248	-0.203

Table 7 lists unconstrained compaction levels extracted from surface depression measurements and the extracted values of Ω from all three methods. Because good reflection interferometry data was not obtained for the Suprasil 300 sample and for spot #3 on the Corning sample, only the other five sets of measurements are used for that extrapolation.

Table 7
Unconstrained Densification Levels Extracted from Surface Depression Measurements and Extracted Polarizability Changes Ω [($\Delta\alpha/\alpha$) / ($\Delta\rho/\rho$)]

Sample and Length	Unconstrained ($\Delta\rho/\rho$)	Ω_t (method 1)	Ω_{UV} (method 2)	Ω_{UV} (method 3)
Suprasil 311 (25mm)	20.1ppm	-0.141	-0.251	-0.206
SV2G1 (9.5mm)	9.7 ppm	0.135	-0.060	-0.035
Suprasil 300 (9.5mm)				
Suprasil 2 (9.5mm)	7.0 ppm	0.123	-0.068	-0.043
7940 spot #1 (25mm)	14.1 ppm	-0.111	-0.235	-0.190
7940 spot #2 (25mm)	14.4 ppm	-0.115	-0.237	-0.193
7940 spot #3 (25mm)				

Using the most rigorous technique for calculating refractive indices from densification (method 3), an average value of -0.23 is found for Ω using density levels extracted from birefringence measurements compared to -0.19 found using the historical data in Table 3. The extracted Ω values for Suprasil 300 ("dry" fused silica), -0.39, and SV2G1 (unannealed and "fast-relaxer"), -0.10, differ the most from this average, indicating that density-induced polarizability changes may be material dependent. The average Ω for the five tests using UV-grade fused silicas was -0.23 with a standard deviation of 0.04. When density levels extracted from surface depression measurements are used, the average Ω for UV-grade samples was -0.16 with a standard deviation of 0.08. The polarizability changes

extracted using density levels extracted from both birefringence and surface depression depth measurements agreed well with the previous published values in Table 3.

Using the extracted polarizability changes from densification, the net refractive index change from densification can now be calculated. Table 8 illustrates the net refractive index change calculated for different sample and illumination geometries using the three methods. The net densification and stress levels from unconstrained densification are found using finite element analysis as previously described. Both Methods (1) and (2) agree with Method (3), the most rigorous technique, within 10% for most sample and illumination geometries of interest to lithography. Using the results presented in the next section, for a thin sample with an illumination diameter equal to roughly half of the sample diameter, the following approximate relation is obtained: $(\Delta n/n)_{193nm} = 0.27 \ (\Delta\rho/\rho)_u$.

Table 8
Net Refractive Index Changes (633nm) versus Densification
(30mm Diameter Sample)

		$(\Delta n/n)_{net}$		
Sample Length	Damage Diameter	Method 1 $(\Omega_t = -0.19)$	Method 2 $(\Omega_{UV} = -0.27)$	Method 3 $(\Omega_{UV} = -0.23)$
∞	(<< 30mm)	$0.139 \ (\Delta\rho/\rho)_u$	$0.146 \ (\Delta\rho/\rho)_u$	$0.141 \ (\Delta\rho/\rho)_u$
2.5cm	3mm	$0.162 \ (\Delta\rho/\rho)_u$	$0.163 \ (\Delta\rho/\rho)_u$	$0.159 \ (\Delta\rho/\rho)_u$
1cm	3mm	$0.189 \ (\Delta\rho/\rho)_u$	$0.184 \ (\Delta\rho/\rho)_u$	$0.183 \ (\Delta\rho/\rho)_u$
1cm	10mm	$0.237 \ (\Delta\rho/\rho)_u$	$0.220 \ (\Delta\rho/\rho)_u$	$0.232 \ (\Delta\rho/\rho)_u$
1cm	20mm	$0.263 \ (\Delta\rho/\rho)_u$	$0.240 \ (\Delta\rho/\rho)_u$	$0.249 \ (\Delta\rho/\rho)_u$

5.8 Total UV-Induced OPD Formation for arbitrary geometry and wavelength

5.8a OPD Dependence on Wavelength

The contributors to OPD formation in damaged fused silica all have distinct wavelength dependencies. The dependence of refractive index changes from the E' color center band is shown directly in Figure 1. At 193-nm, as opposed to at 633-nm, the index is actually lowered from the E' color center band. The OPD from a surface crater of depth ΔL is (n - 1)ΔL, so the magnitude of surface induced OPD's follows the (n - 1) dependence with wavelength. The OPD's from surface craters at 193nm are about 22% greater in magnitude than at 633nm.

Directional refractive index changes from stress will scale directly with the wavelength dependence of the stress-optic coefficient. The wavelength dependence of the stress-optic coefficient has been found to follow the same wavelength dependence as the birefringence of crystalline quartz so the 193-nm value is estimated as -5.21 (nm/cm)/(kg/cm^2) using[19]

$$\Re(\lambda) = \Re(\lambda_0) \bullet \frac{n(\lambda_0)}{n(\lambda)} \bullet \frac{\lambda^2}{\lambda_0^2} \bullet \frac{\lambda_0^2 - \lambda_1^2}{\lambda^2 - \lambda_1^2} \bullet \frac{\lambda^2 - \lambda_2^2}{\lambda_0^2 - \lambda_2^2} \tag{13}$$

where λ_0 is 633-nm, λ_1 is 121.5-nm, λ_2 is 6900-nm, and $\Re(\lambda_0)$ is -3.5[16] (nm/cm)/(kg/cm^2). So while the refractive index only increases about 7% (from 1.46 to 1.56) between 633-nm and 193-nm, the stress-optic coefficient increases by almost 50%. Unfortunately, no definitive data exists on the wavelength dependence of the individual stress-optic

126

coefficients. Primak[16] gives values for C_2 and $\Re$ which show that the magnitudes of each

change roughly the same amount over a wavelength range between 436nm and 644nm.

The wavelength dependence of refractive index changes from stress-free density changes

is embodied within the refractive index terms in the differentiated Lorentz - Lorenz

relation (Equation 6). Inserting the refractive index values at the respective wavelengths,

one would get the following for the differentiated Lorentz - Lorenz relation:

$$\Delta n = \frac{\Delta \rho}{\rho} \bullet (1+\Omega) \bullet \begin{Bmatrix} 0.530 --- 633\text{nm} \\ 0.679 --- 193\text{nm} \end{Bmatrix} \tag{14}$$

where Ω, the ratio of relative polarizability change to relative density change, is assumed

to be independent of wavelength. While the wavelength dependence of Ω is unknown,

even a 20% change from a nominal value of -0.20 would only cause about a 5% shift in

Δn.

The contribution to OPD formation at 193nm from color center formation is assumed

small compared to the other effects just as at 633nm. With this assumption, index changes

at 193-nm are then predicted to be about 27% larger than at 633-nm. Both the OPD

components from densification and surface crater formation increase going from 633-nm

to 193-nm, but because the densification contribution is larger, the total OPD will be

larger at 193-nm. For example, if at 633nm surface depressions offset 50% of the OPD increase from densification, the total OPD at 193nm would be 29.5% larger.

5.8b OPD Dependence on Damage and Sample Geometry

While method (3) is the most rigorous method to calculate refractive index changes from densification, method (2) will be used here because of its greater simplicity. The refractive index changes predicted by method (2) are within a few percent of those predicted by method (3) in general and always so for shorter samples which will be emphasized here. Ignoring the index changes from color center formation, Equations (7) and (11) describe the OPD formed from a compacted region for method (2). Given the unconstrained irradiation-induced compaction, the surface depth and net compaction can be determined using FEA. The unconstrained compaction level can be considered to be the geometry-independent result of UV-radiation.

FEAP simulations were performed using a 1ppm unconstrained densification where the sample and damaging beam geometries were varied. Figure 3 shows the relative contributions to OPD formation in a 3cm diameter sample with a 3mm diameter damaging beam as the sample length is varied. The 193-nm OPD values are calculated here using the machinery developed in Section 5.6a. As the length is decreased, resistance to compaction by the undamaged portion is reduced and the net compaction increases. The relative contribution of the surface depressions formed, however, also increases when one considers OPD formation per centimeter of path length as the parameter of interest. The

128

OPD per centimeter is actually smaller for shorter samples because of the greater

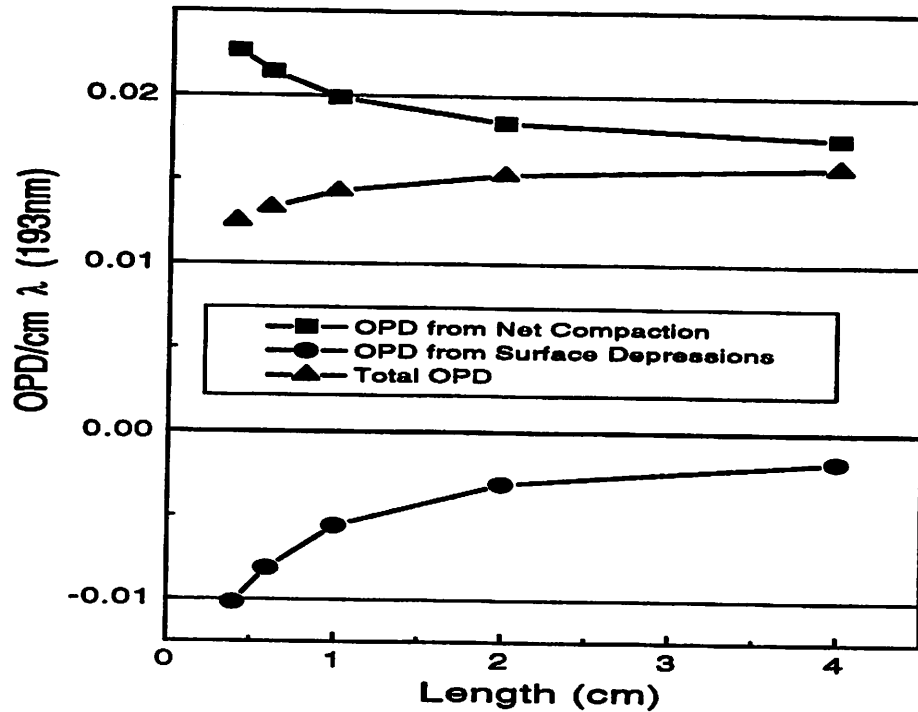cancellation of density-induced index increases by surface depressions.

Figure 3. OPD formed from densification and surface depressions for a 3cm diameter fused silica with a 3mm diameter damage region with 1ppm unconstrained densification. The net densification and surface depression depth were calculated using FEA and the OPD's were calculated using Equations (7) and (11).

Figure 4 shows the relative contributions to OPD formation for a 1cm long, 3cm diameter

optic as the damage diameter is increased. These dimensions are similar to the

experimental conditions used to irradiate samples in the tests presented in Chapters 3, 4

and 6. As the damage diameter is enlarged, resistance to compaction by the undamaged

portion is reduced and the net compaction increases. The surface depression depth also

increases with damage diameter, however, making the variations in OPD formation only weakly dependent of damage diameter for these geometries.
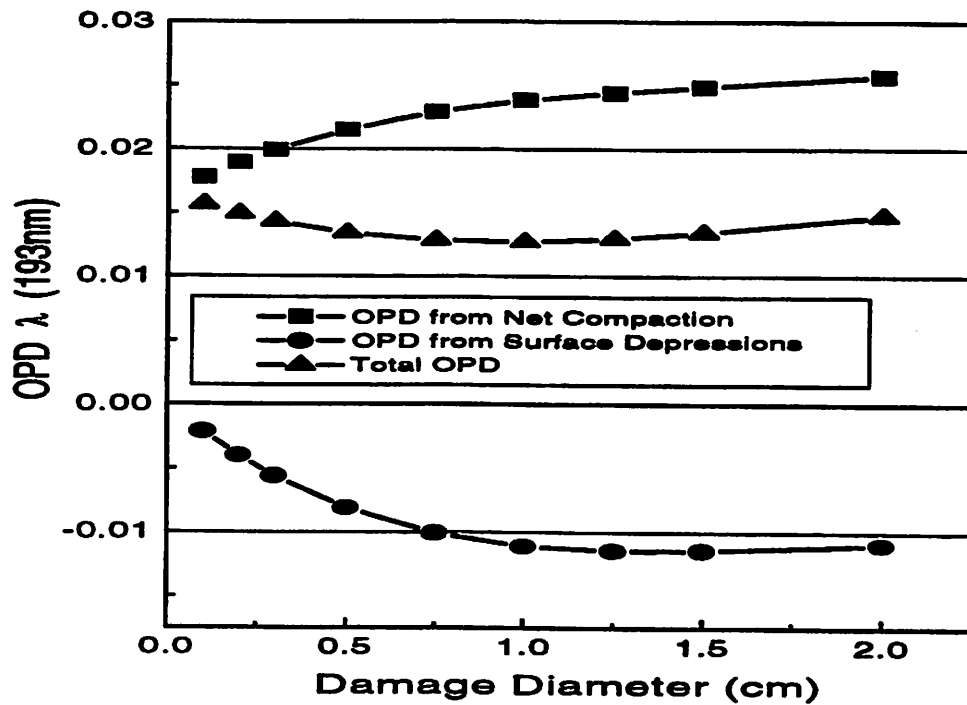

Figure 4. OPD formed from densification and surface depressions for a 1cm long, 3cm diameter fused silica sample with a 1ppm unconstrained densification of variable diameter. The net densification and surface depression depth were calculated using FEA and the OPD's were calculated using Equations (7) and (11).

Larger diameter optics are also evaluated because lithographic systems have elements which can be larger than 15cm in diameter. Simulations found that the OPD formation was nearly independent of sample length (about a 1% variation for lengths from 3mm to 4cm for a 10cm sample and 5cm damage diameter). Total OPD formation in larger optics has a stronger dependence on damage diameter than sample length. Figure 5 shows the relative contributions to OPD formation for a 1cm long, 10cm diameter optics as the damage diameter is increased. Like with smaller optics, as the damage diameter is

130

enlarged, resistance to compaction by the undamaged portion is reduced and the net compaction increases. As the damage diameter is enlarged, the surface depression depth decreases, opposite of what was found for the 3cm diameter optic. The surface depth decreases because as the damage diameter is increased, the tensile radial stress is lowered which, in turn, reduces the shortening of the center region brought on by the Poisson effect.

The total OPD in a 1cm long, 10cm diameter optics increases by over about a factor of 40% as the damage diameter is varied from 1cm to 9cm. The dependence of OPD formation on damage diameter shown Figure 5 can be considered somewhat analogous to the dependence of OPD in a lithographic elements on the sigma of the illumination system. This is most valid for optics near the pupil plane of the system where the pupil fill resembles more closely the illumination sources. The results in Figure 5 suggest that as sigma is varied from 0.3 to 0.7, as much as a 30% higher OPD formation would be observed for the same amount of dose per area. This, however, does not take into account the larger intensities expected in optics with smaller sigma values.
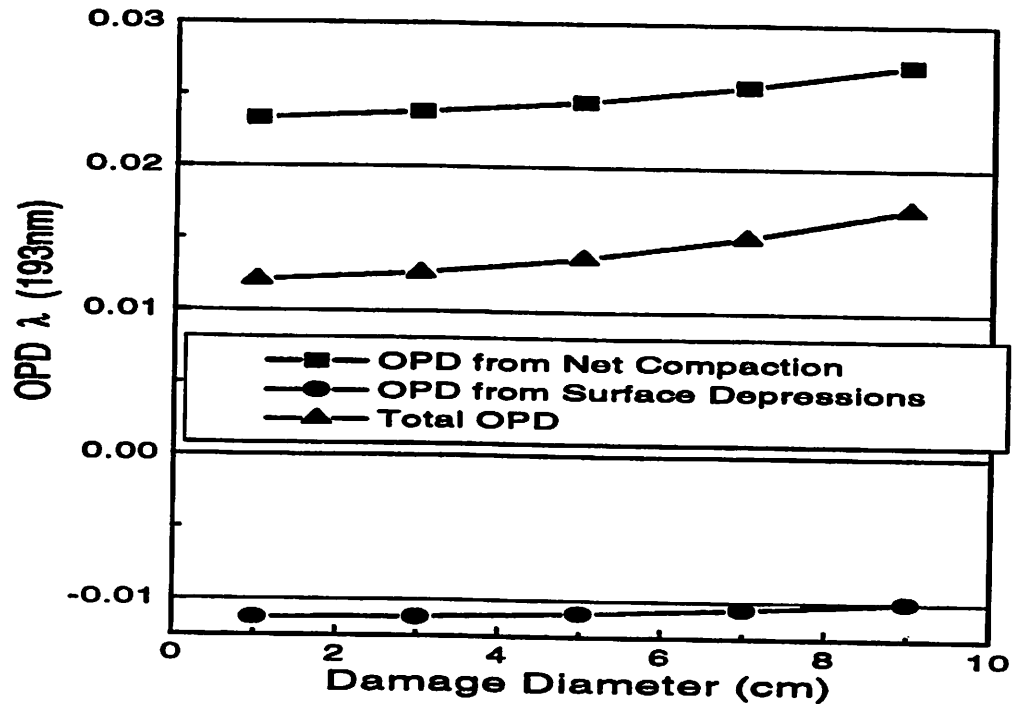
Figure 5. OPD formed from densification and surface depressions for a 1cm long, 10cm diameter fused silica sample with a 1ppm unconstrained densification of variable diameter. The net densification and surface depression depth were calculated using FEA and the OPD's were calculated using Equations (7) and (11).

5.9 Conclusions

Because the index changes resulting from elastic density changes are different than those from irradiation-induced density changes (inelastic deformations), the two forms of densification need to be considered independently when computing refractive index changes. Comparisons of refractive index changes to density changes indicate that Ω_{uv} (relative change in polarizability per relative density change) equals -0.20 +/- 0.08, compared to -0.38 for pressure-induced compaction. The UV-compaction value is in agreement with index changes found from other forms of stress-free compaction including gamma and neutron-induced compaction. This is an indication that UV-induced

compaction has a similar structural manifestation as compaction resulting from the other radiation sources. Preliminary data indicate that density-induced polarizability changes possibly depend upon fused silica type where polarizability shifts per unit compaction are larger for faster damaging samples.

Given the radiation conditions, the net OPD formation for arbitrary sample/damage geometries and at any wavelength can be predicted using the established relations between refractive index and path length changes, and unconstrained densification. With this machinery, data from tests using one geometry and wavelength can be used to predict the effects of compaction on the imaging performance of complete optical systems.

References

[1] Rothschild, D.J. Ehrlich, and D.C. Shaver, "Effects of excimer laser irradiation on the transmission, index of refraction, and density of ultraviolet grade fused silica," Appl. Phys. Lett. 55 (13), pp. 1276-1278, Sept. 25, 1989.

[2] for more background, consult E. D. Palik, *Handbook of Optical Constants of Solids I*, Academic Press Inc., 1985.

[3] *Heraeaus Application Note*, "Considerations for UV excimer optics and other high intensity UV light source," 1994.

[4] measurements performed by Dr. Douglas Allan at Corning Inc.

[5] developed and written by Prof. R. L. Taylor at the civil engineering department of UC-Berkeley.

[6] for more information see M. Born and E. Wolf, Principles of Optics: *Electromagnetic Theory of Propagation, Interference and Diffraction of Light*, Pergamon Press, Sixth Edition, 1993.

[7] K. Vedam, E. D. D. Schmidt, R. Roy, "Nonlinear Variation of Refractive Index of Vitreous Silica with Pressure to 7 Kbars," Journal of the American Ceramic Socity, Vol. 49, No. 10, pp. 531-535, Oct. 1966.

[8] N. Kitamura, Y. Toguchi, S. Funo, H. Yamashita, M. Kinoshita, "Refractive index of densified silica glass," Journal of Non-Crystalline Solids 159, pp. 241-245, 1993.

[9] J. E. Shelby, "Effect of radiation on the physical properties of borosilicate glasses," Journal of Applied Physics 51 (5), pp. 2561-2565, May 1980.

[10] J. Arndt, D. Stoffler, "Anomalous changes in some properties of silica glass densified at very high pressure," Physics and Chemistry of Glasses, Vol. 10 No. 3, pp. 117-124, June 1969.

[11] J. Arndt, "Densification of glasses of the system TiO_2 - SiO_2 by very high static pressures," ," Physics and Chemistry of Glasses, Vol. 24 No. 4, pp. 104-110, Aug. 1983.

[12] J. Arndt, U. Hornemann, W. F. Muller, "Shock-wave densification of silica glass," Physics and Chemistry of Glasses, Vol. 12 No. 1, pp 1-7, Feb. 1971.

[13] W. Primak, "Fast-Neutron-Induced Changes in Quartz and Vitreous Silica," Physical Review, Volume 110, Number 6, pp. 1240-1254, June 1958.

[14] T. A. Dellin, D. A. Tichenor, E. H. Barsis, "Volume, index-of-refraction, and stress changes in electron-irradiated vitreous silica," Journal of Applied Physics, Vol. 48, No. 3, pp. 1131-1138, March 1977.

[15] N. F. Borrelli, R. A. Miller, "Determination of the Individual Strain-Optic Coefficients of Glass by an Ultrasonic Technique," Applied Opitcs, Vol. 7, No. 5, pp. 745-750, May 1968.

[16] W. Primak, D. Post, "Photoelastic constants of vitreous silica and its elastic coefficient of refractive index," J. Appl. Phys. 30 (5), pp. 779-788, May 1959.

[17] special thanks to Douglas Allan of Corning Inc. for performing measurements.

[18] polishing performed at Integrated Optical Services in Milpitas California.

[19] A .J. Barlow, D.N. Payne, "The stress-optic effect in optical fibers," IEEE J. Quantum Electronics, Vol. QE-19 (5), May 1983.

Chapter 6

Evaluation of UV-Induced Compaction in Fused Silicas

By monitoring stress-induced birefringence we are able to measure UV-induced compaction rates at lithographic intensity levels. Birefringence distributions corresponding to relative refractive index changes of only a few tenths parts per billion can be resolved. Compaction rates have a non-linear dependence on pulse count, with rates higher at low levels of compaction. For pulse energy densities varying from $1mJ/cm^2$ to $20mJ/cm^2$, the total level of compaction can be predicted from a universal fluence parameter: pulse count multiplied by the pulse energy density squared. The densification $(\Delta\rho/\rho)$ for uniform exposures can be approximated as $\kappa \cdot \left[\dfrac{N_p}{10^6} \cdot \left(\dfrac{I}{I_o} \right)^2 \cdot \dfrac{\tau_o}{\tau} \right]^{0.7}$ where τ is the pulse length $(\tau_o = 1ns)$, N_p is the pulse count, κ is a constant, and I is the 193-nm energy density $(I_o = 1\ mJ/cm^2)$. When defining dose as the total energy absorbed in the production of "ionization" events, the efficiency of UV-radiation in inducing densification is within 15% of that previously found for electrons, gamma-rays and protons. Only a plus or minus 20% compaction rate variation is found among the (1990-1994) UV-grade fused silica samples tested. The extracted value of κ varies from 84ppB to 660ppB for experimental (1995-1996) fused silicas, as much as a factor of two improvement compared to (1990-1994) grades.

6.1 Introduction

In a production type environment, more than 90 million pulses a day could be transmitted through the optics of a lithographic system; or almost 35 billion pulses per year. For obvious reasons, testing fused silica samples for damage after several billion pulses is impractical. Because of this, experiments were performed to better characterize the pulse count and energy dependence of UV-induced compaction with the goal of being able to use low pulse count data to predict damage in future production systems.

6.2 Experimental methods

Fused silica samples were irradiated at UC-Berkeley using a Lambda Physic ArF excimer laser (LPX140i) operated at 350Hz. Birefringence distributions were measured using the "third-generation" setup described in Chapter 2 and used to extract compaction levels with the modeling presented in Chapters 2 and 5. A CCD camera monitored attenuated spatial profiles of the beam to insure acceptable beam uniformity. The peak to valley intensity difference within the 3mm diameter of the beam generally varied by no more than 15 percent. The pulse width of the laser was measured to be about 11 nanoseconds after the irradiations were all completed.

6.3 Compaction as a function of pulse count and pulse intensity

6.3a Experimental Results

Compaction data in this chapter are given in $(\Delta\rho/\rho)_u$, the relative density change which would be produced in the sample if the sample were irradiated uniformly. $(\Delta\rho/\rho)_u$ will be referred to as the unconstrained compaction or density change. Because only a small area of the samples is irradiated, the net density change is less than $(\Delta\rho/\rho)_u$ due to the resistance of the undamaged portion of the sample to displacements from the compacted region. As shown in Chapter 5, the net density change is a function of the geometry of the sample and damage area, but for small damage beams is about half $(\Delta\rho/\rho)_u$. Because different sample/damage geometries are used in this work and in other studies, the unconstrained compaction serves as the best standard description of compaction for comparison, from which the actual compaction can be computed.

Figure 1 shows the pulse count dependence of compaction for a single sample of Corning 7940 fused silica at three different pulse energy density levels. The dependence is non-linear, with compaction rates highest initially. For a fixed pulse energy density, compaction follows the pulse count to a power of about 0.65 to 0.7. For this sample as well as all others tested, no saturation is observed.
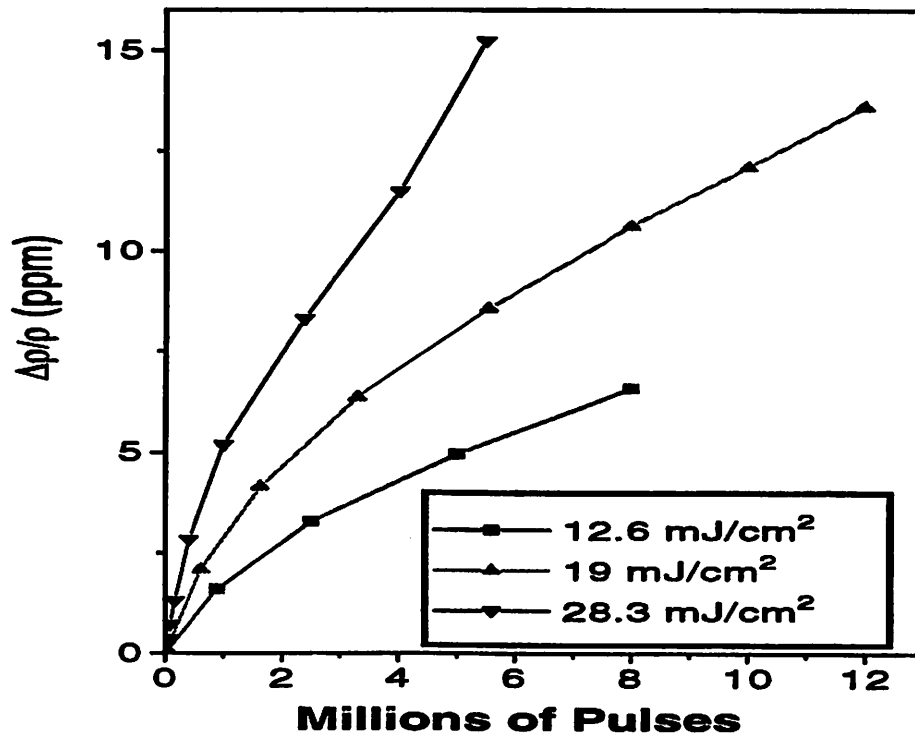
Figure 1. Unconstrained densification in Corning 7940 versus pulse count at three different pulse energy densities.

Evidence presented in Chapter 4 strongly suggests that UV-induced damage in fused silica

is initiated by a two-photon damage process. The compaction levels listed in Table 1,

however, show less than an intensity squared dependence.

Table 1

Unconstrained compaction in fused silica after 8 million pulses for different pulse energy densities

(single sample of Corning 7940)

Pulse Energy Density	$(\Delta \rho / \rho)_u$
1.05 mJ/cm^2	0.138 ppm
2.6 mJ/cm^2	0.684 ppm
12.6 mJ/cm^2	6.61 ppm
19 mJ/cm^2	10.6 ppm

Given the non-linear dependence of compaction on fluence, this discrepancy is not surprising. To properly test the intensity squared damage rate hypothesis, we replot the data of Figure 1 in Figure 2, normalizing the fluence in the form of pulse count times per pulse fluence squared divided by the pulse length. This fluence parameter is proportional to the number of two-photon occurrences in the sample. We also add data at lower intensities. All data lie on a single universal curve. Figure 3 expands the low fluence region of Figure 2 by plotting on a log-log scale. To test the universality of the single relationship seen in Figures 2 and 3, a different sample was tested over a similar range of pulse intensities. As seen in Figure 4, similar damage behavior is observed for Suprasil 311.
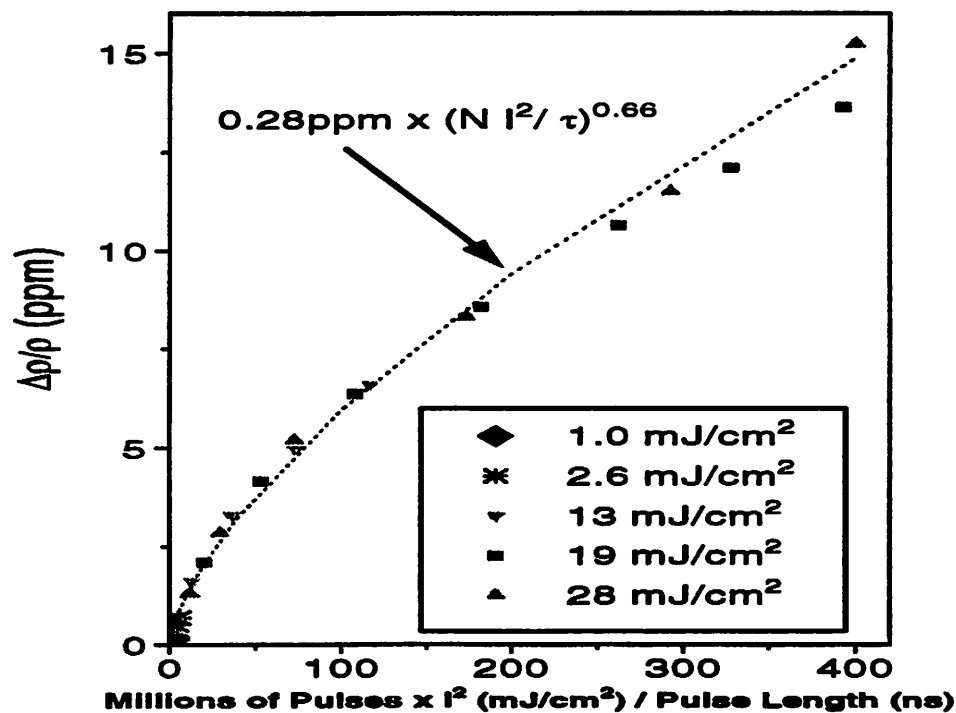
Figure 2. Unconstrained densification in Corning 7940 for five different pulse energy densities versus number of pulses times the pulse energy density squared divided by pulse length.
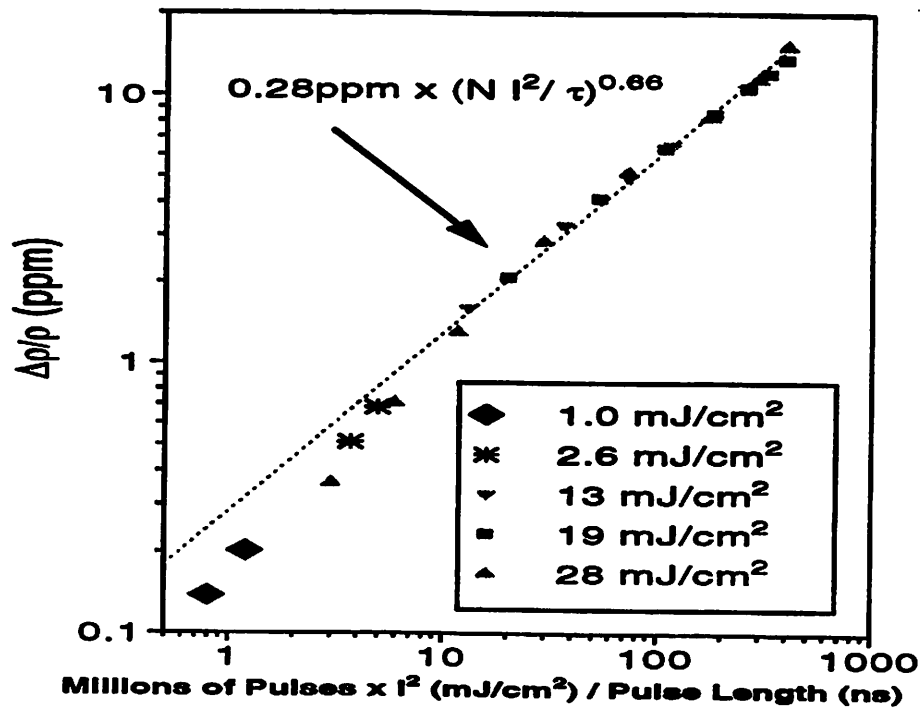
Figure 3. Unconstrained densification in Corning 7940 for five different pulse energy densities versus number of pulses times the pulse energy density squared divided by pulse length. (log-log scale)
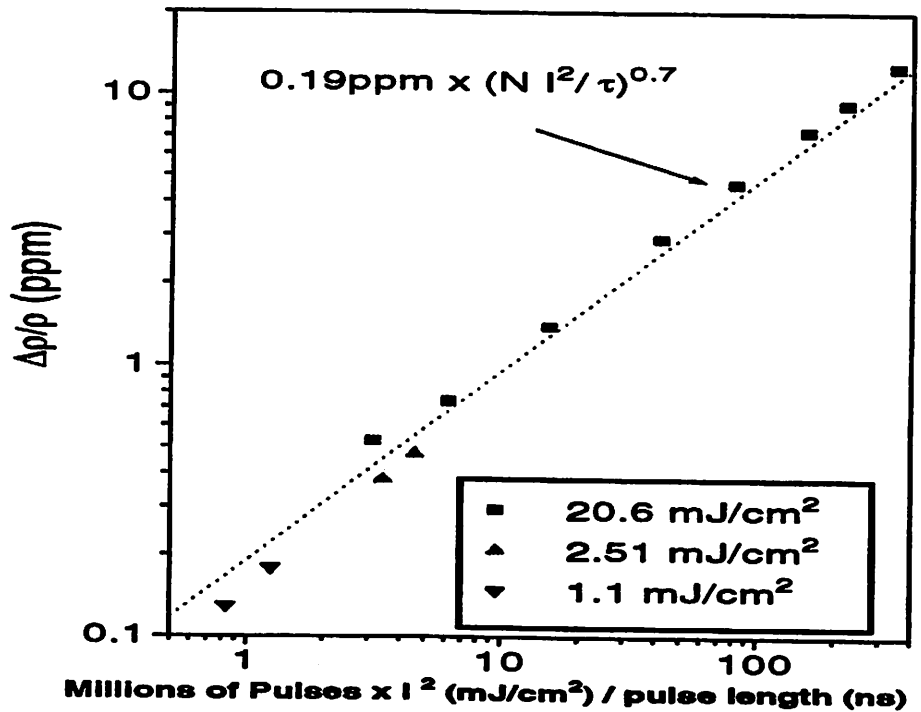

Figure 4. Unconstrained densification in Suprasil 311 for three different pulse energy densities versus number of pulses times the pulse energy density squared divided by pulse length.

140

Figures 3 and 4 show the best fit of the data to a curves given by

$$\left(\frac{\Delta\rho}{\rho}\right)_{u} = \kappa\cdot\left(\frac{N\cdot I^{2}}{\tau}\right)^{c} \qquad (1)$$

where N is the number of pulses in millions, τ is the pulse length in nanoseconds, κ is a constant, I is the 193-nm energy density in mJ/cm^{2} and c, the exponent, is equal to 0.66 and 0.7 for the two figures respectively. As suggested by Sandstrom[1], a more rigorous expression for the densification is:

$$\left(\frac{\Delta\rho}{\rho}\right)_{u} = \kappa\cdot\left(\int_{t_{pulse}} N\cdot P^{2}\cdot dt\right)^{c} \qquad (2)$$

where P is the instantaneous intensity in (W/cm^{2}). The integral of Equation (2) is the precise measure of two-photon events in the sample. Equation (1) is equivalent to Equation (2) for pulses with uniformly intensity over time ("top-hat" shape versus time). If pulse shapes are identical but with different pulse widths, Equation (1) can be used for comparative purposes.

6.3b Comparison to Other Compaction Studies

Allan[2] et al. noted that almost three decades ago Primak and Kampwirth reported[3] comprehensive results of fused silica compaction for γ-ray, protons, and electron sources.

There, a 0.65 - 0.7 dose dependence was reported for all three types of irradiation as seen in Figure 5. The UV-induced compaction results followed an almost identical dependence if one uses the total energy absorbed from two-photon absorption as the dose parameter instead of total dose absorbed in the sample. For neutron irradiation, Primak found a linear dependence of compaction on dose. Table 2 lists the extracted dose exponents (c) found when the previous compaction data was fit to a relation:

$$\Delta\rho/\rho = A\ D^c \qquad\qquad (3)$$

where ρ is the density, D is the dose and A and c are constants.

Table 2
Dose Exponent for Compaction Formation from Previous Compaction Studies

Work	Radiation Source	Compaction Range ($\Delta\rho/\rho$)	Fused Silica	Dose Exponent (c)
Primak[3]	neutron, He+, D+	$10^{-6} - 10^{-3}$	Suprasil	1
	gamma, e-beam	$10^{-6} - 10^{-3}$	**Suprasil**	**0.66**
	H+	$10^{-6} - 10^{-3}$	**Suprasil**	**0.71**
Higby[4,5]	e-beam	$10^{-5} - 10^{-3}$	Optosil	$0.32^4, 0.37^5$
			Suprasil 2	**0.59**
			Suprasil 300	0.56
			Suprasil W2	0.77
Friebele[6]	e-beam	$10^{-5} - 10^{-3}$	**Suprasil 2**	**0.64**
			Suprasil W2	0.67
			Optosil	0.3
Norris[7]	e-beam	$10^{-4} - 10^{-3}$	Infrasil	0.65*
		$10^{-4} - 10^{-3}$	**Corning 7940**	**0.65***
		$10^{-5} - 10^{-4}$	**Corning 7940**	**0.70***
Rajaram[8]	e-beam	$10^{-4} - 10^{-2}$	Optosil	0.37
			ULE#	0.37
Merzbacher[9]	e-beam	$10^{-4} - 10^{-2}$	**Suprasil 2**	**0.5**
Dellin[10]	e-beam	$10^{-4} - 10^{-3}$	T-08	0.5*
Shelby[11]	gamma	$10^{-5} - 10^{-3}$	Suprasil W	0.81

*denotes values that were estimated from published data plots.
ultra-low-expansion glass manufactured by Corning.

Data for type 3 fused silicas are highlighted in the table. The various fused silica types are described in chapter 1 except for ULE which is a Ti-doped silica. Several of the authors also examined glass ceramics[4,6,7,9] which are glass-crystal composites balanced to reduce the coefficient of thermal expansion. The Norris and EerNisse work[7] is cited by several authors[6,8,12] as having found a value of 1 for c for Infrasil and Corning 7940 and the Norris et al. describe the initial dose dependence of compaction as linear. A close examination of the data, however, reveals a sublinear dependence of densification on dose over the first decade of compaction.

It is informative to compare the efficiency of UV-induced compaction to that found for other radiation sources. We will assume that for 193nm UV radiation two photons (total energy = 12.8eV) are used to produce one exciton (bandgap ~ 8.3eV). Consequently the "available" dose for ionization, D_a, is (8.3/12.8) x absorbed dose and is given by:

$$D_a (Mega - rads) = \frac{8.3}{12.8} \frac{0.1 \, N(\text{millions of UV pulses}) \, I_o^2 (mJ \, / \, cm^2) \, \alpha_2 (cm \, / \, GW)}{\rho(g \, / \, cm^3) \, \tau(ns)} \quad (4)$$

where α_2 is the two-photon absorption coefficient. Since the published[13] two-photon absorption coefficient was measured with pulse shapes similar to those used here, non-uniformities in the pulse shape are not accounted for in calculating total energy absorbed from two-photon absorption. For higher energy ionizing radiation such as electron beams and gamma rays we will assume, following Everhart and Hoff[14], that approximately 33% of the energy is used in exciton creation, thus for electron and gamma radiation:

143

$$D_a = 0.33 \, D_{\gamma\text{-ray and e-beam}}.$$ (5)

Using this definition for "available" dose, Primak[3] and Kampwirth's data approximately fit the form $((\Delta\rho/\rho)_a \approx 1.7\text{ppm} \times (D_a)^{0.66})$. For three Suprasil 2 samples tested, we found an average κ value of 0.23 ppm when the data was fit to $(\Delta\rho/\rho)_a = \kappa \times (N \times I^2/\tau)^{0.66}$. Assuming an 11ns pulse width, a density of 2.2 gr/cm^3 and 2 cm/GW two-photon absorption coefficient[13], the UV data is characterized by $((\Delta\rho/\rho)_a = 1.5\text{ppm} \times (D_a)^{0.66})$, in close agreement with the gamma and electron description. This agreement supports an ionization-induced damage process for UV, gamma and electron radiation and indicates that the mechanisms involved with UV-induced compaction are similar to those involved with compaction from other sources.

Radiation-induced expansion has been reported in some fused silicas. As mentioned in Chapter 1, Shelby[11] observed expansion of hydrogen impregnated Suprasil-W when exposed to gamma irradiation. This appeared to result from the rapid formation of SiOH and SiH groups. Norris[7] observed modest expansion after low-doses of electron radiation in Infrasil. At higher doses, the density changes in the Infrasil sample were almost identical to the Corning 7940 sample, indicating that the initial expansion was related to the higher impurity density in Infrasil. The expansion in Infrasil, as well, was only
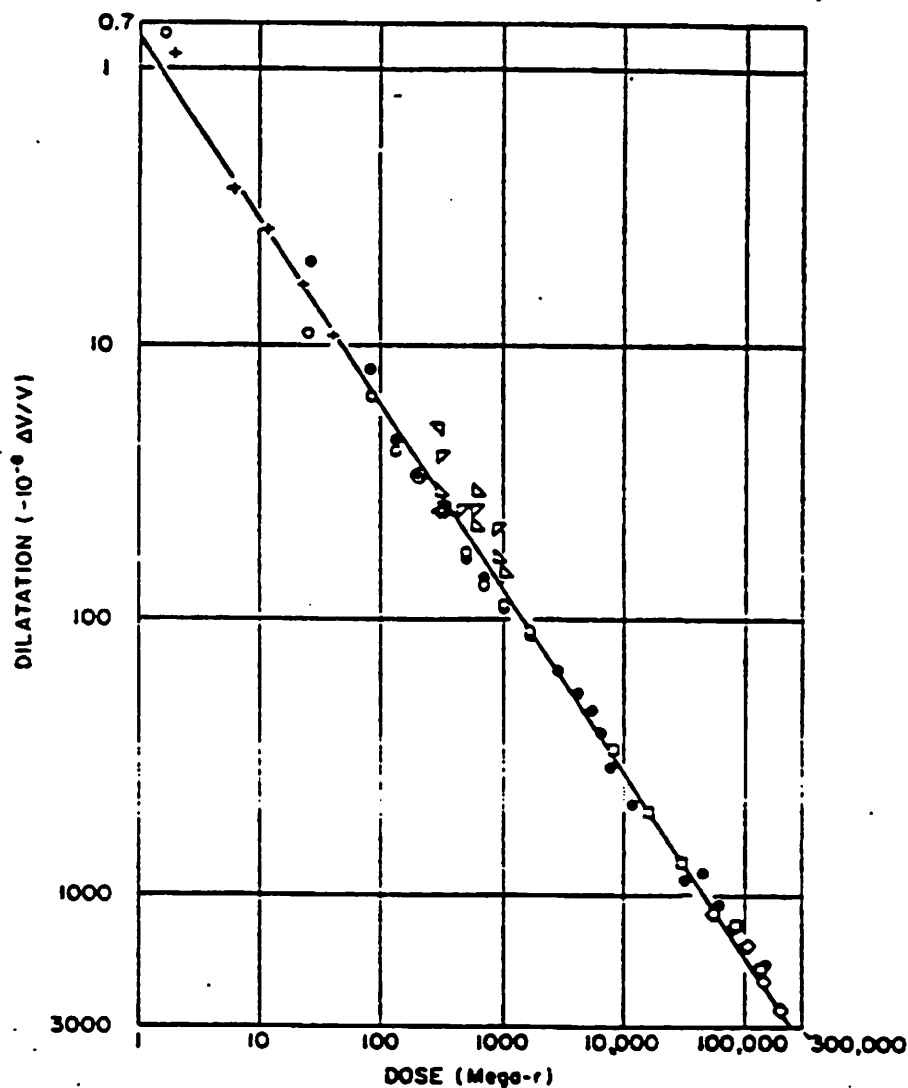
Figure 5. [Figure caption copied verbatim from Primak and Kampwirth, J. Appl. Phys., 39, pp. 5651] *The dilation of Suprasil at the point of maximum damage along the range of electrons plotted against the dose at this point; circles, actual measurements; round spots, calculated from the mean dilation (both for progressive 0.6 MeV electron irradiations of specimen 2883); squares and diamonds, respective progressive 0.3 MeV irradiation of two specimens; crosses, respective single 0.6 MeV irradiations of five specimens. Triangles are comparative points for gamma irradiations of end-standards; the quadrants are for the respective temperatures 7°, 25°, 50°, 95°C. The left half-diamond is for 75°C. The line is drawn for a slope of 0.66 (2/3 power dependence).*

145

observed to initially expand when an AC (pulsed) electron source was used for the irradiations, showing only compaction with a continuous electron source[7]. Norris[7] infers that because AC radiations are more likely to induce structural changes involving impurities, this is another indication that the expansion was impurity related. Ruller[12] reported initial expansion from gamma radiation for Optosil, Ultrasil and Suprasil 1. The expansion presented for the Suprasil 1 sample was of similar magnitude to the experimental error of the measurements (10^{-5} in $\Delta\rho/\rho$). It is possible that irradiation-induced expansion is an impurity related phenomenon.

It should be pointed out that past compaction studies involving electron irradiation have shown non-linear responses between compaction and the stress fields associated with that compaction[10]. While such a non-linear elastic response could contribute to the non-linear dependence of compaction extrapolated from stress birefringence on pulse count, the levels of compaction measured here are several orders of magnitude smaller than those where the non-linear elastic behavior was previously observed from electron irradiation.

6.4 Comparison of compaction rates of fused silica materials

6.4a 1990-1994 grade fused silicas

Five 1990-1994 grade fused silica samples were irradiated; Suprasil 311, SV2G1, Suprasil 2, Suprasil 300, and Corning 7940. The basic sample properties are described in Chapters 2 and 3. The Corning sample and the Suprasil 311 sample were 2.5cm thick while the

other samples were 1cm thick. Figure 6 shows the compaction-induced refractive index changes for the five different materials tested versus the number of pulses delivered multiplied by the intensity squared divided by the pulse length. The x-axis is directly proportional to the total number of two-photon events within the sample.
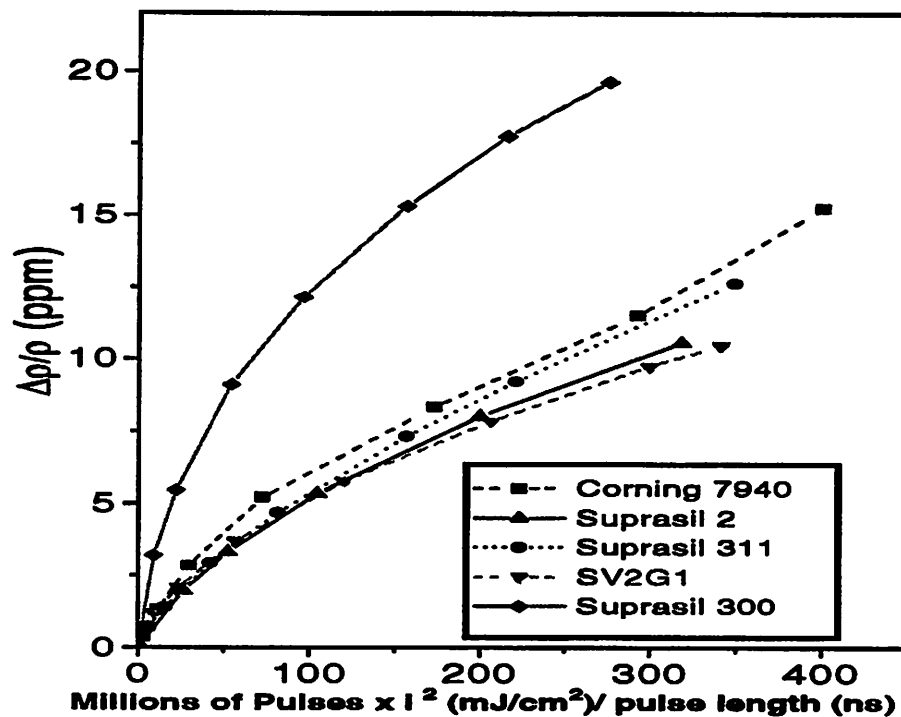

Figure 6. Unconstrained densification for five different samples versus number of pulses times the pulse energy density squared divided by pulse length. Suprasil 300 is a "low water content" fused silica.

The compaction data in Figure 6 is replotted in Figures 7 and 8 to further examine the effects of differences in fused silica manufacturing on compaction rates. As seen in Figures 3, 7 and 8, the three UV-grade fused silicas, Suprasil 2, Corning 7940 and Suprasil 311, and the unhomogenized version of Suprasil 2 (SV2G1) all followed the dose parameter to a power of about 0.65 to 0.7 and had values of (κ) that varied by less than plus or minus 20% among all samples tested when keeping c set to 0.7. Suprasil 300,

however, followed the dose parameter to a somewhat lower power (0.55) and showed

higher levels of UV-induced compaction within the tested dose range as illustrated in

Figure 8. This indicated that the removal of hydrogen from fused silica may reduce the

sample's durability to UV-induced damage. The similarity in damage performance of

Suprasil 2 and SV2G1 indicated that the "homogenization process" used in the production

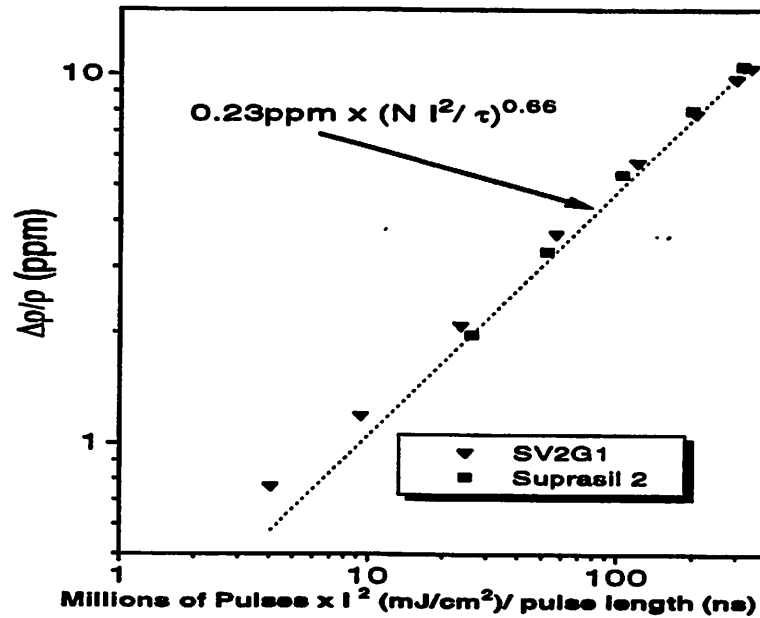of Suprasil 2 did not significantly effect its compaction performance.

Figure 7. Unconstrained densification in Suprasil 2 and SV2G1 versus number of pulses
times the pulse energy density squared divided by pulse length. SV2G1 is an
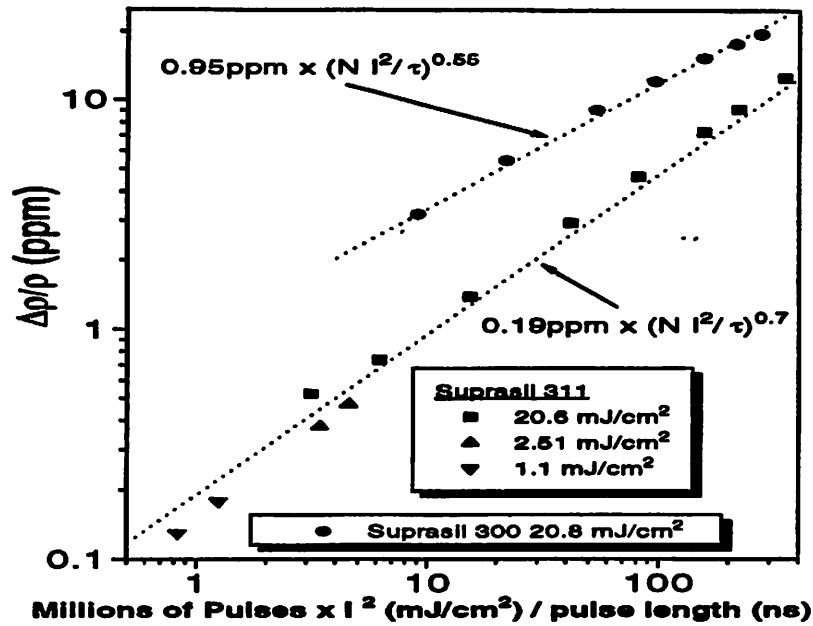unhomogenized precursor to Suprasil 2.

Figure 8. Unconstrained densification in Suprasil 300 and Suprasil 311 versus number of pulses times the pulse energy density squared divided by pulse length. Suprasil is a chemically dehydrated version of Suprasil 311.

6.4b Experimental fused silicas

Five experimental fused silicas were examined within a SEMATECH program to improve the intrinsic absorption and damage durability of fused silica for 193nm lithography. The five fused silicas were Corning 7940, Suprasil 311, Suprasil 1, Shin-Etsu X103, and Shin-Etsu X103A. Among the different fused silicas, several batches were tested. The samples were randomly labeled A, B, C, D, and E in accordance with the wishes of the suppliers and SEMATECH. In addition to the samples exposed at Berkeley, samples exposed at MIT Lincoln Laboratories were measured for compaction. The Berkeley samples were 4cm x 2cm x 1cm long and used a 3mm diameter damaging beam while the Lincoln samples were 4cm x 4cm x 2.5cm long and used a 5mm diameter damaging beam. The pulse length used for the Lincoln tests was approximately 22 nanoseconds, twice that for

dosimetry (intensity measurements) was less frequent at MIT, so there may be dosimetry differences in data from the two sites.

Figures 9 - 13 plot the measured compaction for the five fused silicas. Different shapes indicate the different batch types within the fused silica type. Pulse energy densities are also listed for the Berkeley samples. All the samples tested follow roughly the same κ * $(N * I^2 / \tau)^{0.7}$ dependence, differing only by the magnitude of the constant κ.
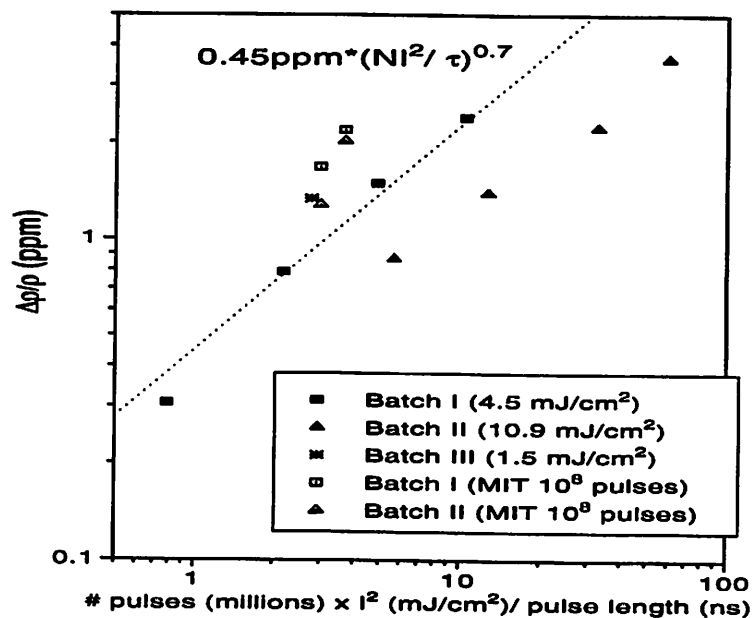

Figure 9. Unconstrained densification in experimental fused silica A versus number of pulses times the pulse energy density squared divided by pulse length. MIT data points are for individual samples.
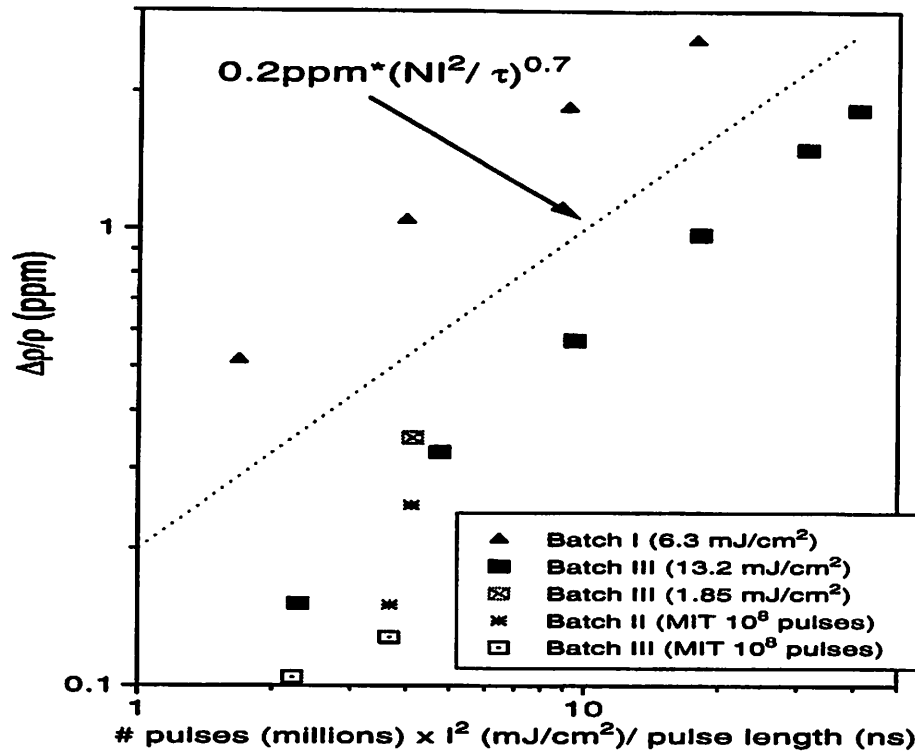
Figure 10. Unconstrained densification in experimental fused silica B versus number of pulses times the pulse energy density squared divided by pulse length. MIT data points are for individual samples.
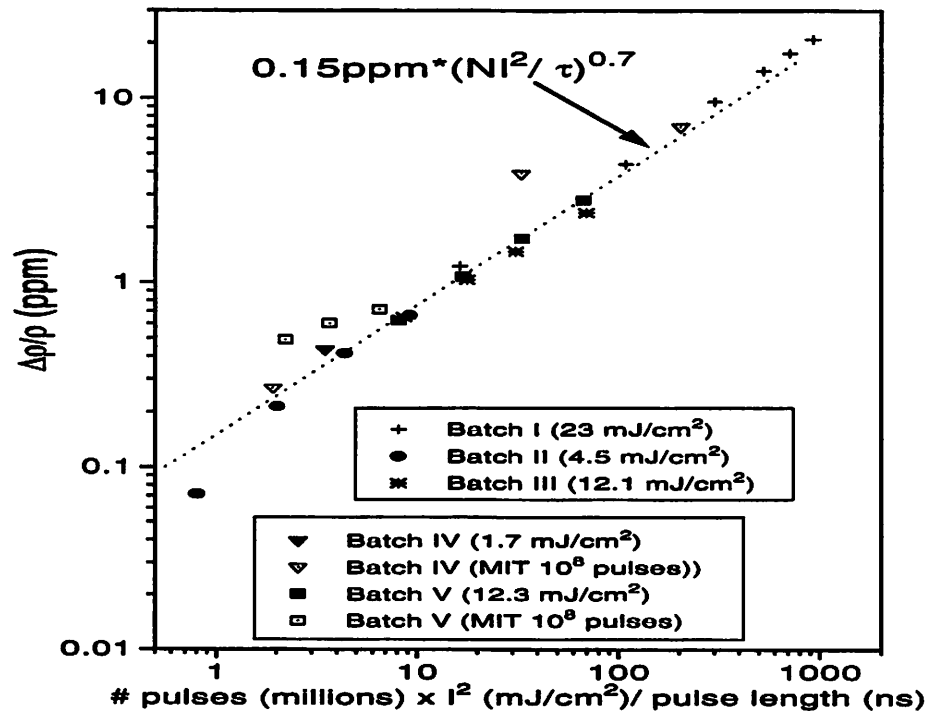
Figure 11. Unconstrained densification in experimental fused silica C versus number of pulses times the pulse energy density squared divided by pulse length. MIT data points are for individual samples.

151
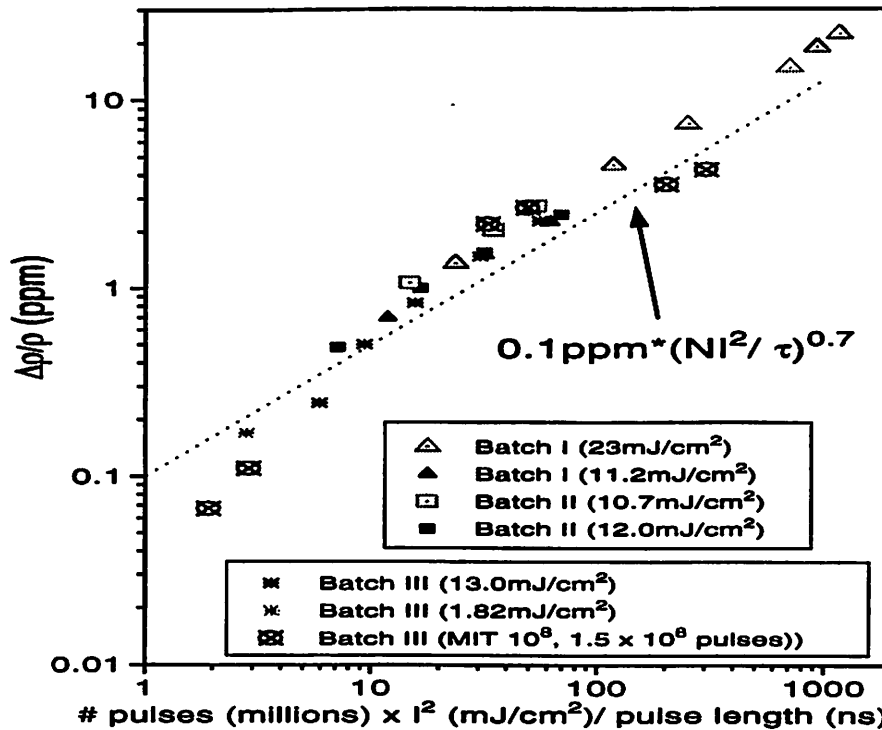
Figure 12a. Unconstrained densification in experimental fused silica D versus number of pulses times the pulse energy density squared divided by pulse length, batches I-III. MIT data are for three individual samples measured after 100 and 150 million pulses.

Figure 12b. Unconstrained densification in experimental fused silica D versus number of pulses times the pulse energy density squared divided by pulse length, batch IV. MIT data points are for three individual samples measured after 100 million pulses.
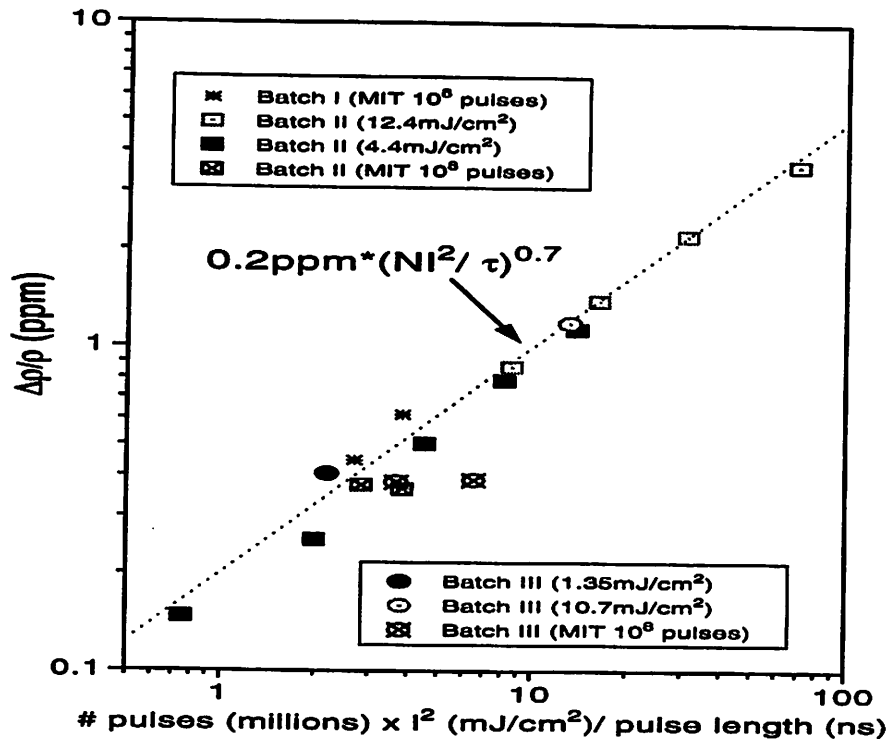
Figure 13. Unconstrained densification in experimental fused silica E versus number of pulses times the pulse energy density squared divided by pulse length. MIT data points are for individual samples.
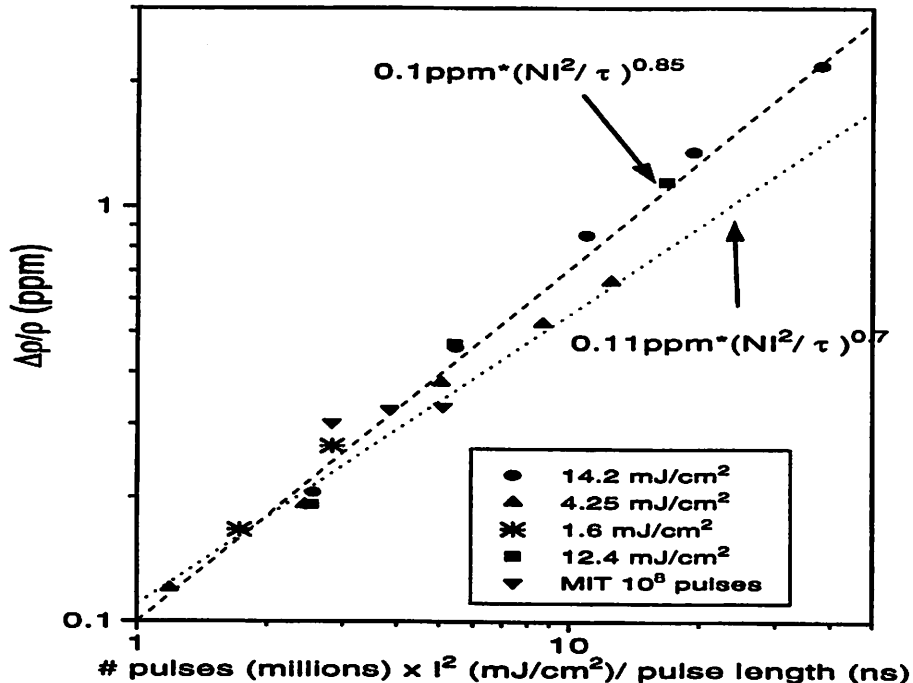
Because all experimental fused silicas and the standard UV-grade fused silicas follow

Equation (1) with similar values for c, we can force c to a single value (0.7) and compare

radiation sensitivity with a single parameter, κ. Table 3 summarizes the compaction rates

for the experimental samples exposed at Berkeley. The extracted value of κ varies from

84ppB to 660ppB among all fused silicas tested. The most durable samples examined

show compaction rates with as much as a factor of two improvement compared to (1990-

1994) grades. Basic statistics were used to determine the experimental error involved in

the measurements. For tests done on the same samples, a standard deviation of 22ppB in

κ was calculated with 9 degrees of freedom. The standard deviation for tests done on

different samples in the same batch was 21ppB with 8 degrees of freedom; indicating that

sample to sample variations in damage rate within a single batch were not statistically significant. Clear batch to batch variations in compaction rates are found for fused silica types A and B where the range of extracted κ values among the batches was much more than four standard deviations. Fused silica types C and D show smaller batch to batch damage rate variability while type E has batch to batch variability less than three standard deviations of sample to sample variability.

The compaction levels measured in the samples exposed at Lincoln Laboratories on average agreed with the Berkeley compaction data. This indicated that the universal relation describing compaction, $(\Delta\rho/\rho) = \kappa * (N * I^2/\tau)^{0.7}$, remained valid in the 100 million pulse regime. However, larger than expected variations between the Berkeley and Lincoln samples were found in some samples, pointing out the need to better standardize calibration and exposure procedures.

Table 3
Compaction Rates of Different Fused Silicas
(Compaction Data fit to $(\Delta\rho/\rho)_u = \kappa (N I^2/\tau)^{0.7}$)

Fused Silica	# Batches Tested	# Samples Tested	κ	
			Mean	Range
1990-1994 Grades	3 Types	8	210ppB	170 - 240ppB
Type A	3	3	490ppB	360 - 660ppB
Type B	2	3	210ppB	130 - 340ppB
Type C	5	6	160ppB	120 - 200ppB
Type D	4	10	140ppB	84 - 190ppB
Type E	2	4	200ppB	180 - 230ppB

6.5 Error Analysis

The most significant sources of experimental error are likely due to differences in 193nm beam profiles and errors in energy density calibration. Variations in laser pulse length may also lead to errors and should be monitored more regularly in future tests. Complications in extracting compaction levels from samples with large levels of intrinsic birefringence also add to the error. Because repeated measurements of birefringence distributions, even months after the initial measurement, yielded almost identical distributions, the actual measurement of birefringence is not considered a significant source of error. Using birefringence distributions to extract compaction levels, furthermore, provides additional accuracy because the birefringence level follows the level of compaction squared. A 4% error in measuring the birefringence distribution would hence only result in about a 2% error in the extracted densification.

Figure 12b, which shows compaction measurements for four different samples in a single batch of type D fused silica, illustrates that errors in extracting a κ value result from more than just experimental errors. The plot shows that despite having nearly identical damage values after dosed of NI^2/τ equal to approximately 3, different κ values are extracted depending on the total dose delivered (dose in units of NI^2/τ). It appears that not all samples exactly follow an $(NI^2/\tau)^{0.7}$ dependence, but rather NI^2/τ to a different exponent.

6.6 Conclusions

Birefringence monitoring is capable of measuring the compaction-induced birefringence distribution in very lightly damaged samples. The ability to measure low compaction levels enables the characterization of compaction at low fluences. The total unconstrained UV-induced density changes ($\Delta\rho/\rho$) can be approximated as $\kappa * (N * I^2/\tau)^{0.7}$ where N is the number of pulses, κ is a constant, τ is the pulse length, and I is the 193-nm energy density. This behavior is consistent with previous compaction studies using electron beam and gamma radiation if one uses the total energy absorbed from two-photon absorption as the dose parameter, suggesting like densification mechanisms for all forms of radiation. Using the measured compaction dependence on pulse count and intensity, one can now properly scale higher energy density tests to predict damage rates of materials at lower fluences. The differences found in compaction rates between different fused silicas is encouraging in that it indicates that more durable materials can be developed.

References

[1] R. Sandstrom, "Progress on the development of a 5 pm line-narrowed 193nm ArF excimer laser for microlithography," presented at Second International Symposium on 193nm Lithography.

[2] D. C. Allan, N. F. Borrelli, C. Smith, T. P. Seward III, "Densification of Fused Silica under 193nm Excitation," presented at Second International Symposium on 193nm Lithography, 1996.

[3] W. Primak, R. Kampwirth, "The Radiation Compaction of Vitreous Silica," Journal of Applied Physics, Vol. 39, No. 12, pp. 5651-5657, Nov. 1968.

[4] P. L. Higby, E. J. Friebele, C. M. Shaw, M. Rajaram, E. K. Graham, D. L. Kinser, E. G. Wolff, "Radiation Effects on the Physical Properties of Low-Expansion-Coefficient Glasses and Ceramics," Journal American Ceramic Society, Vol. 71, No. 9, pp. 796-802, 1988.

[5] P. L. Higby, E. J. Friebele, American Ceramic Society Bulletin, 67, (1988) 615.

[6] E. J. Friebele, P. L. Higby, "Radiation Effects in Amorphous SiO_2 for Windows and Mirror Substrates," in Laser Induced Damage in Optical Materials: 1987, NIST Spec. Pub. 756, pp. 89-97, 1988.

[7] C. B. Norris, E. P. EerNisse, "Ionization dilation effects in fused silica from 2 to 18-keV electron irradiation," Journal of Applied Physics, Vol. 45, No. 9, pp. 3876-3882, Sep. 1974.

[8] M. Rajaram, T. Tsai, E. J. Friebele, "Radiation-Induced Surface Deformation in Low-Thermal-Expansion Glasses and Glass-Ceramics," Advanced Ceramic Materials, Vol. 3, No. 6, pp. 598-600, 1988.

[9] C. I. Merzbacher, E. J. Friebele, J. A. Ruller, P. Matic, "Finite element analysis of deformation in large optics due to space environment radiation," SPIE Vol. 1533 Optomechanics and Dimensional Stability, pp. 222-228, 1991.

[10] T. A. Dellin, D. A. Tichenor, E. H. Barsis, "Volume, index-of-refraction, and stress changes in electron-irradiated vitreous silica," Journal of Applied Physics, Vol. 48, No. 3, pp. 1131-1138, March 1977.

[11] J. E. Shelby, "Radiation effects in hydrogen-impregnated vitreous silica," Journal of Applied Physics, Vol. 50, No. 5, pp. 3702-3706, May 1979.

[12] J. A. Ruller, E. J. Friebele, "The effect of gamma-irradiation on the density of various types of silica," Journal of Non-Crystalline Solids 136, pp. 163-172, 1991.

[13] R. K. Brimacombe, R. S. Taylor, K. E. Leopold, "Dependence of the nonlinear transmission properties of fused silica fibers on excimer wavelength," J. Appl. Phys. 66 (9), pp. 4035-4040, Nov. 1, 1989.

[14] T. E. Everhart, P. H. Hoff, "Determination of Kilovolt Electron Energy Dissipation vs Penetration Distance in Solid Materials," Journal of Applied Physics, Vol. 42, No. 13, pp. 5837-5846, Dec. 1971.

Chapter 7

The Effects of Compaction on Lithographic Imaging

A model optic was evaluated for its susceptibility to compaction damage. Zernike phase aberration terms from compaction in elements near the pupil plane of the system were calculated using Fourier optics while aberrations from other elements were estimated using ray-tracing. Significant distortion and focal shifts at the edge of the image field were predicted from simulations for only a 0.05λ total RMS compaction-induced wavefront aberration. System lifetime was calculated using a compaction scaling rule of $\Delta n/n = 24ppB \times (N * I_o^2/\tau)^{0.7}$ (N is the pulse count in millions, τ is the pulse length in nanoseconds and I_o is the 193-nm energy density in (mJ/cm^2)). Lifetime was found to depend strongly on illumination conditions, image field size, and wafer plane intensity. Lifetimes increased substantially for systems with less source coherence and lower wafer plane intensities.

7.1 Introduction

Lithography steppers and have been predominantly historically "refractive" designs where all the focusing and beam shaping have been achieved by refractive lenses. The bandwidth or range of allowable optical wavelengths with acceptable imaging of all-refractive systems is enlarged by "color correction" achieved by using multiple optical materials with different magnitudes of dispersion or ($\Delta n/\Delta\lambda$). This allows for the use of positive and negative lens combinations which still has positive focusing power after canceling

dispersion[1]. At 193nm, however, only fused silica has enough transmission, surface

quality and homogeneity at this time to be used as an optical material, making chromatic

compensation by use of multiple materials impossible. The dispersion of the refractive

index at 193nm, furthermore, is more than three times worse than at 248nm and five times

worse than at 365nm, additionally reducing the allowed bandwidth. Recently, a

catadioptric design has been patented[2,3] which greatly enlarges the allowed system

bandwidth by using a dielectric aspherical mirror to perform a portion of the system

positive focusing. The mirror is inserted into the optical path of the system by use of a

beam-splitter cube as seen in a typical catadioptric design shown in Figure 1. The design

has additional advantages of being less sensitive to changes in ambient temperature and

pressure. Because of the advanced state of the design of this optic and its attractiveness, it

has been chosen as the model for this study.

Production quality lithographic steppers and scanners are complex, containing dozens of

optical elements and at least a half meter of optical path length through fused silica. This

dissertation will present a prediction of the effects of compaction on imaging based on

approximations of intensity distributions within the optics of a model by use of Fourier and

Statistical optics. Ray-tracing will also be utilized to estimate the aberrations produced by
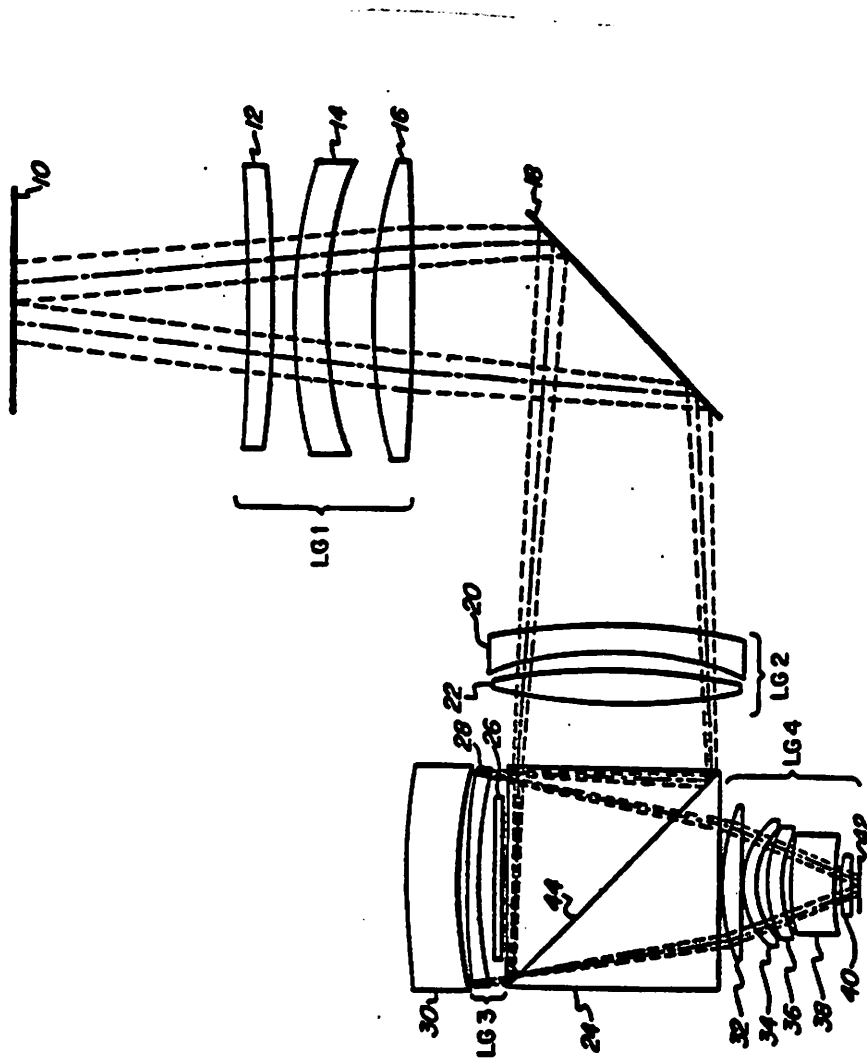
a defined compacted region within the model system.

Figure 1. Illustration of catadioptric lithographic lens design in U. S. Patent 5,212,593 authored by David Williamson of SVG Lithography Systems. The beam-splitting cube (24) allows for the insertion of an aspherical mirror (30) into the beam path.

For this analysis we will assume an optimistic compaction susceptibility given by $(\Delta\rho/\rho)_u =$ 0.15ppm x $(N * I_o^2/ \tau)^{0.7}$ where N is the pulse count in millions, τ is the pulse length in nanoseconds and I_o is the 193-nm energy density in (mJ/cm^2). Using method (2) presented in Chapter 5 for calculating refractive index changes from damage and assuming net density change equal to 80% of the unconstrained compaction, one finds $(\Delta n/n)_{193} =$ 40ppB x $(N * I_o^2/ \tau)^{0.7}$. Since the partial cancellation of compaction-induced OPD's by surface depression formation is not directly accounted for in this analysis, we use an smaller "effective" damage rate to account for compaction-induced shortening of the elements in the system. Assuming that the net OPD is 60% (due to partial cancellation of OPD's from surface depressions) of the OPD predicted by refractive index changes alone, we use an effective $(\Delta n/n)_{193}$ equal to 24ppB x $(N * I_o^2/ \tau)^{0.7}$ for this modeling.

7.2 Model Catadioptric System

A model optical system was used to evaluate the effects on imaging of compaction. The model system, shown in Figure 2, is a simplification of a catadioptric system. The optical diagram shows the beam-splitter "unfolded" and the aspherical mirror modeled by a thin lens. Focal lengths, spacings between elements, and bulk material sizes were selected to best emulate ray-paths within the actual system. The model system has a four times reduction, a 4mm working distance, a 5 by 26mm field size, and is capable of being operated with a numerical aperture of 0.6.
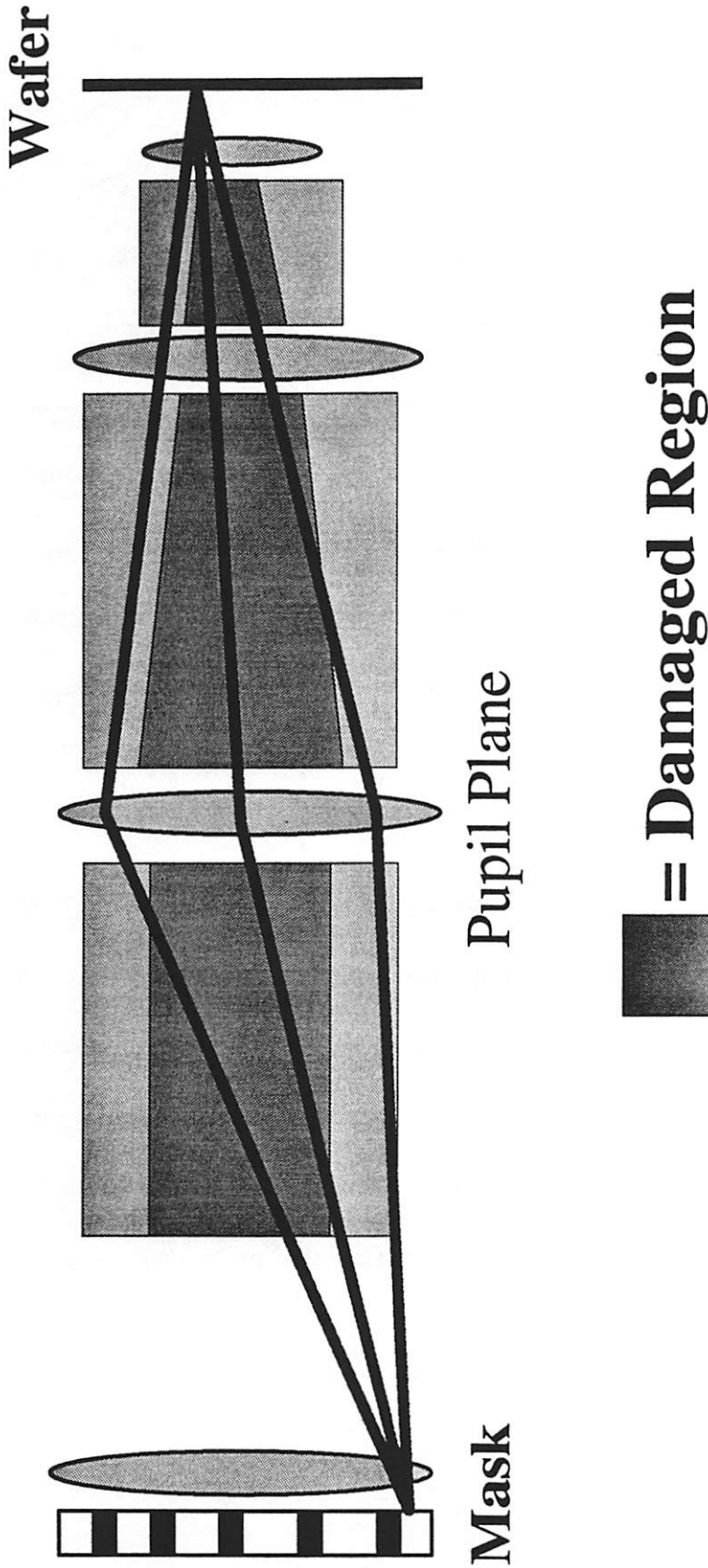
Figure 2. Model optical system for evaluation of compaction on system imaging. The blocks are 18cm, 16cm and 6cm long. The lenses have focal lengths of 45.5cm, 11.9cm, 15.5cm and 15.5cm. The distance from the first lens to the first block is 34cm and the distance from the last lens to the wafer is 4mm. Rays shown are zero, plus one and minus one diffracted orders for minimum sized lines and spaces at the edge of the image field. One of the diffracted orders travels through a large portion of the damaged region while the other travels through mostly undamaged material.

The compaction damage rate at any element in such an optic depends strongly on the "filling" of the element by the optical energy passing through. From the compaction scaling rule presented in Chapter 6, the magnitude of the damage is proportional to (intensity)$^{1.4}$, i.e., (1/(beam diameter))$^{2.8}$. But the impact of the damage depends also on the path length of rays leaving the element going to the image plane. Elements near the pupil are very sensitive to damage, but because of lower intensity, are damaged relatively little. Elements near the wafer, because of high intensity, are damaged more severely, but do not play as key a role in imaging. A Fourier analysis is used to evaluate compaction in elements near the pupil plane while ray-tracing is used to evaluate the effects of compaction in elements near the wafer.

7.3 Damage in Elements near the Pupil Plane

7.3a Calculation of intensity at pupil plane using Fourier optics

Most lithography tools are used with numerous reticles over their lifetime and even over the course of a single day. At first glance it might appear that the intensity distribution within the system optics would significantly change from reticle to reticle and hence make the prediction of the damage profile in the optics excessively complex. However, through much of the optics (near the pupil plane) the intensity follows more closely the spatial frequency distribution of the object being imaged than the object itself. This fact will be utilized to predict the intensity within the optics of a generic system near the pupil plane.

In an ideal imaging system, the exit pupil limits the angular frequency of the waves which compose the image. In a complex system, the pupil planes do not necessary correspond to the location of a physical aperture. The effective pupil planes, however, give the location so as to apply the Fraunhofer diffraction formula to an imaging system. In a lithography system, it is a requirement to have the quality of the image to be uniform across the image field. To achieve this, the allowed angular frequencies must be uniform across this field. This therefore requires the intensity at the pupil plane or angular frequency filter of the system to be independent of location in the image field. In other words, the intensity at the pupil plane only depends on the spatial frequencies of the object and illumination, not on the location of any particular part of the image within the complete image field.

Figure 3 is a diagram of a simplified optical system which will be used to calculate the mutual intensity at the pupil plane. Note, that even though the focal plane of the condenser lens is not at the pupil plane, the pupil plane is the plane where one gets the Fourier transform of the object when using spatially coherent illumination. In fact, as shown by Goodman[4], the Fourier transform always appears in the plane where the source is imaged. It should be stressed that this statement is only valid for full spatial coherence or full spatial incoherence. In the case of partial coherence, a strict Fourier transform plane is not produced in general.
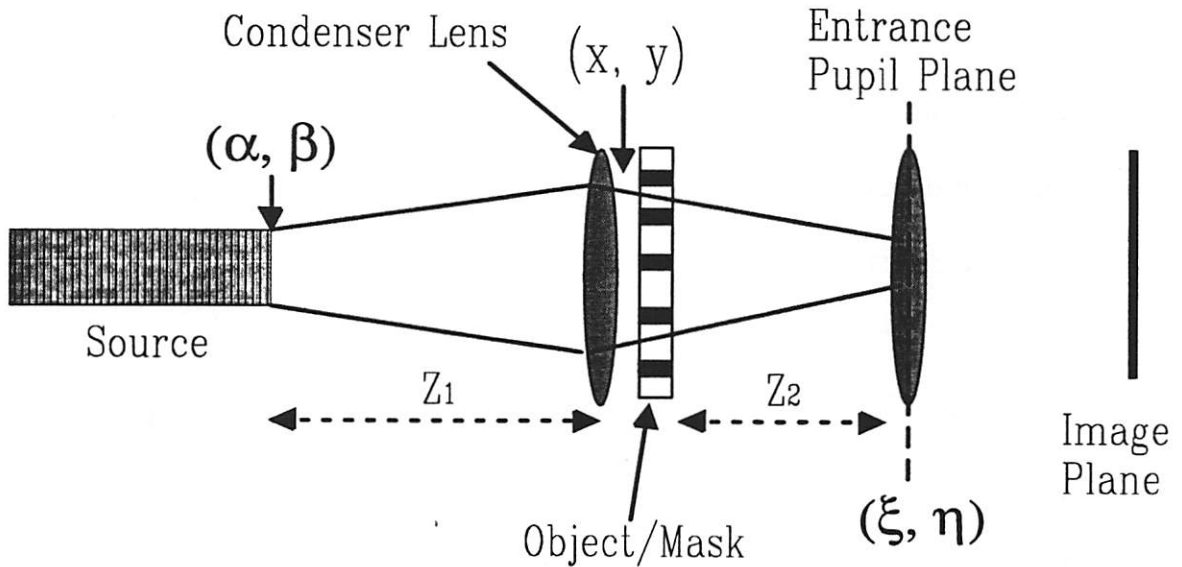
Simplified Optical Reduction System

Figure 3. Simplified illumination system for calculation of mutual intensity at exit pupil plane. The source is imaged onto the pupil plane by the condensor lens.
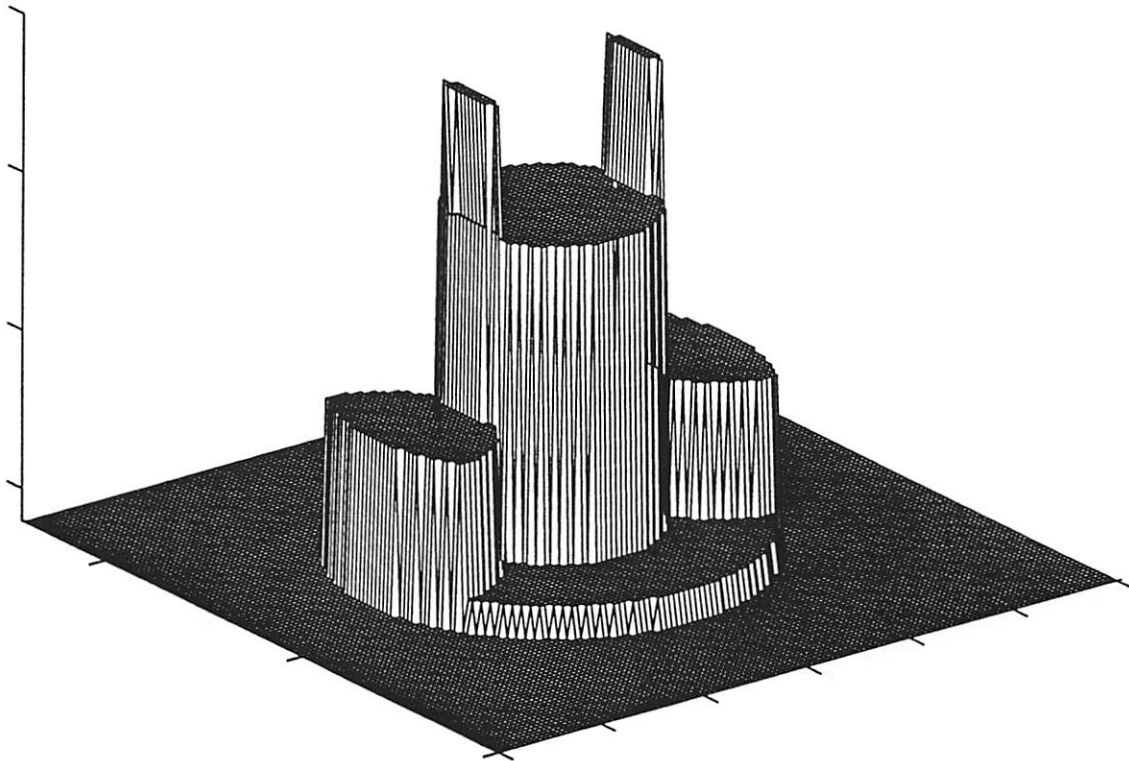

Figure 4. Calculated pupil plane intensity for an object with 0.18um periodic lines and spaces. The sigma of the system is 0.5, the numerical aperature is 0.6, and the wavelength is 193nm.

Using the above concepts, if an object were illuminated by a coherent point source, the intensity distribution at the pupil would simply be the Fourier transform of the reticle squared. If an illumination source of a partially coherent lithography system is approximated as a collection of independent coherent input sources, it is intuitive to predict that the pupil intensity distribution would be given by the convolution of the source and the transform of the reticle squared. This is derived below.

The coordinate systems to be used in this section defined are defined in Figure 3. The light source is assumed to be quasi-monochromatic and to have a small enough coherence area to be considered spatially incoherent. In practice, such a source can be produced using a diffuser or "fish-eye" lens array when the diffusing elements are very small. Under this approximation, the mutual intensity at the source will be taken as:

$$J_1(\Delta\alpha, \Delta\beta) = \kappa \bullet \delta(\Delta\alpha, \Delta\beta) \tag{1}$$

where κ is the source intensity and δ represents a delta function. Throughout this section the a paraxial approximation will be applied to the Van Cittert-Zernike theorem[5] so that its form that will be applied here is:

$$J(x_1, y_1, x_2, y_2) = \frac{e^{-j\psi}}{(\lambda z)^2} \cdot \iiint J(x_1, y_1, x_2, y_2)_o \bullet \exp\{-j\frac{\pi}{z\lambda} \cdot [(\xi_2^2 + \eta_2^2) - (\xi_1^2 + \eta_1^2)]\} \bullet$$

$$\bullet \exp\{j\frac{2\pi}{\lambda z} \cdot [x_2 \cdot \xi_2 + y_2 \cdot \eta_2 - x_1 \cdot \xi_1 - y_1 \cdot \eta_1]\} \bullet d\xi_1 \cdot d\xi_2 \cdot d\eta_1 \cdot d\eta_2 \tag{2}$$

where z is the propagation distance and ψ equals $\frac{\pi}{\lambda \cdot z}[(x_2^2 + y_2^2) - (x_1^2 + y_1^2)]$. Using the

Van Cittert-Zernike theorem for propagation of mutual intensity the mutual intensity

impinging upon the condenser lens is given as:

$$J_l(x_1, y_1, x_2, y_2) = \frac{\kappa}{(\lambda \cdot z_1)^2} \cdot \exp\{-j\frac{\pi}{\lambda \cdot z_1}[(x_2^2 + y_2^2) - (x_1^2 + y_1^2)]\} \cdot \mathfrak{I}_s(\frac{\Delta x}{\lambda \cdot z_1}, \frac{\Delta y}{\lambda \cdot z_1}) \quad (3)$$

where z_1 is the source condenser lens spacing, and $\mathfrak{I}$ is the scaled Fourier transform of the

source evaluated at the spatial frequencies or

$\iint I_s(\alpha, \beta) \bullet \exp\{j\frac{2\pi}{\lambda z_1} \cdot [\Delta x \alpha - \Delta y \beta]\} \bullet d\alpha \cdot d\beta$. Δx equals $(x_2 - x_1)$. The condenser lens

and object (reticle) modify the mutual intensity by direct phase and amplitude shifts. The

mutual intensity exiting the object is given by:

$$J_o' = J_1 \cdot |P_c(x,y)|^2 \cdot t_o(x_1, y_1) \cdot t_o(x_2, y_2) \cdot \exp\{j\frac{\pi}{\lambda \cdot f}[(x_2^2 + y_2^2) - (x_1^2 + y_1^2)]\} \quad (4)$$

where t_o is the object amplitude transmission function, f is the focal length of the

condenser lens, and $P_c(x, y)$ is the complex lens transmission function. Here it is assumed

that incident mutual intensity was narrow in $(\Delta x, \Delta y)$ so that $P_c(x_1, y_1) \bullet P_c(x_2, y_2)^*$ could

be approximated as $|P_c(x, y)|^2$. The condenser lens will be assumed to be large enough so

that this term can be ignored. The pupil plane mutual intensity is found by applying the

Van Cittert-Zernike theorem again:

167

$$J_p(\xi_1,\eta_1,\xi_2,\eta_2) = \kappa' \cdot \iint \iint t_o(x_1,y_1) \cdot t_o(x_2,y_2) \bullet \exp\{j\frac{\pi}{\lambda} \cdot (\frac{1}{f}-\frac{1}{z_1}-\frac{1}{z_2})[(x_2^2+y_2^2)-(x_1^2+y_1^2)]\} \bullet$$

$$\Im_s(\frac{\Delta x}{\lambda \cdot z_1},\frac{\Delta y}{\lambda \cdot z_1}) \bullet \exp\{j\frac{2\pi}{\lambda z_2} \cdot [x_2 \cdot \xi_2 + y_2 \cdot \eta_2 - x_1 \cdot \xi_1 - y_1 \cdot \eta_1]\} \bullet dx_1 \cdot dx_2 \cdot dy_1 \cdot dy_2 \quad (5)$$

where κ' groups together constant terms. The expression is simplified by noting that the first exponential reduces to unity when the pupil plane is at the image plane of the source. The intensity at the pupil plane is the mutual intensity reduced to a single point and is now given as:

$$I_p(\xi,\eta) = \kappa' \cdot \iint \iint \Im_s(\frac{\Delta x}{\lambda \cdot z_1},\frac{\Delta y}{\lambda \cdot z_1}) \bullet t_o(x_1,y_1) \cdot t_o(x_2,y_2) \bullet$$

$$\bullet \exp\{j\frac{2\pi}{\lambda z_2} \cdot [(x_2-x_1) \cdot \xi + (y_2-y_1) \cdot \eta]\} \bullet dx_1 \cdot dx_2 \cdot dy_1 \cdot dy_2 \quad (6)$$

Expanding all terms and using the change of variables $(\alpha', \beta') = (z_2/z_1) * (\alpha, \beta)$ this equation becomes:

$$I_p(\xi,\eta) = \kappa'' \cdot \iint \iint \iint I_s(\alpha', \beta') \bullet t_o(x_1,y_1) \cdot t_o(x_2,y_2) \bullet$$

$$\bullet \exp\{j\frac{2\pi}{\lambda z_2} \cdot [(x_2-x_1) \cdot (\xi+\alpha') + (y_2-y_1) \cdot (\eta+\beta')]\} \bullet d\alpha' \cdot d\beta' \cdot dx_1 \cdot dx_2 \cdot dy_1 \cdot dy_2 \quad (7)$$

Rearrangement of the integration order gives:

$$I_p(\xi,\eta) = \kappa'' \cdot \iint d\alpha' \cdot d\beta' \cdot I_s(\alpha',\beta') \cdot$$

$$\iint dx_1 \cdot dy_1 \cdot t_o(x_1,y_1) \cdot \exp\{-j\frac{2\pi}{\lambda z_2} \cdot [x_1 \cdot (\xi + \alpha') + y_1 \cdot (\eta + \beta')]\} \cdot$$

$$\iint dx_2 \cdot dy_2 \cdot t_o(x_2,y_2) \cdot \exp\{j\frac{2\pi}{\lambda z_2} \cdot [x_2 \cdot (\xi + \alpha') + y_2 \cdot (\eta + \beta')]\} \quad (8)$$

By definition of the Fourier transform this is simply:

$$I_p(\xi,\eta) = \kappa'' \cdot \iint d\alpha' \cdot d\beta' \cdot I_s(\alpha',\beta') \cdot \Im^*(\frac{\xi+\alpha'}{\lambda z_2},\frac{\eta+\beta'}{\lambda z_2}) \cdot \Im(\frac{\xi+\alpha'}{\lambda z_2},\frac{\eta+\beta'}{\lambda z_2}) \quad (9)$$

Using the definition of convolution this becomes:

$$I_p(\xi,\eta) = \kappa'' \cdot \{I_s(\xi,\eta) \otimes \left|\Im(\frac{\xi}{\lambda z_2},\frac{\eta}{\lambda z_2})\right|^2\} \quad (10)$$

where the symbol $\otimes$, denotes the convolution function, and $I_p(\xi,\eta)$ is the geometric optics projection of the source onto the pupil. Equation 10 is equivalent to the convolution of the (z_2/z_1) magnified source with the squared magnitude of the transform of the object transmission function.

Sigma is generally defined as the ratio of allowed spatial frequencies by the illumination to those allowed by the imaging optics. In this geometry of Figure 3, the sigma of the system is equal to z_2/z_1 multiplied by the ratio of the source to entrance pupil radii. This is found easily by noting that the half spread of angles incident upon the object at any point is approximately $((x + R_s)/z_1) - (x/z_1)$ or R_s/z_1, where R_s is the radius of the source. Likewise, the allowed angular spread at the pupil is R_p/z_2.

Figure 4 shows a sample intensity distribution at the pupil plane for a 193-nm system with a sigma of 0.5 and a reticle with 0.18um periodic lines and spaces. For an NA of 0.6, the center of the first diffracted orders are at 0.90 of the radial distance to the pupil cutoff as calculated by:,

$$F_{1/-1} = \lambda / (P * NA) \tag{11}$$

where P is the mask period, 0.36um in this case.

The normalized one dimensional transform of a periodic line and space mask is equal to:

$$\sin c(\frac{\xi}{\lambda \cdot z_2 \cdot w_l}) \bullet \delta\left[\frac{\xi}{\lambda \cdot z_2} - \frac{n}{4} \cdot (w_l + w_s)\right] \tag{12}$$

where n is an integer, w_l is the line width and w_s is the space width. Squaring the magnitude the transform one finds the intensity of the first diffracted orders to be

approximately 0.41 that of the zero or undiffracted order. For a pattern with equal line and space dimensions, the second diffracted order falls on the first zero of the sinc envelope. As seen in Figure 4, parts of the first diffracted orders overlap the DC order while other parts are cutoff by the NA of the system. The other diffracted orders are completely cut off by the finite NA of the system. Reticles used in production, of course, contain many types of features with a wide spectrum of spatial frequencies. While the spectra will vary from mask to mask, the consistent feature among almost all pupil plane intensity patterns for systems with conventional illumination will be a peak intensity at the center of the pupil resulting from contributions from the zero order and low frequency diffracted orders.

Figure 5 shows a generic mask with several feature types including periodic lines and spaces of different pitch and period, isolated lines, contact holes of different sizes, and elbow and straight interconnect lines. The mask is predominantly transparent, with only 30.55% of the surface being opaque. Figure 6 shows the FFT of this mask as calculated by Matlab. The DC spatial frequency component dominates the spectrum, being nearly ten times larger than any other frequency component. Figure 7 shows the convolution of the FFT squared with a circular source with a sigma of 0.5. The intensity pattern resembles the clear field pattern which would simply be the intensity distribution of the source. Figure 8 shows the calculated intensity pattern at the pupil for the same reticle but with an annular illumination source with an outer sigma of 0.7 and an inner sigma of 0.5.
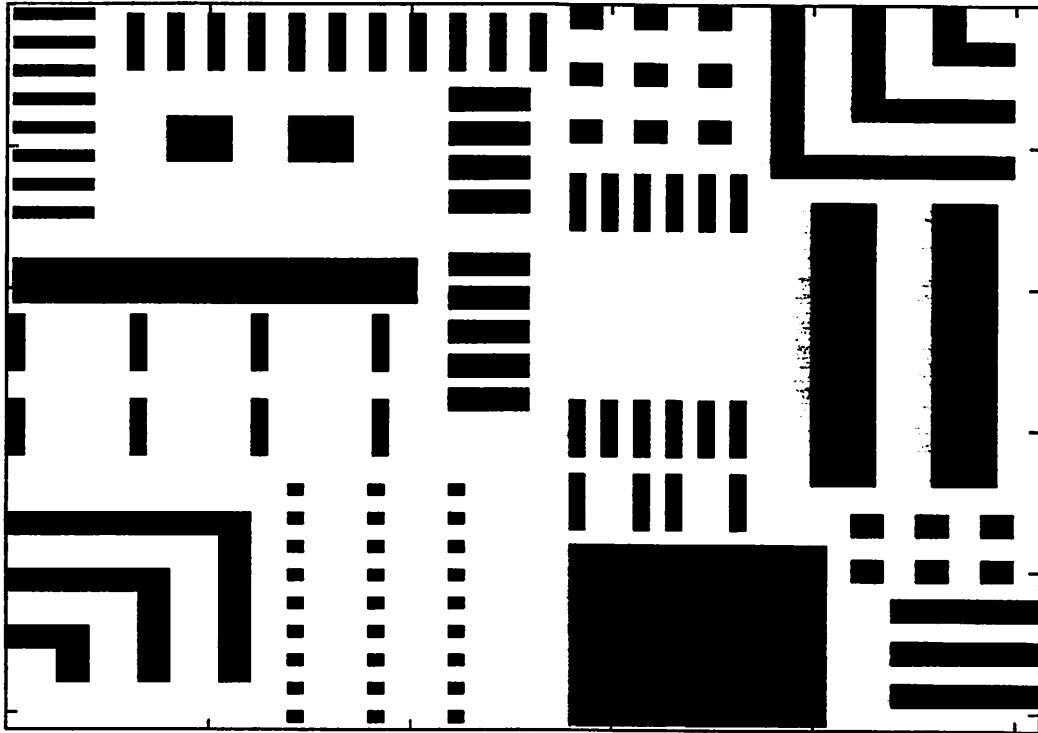
Figure 5. Generic reticle used for pupil plane intensity calculations. The smallest size of any feature is 0.18um.
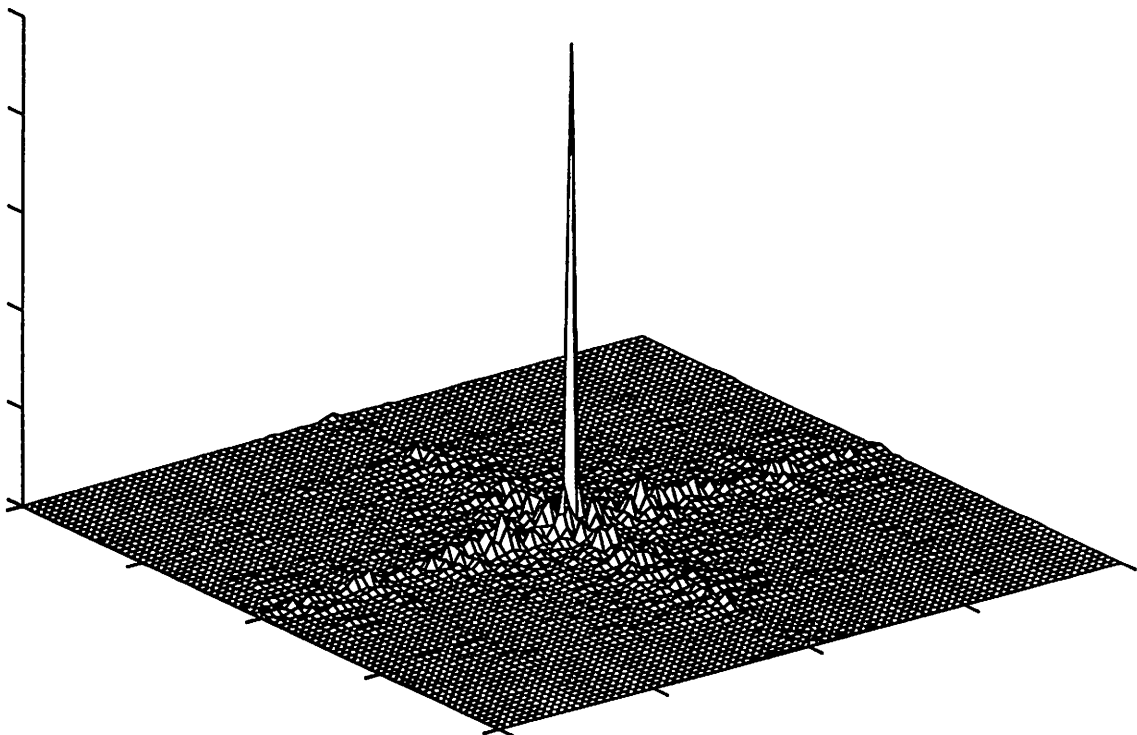
Figure 6. Two dimensional Fourier transform of generic mask.

172

Figure 7. Calculated pupil plane intensity with generic reticle and a sigma of 0.5, NA of 0.6, and wavelength of 193nm. Intensity is in arbitrary units and the pupil edge corresponds to the circle where the intensity falls to zero.

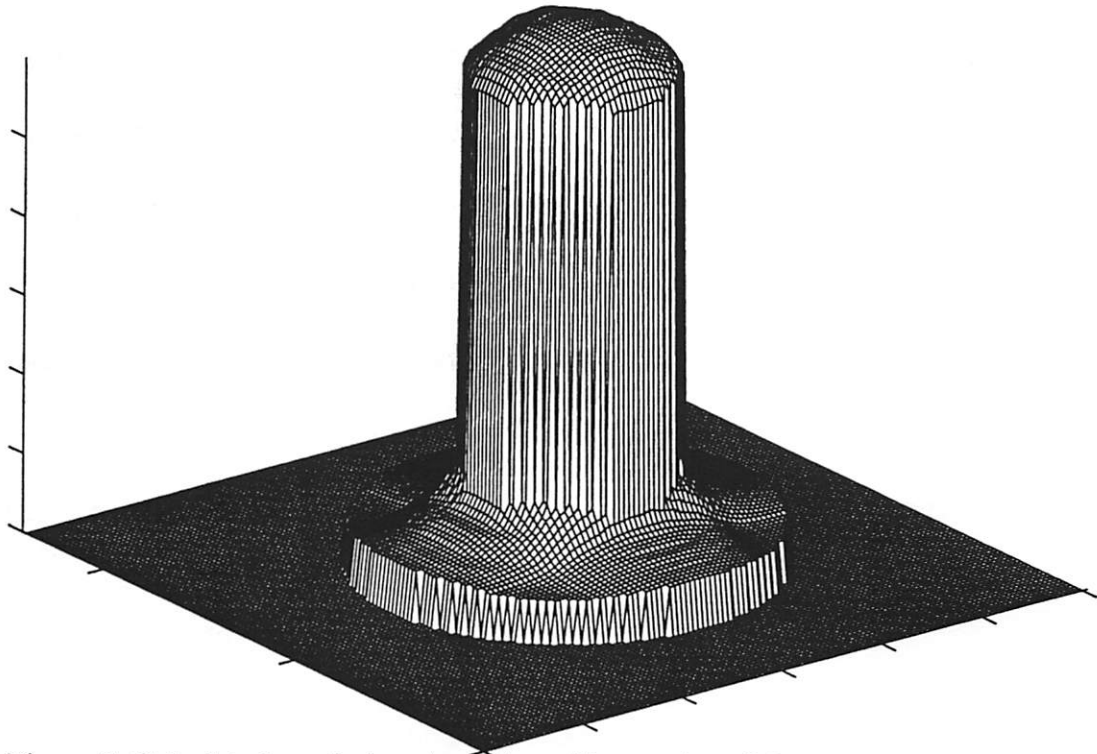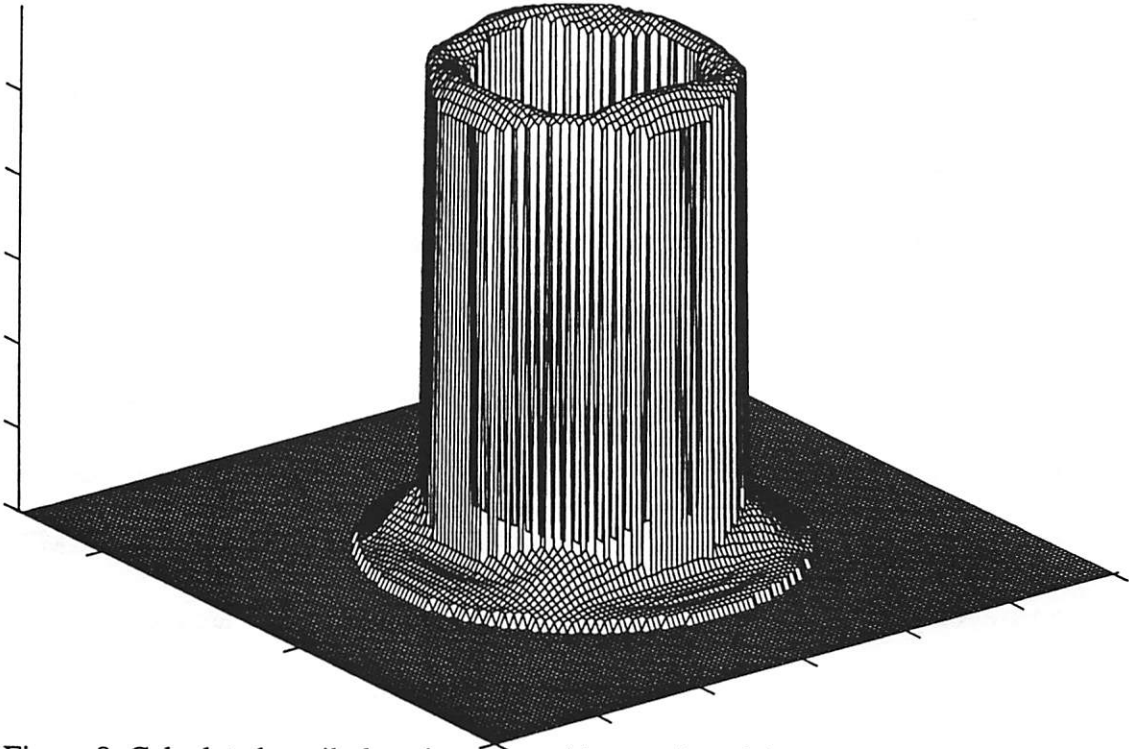Figure 8. Calculated pupil plane intensity with generic reticle and an annular illumination source with an inner sigma of 0.5 and an outer sigma of 0.7, NA of 0.6, and wavelength of 193nm.

Again, the intensity pattern follows closely the source intensity distribution. In both cases, relatively little energy is contained in the diffracted orders compared to the undiffracted DC component of the distribution. It appears, therefore, that the intensity distributed at the pupil does not have a strong dependence on the reticle used, only on the illumination source. This fact makes the task of predicting the long term effects of compaction in elements near the pupil more reasonable since the precise mask patterns being used are not needed to calculate pupil plane intensities. The role of the mask for such elements is only an attenuator whose value is approximately equal to the ratio of dark pattern area to total area on the reticle.

7.3b Aberrations from Pupil Plane Compaction

Given the intensity at the pupil plane, it is straightforward to calculate to system aberrations induced from compaction in elements near the pupil plane. From the compaction scaling rule presented in Chapter 6, the compaction distribution is proportional to the intensity distribution to the 1.4 power. The phase aberration distribution is therefore the pupil plane intensity distribution to the 1.4 power. The first seven radially symmetric Zernike[6] aberration terms are fit to the previously calculated intensity distributions to the 1.4 power for the three illumination sources and the generic reticle. Zernike polynomials serve as a useful method for describing aberrations, because the sum of the magnitudes of the normalized Zernike coefficients is the total RMS aberration in the system due to the property that the polynomials are orthonormal. Table 1a lists the Zernike aberration terms calculated for compaction after 1 billion pulses (τ =

11ns) at the pupil plane with a peak intensity of 1-mJ/cm^2 and an optical path length through fused silica of 30cm.

Table 1a
Induced wavefront aberrations* in waves (λ = 193nm) from compaction in elements near the pupil plane for single beam pass (30cm total path length)

Zernike Term	Aberration Type	$\sigma = 0.5$	$\sigma = 0.7$	$\sigma = 0.5 - 0.7$
1	Piston	0.38 λ	0.64 λ	0.34 λ
$\sqrt{3}(2\rho^2 - 1)$	Defocus	-0.40 λ	-0.57 λ	-0.14 λ
$\sqrt{5}(6\rho^4 - 6\rho^2 + 1)$	Spherical	0.27 λ	0.03 λ	-0.25 λ
$\sqrt{7}(20\rho^6 - 30\rho^4 + 12\rho^2 - 1)$	2nd Spherical	-0.02 λ	0.16 λ	0.29 λ
$\sum$ | higher order terms|	Higher Spherical	0.12 λ	0.01 λ	0.34 λ

*assumes 1 billion pulses (11ns) with peak pupil plane intensity of 1-mJ/cm^2.

For a given image pattern, aberrations at the pupil plane effect the imaging of all points in the image field equally. The defocus induced from compaction near the pupil plane is easily removed from a lithography system by adjusting the wafer position. Piston does not effect imaging. The sum of the magnitudes of the remaining aberrations ("uncorrectable" aberrations) which effect imaging are 0.41λ, 0.20λ and 0.88λ for (σ = 0.5), (σ = 0.7) and annular illumination cases respectively. Despite having the same peak pupil plane intensity, the magnitude of the total "uncorrectable" phase aberrations varied by over a factor of four among the three illumination sources. The (σ = 0.7) case produces the least uncorrectable aberrations because the phase distribution resulting from the compaction associated with a (σ = 0.7) "filling" of the pupil most closely follows the phase distribution corresponding to defocus.

Since all lithography systems have a large amount of optical path near the pupil plane, it is worthwhile to predict system lifetime limited by pupil plane compaction alone. We define lifetime as the time to induce 0.05λ total RMS phase aberrations (not including defocus or piston). It will be demonstrated later that this level of damage substantially effects image fidelity. To predict lifetime for a system with conventional illumination, we first estimate the pupil plane intensity by the following equation:

$$I_{pupil} = \frac{I_{wafer} \cdot A_f \cdot T_{pw}}{\pi \cdot (\sigma D_{pp} / 2)^2 \cdot T_{mask}} \tag{13}$$

where I_{wafer} is the clear field wafer plane pulse energy density, T_{mask} is the mask pattern transmission, T_{pw} is the transmission from the pupil plane to the wafer plane, A_f is the area of the image field and D_{pp} is the pupil plane diameter.

System lifetime will be calculated using an optimistic compaction scaling rule of $\Delta n/n = 24ppB \times (N * I_o^2 / \tau)^{0.7}$ (N is the pulse count in millions, τ is the pulse length in nanoseconds and I_o is the 193-nm energy density in (mJ/cm^2)). As explained in the introduction to this chapter, this compaction scaling rule is analogous to assuming a densification rate of $(\Delta\rho/\rho)_a = 0.15ppm \times (N * I_o^2 / \tau)^{0.7}$. A 1000Hz laser fires over 86 million pulse per day (~32 billion per year). Using this pulse rate, the previously described compaction scaling, and assuming that 50 pulses per field are required for a uniform

exposure (resist sensitivity equals 50 I_{wafer}), the lifetime limited by pupil plane compaction for a system is given as follows:

$$\text{Lifetime} = \beta_\sigma \left\{ \left(\frac{\tau}{1\,\text{lns}}\right) \cdot \left(\frac{50\text{mJ}/\text{cm}^2}{J_o}\right)^2 \cdot \left(\frac{1.3\text{cm}^2}{A_f}\right)^2 \cdot \left(\frac{30\text{cm}}{L}\right)^{\left(\frac{1}{0.7}\right)} \cdot \left(\frac{D_{PP}}{15\text{cm}}\right)^4 \frac{(T_{PW}/0.78)^2}{T_{mask}^2 \cdot U_{eff}} \right\}$$

$$\beta_\sigma = \begin{cases} 1.1\ \text{years} \quad \text{---} \quad (\sigma = 0.5) \\ 11.5\ \text{years} \quad \text{---} \quad (\sigma = 0.7) \\ 0.33\ \text{years} \quad \text{---} \quad (\sigma = 0.5\text{-}0.7) \end{cases} \qquad (14a)$$

where L is the optical path length through fused silica and J_o is the resist sensitivity. U_{eff} is the usage efficiency of the system which, by definition, is less than one.

The ($\sigma = 0.5$) "filling" not only produces a phase distribution corresponding to higher levels of uncorrectable aberrations than the ($\sigma = 0.7$) case, but also produces a high pupil plane intensity (for a given wafer plane intensity); resulting in the large difference between the lifetime predictions for the ($\sigma = 0.5$) and ($\sigma = 0.7$) cases. We will extend our analysis next to emphasize the effects of damage on the model system where "folding" of the beam path and damage in elements near the wafer plane (much higher intensity) reduce the above lifetime predictions. While the effects on lifetime from optical path "folding" and damage in elements close to the image plane depend upon the specific design of a system, the above analysis is applicable to almost any lithographic tool and can be considered a "best-case" prediction.

7.3c The effects of path "folding" on system damage

In our model catadioptric system, the beam path is "folded" by a beam-splitting cube which is positioned near the pupil plane. Because of the "folding" of the beam at the center of the cube and the reflection of the beam back through the cube, the intensity distribution is less uniform than suggested by Figure 2. In fact, as illustrated in Figure 9, some areas of the cube will have three passes of the beam while others will have only one. We may approximately model this multi-path effect on damage by passing various rays of the single pass intensity distribution (Figure 7) through the beam-splitter, keeping track of distance traversed in the 1X, 2X, and 3X intensity regions. To calculate the phase errors introduced by the beam-splitter, the damage-effective distribution was found for various rays ranging from the chief ray to the extreme rays. The phase error is proportional to the intensity to the 1.4 power times the path length.

The polarization of the beam is rotated by 90 degrees after a double pass through a quarter waveplate positioned in front of the aspherical mirror. Because the polarization of the second pass through the beam-splitter is orthogonal to the initial pass it is not immediately apparent that the intensity in the cross-over region is simply two or three times that of a single pass. By keeping track of the electric fields this, however, can be shown in a straightforward manner. The electric field of the input beam, the beam after
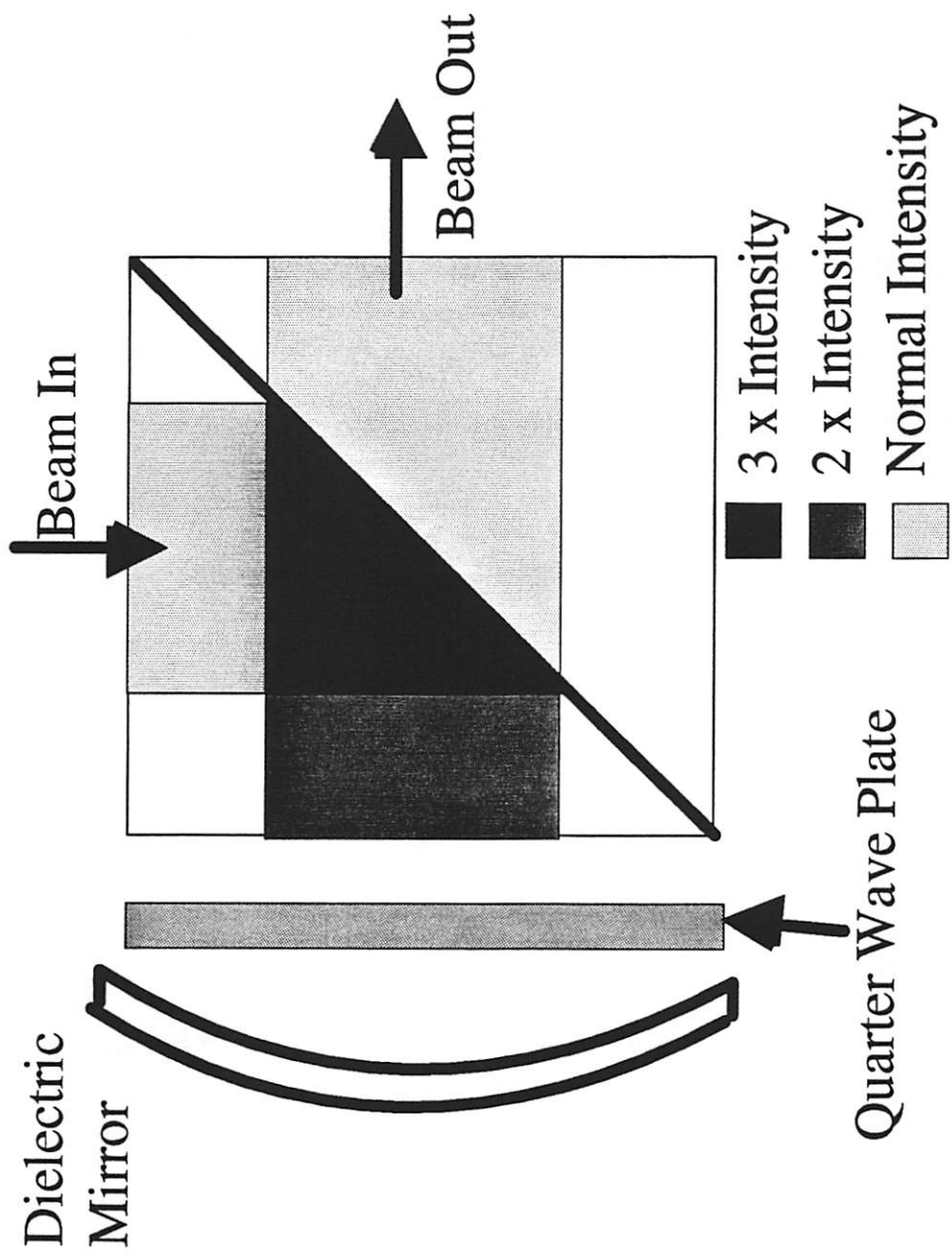
Figure 9. Simplified beam path through beamsplitter cube of catadioptric system. The ratio of beam width to cube width is approximately equal to the illumination sigma.

reflection off the beam-splitter, and after output beam can be represented as follows:

$$\vec{E}_1 = E_o \cdot \vec{z} \cdot \exp[j(ky - \omega t)] \qquad (15a)$$

$$\vec{E}_2 = E_o \cdot \vec{z} \cdot \exp[j(kx - \omega t + \phi(t))] \qquad (15b)$$

$$\vec{E}_3 = E_o \cdot \vec{y} \cdot \exp[j(kx + \omega t + \theta(t))] \qquad (15c)$$

where ϕ and θ are random phase differences accounting for the fact that the temporal coherence length of the beam is much shorter than the path lengths between the overlapping beams. The intensity is simply the time average of the squared electric field or:

$$I = \frac{1}{T} \cdot \int_T |\vec{E}|^2 dt \qquad (16)$$

where T is the period. Applying Equation 16 to the center "3X" region in the cube one finds:

$$I = \int_T E_o^2 \{1 + \{\exp[j(kx - \omega t + \phi(t))] + \exp[j(ky - \omega t)]\} \bullet$$
$$\{\exp[j(\omega t - kx - \phi(t))] + \exp[j(\omega t - ky)]\}\} dt. \qquad (17)$$

This simplifies to the following:

$$I = \int_T E_o^2 \{3 + \exp[j(kx - ky + \phi(t))] + \exp[j(ky - ky - \phi(t))]\} dt \qquad (18)$$

Integrating the above yields simply $3E_o^2$ or three times the single pass intensity.

The effective damage distribution was fit by Zernike phase aberration terms by first separating the compaction distribution into four components. The first component was that of the single pass intensity distribution to the 1.4 power which was fit by the first seven radially symmetry Zernike terms as illustrated in Figure 10. The second component was that with "odd symmetry" about the pupil which was fit by the first six tilt or $\cos\phi$ Zernike terms as demonstrated in Figure 11. This component accounted for the side to side asymmetries in the effective damage distribution (using the convention that one is viewing the cube from above in Figure 9). The third component, fit by the first five coma or $\cos2\phi$ Zernike terms, represents the asymmetries in the effective damage distribution from paths at the top and bottom center of the beam compared to those at the sides. At the top and bottom centers of the beams, the width of the beam from a top-down view shrinks to a line so that only 2X and 1X intensity regions are present. The fourth component, fit by the first seven radially symmetry Zernike terms, was needed to account for larger difference between phase degradation between the chief ray and the average of extreme rays resulting from the path folding. The third and fourth component Zernikes were fit to the same radial phase distribution as that of the second (shown in Figure 11) but scaled appropriately. The relative contributions of the four components for sigma of 0.5, for example, were 1, 0.1644, 0. 1728, and (-0.1725).
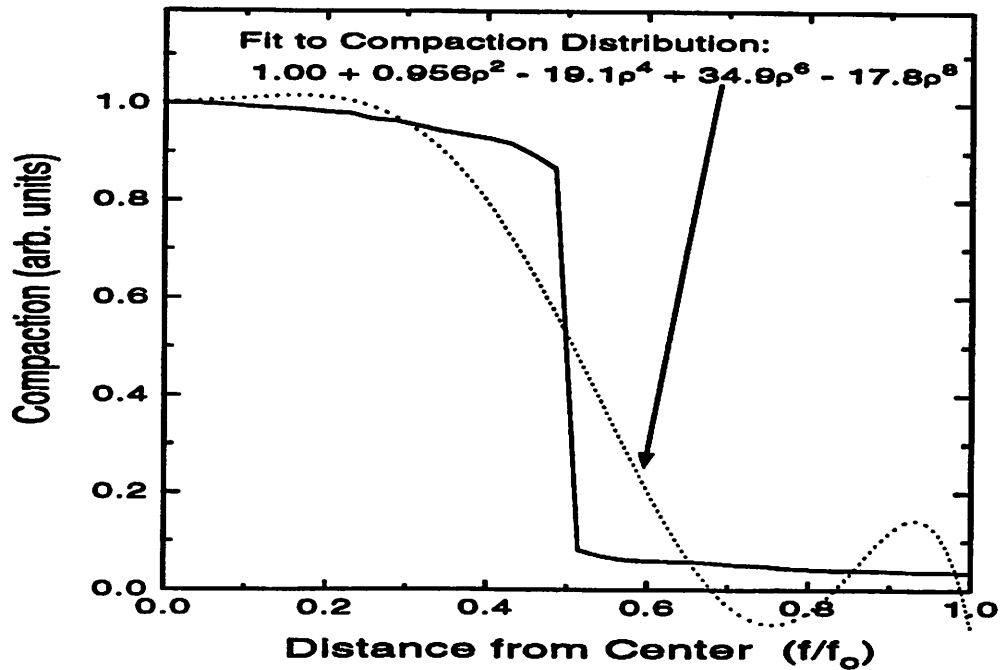
Figure 10. Best fit of radially symmetric Zernike terms to radially symmetric compaction distribution from pupil plane compaction. The compaction distribution is equal to the calculated radial intensity distribution to the 1.4 power.
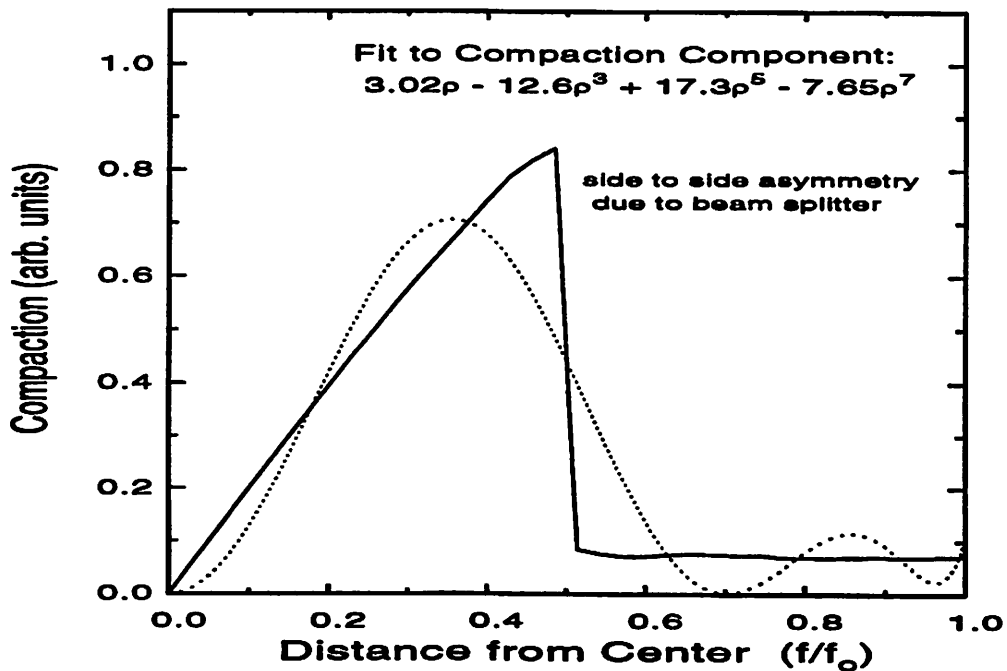
Figure 11. Best fit of tilt Zernike terms ($\cos\phi$) to compaction distribution component resulting from side to side compaction distribution asymmetries. "Folding" of the beam path in the beamsplitter cube produces a non-symmetric intensity and hence compaction distribution.

Figure 12 shows the best fit of the Zernike phase aberration terms as described above to the pupil plane effective intensity distribution to the 1.4 power for a source with sigma equal to 0.5. To relate damage at the pupil to wafer plane intensity, we calculate the damage-effective intensity in the beam-splitter. Using the ratios of pupil plane area to image plane area, the single pass pupil plane intensities are calculated to be 0.045 (σ = 0.5), 0.023 (σ = 0.7) and 0.047 (σ = 0.5 - 0.7) of the average wafer plane intensity (I_o). We account for the higher intensity from "folding" in the cube by tracing the chief ray through the 1X, 2X and 3X intensity regions and then calculating the "effective" intensity that would produce an equal total phase error through the same path length if the intensity were constant throughout the path. The effective damage intensities were estimated to be 0.093 (σ = 0.5), 0.052 (σ = 0.7) and 0.072 I_o (σ = 0.5 - 0.7). Table 1b lists the estimated pupil-plane-compaction-induced Zernike coefficients normalized for 1 million pulses with an average energy density of 1-mJ/cm^2 **at the wafer plane**, and assuming 30cm of path length near the pupil and an effective 193-nm index change rate of $\Delta n/n$ = 24ppB x (N * I^2/τ)$^{0.7}$ and an 11ns pulse length. The magnitude of the Zernike coefficients will scale with the pupil plane compaction or with (N * I_o^2)$^{0.7}$ where N is the pulse count in millions.
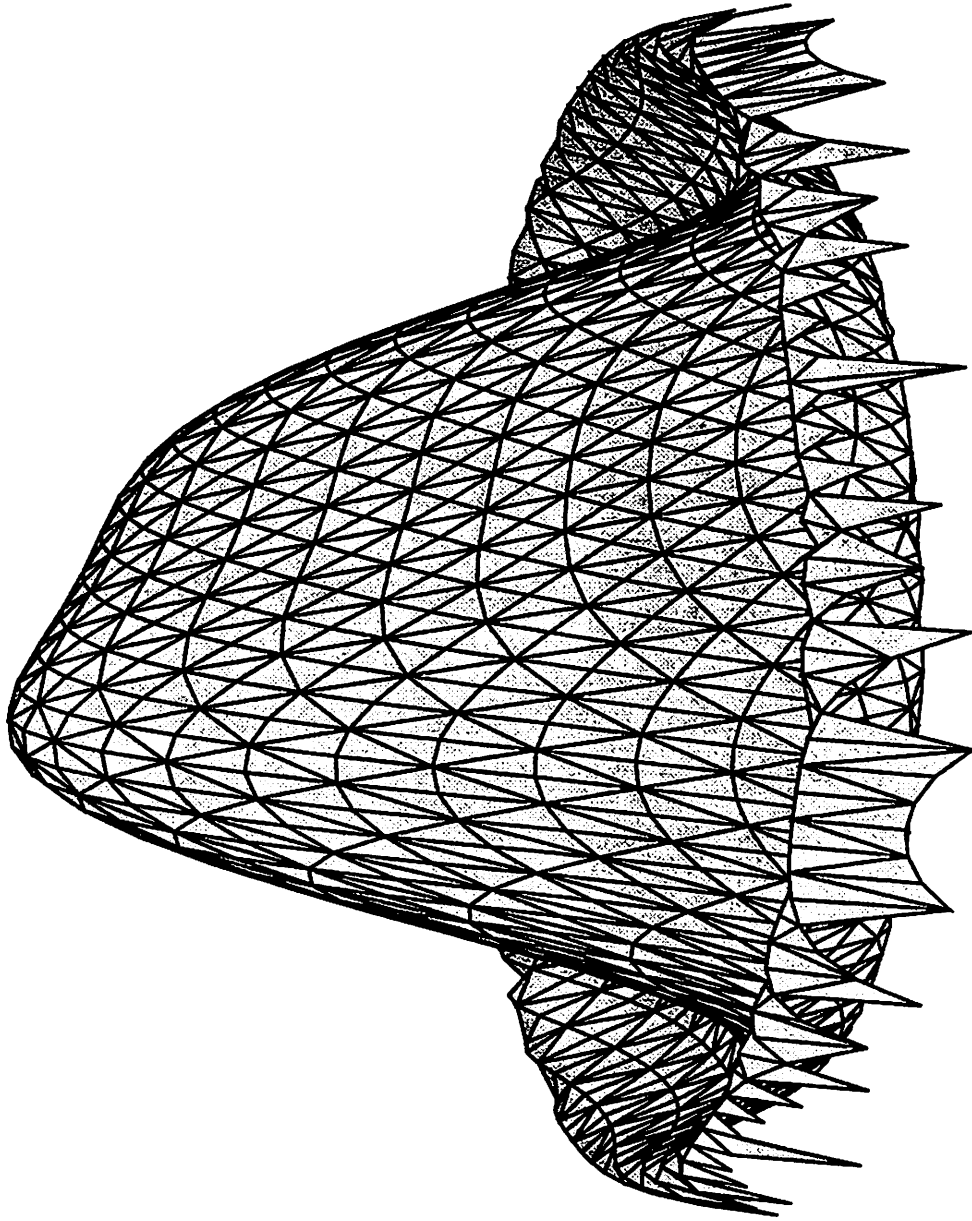
Figure 12. Best fit of first 49 Zernike aberration terms to effective pupil plane compaction distribution (σ=0.5). Asymmetries result from "folding" of beam path in beamsplitting cube.

Zernike Term	Aberration Type	$\sigma = 0.5$	$\sigma = 0.7$	$\sigma = 0.5 - 0.7$
1	Piston	83.3ppm	61.9ppm	-60.2ppm
$2\rho\cos\theta$	Tilt	5.7ppm	5.2ppm	19.1ppm
$\sqrt{3}(2\rho^2 - 1)$	Defocus	-90.6ppm	-58.0ppm	-24.0ppm
$\sqrt{6}\rho^2\cos2\theta$	Astigmatism	4.0ppm	3.9ppm	0.0ppm
$\sqrt{8}(3\rho^3 - 2\rho)\cos\theta$	Coma	-6.9ppm	-7.1ppm	-3.2ppm
$\sqrt{5}(6\rho^4 - 6\rho^2 + 1)$	Spherical	64.3ppm	6.8ppm	-44.5ppm

Zernike Term	$\sigma = 0.5$	$\sigma = 0.7$	$\sigma = 0.5-0.7$
$\sqrt{10}(4\rho^4 - 3\rho^2)\cos2\theta$	-5.8ppm	-7.3ppm	0.0ppm
$\sqrt{12}(10\rho^5 - 12\rho^3 + 3\rho)\cos\theta$	7.0ppm	2.5ppm	4.7ppm
$\sqrt{7}(20\rho^6 - 30\rho^4 + 12\rho^2 - 1)$	-7.5ppm	12.1ppm	52.5ppm
$\sqrt{14}(15\rho^6 - 20\rho^4 + 6\rho^2)\cos2\theta$	7.4ppm	5.5ppm	0.0ppm
$4(35\rho^7 - 60\rho^5 + 30\rho^3 - 4\rho)\cos\theta$	-3.1ppm	1.8ppm	12.8ppm
$3(70\rho^8 - 140\rho^6 + 90\rho^4 - 20\rho^2 + 1)$	-23.2ppm	2.2ppm	18.7ppm
$\sqrt{18}(56\rho^8 - 105\rho^6 + 60\rho^4 - 10\rho^2)\cos2\theta$	-7.3ppm	-0.5ppm	0.0ppm
$\sqrt{20}(126\rho^9 - 280\rho^7 + 210\rho^5 - 60\rho^3 + 5\rho)\cos\theta$	0.0ppm	-1.0ppm	-3.0ppm
$\sqrt{11}(252\rho^{10} - 630\rho^8 + 560\rho^6 - 210\rho^4 + 30\rho^2 - 1)$	-4.6ppm	1.2ppm	-37.0ppm
$\sqrt{22}(210\rho^{10} - 504\rho^8 + 420\rho^6 - 140\rho^4 + 15\rho^2)\cos2\theta$	3.9ppm	-1.0ppm	0.0ppm
$\sqrt{24}(462\rho^{11} - 1260\rho^9 + 1260\rho^7 - 560\rho^5 + 105\rho^3 - 6\rho)\cos\theta$	0.0ppm	0.0ppm	-6.3ppm
$\sqrt{13}(924\rho^{12} - 2772\rho^{10} + 3150\rho^8 - 1680\rho^6 + 420\rho^4 - 42\rho^2 + 1)$	0.0ppm	0.0ppm	-4.5ppm

The coefficients scale with $(N * I_o^2)^{0.7}$, where N is the number of pulses in millions, I_o is the average 193-nm energy density in mJ/cm^2 at the wafer plane.

The total "uncorrectable" RMS aberrations from pupil plane compaction for $(N * I_o^2)$ equal to unity are 145ppm, 52.9ppm, and 187ppm for σ=0.5, σ=0.7, and annular illumination respectively. Piston, first order tilt, and defocus Zernike coefficients are not included in the sum of total RMS aberrations. Defocus is obviously a correctable term as is tilt because the pupil plane aberrations effect all parts of the field equally. Pure tilt will shift the entire field by an equal amount. The σ=0.5 case yields about three times more

total compaction-induced RMS aberrations than the σ=0.7 case. Re-normalizing the data in Table 1a to one million pulses with an average energy density of 1-mJ/cm^2 at the wafer plane (T_{pw} = 0.78, A_f = 1.3cm^2), the total "uncorrectable" RMS aberrations from a single pass (without folding) through the pupil plane are 42.4ppm, 8.1ppm, and 96.7ppm for σ=0.5, σ=0.7, and annular illumination respectively. Folding of the beam path near the pupil plane acts to increase compaction-induced aberrations by a factor of 2 to 6. With beam path folding, however, system lifetime limited by pupil plane damage becomes less dependent on the illumination source as, without folding, lifetime predictions varied by over about a factor of 35 among systems using the three illumination sources while with folding they vary by about a factor of 6. Using Equation (14) again to describe system lifetime, the following "lifetime" coefficients are now obtained when the effects of "folding" near the pupil plane are considered:

$$\beta_\sigma = \begin{cases} 0.19 \text{ years} & \text{---} & (\sigma = 0.5) \\ 0.79 \text{ years} & \text{---} & (\sigma = 0.7) \\ 0.13 \text{ years} & \text{---} & (\sigma = 0.5\text{-}0.7) \end{cases} \tag{14b}$$

7.4 Damage in Elements near the Wafer Plane

Ray-tracing was used to evaluate the effects of compaction in elements away from the pupil plane within the model system. For simplicity, the fused silica in the model system was assumed to be either compacted or undamaged depending on its location in the system. Owing to the fact that the compacted region at the pupil closely followed the illumination shape, the compacted region at the pupil was taken to be the radius defined by

186

the sigma of the illumination source. The damage region at the wafer was defined to be
that of the field shape. The damage radius between the pupil plane and the wafer was
defined by tracing a ray from the edge of the field at the wafer to the edge of damage
region at the pupil. This was done separately for both field axis directions. For example,
the damage radii were defined as follows for the sigma of 0.5 case:

$$r_d(wide)_I = 3.868 - 0.02489 \cdot Z_1$$
$$r_d(wide)_{II} = 3.42 - 0.06281 \cdot Z_2 \tag{19a-c}$$
$$r_d(wide)_{III} = 2.415 - 0.01627 \cdot Z_3$$

$$r_d(narrow)_I = 2.803 + 0.03428 \cdot Z_1$$
$$r_d(narrow)_{II} = 3.42 - 0.1219 \cdot Z_2 \tag{20a-c}$$
$$r_d(narrow)_{III} = 1.469 - 0.1826 \cdot Z_3$$

where narrow and wide denote the optical radii in the scan and slit directions respectively;

I, II, and III denote the fused silica block in the model system with block I being closest to

the mask; and Z_1, Z_2, and Z_3 denote distances from the front edge of each block. All

distances are in centimeters.

Given the compacted region as specified above, it was straightforward to determine where

rays originating from the mask plane are within the compacted region and hence phase

delayed. The magnitude of that phase delay depended upon the intensity within the optics

which was taken as the average intensity at the wafer scaled by the ratio of the wafer field

area to damage plane area. The illuminated area was approximated by an ellipse whose

major and minor extremes were equal to the damage radii. A 1% energy loss per centimeter of path (accounting for both absorption and reflection losses) was used.

The path length delay for a ray is approximated as the sum of its path delays accumulated from traveling through damaged regions. For a zero order or DC ray at the center of the field ($\sigma = 0.5$), the ray passes through the entire compacted region and has an integrated phase delay in wavelengths ($\lambda = 193$nm) equal to 760ppm $* (N * I_o^2)^{0.7}$. For I_o of 1 mJ/cm^2 and 1 billion pulses, this would predict that the ray would be delayed by about one tenth of a wavelength. Over half the integrated phase delay occurs in the final fused silica block closest to the wafer. Again, a compaction rate of $\Delta n/n = 24$ppB x $(N * I_o^2/ \tau)^{0.7}$ and an 11ns pulse length is assumed.

Rays from both the center and edge of the field are traced to estimate the compaction-induced wavefront error in the model system. Table 2 lists the best fit of the five primary Zernike coefficients to the phase delays calculated from ray-tracing. The spherical and defocus aberration terms from the pupil plane analysis are subtraction from the terms found here so as to avoid accounting for them twice. The astigmatism at the center of the field is a direct result of the image field shape asymmetry which produces an asymmetric compaction profile in the optics. Compaction induces both tilt and coma aberrations at the edge of the field. This is illustrated in Figure 2, where one of the diffracted orders (+1) for periodic minimum sized lines and spaces travels through a large portion of the compacted region while the other diffracted order (-1) essentially travels through only

undamaged material. The defocus and spherical aberration terms are calculated from only elements not included in the previous pupil plane analysis. Higher order aberration terms resulting from damage in elements near the wafer plane cannot be accurately predicted using this simple ray-trace analysis. Unlike aberrations from pupil plane compaction, aberration terms from elements near the wafer depend strongly on field size, shape and element placement.

Table 2
Induced wavefront aberrations* in waves (λ = 193nm) from compaction in optical elements near wafer plane

Zernike Term	Aberration Type	Center of Field		Edge of Field (r = 1.3cm)	
		$\sigma = 0.5$	$\sigma = 0.7$	$\sigma = 0.5$	$\sigma = 0.7$
1	Piston	365ppm	255ppm	214ppm	126ppm
$2\rho\cos\theta$	Tilt	---	---	131ppm	87.5ppm
$\sqrt{3}(2\rho^2 - 1)$	Defocus	-71.8ppm	-18.1ppm	-104ppm	-65.8ppm
$\sqrt{6}\rho^2\cos2\theta$	Astigmatism	61.6ppm	25.6ppm	60.6ppm	42.2ppm
$\sqrt{8}(3\rho^3 - 2\rho)\cos\theta$	Coma	---	---	-11.9ppm	-12.6ppm
$\sqrt{5}(6\rho^4 - 6\rho^2 + 1)$	Spherical	-17.5ppm	0.0ppm	25.6ppm	20.6ppm

*The coefficients scale with $(N * I_o^2)^{0.7}$, where N is the number of pulses in millions, I_o is the 193-nm energy density in mJ/cm^2.

The total "uncorrectable" RMS phase aberrations found from ray-tracing for $(N * I_o^2)$ equal to unity are 261ppm and 211ppm for (σ=0.5) and (σ=0.7) respectively for the model system. Because defocus and tilt varied between the center and edge of the field, the field dependent portions of these aberrations are included in this total.

System lifetime from damage near the wafer plane will be calculated using the compaction scaling rule of $\Delta n/n$ = 24ppB x $(N * I_o^2/ \tau)^{0.7}$ (N is the pulse count in millions, τ is the pulse length in nanoseconds and I_o is the 193-nm energy density in (mJ/cm^2)). The

assumptions of a 1000Hz laser and that 50 pulses per field are required for a uniform exposure (resist sensitivity equals 50 I_{wafer}) are again made. The lifetime limited by compaction in elements away from the pupil plane in the model system is given as follows:

$$\text{Lifetime} = \beta_\sigma \left\{ \left(\frac{\tau}{1\text{lns}} \right) \cdot \left(\frac{50\text{mJ}/\text{cm}^2}{J_o} \right)^2 \cdot \left(\frac{1.3\text{cm}^2}{A_f} \right)^2 \cdot \frac{1}{T_{mask}^2 \cdot U_{eff}} \right\}$$

$$\beta_\sigma = \begin{cases} 0.081 \text{ years} & --- & (\sigma = 0.5) \\ 0.11 \text{ years} & --- & (\sigma = 0.7) \end{cases}$$

(21)

Unlike Equation (14), Equation (21) does not describe the dependence of lifetime on pupil plane diameter (D_{pp}), total optical path length through fused silica (L), or pupil plane to wafer transmission (T_{pw}). Because more damage is caused in elements near the wafer plane, a weaker dependence on D_{pp} and T_{pw} is expected as suggested by the weaker dependence of lifetimes on sigma. The 1%/cm loss assumption is equivalent to choosing T_{pw} equal to 0.78 for the pupil plane lifetime calculations. A similar dependence on path length (L) is expected damage in all elements. Repeating the above ray-tracing analysis on the model system for a wafer to final elements separation (s) of 6mm instead of 4mm shows an increase in system lifetime (limited by damage in elements away from the pupil plane) of only 20%, suggesting that lifetime has a weak dependence on working distance.

7.5 Aerial-image simulations of the effects of aberrations on imaging

"Diffraction-limited" lithography systems[3] often have maximum intrinsic wavefront aberrations much less than 0.05λ. It is unclear, however, how much compaction-induced

190

aberrations a system can tolerate before imaging is substantially degraded. Using the previously derived Zernike aberration terms, Splat[7] version 5.0 is used to simulate the effects compaction on the imaging in the model system. Table 3a lists the change in feature contrast, focal position and feature location (distortion) for minimum sized lines and spaces (0.18um) for 0.05λ and 0.1λ total "uncorrectable" RMS compaction-induced wavefront aberrations at the pupil alone (with folding). Vertical lines and spaces are parallel to the long field direction. Piston, first order tilt, and defocus Zernike coefficients are not included in the sum of total RMS aberrations or the simulations. The maximum contrast drops more gradually with conventional sources with increasing pupil plane aberrations than that with the annular illumination source because many of the conventional phase aberrations could be offset by shifts in focus position. Since the "best focus" depends on feature type, a large focus shift may be equally intolerable to contrast loss.

Table 3a
Simulated effects of pupil plane compaction-induced
wavefront aberrations on imaging (with path "folding")
(0.18um periodic lines and spaces)

RMS Aber.	Feature Align.	Contrast Loss			Focal Shift			Distortion		
		$\sigma=0.5$	$\sigma=0.7$	Annular	$\sigma=0.5$	$\sigma=0.7$	Annular	$\sigma=0.5$	$\sigma=0.7$	Annular
0.05λ	Vert.	0.8%	0.7%	3.1%	40 nm	20 nm	15 nm	0.0 nm	0.0 nm	0 nm
	Hor.	1.4%	0.5%	3.1%	25 nm	-15 nm	10 nm	1.2 nm	3.6 nm	1.9 nm
0.1λ	Vert.	3.2%	2.6%	12.0%	80 nm	40 nm	25 nm	0.0 nm	0 nm	0 nm
	Hor.	5.5%	1.8%	12.1%	50 nm	-25 nm	25 nm	2.4 nm	7.3 nm	3.9 nm

Table 3b lists the change in feature contrast, focal position and feature location (distortion) for minimum sized lines and spaces (0.18um) for a total system 0.05λ and 0.1λ RMS compaction-induced wavefront aberrations at the edge of the field. The total RMS wavefront aberration is the sum of the magnitudes of the normalized Zernike coefficients from ray-tracing and pupil plane analysis not including piston and field independent tilt and defocus. Because defocus and tilt varied between the center and edge of the field, the field dependent portions of these aberrations are included in the simulations and total RMS wavefront aberration. Pupil plane aberrations are an appreciable fraction of the total predicted system RMS aberrations. For a 0.1λ total RMS wavefront aberration, a 21nm and 25nm distortion are predicted at the edge of the field for sigma equal to 0.5 and 0.7 respectively. Such levels of distortion are significant when one considers a typical total overlay budget for a 0.18um technology would be only about 50nm[8]. The variations in focal position (0.12um and 0.15um) are also large portions of the specification limits for a 0.6 NA system. The total RMS aberrations for $(N * L_o^2)$ equal to unity were 448ppm and 264ppm for $\sigma=0.5$ and $\sigma=0.7$ respectively.

Table 3b
Simulated effects of total system compaction-induced
wavefront aberrations on imaging
(0.18um periodic lines and spaces)

RMS Aberration	Location in Image Field	Feature Orientation	Contrast Loss σ=0.5	Contrast Loss σ=0.7	Focal Shift σ=0.5	Focal Shift σ=0.7	Distortion σ=0.5	Distortion σ=0.7
0.05λ	center	Vertical	0.0%	0.0%	30 nm	20 nm	0.0 nm	0.0 nm
	center	Horizontal	0.2%	0.0%	-10 nm	-15 nm	0.5 nm	0.7 nm
	edge (1.3cm)	Vertical	0.3%	0.1%	50 nm	60 nm	0.0 nm	0.0 nm
	edge (1.3cm)	Horizontal	0.5%	0.1%	10 nm	15 nm	10 nm	12.5nm
0.1λ	center	Vertical	0.3%	0.1%	60 nm	35 nm	0.0 nm	0.0 nm
	center	Horizontal	0.6%	0.1%	-20 nm	-30 nm	1.0 nm	1.5 nm
	edge (1.3cm)	Vertical	1.1%	0.5%	100 nm	120 nm	0.0 nm	0.0 nm
	edge (1.3cm)	Horizontal	1.6 %	0.6%	25 nm	35 nm	21 nm	25 nm

7.6 System Lifetime Predictions

Assuming 10 million pulses per day and a 70% clear field mask, Figure 13 shows the estimated system lifetimes using a 0.05λ compaction-induced RMS wavefront aberration lifetime criteria. Assuming a 50% clear field mask would essentially double the lifetime predictions because of the non-linear dependence of compaction on intensity. If a 0.4mJ/cm^2 per pulse wafer energy density were used (50 pulses per field for a resist with a sensitivity of 20mJ/cm^2), one would predict lifetimes of three (σ=0.5) and seven years (σ=0.7) using the 0.05λ wavefront aberration criteria. The relative contribution of pupil plane aberrations limiting system lifetime is higher for lower coherence operation. While the annular illumination case was not analyzed for compaction-induced aberrations in elements away from the pupil plane, it appears from the relatively high pupil plane aberration terms that system lifetime would be even worse if annular illumination were used.
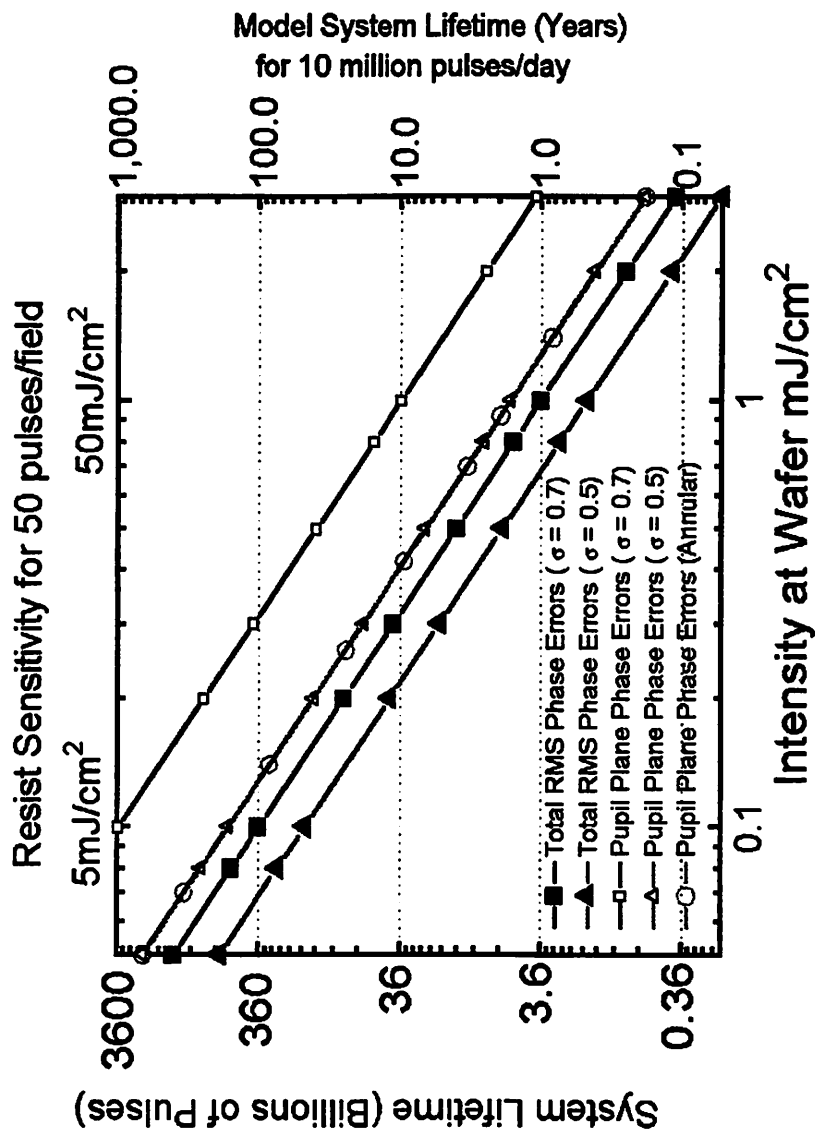
Figure 13. System lifetime predictions versus wafer plane energy density with a 0.05λ total compaction-induced wavefront aberration (field independent defocus and tilt not included) loss criteria assuming a 70% clear field mask and 10 million pulses per day. The optical material is assumed to compact according to the expression $\Delta n/n = 4\text{ppB} \times (N * L_o^2)^{0.7}$.

The maximum change in relative refractive index within the system is only about 350ppB to produce a 0.05λ RMS wavefront aberration (σ=0.5). Despite the fact the pupil plane compaction contributed to over 40% of the total compaction-induced aberrations, only about 20ppB total relative refractive index change is calculated at the pupil for the a 0.05λ RMS wavefront aberration case (σ=0.5). A 1ppm Δn/n lifetime criteria and lower estimated intensities within system optics led to previous system lifetime predictions that were significantly longer[9]. While fused silica is generally only quoted to have 0.5 to 1ppm peak to peak intrinsic homogeneity, the fact that compaction in a lithography system leads to cumulative phase errors makes imaging much more sensitive to compaction-induced refractive index inhomogeneities. One should consider RMS refractive index inhomogeneities when evaluating phase aberrations. It is stressed that these predictions assumed the consistent use of same source and field aperture, changing either over the course of system operation would most likely result in a drop in system lifetime.

7.7 Generalizations about System Lifetime

The lifetime of an actual lithographic system is a complex function of system design and operating conditions. Because of the high relative intensity at the last few elements in the system and the super-linear dependence of compaction rates on intensity, it is natural to concentrate on those elements as the primary area of concern. It has been suggested that if the last few lenses in the system were easily replaceable that the system lifetime could be indefinitely extended at the cost of periodic replacement of those elements. Along the same reasoning, calcium fluoride elements could be used for optics near the wafer plane

195

since the system is less sensitive to material inhomogeneities in those last few elements. These techniques, however, would have limited usefulness, because optics in the system away from the wafer plane contribute significantly to the aberration budget with only modest compaction damage. In fact, in our model system we found about a 50% contribution to the total at ($\sigma = 0.5$) from those elements. The relative contribution to total system aberrations from elements away from the wafer plane, furthermore, will increase substantially for systems with larger image field sizes.

An unequivocal method for increasing lifetime would be to lower the peak optical intensity by increasing the pulse repetition rate and/or using longer laser pulses at lower peak power. For example, doubling the pulse length and halving the intensity would double the system lifetime while keeping throughput constant. The availability of both positive and negative 193-nm resists would create the ability to use only dark field masks in printing. This would lower the energy density within most of the optics without lowering the energy density at a bright area of the image. The use of more sensitive resists would permit a reduction in optical intensities within all the optics, including those near the wafer, while maintaining a constant throughput.

Optical designers already have experience in compensating for environmental-induced changes to the imaging properties of a system such as temperature and pressure variations. In fact, methods for compensating for thermal loading from absorption within optics have already been successfully implemented[10]. Generally defocus and magnification are the

196

only adjustable parameters. Magnification adjustments, in fact, could adjust for much of the compaction-induced distortion predicted above. Development of the ability to compensate for other aberrations from compaction would certainly enhance system lifetime.

7.8 Conclusions

The modeling presented in this chapter indicates that even modest levels of compaction will degrade the imaging of a production lithography system. In fact, tens of parts per billion changes are important for elements in the pupil plane. Despite the much lower relative intensity, damage in elements near the pupil plane are significant along with damage in elements closer to the wafer plane. The above analysis predicts that a resist with high sensitivity (5 - 20 mJ/cm^2) will be needed to insure acceptable 193-nm lithographic system lifetime.

References

[1] concepts such as this are presented in W. J. Smith, *Modern Optical Engineering, The Design of Optical Systems*, Second Edition, 1990.

[2] D. M. Williamson, US Patent # 5,212,593.

[3] D. M. Williamson et. al., "Micrascan III, 0.25um resolution step and scan system," SPIE vol. 2726, Optical Microlithography IX, 1996.

[4] J. W. Goodman, *Introduction to Fourier Optics*, Second Edition, 1995.

[5] J. W. Goodman, *Statistical Optics*, Second Edition, 1985.

[6] V. N. Mahajan, "Zernike Circle Polynomials and Optical Aberrations of Systems with Circular Pupils," Supplement to Applied Optics, pp. 8121-8124, Dec. 1 1994.

[7] D. Lee, D. Newmark, K. Toh, P. Flanner, A. R. Neureuther, "Splat v5.0 Users' Guide," Memorandum No. UCB/ERL M95/13, 3/1/95.

[8] The National Technology Roadmap for Semiconductors, Semiconductor Industry Association.

[9] N. Harned, J. McClay, J. J. Shamaly, "Laser-Damage Impact on Lithography System Throughput," IEEE Journal of Selected Topics in Quantum Electronics, Vol. 1, No. 3, pp. 837-840, Sept. 1995.

[10] personal communication with Jan Mulkens of ASM Lithography Inc.

Chapter 8

Conclusions and Future Work

8.1 Conclusions

In this thesis, Deep-UV damage in fused silica was investigated to characterize the limitations of using refractive optics for DUV lithography. A relatively simple technique was adopted using birefringence measurements which enabled the real-time monitoring of compaction. The method, described in Chapter 2, proved capable of measuring compaction in the 10 parts per billion range, orders of magnitude more sensitive than previous methods. Using the birefringence monitor and absorption measurements, drastically different transient and thermal properties between color center formation and compaction were observed, indicating that the two were distinct damage forms.

In this work, a universal relation describing UV-induced compaction was found where, using the total energy absorbed from two-photon absorption as the dose parameter, density changes are equal to a material dependent constant times the dose parameter to a power of about 0.7. With the exception of the two-photon damage excitation, this behavior was consistent with past compaction studies using electron beam and gamma radiation, suggesting like densification mechanisms. Additional evidence, presented in Chapter 4, further supported a two-photon absorption damage process for compaction and color center formation. Despite this seemingly fundamental damage behavior, substantial differences in damage rates were found among the many fused silicas evaluated

in Chapters 3 and 6. This was an encouraging result because it suggests that more durable fused silicas can be developed for UV-applications.

The analysis of the component contributing to optical path difference formation in damage fused silica presented in Chapter 5 was motivated by the need to better predict the effects of radiation in elements in a real lithographic tool. The modeling of the effects of damage on lithographic performance presented in Chapter 7 would have been more accurate if the relations developed in Chapter 5 were more rigorously applied. The analysis in Chapter 7 gave a useful estimate of how much damage could be allowed in a system without severely degrading image performance. Compaction in elements near the pupil plane of the system was shown to be important despite the much lower relative intensities in those elements. The effects of different illumination sources was also characterized where systems with less coherence were predicted to have longer lifetimes.

Certainly, one could envision a more rigorous modeling of the effects of compaction on system performance by taking into account damage in each of the 20 or so optical elements individually. Using the experimental relations for compaction formation and the machinery developed describing the optical effects of compaction for arbitrary geometries and wavelengths, the tools are now available perform such an analysis.

Still, much is unknown about the mechanisms involved with UV-induced damage in fused silica. This thesis will conclude by first describing initial observations on irradiated-

induced fluorescence in fused silica. A discussion of the origin of the power-law dependence of damage on dose is then included in this chapter. Finally, preliminary work on characterizing the structural form of compaction is described followed by a discussion of two relevant models.

8.2 The Role of Fluorescence in Damage

One of the phenomenon involved with damage that should be studied further is that of radiation-induced fluorescence. Krajnovich[1,2] et al. recorded the transient 650nm fluorescence induced from 248nm radiation in a variety of fused silicas. Suprasil 311, Suprasil 2 and Corning 7940 all had similar magnitudes of red fluorescence that remained steady or increased slightly during exposure. The "fast-relaxers" (SV1A1, SV2G1, P20 and P30) had about a factor of three weaker red fluorescence. Suprasil 300 ("dry" fused silica) had no measurable red fluorescence at the beginning of the irradiation but had fluorescence of similar magnitude to the "fast-relaxers" later in the exposure. Sharp increases in fluorescence were observed after pauses in the exposures which were later attributed[3] to temperature changes in the sample. Fluorescence was found to decrease sharply as the sample temperature increased from absorption-induced heating.

Only qualitative observations were recorded during the irradiations described in this thesis. Because the exposures here were performed at much lower pulse energy densities on samples with less absorption, temperature changes were small and most likely did not effect fluorescence. The observations described below were recorded at UC-Berkeley

using 193nm radiation on the (1990-1994) grade specimens. Suprasil 300, again with no

initial fluorescence, gradually fluoresced red with a relatively low intensity. Corning 7940

began with very faint white fluorescence that gradually developed to red. Suprasil 2 had

faint blue fluorescence that faded with continuing exposure. SV2G1 fluoresced white with

a sharp decrease in magnitude at the beginning of the exposure. Both samples of Suprasil

311 showed the same fluorescence phenomenon after an (NI^2/τ) dose of about 1000 that

was one half fluoresced red while the back half fluoresced green (N in millions of pulses, τ

in nanoseconds, I in mJ/cm^2). By flipping the samples around with respect to the incoming

beam, it was verified that the fluorescence differences resulted from material differences

though the thickness of the sample and not due to intensity variations through the sample.

As described in Chapter 5, the side of the sample which fluoresced red had a much larger

surface depression induced from the exposure, indicating higher compaction. The

experimental samples provided by SEMATECH showed the same general trend where

those which fluoresced white or blue had lower compaction rates while those which

fluoresced red showed the worst compaction behavior.

Little concrete knowledge on the phenomenon is available despite the presence of

fluorescence during the numerous fused silica radiation studies previously cited in Chapter

1. The red fluorescence band has often been associated with the Non-Bridging Oxygen

Hole Center (NBOHC). Griscom[4], however, presents evidence inconsistent with this

conclusion. Griscom also reviews other possible theories on the electronic or defect states

involved with the fluorescence. While fluorescence is generally believed to be a sign that

damage is occurring, for a given dose rate the samples with the least fluorescence tend to damage with a faster rate. This observation coupled with the trend of lower damage in samples fluorescing at lower wavelengths (higher energy), suggests that the release of energy radiolytically through fluorescence may reduce damage rates by providing a benign mechanism for energy dissipation.

8.3 Origin of Power-Law Dependence of Damage on Dose

The studies presented in Chapter 1 showing a sub-linear dependence of paramagnetic defect generation on dose generally monitors defect generation over at most two orders of magnitude. Galeener[5] attributed the non-linear production of defects to a simultaneous "activation" of pre-existing precursor sites and linear increase of additional precursor sites. Primak[24] shows a nearly 2/3 power law dependence of compaction on radiation dose over three orders of magnitude ($\Delta\rho/\rho \sim 10^{-6}$ - 10^{-3}). In this thesis, a nearly identical dose dependence (taking into account two-photon excitation) is found over an additional 1.5 orders of magnitude ($\Delta\rho/\rho \sim 4 \times 10^{-8}$ - 10^{-6}). This behavior cannot be easily explained by any simple form of saturating behavior, simultaneous production of damage precursors, or competing compaction-expansion processes.

Primak[6] attributes the reduced power dependence of compaction on dose as a "hardening" effect. He asserts that compaction occurs most readily in stressed portions of the network. Because the compaction acts to reduce stress in the network, this is no longer a

simple saturation process. Compaction would be then inversely proportional to the number of sites compacted.

Griscom[7,8] et al. suggest a different model where the power-law growth is described as an ensemble of saturating exponentials. The model assumes that defect growth results from independent subpopulations, each with a characteristic production rate constant and recombination rate constant. Subpopulations with larger growth rates saturate with faster recombination rates. Subpopulations with lower growth rates, while having minimal contributions to the initial defect generation rate, become dominant at higher defect densities. The Griscom model is successful in predicting the transient annealing behavior of damaged optical fibers[9] using second-order kinetics without any additional assumptions.

The power-law dependence of damage on dose seems fundamental to both color center formation and compaction in fused silica. Such behavior over several orders of magnitude is unique and counter-intuitive. Neither the Griscom or Primak models, furthermore, have sufficient support to be convincing at this time. While we present no new theory, we point to the unusual annealing behavior of damaged fused silica as an area for further scrutiny. The post-irradiation thermal decay of damage generally follows a "stretched" behavior that cannot be assigned to a single activation energy[9,10]. The fact that annealing occurs at relatively low temperatures suggests that simultaneous annealing may be occurring during radiation as the effective temperature of an irradiated area is temporarily raised due to

absorbed energy. A better understanding of the annealing process may, therefore, yield

insight into the origin of the power-law dependence of damage on dose.

8.4 The Structural Form of Compaction

8.4a Raman Spectroscopy and X-Ray Diffraction Experiments

The samples studied in this work generally have density changes of a few ppm or less.

Obtaining structural information via diffraction or spectroscopic techniques resulting from

such small alterations is difficult. To partially alleviate this concern, a Suprasil 2 sample

which had been irradiated for 70 million, $40mJ/cm^2$, 193-nm pulses was obtained from

MIT Lincoln Laboratories[11]. Using the data of Chapter 6, at least a 50 ppm density

increase would be expected. The sample is cylindrical with a 2.54-cm diameter and a 1-

cm. The irradiated region is rectangular, roughly 15mm by 7mm, and offset from the

center by about 5mm. The lack of symmetry of the compaction makes the extrapolation

of the compaction level from birefringence monitoring excessively arduous.

The Raman spectra of a 0.16mm diameter portion of the sample within and outside the

irradiated region were measured using a 547nm source[12]. Figure 1 shows both spectra as

well as the difference between the two spectra. The irradiated portion has a larger

intensity uniformly across the entire Raman spectra. This is consistent with data measured

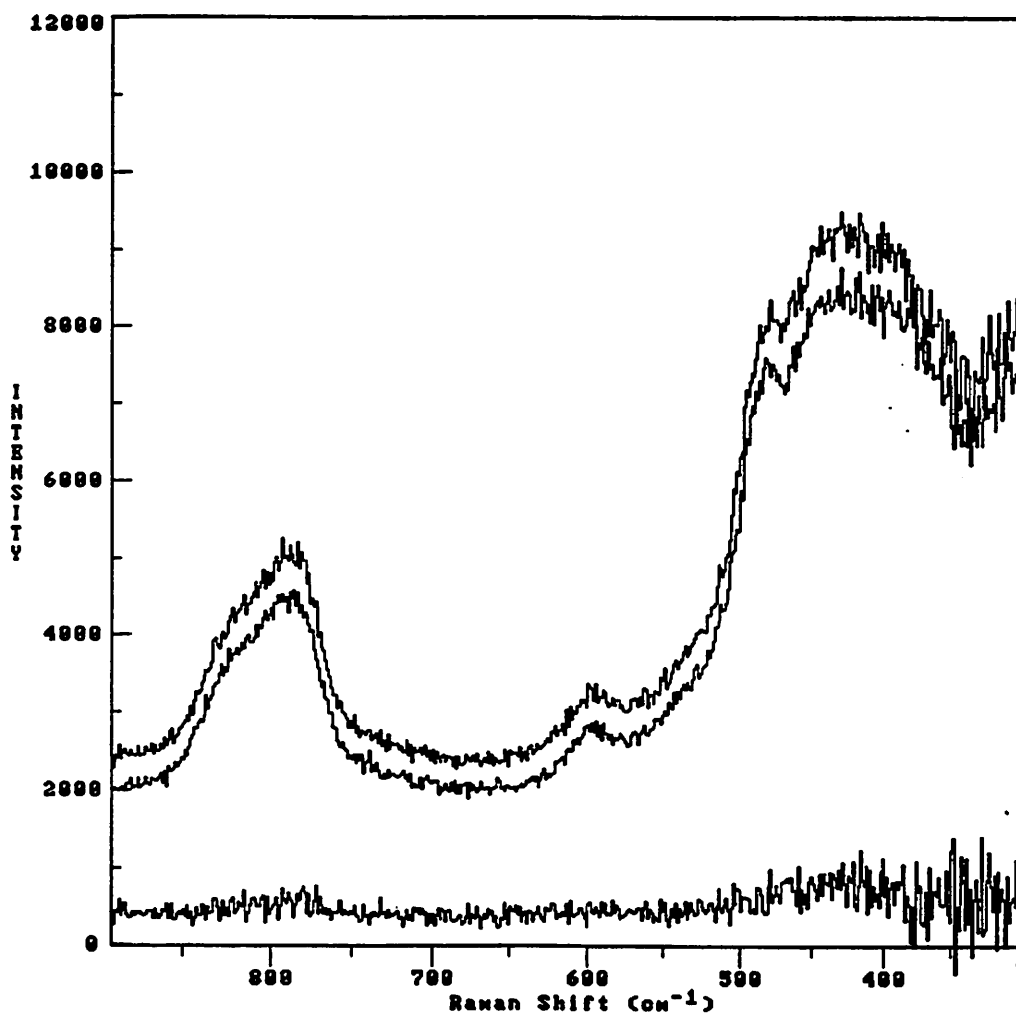by Bates[13] which showed an increase of the Raman spectra intensity after neutron

205

Figure 1. Raman spectra of Suprasil 2. Lower spectra for unirradiated area, upper spectra for area on same sample irradiated with 70 million, 40mJ/cm^2, 193-nm pulses. The difference between the two spectra is also shown. The D_1 and D_2 bands are at 490 cm^{-1} and 605 cm^{-1} respectively.

irradiation. The increased Raman signal may be at least partially a result of the tensile stress formed in the irradiation region as past work[14,15] has shown that the Raman spectra is lowered during the presence of compression stress from external pressure.

No measurable increase in the D_2 (605 cm^{-1}) or D_1 (490 cm^{-1}) Raman peaks is observed, consistent with past findings[16,17]. The D_2 and D_1 bands have been assigned[18] to 3 and 4 silicon ring structures respectively. It appears that compaction is not a result of formation of additional 3 and 4 member ring structures, at least not of the order of the intrinsic ring densities.

The X-ray diffraction spectra of a portion of the sample within and outside the irradiated region were measured[19] using a un-narrowed Copper Kα X-ray source (1.5 Angstrom wavelength). The X-ray beam diameter is approximately 5mm. Figure 2 shows the spectra from the irradiated and unirradiated areas. The signal from intrinsic scattering is not subtracted, but the property that both spectra have equal magnitudes at high diffraction angles indicated that scattering was equal for both measurements. Like the comparison of the spectra from undamaged material to neutron irradiated material presented in Chapter 1, the characteristic first broad X-ray diffraction peak is smaller for the UV-irradiated sample. Unlike for the neutron spectra, the entire spectra of the irradiated sample is smaller. Since the spectrum is related to the transform of the electron probability density, this suggests that the irradiated area has a less-ordered structure than does the pristine material. Because later X-ray diffraction tests[20] on the same sample were

unable to reproduce the results presented here, further experiments on additional samples are needed to characterize the effects of UV-induced compaction on the X-ray diffraction spectrum of fused silica.
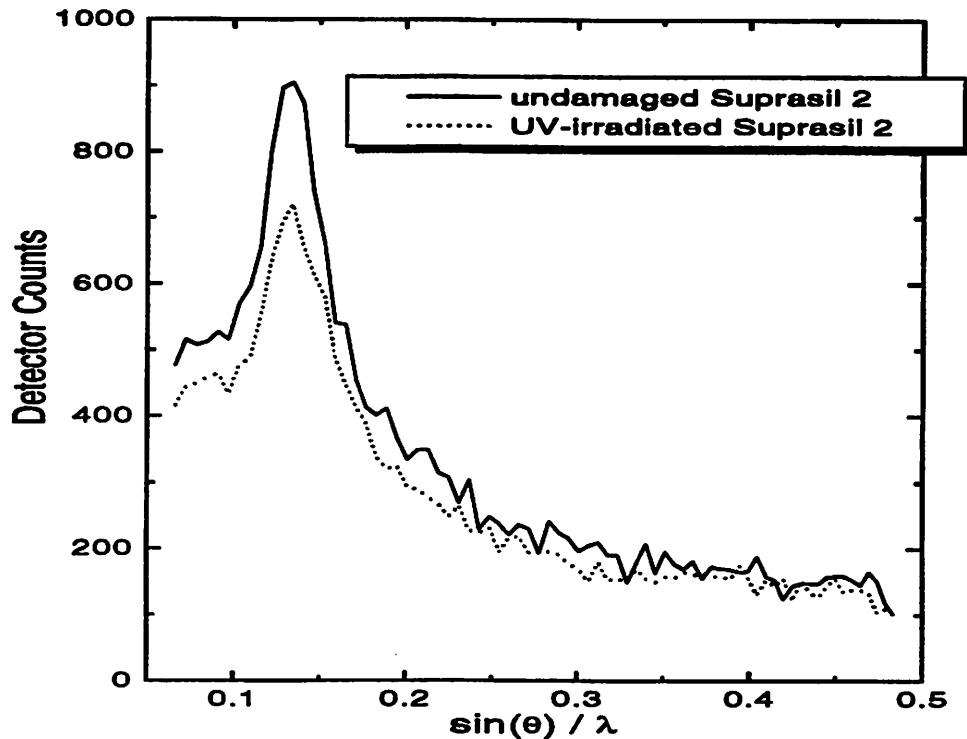

Figure 2. X-ray diffraction spectra of Suprasil 2. Upper spectra for undamaged area, upper spectra for area on same sample irradiated with 70 million, 40mJ/cm^2, 193-nm pulses.

8.4b Revesz Compaction Model

As alluded to in Chapter 1, Revesz[21] proposes a model which describes compaction as a result of decreased π-bonding in the fused silica system. π-bonding orbitals, unlike spherically shaped σ bonds, are "figure-eight" shaped with a null in the electron probability function half way between the centers of the two bonding atoms. In the SiO$_2$ network, π-

bonding results from the overlap of the originally empty Si 3d orbitals with the O 2p orbital containing the lone pair electron. This $d\pi$-$p\pi$ bond is more delocalized than the σ bond between the Si sp^3 hybrid and O 2p orbitals, and hinders rotation about the Si-O bond. A decrease in π-bonding would be expected to correspond to a decrease in the average Si-O-Si angle[22] (less overlap between Si 3d orbitals with the O 2p orbital) which naturally would yield a density decrease. The model describes the metamict state (as defined in Chapter 1) of silica as a result of an equilibrium between the tendencies to minimize bond strain and to maximize the level of π-bonding. While π-bonding is energetically favorable for an individual SiO_2 molecule, π-bondings hinders rotation about the Si-O bond which tends to cause bond strain. The ionic component of the Si-O bond increases with a decrease in π-bonding. The consistency of the Revesz model with some of the observed property changes in fused silica induced from radiation is detailed below. The model does not identify the structural modifications inducing the decrease in π-bonding. Both network relaxations from bond cleavage and denser SiO_2 packing from bond angle reorganization could be responsible.

1) Bond polarizability is expected to decrease with a decrease in π-bonding[23]. The polarizability of fused silica, as shown in Chapter 5, decreases with compaction which is consistent with Revesz's model. Also in agreement with the model, the bond polarizability of quartz increases during radiation-induced expansion[21].

2) One of the strengths of the Revesz compaction model is its agreement with the annealing properties of densified silica. From the initial slope of annealing curves, an "unusually low" activation energy (0.04-0.4 eV) is measured[10] for densified fused silica. Similarly low annealing activation energies are being found in tests[20] on UV-irradiated fused silicas. This indicates that viscous flow is not responsible for annealing because viscous flow requires the breaking of Si-O bonds at an activation energy[10] of 5-7 kcal mole^{-1}. Bond angle rearrangement is innately a lower energy process.

3) The Revesz compaction model similarly agrees with the activation energy of compaction formation. Data presented in Chapter 4 shows a very weak dependence of compaction rate on sample temperature. The activation energy for compaction formation is found to be about 0.2 eV, very similar to the activation energy of annealing. More recent tests[20] for 193-nm compacted samples show, within experimental error, no increase in compaction rate with sample temperature. More experiments are required to determine if this discrepancy is a result of different fused silicas being studied or due to using a much lower intensity for the 193-nm tests. Past compaction studies using gamma rays did not find a temperature dependence for compaction rates[24] up to 100°C.

4) Since π-bondings hinders rotation about the Si-O bond, a reduction in π-bonding would seemingly allow for greater flexibility in the fused silica network. This flexibility would most likely result in a more random distribution of SiO_2 building blocks within the network. The X-ray diffraction results presented in Figure 2, although likely a product of

experimental error, are consistent with a more random electron distribution in the SiO₂ network.

8.4c The role of the NBOHC in Compaction

As alluded to in Chapter 1, the best correlation between a specific defect and radiation-induced compaction are found with the NBOHC. Rajaram[25] et al. reported a linear relationship between compaction-induced surface depression depths and NBOHC concentrations for some silicas from electron exposures. Tsai et al. also report a correlation between the annealing characteristics of compaction of Zerodur[26] and Optosil[27] and the ESR signal of NBOHC's. Zerodur is a glass-ceramic material composed of 80% lithium aluminum silicate crystal and 20% high silica glass. Like compaction, furthermore, no saturation of NBOHC concentration is reported for gamma, X-ray or UV-radiation. The fact that several paramagnetic defects follow a similar dose dependence as compaction and makes these correlations less meaningful. More studies are needed, especially on UV-grade fused silicas. Compaction may indeed be a result of reorganization of the existing bond structure as opposed to being a product of bond rupturing or defect formation. A deeper understanding of the structure and mechanisms behind radiation-induced compaction would undoubtedly facilitate the development of more damage resistant optical materials.

References

[1] D.J. Krajnovich, I.K. Pour, A.C. Tam, W.P. Leung, M.V. Kulkarni, "248 nm lens materials: performance and durability issues in an industrial environment," Proc. SPIE 1848, 544-560, 1993.

[2] D.J. Krajnovich, I.K. Pour, "Long-term effects of pulsed KrF laser radiation on crystalline and amorphous SiO_2," SPIE Vol. 2114, 1994.

[3] personnel communication with Douglas Krajnovich of IBM Almaden.

[4] D. L. Griscom, "Optical properties and structure of defects in silica glass," Journal Ceramic Society of Japan, 99, pp. 923-942, 1991.

[5] F. L. Galeener, "Non-linear γ-ray activation of defect spins in vitreous silica," Journal of Non-Crystalline Solids 149, pp. 27-31, 1992.

[6] W. Primak, "Mechanism for the Radiation Compaction of Vitreous Silica," Journal of Applied Physics, Vol. 43, No.6, pp. 2745-2754, June 1972.

[7] D. L. Griscom, M. E. Gingerich, E. J. Friebele, "Radiation-Induced Defects in Glasses: Origin of Power-Law Dependence of Concentration on Dose," Physical Review Letters, Vol. 71, No. 7, pp. 1019-1022, 16 Aug. 1993.

[8] D. L. Griscom, M. E. Gingerich, E. J. Friebele, "Model for the Dose, Dose-Rate and Temperature Dependence of Radiation-Induced Loss in Optical Fibers," IEEE Transactions on Nuclear Science, Vol. 41, No. 3, pp. 523-527, June 1994.

[9] E. J. Friebele, M. E. Gingerich, D. L. Griscom, "Survivability of optical fibers in space," SPIE Vol. 1791 *Optical Materials Reliability and Testing* , Ed. R. A. Greenwell, D. K. Paul, pp. 177-188, 1992.

[10] R. Bruckner, "Properties and Structure of Vitreous Silica. I," Journal of Non-Crystalline Solids, Vol. 5, pp. 123-175, 1970.

[11] Special thanks to Mordy Rothschild and Jan Sedlacek for donating the sample. The energy density stated is a rough estimate.

[12] Special thanks to Joel Ager of Lawrence Berkeley Laboratories for performing the measurements.

[13] J. B. Bates, R. W. Hendricks, L. B. Shaffer, "Neutron irradiation effects and structure of noncrystalline SiO_2," The Journal of Chemical Physics, Vol. 61, No. 10, pp. 4163-4176, 15 Nov. 1974.

[14] D. R. Tallant, T. A. Michalske, W. L. Smith, "The Effects of Tensile Stress on the Raman Spectrum of Silica Glass," Journal of Non-Crystalline Solids 106, pp. 380-383, 1988.

[15] R. J. Hemley, H. K. Mao, P. M. Bell, B. O. Mysen, "Raman Spectroscopy of SiO_2 Glass at High Pressure," Physical Review Letters, Vol. 57, No. 6, pp. 747-750, 11 Aug. 1986.

[16] J. A. Ruller, E. J. Friebele, "The effect of gamma-irradiation on the density of various types of silica," Journal of Non-Crystalline Solids 136, pp. 163-172, 1991.

[17] H. Hitzler, Ch. Pfleiderer, N. Leclerc, J. Wolfrum, K. O. Greulich, S. Thomas, H. Fabian, R. Takke, W. Englisch, "Transient 210-nm absorption in fused silica induced by high-power UV laser irradiations," Optics Letters, Vol. 16, No. 12, pp. 940-942, June 15, 1991.

[18] F. L. Galeener, F. A. Barrio, E. Martinez, R. J. Elliott, "Vibrational Decoupling of Rings in Amorphous Solids," Physical Review Letters, Vol. 53, No. 25, pp. 2429-2432, Dec. 1984.

[19] Special thanks to James Chan, a former UCB EECS graduate student for performing measurements.

[20] tests performed by F. Piao at UC-Berkeley.

[21] A. G. Revesz, "π Bonding and Delocaliazation Effects in SiO$_2$ Polymorphs," Physical Review Letters, 27 (23), pp. 1578-1581, 1971.

[22] concepts like this can be reviewed in any of a number of organic chemistry texts.

[23] A. G. Revesz, "Defect Structure and Irradiation Behavior of Noncrystalline SiO$_2$." IEEE Transactions on Nuclear Science, NS-18 (6), pp. 113-116, 1971.

[24] W. Primak, R. Kampwirth, "The Radiation Compaction of Vitreous Silica," Journal of Applied Physics, Vol. 39, No. 12, pp. 5651-5657, Nov. 1968.

[25] M. Rajaram, T. E. Tsai, E. J. Friebele, "Radiation-Induced Surface Deformation in Low-Thermal-Expansion Glasses and Glass-Ceramics" Advanced Ceramic Materials, Vol. 3, No. 6, pp. 598-600, 1988.

[26] T. E. Tsai, P. L. Higby, E. J. Friebele, D. L. Griscom, "Radiation effects on a low-thermal-expansion glass ceramic," Journal of Applied Physics, Vol. 62, No. 8, pp. 3488-3490, 15 Oct. 1987.

[27] E. J. Friebele, P. L. Higby, "Radiation Effects in Amorphous SiO$_2$ for Windows and Mirror Substrates," in Laser Induced Damage in Optical Materials: 1987, NIST Spec. Pub. 756, pp. 89-97, 1988.